

**Fabrication and Characterization of Flexible Thin-Film Superconducting
Microwave Cables**

by

Vaibhav Gupta

A dissertation submitted to the Graduate Faculty of
Auburn University
in partial fulfillment of the
requirements for the Degree of
Doctor of Philosophy

Auburn, Alabama
August 7, 2021

Keywords: Superconductor, resonator, flexible, dielectric, niobium, microwave, microstrip,
stripline

Copyright 2021 by Vaibhav Gupta

Approved by

Michael C. Hamilton, Chair, James B. Davis Professor of Electrical and Computer
Engineering

Stuart M. Wentworth, Associate Professor of Electrical and Computer Engineering

Mark L. Adams, Associate Professor of Electrical and Computer Engineering

Ryan B. Comes, Thomas and Jean Walter Assistant Professor of Physics

Minseo Park, Professor of Physics

Abstract

The future of superconducting and cryogenic electronic systems depends on densely integrated superconducting multi-layer and multi-signal flexible cables due to the massive number of electrical interconnects needed in systems such as superconducting quantum computers and detector arrays. Flexible superconducting cables, based on Nb and polyimide (PI), in a microstrip and stripline transmission line configuration is demonstrated in this work. In addition to providing useful mechanical and electrical properties, polyimide also offers low thermal leakage and is amenable to multi-layer fabrication, which are important considerations for electrical interconnects in densely-integrated cryogenic electronics systems.

In order to maintain superconductivity in niobium (Nb) thin films, film stress and degradation must be minimized. In a stripline configuration with embedded traces, the superconductor material will be subjected to subsequent fabrication steps; these must not degrade the properties of the superconductor. We observed degradation in the superconducting properties of Nb, such as reduction of both superconducting transition temperature and critical current, as a result of curing a polyimide passivation layer at supplier recommended curing temperature (350 °C). This deterioration in the superconducting properties may be due to the diffusion of hydrogen or oxygen into Nb during the curing process

We have investigated multiple material stack-ups to protect Nb-based superconducting thin film flexible cables. We show that curing polymers above a certain temperature on top of a Nb layer can adversely affect the superconducting properties including superconducting transition temperature (T_c) and critical current (I_c). Multiple barrier materials have been explored: metals such as Al, Cr and Ta, alternative polymer layers such as Asahi Glass AL-X2010. Metal barrier layers may be viable options for potential use in superconducting flexible cables for high frequency use, provided they do not unduly degrade the high frequency

signal propagation due to microwave skin effects or proximity effects. We used nominal curing temperatures of 350 °C for PI-2611 and 190 °C for AL-X2010. Different thicknesses of metal barrier layers (in the range of 10's of nm) and multiple metal stack-ups have been fabricated and tested. Atomic layer deposition (ALD) deposited Al_2O_3 was also investigated as an alternate barrier layer to protect Nb superconductivity at elevated temperatures.

By varying the Ar pressure and applied power during sputter deposition, we have produced both tensile and compressive films in order to find the pressure that yields a near zero stress Nb and Nb/Al thin film. A low stress Nb film was tested with a thin Al barrier layer (of the order of 10's of nm) between Nb and polyimide on both sides (top and bottom) to preserve Nb superconductivity during the curing step in order to overcome the observed degradation effects.

We have designed, fabricated and characterized a fully-shielded stripline structure, with bottom ground – middle signal – top ground configuration, and we report on these efforts here. The stripline fabrication process incorporates thin layers of Al between the Nb and PI, which serves as barrier layers, to protect the Nb superconductivity during the PI curing step. 20 μm thick layers of photo-definable PI (HD-4110), 250 nm thick layers of Nb, 20 nm thick Al layers and an electroplated Cu via process, were used for this work. 25 cm long, 3-metal layer stack-up (i.e., ground-signal-ground) stripline transmission lines were fabricated with a line width of 24 μm , yielding a characteristic impedance of $\sim 50 \Omega$. We also fabricated stripline resonators, with a length of 13 cm, following the same fabrication process as stripline transmission line, in order to provide a sensitive measurement of the loss of the stripline structures. Both transmission lines and resonators were encapsulated with 4 μm thick HD-4100 to enhance the mechanical reliability and robustness of the cables.

In order to better design and optimize various types of low loss superconducting flexible transmission line cables, we have explored multiple techniques to separate the conductor and dielectric losses using weakly-coupled SC embedded microstrip transmission line resonators.

The high-quality factor resonators provide sensitive measurements of the aggregate loss properties of the conductor and dielectric, as functions of frequency and temperature. Different resonator structures were investigated such as embedded, non-embedded and embedded with a barrier layer of Al_2O_3 . One of the techniques included the measurement of quality factor (Q_l) for each resonator case after being exposed to elevated temperatures: 225 °C, 250 °C and 275 °C. The impact of temperature on the overall resonator internal loss was studied, in order to better characterize and separate the dielectric loss and conductor loss. The other technique involved the use of external magnetic field to suppress the superconductivity and thereby reducing the conductor loss. Different intensities of magnetic field were applied to find the the reduction in T_c of the resonator. Surface resistance analysis was performed on the different resonator structures mentioned previously. Residual resistance and BCS resistance were extracted using the temperature dependence of surface resistance for each resonator. The results of this work are important for understanding loss and transmission properties of similarly designed and fabricated transmission line interconnects.

The data presented in this paper provides design guidance for constructing low-loss, flexible thin-film superconducting interconnects using transmission line configurations. It also provides a solution to robust, multi-layer interconnects, with enhanced shielding and low cross-talk for use in future cryogenic electronics systems.

Acknowledgments

First and foremost, I would like to express my sincere gratitude to my advisor, Dr. Michael C. Hamilton for his continuous support and technical guidance throughout my PhD study at Auburn University. His patience, encouragement and knowledge has immensely helped me in my doctoral study. It has been a great privilege and honor to have him as my advisor.

I am extremely grateful to my dissertation committee: Dr. Mark L. Adams, Dr. Stuart M. Wentworth and Dr. Ryan B. Comes for their helpful feedback on my dissertation. I would also like to extend my sincere thanks to Dr. Minseo Park for serving as University Reader for my PhD work.

The completion of this work could not have been accomplished without the support of our lab manager and my mentor, Drew Sellers. He has always provided the right kind of motivation and enthusiasm which helped me succeed, work hard and grow as an individual. I could not have imagined a better mentor for my PhD study.

A special thanks to Dr. Charles Ellis, for helping me navigate through several challenges in the early years of my graduate career.

This work would not have been possible without the technical guidance from Dr. David B. Tuckerman. Thank you for sharing your expertise.

I would also like to thank my fellow lab-mates, Bhargav Yelamachilli, Sherman Peek, Archit Shah, George Hughes, Ran Cheng, Uday Goteti and Simin Zou for their numerous discussions over various research topics and for making my time at Auburn a memorable one. I would also like to recognize the assistance/help that I received from several undergraduate students, Nick Rush, Jacob Ward and Grant Gleason.

I would like to acknowledge the Alabama Micro/Nano Science and Technology Center (AMNSTC) for providing access to fabrication and characterization facilities used in this work.

I owe a deep sense of gratitude to four beloved people who have meant and continue to mean so much to me. First and foremost, to my paternal grandparents, Kedar Nath Gupta and Santosh Gupta. Although they are no longer of this world, their memories continue to regulate my life. Next, my maternal grandparents, Narendra Kumar Gupta and Prem Lata Gupta, whose love for me knew no bounds. Thank you so much for encouraging me to pursue my dreams.

Lastly and most importantly, I am deeply indebted to my parents Ravi Kumar Gupta and Indu Gupta and my brother Shalabh Gupta for their continuous support, love and care during the course of my doctoral study. My deepest gratitude to my loving and supportive wife, Sasha Lynn Gupta, for her unwavering encouragement during the challenges of graduate school and life. I am truly thankful for having you in my life.

Table of Contents

Abstract	ii
Acknowledgments	v
List of Figures	xii
List of Tables	xxix
List of Abbreviations	xxx
1 Introduction	1
1.1 Background and Motivation	1
1.2 Superconductivity	2
1.3 BCS Theory	4
1.4 Two Fluid Model	5
1.5 Superconducting Material Selection: Nb	8
1.6 Literature Review of Work on Superconducting Flexible Cables and Nb Degradation	10
2 Multiple Ways to Preserve Nb Superconductivity in Thin-Film Superconducting Flexible Cables	15
2.1 Preserving Nb Superconductivity by Curing Polymers at Low Temperatures	15
2.1.1 Low Temperature Curing Tests Using PI-2611 Polyimide	15
2.1.2 Low Temperature Curing Tests Using HD-4110 Polyimide	18
2.1.3 Low Temperature Curing Tests Using PI-2555 Polyimide	19
2.2 Barrier Layers to Protect Nb Superconductivity in Thin Film Superconducting Flexible Cables	21
2.2.1 Fabrication Process	22
2.2.2 Measurement Setup	23

2.2.3	Results and Discussion	25
2.3	Atomic Layer Deposited Materials as Barrier Layers for Preservation of Nb Superconductivity in Multilayered Thin-Film Structures	28
2.3.1	Fabrication Process	30
2.3.2	Measurement Methods and Setup	33
2.3.3	Results and Discussion	34
2.4	Nb Embedded Structures Using Al Barrier Layer and Low Temperature Cured Polyimide	38
2.5	Secondary Ion Mass Spectroscopy (SIMS) Study for Nb Degradation	42
2.6	Sample Preparation and Measurement Results	43
2.6.1	SIMS Analysis on Nb/PI (375 °C)	47
2.6.2	SIMS Analysis on Nb/PI (225 °C)	48
2.6.3	SIMS Analysis on Al/Nb/Al/PI (375 °C)	49
2.6.4	SIMS Analysis on Al ₂ O ₃ /Nb/Al ₂ O ₃ /PI (375 °C)	50
2.6.5	Acknowledgement	51
3	Minimizing Film Stress and Degradation in Thin-Film Nb Superconducting Cables	52
3.1	Fabrication and Measurement setup	53
3.2	Stress of Nb on Kapton	53
3.2.1	Test Results for Different Power Levels - 0.75 kW and 1.25 kW	55
3.3	Stress of Al/Nb/Al Film on Kapton	60
4	Design, Fabrication and Characterization of Superconducting Flexible Stripline Transmission Line and Resonators	63
4.1	Introduction	63
4.2	ADS Layout of Stripline Transmission Line and Transmission Line Resonator	64
4.3	Fabrication Process	66
4.4	Measurement Methods	72
4.5	Results and Discussion	74

4.5.1	DC Properties of Stripline Transmission Lines	74
4.5.2	Microwave Measurement of Stripline Transmission Lines	76
4.5.3	Microwave Characterization of Stripline Resonators	80
4.5.4	Conclusion	81
4.6	Microwave Optimization of Connector Transitions For Superconducting Ca- bles Using Microstrip Transmission Lines	82
4.6.1	Fabrication and Measurement Methods	86
4.6.2	DC Measurement Results of Microstrip Transmission Lines	89
4.6.3	Microwave Measurement Results of Microstrip Transmission Lines	91
4.7	Conclusion	94
5	Multiple Approaches to Separate Conductor Loss From Dielectric Loss Using Superconducting Resonator Structures	96
5.1	Resonator Theory	96
5.1.1	Parallel Resonator	97
5.1.2	Series Resonator	98
5.1.3	Quality Factor Calculation	99
5.1.4	Resonator Design	101
5.2	Fabrication and Microwave Characterization of Flexible Thin Film Nb Res- onator Structures	102
5.2.1	Resonator Fabrication Process	102
5.2.2	Cryogenic and Microwave Measurement Setup	104
5.2.3	Design and Characterization of Non-Embedded Resonator Structure at Cryogenic Temperatures	104
5.2.4	Design and Characterization of Embedded Resonator Structure at Cryogenic Temperatures	109
5.2.5	Design and Characterization of Embedded Resonator Structure With a Barrier Layer of Al ₂ O ₃ at Cryogenic Temperatures	112

5.3	Separation of Conductor and Dielectric Losses Using Resonators Measured at Multiple Temperatures	115
5.3.1	Measurement Results and Discussion	118
5.3.2	Extraction of Dielectric Loss for Different Resonator Structures	125
5.3.3	Extraction of Conductor Loss for Different Resonator Structures	131
5.4	Separation of Conductor and Dielectric Losses Using an External Magnetic Field on Microstrip Resonators	138
5.4.1	Magnetic Test Fixtures	139
5.4.1.1	Fixture for Magnetic Field Strength of 0.5 kG	139
5.4.1.2	Fixture for Magnetic Field Strength of 2 kG	140
5.4.1.3	Fixture for Magnetic Field Strength of 4 kG	141
5.4.2	Measurement Setup	142
5.4.3	Results and Discussion	143
5.5	Surface Resistance Analysis for Resonator Structures Cured at Multiple Temperatures	165
5.5.1	Residual Resistance	173
5.5.2	BCS Resistance	176
6	Summary and Conclusion	183
7	Future Work	186
	Bibliography	188
	Appendices	194
A	Microwave Measurement of Thin Film Superconducting Resonator Structures with Different Linewidth	195
B	Moisture Effect on Microwave Performance of Microstrip Resonators on Polyimide	197
B.1	Embedded Resonator Structure	197
B.2	Non-embedded Resonator Structure	199
B.3	Embedded Resonator Structure With a Barrier Layer of Al ₂ O ₃	201

C Fabrication Travelers 204

List of Figures

1.1	Graphical representation of normal metals and superconductors. Adapted from [1].	2
1.2	Image showing the magnetic phase diagram of type 1 and type 2 superconductors. Adapted from [2]	3
1.3	Periodic table indicating the superconducting elements. Adapted from [3].	4
1.4	Cross-section image of microstrip (left) and stripline (right) structures. Adapted from [4].	4
1.5	Image showing the electron-phonon interaction leading to formation of cooper pairs. Adapted from [5].	5
1.6	BCS energy gap for density of cooper pairs and quasi-particles and two-fluid circuit model for superconductor. Adapted by [6]	6
1.7	n_s vs. temperature as shown in Eq. 1.7. Adapted from [7].	8
1.8	CHA Mark 50 metal deposition system.	9
1.9	Nb based flexible connector attached to LC-filter by a bump array. Adapted from [8].	10
1.10	Schematic representation of the lithographic fabrication process for the connector, including interfaces with LC filter- and detector-chips. Adapted from [8].	11

1.11	Resistance vs. temperature measurement measurement of Nb-based traces across the flexible connector. Track with highest T_c : 14 μm wide bottom line. Track with lowest T_c : 10 μm wide upper line. Adapted from [8].	11
1.12	Schematic representation of the layer build-up of the flex cable (left) and solder pads (right). Adapted from [9].	12
1.13	Superconducting transition of a Ti/Nb/Ti flex cable, 25 μm track width. Adapted from [9].	13
1.14	Nb flex cable mounted using solder interconnect onto a PCB. Adapted from [9].	13
1.15	Experimental setup used to measure the thermal conductivity of the flex cable. Adapted from [9].	14
2.1	Resistance vs. temperature measurement for PI-2611 coated sample cured at different temperatures for one sample.	16
2.2	Plot of normalized resistance vs. temperature measurement for PI-2611 coated sample cured at different temperatures for a different sample.	17
2.3	Plot of normalized resistance vs. temperature measurement of samples with PI-2611 cured at 225 $^{\circ}\text{C}$ on Nb/Al(20 nm).	18
2.4	Plot of normalized resistance vs. temperature measurement of samples with HD-4110 cured at 225 $^{\circ}\text{C}$ on Nb.	19
2.5	Plot of normalized resistance vs. temperature measurement of Nb samples with and without PI-2555 cured at 200 $^{\circ}\text{C}$	20
2.6	Plot of normalized resistance vs. temperature measurement of Nb/Al (20 nm) samples with and without PI-2555 cured at 200 $^{\circ}\text{C}$	21

2.7	Optical image of a fabricated 50 μm wide line with metal stack of Nb (250 nm)/Al (10 nm). A portion of a test probe pad is visible on the left side of the image.	23
2.8	Pulse-tube cryostat.	24
2.9	PCB mounted onto a Cu sample holder for making 4-point probe resistance measurements low temperatures.	24
2.10	Plot of normalized resistance vs. temperature measurement of different types and thicknesses of metallic capping layers with no polymer overcoat.	26
2.11	Plot of normalized resistance vs. temperature measurement after over-coating metal lines with 10 μm of PI-2611 cured at 350 $^{\circ}\text{C}$	26
2.12	Plot of normalized resistance vs. temperature measurement after over-coating metal lines with 12 μm of AL-X2010 cured at 190 $^{\circ}\text{C}$	27
2.13	Plot of normalized resistance vs. temperature measurement of two independent depositions of 250 nm Nb traces capped with 20 nm Al before applying polyimide.	27
2.14	Plot of normalized resistance vs. temperature measurement of 250 nm Nb traces capped with 20 nm Al after over-coating with 10 μm of PI-2611 and curing at 350 $^{\circ}\text{C}$	28
2.15	Image of the thermal ALD system including the deposition chamber, pressure monitor, precursors, valves and other electrical components.	31
2.16	Schematic showing the detailed step-by-step process for depositing one atomic layer of Al_2O_3 on a substrate using the precursors (TMA and H_2O).	31
2.17	50 μm wide Nb lines on Si substrate with pads on each side to make 4-point probe measurement.	32

2.18	Schematic cross-section of 250 nm Nb sputter deposited on bare Si (Sample 1(a)).	33
2.19	Schematic cross-section of 250 nm Nb sandwiched between two Al ₂ O ₃ layers (Sample 2 (a)).	33
2.20	Schematic cross-section of 250 nm Nb over-coated with 20 μm HD-4110 (Sample 1(b)).	34
2.21	Schematic cross-section of 250 nm Nb capped with Al ₂ O ₃ and over-coated with HD-4110 (Sample 2 (b)).	34
2.22	Plot of normalized resistance vs. temperature showing superconducting transition temperature of Sample 1(a) without over-coated HD-4110 and of same sample (now Sample 1(b)) with over-coated HD-4110 cured at 225 °C.	35
2.23	Plot of normalized resistance vs. sample temperature showing superconducting transition temperatures of Sample 2(a) with Al ₂ O ₃ /Nb/Al ₂ O ₃ without over-coated HD-4110 and of same sample (now Sample 2(b)) with over-coated HD-4110 and cured at different temperatures (225 °C and 375 °C).	36
2.24	Plot of normalized resistance vs. sample temperature showing superconducting transition temperatures of Sample 3 with Al ₂ O ₃ /Nb/Al ₂ O ₃ without over-coated HD-4110 and of same sample with over-coated HD-4110 and cured at different temperatures (225 °C and 375 °C).	37
2.25	Image of a released PI-2611/Nb/PI-2611 sample.	38
2.26	Plot of normalized resistance vs. temperature measurement of PI-2611/Nb/PI-2611 samples with bottom PI-2611 cured at 350 °C and top PI-2611 cured at 225 °C.	39
2.27	Image of a released PI-2611/Nb/Al(20 nm)/PI-2611 embedded sample.	39

2.28	Plot of normalized resistance vs. temperature measurement of PI-2611/Nb/Al(20 nm)/PI-2611 samples with bottom PI-2611 cured at 350 °C and top PI-2611 cured at 225 °C.	40
2.29	Embedded PI-2611/Al(20 nm)/Nb/Al(20 nm)/PI-2611 released.	41
2.30	Plot of normalized resistance vs. temperature measurement of PI-2611/Al(20 nm)/Nb/Al(20 nm)/PI-2611 samples with bottom PI-2611 cured at 350 °C and top PI-2611 cured at 225 °C.	41
2.31	adapted from [10].	42
2.32	Image of the etched area in Si of Nb/PI (375 °C) sample.	44
2.33	Image of the etched area in Si of Nb/PI (225 °C) sample.	45
2.34	Image of the etched area in Si of Al/Nb/Al/PI (375 °C) sample.	46
2.35	Image of the etched area in Si of Al ₂ O ₃ /Nb/Al ₂ O ₃ /PI (375 °C) sample.	47
2.36	Depth profile for Nb/PI (375 °C) structure. The interfaces of interest are highlighted in red.	48
2.37	Depth profile for Nb/PI (225 °C) structure. The interfaces of interest are highlighted in red.	49
2.38	Depth profile for Al/Nb/Al/PI (375 °C) structure. The interfaces of interest are highlighted in red.	50
2.39	Depth profile for Al ₂ O ₃ /Nb/Al ₂ O ₃ /PI (375 °C) structure. The interfaces of interest are highlighted in red.	51
3.1	Images of 250 nm thin-film Nb deposited using different Ar pressures on 50 μm thick Kapton substrates, exhibiting different stress characteristics.	54

3.2	Plot of normalized resistance vs. temperature measurement comparison of \sim 250 nm Nb deposited on 50 μ m thick Kapton using different Ar pressures. The sputtering power used was 1 kW over a target area of \sim 127 cm ²	55
3.3	Plot of normalized resistance vs. temperature measurement of Nb deposited using Ar pressure of 4 mTorr and power or 0.75 kW.	56
3.4	Image of Nb deposited on Kapton substrate using Ar pressure of 4 mTorr and power of 0.75 kW exhibiting slightly compressive stress.	57
3.5	Plot of normalized resistance vs. temperature measurement of Nb deposited using Ar pressure of 4 mTorr and power or 1.25 kW.	58
3.6	Image of Nb deposited on Kapton substrate using Ar pressure of 4 mTorr and power of 1,25 kW exhibiting compressive stress.	59
3.7	Image of metal stack Al (20 nm)/ Nb (250 nm)/ Al (20 nm) on a 50 μ m thick Kapton substrate. Nb was deposited using 4 mTorr Ar pressure. The room temperature stress on Kapton was approximately neutral as exhibited by the flatness of the free (unmounted) sample.	60
3.8	Plot of normalized resistance vs. temperature measurement comparison of metal stack Al(20 nm)/Nb (250 nm)/Al (20 nm). Nb was deposited using 4 mTorr Ar pressure.	61
4.1	ADS layout of stripline transmission line and transmission line resonators on a 150 mm diameter Si wafer. The layout includes 3 stripline transmission lines (centre), 4 stripline transmission line resonators (bottom), 2 microstrip transmission line (one on each side) and via chains structures.	65
4.2	ADS layout of a stripline transmission line (left) and transmission line resonator (right).	66

4.3	Schematic sample cross-sections at various points during fabrication, showing key fabrication process steps for superconducting stripline transmission lines.	69
4.4	Wafer level image of the stripline transmission line after spin-coating HD-4110 and creating openings to catch-pad for plating.	70
4.5	Wafer level image of the stripline transmission line after spin-coating HD-4110 on top of signal layer and plating Cu through the openings in HD-4110 to connect bottom and top ground layers.	70
4.6	Wafer level image of the stripline transmission line after depositing UBM (Ti/Cu/Au) layer to make connections for signal and ground layer.	71
4.7	Flexible Al/Nb/Al stripline transmission line (25 cm long, meandered), with Southwest Microwave, Inc. SMA end-launch connectors attached and mounted to a PCB support board. Note that two transmission lines, involving four external connections, are connected in this structure. The design provides meandered lines that are in close proximity over a substantial portion of their length and is also used for cross-talk characterization.	71
4.8	Flexible Al/Nb/Al stripline transmission line resonator (13 cm length for resonant section), with Southwest Microwave, Inc. SMA end-launch connectors attached and mounted to a PCB support board.	72
4.9	A stripline transmission line sample mounted on a sample holder, connected to cryogenic cables, for use in the PT system.	73
4.10	Agilent (Keysight) N5227A network analyzer with multiple ports.	73
4.11	T_c measurement results for flexible stripline transmission lines measured in a pulse tube cryostat.	75

4.12 T_c measurement results for the stripline ground plane measured in a pulse tube cryostat.	75
4.13 I_c measurement results for flexible stripline transmission lines measured in a pulse-tube (PT) cryostat at different temperatures or in a LHe dewar at 4.2 K.	76
4.14 S_{11} of a 25 cm long flexible superconducting stripline transmission line measured in a LHe dewar ($T = 4.2$ K). ADS simulation result is also shown.	77
4.15 S_{21} of a 25 cm long flexible superconducting stripline transmission line measured in a LHe dewar (4.2 K). ADS simulation result is also shown.	78
4.16 S_{21} per unit length of a 25 cm long flexible superconducting stripline transmission line measured in a LHe dewar (4.2 K).	78
4.17 Near end cross-talk measurement and simulation of Al/Nb/Al stripline transmission line cables at 4.2 K.	79
4.18 Far end cross-talk measurement and simulation of Al/Nb/Al stripline transmission lines at 4.2 K.	80
4.19 $1/Q_l$ vs. resonant frequency comparison of stripline transmission line resonators for measurements at different temperatures.	81
4.20 Close-up view of the anti-pad opening in the ground plane.	82
4.21 ADS layout of a microstrip transmission line.	83
4.22 S_{21} simulation of 2 cm long microstrip with varying anti-pad widths in Sonnet.	84
4.23 S_{21} simulation of 1 cm long microstrip with varying anti-pad widths in HFSS.	85
4.24 Image showing the connection regions with varying anti-pad width of 132 μm , 176 μm and 220 μm in ground layer.	86

4.25	Image of flexible Al/Nb/Al microstrip transmission line after release.	87
4.26	Schematic sample cross-section at various points during fabrication, showing key fabrication process steps for superconducting microstrip transmission lines.	88
4.27	T_c measurement results for flexible microstrip transmission lines measured in a pulse tube cryostat.	89
4.28	I_c measurement results for flexible microstrip transmission lines measured in a pulse tube cryostat.	90
4.29	S_{21} of a 13 cm long flexible superconducting microstrip transmission line measured in a LHe dewar ($T = 4.2$ K) with anti-pad width of $132 \mu\text{m}$	91
4.30	S_{21} of a 13 cm long flexible superconducting microstrip transmission line measured in a LHe dewar ($T = 4.2$ K) with anti-pad width of $176 \mu\text{m}$	92
4.31	S_{21} of a 13 cm long flexible superconducting microstrip transmission line measured in a LHe dewar ($T = 4.2$ K) with anti-pad width of $220 \mu\text{m}$	92
4.32	S_{21} of a 13 cm long flexible superconducting microstrip transmission line measured in a LHe dewar ($T = 4.2$ K) with no anti-pad.	93
4.33	Comparison of normalized S_{21} for microstrip transmission lines (with different antipad widths).	93
4.34	Peak and trough analysis, along with corresponding quadratic fit, for microstrip with no anti-pad and microstrip with anti-pad width of $176 \mu\text{m}$	94
5.1	Parallel R-L-C circuit. Adapted from [11].	97
5.2	Magnitude response of input impedance as a function of frequency. Adapted from [12].	97

5.3	Series RLC circuit. Adapted from [11]	98
5.4	Magnitude response of input impedance as a function of frequency. Adapted from [12].	99
5.5	Bandwidth of a resonant circuit indicating resonance frequency. Adapted from [13].	100
5.6	Top view of both ends of the microstrip transmission line resonator indicating the coupling region.	101
5.7	Process flow for embedded microstrip transmission line resonator.	103
5.8	Flexible Nb resonator assembly with Southwest Microwave, Inc SMA end-launch connectors mounted, attached to a support board.	104
5.9	3D view of one end of a non-embedded microstrip resonator structure.	105
5.10	S_{21} measurement results of non-embedded resonator structure measured at 4.2 K over a wide frequency range (1 GHz - 21 GHz).	106
5.11	Fundamental resonance measurement and the corresponding Lorentz fit for non-embedded resonator structure.	107
5.12	$1/Q_l$ vs. temperature plot showing degradation of non-embedded sample after different curing temperatures.	108
5.13	$1/Q_l$ vs. temperature plot showing degradation of non-embedded sample after different curing temperatures.	109
5.14	3D view of one end of a embedded microstrip resonator structure.	110
5.15	$1/Q_l$ vs. temperature plot showing degradation of embedded sample after different curing temperatures.	111

5.16	1/ Q_l vs. temperature plot showing degradation of embedded sample after different curing temperatures.	112
5.17	3D view of one end of a embedded microstrip resonator structure with a 20 nm thick Al ₂ O ₃ barrier layer.	113
5.18	1/ Q_l vs. temperature plot showing degradation Al ₂ O ₃ /Nb/Al ₂ O ₃ sample after different curing temperatures.	114
5.19	1/ Q_l vs. temperature plot showing degradation Al ₂ O ₃ /Nb/Al ₂ O ₃ sample after different curing temperatures.	115
5.20	Simulation results of embedded resonator structure at multiple temperatures for varying T _c	117
5.21	Simulation results of non-embedded resonator structure at multiple temperatures for varying T _c	117
5.22	Extracted $\tan\delta$ from embedded and non-embedded resonator structures for varying T _c	118
5.23	1/ Q_l vs. temperature for embedded sample cured at 225 °C.	119
5.24	1/ Q_l vs. temperature for embedded sample cured at 250 °C.	120
5.25	1/ Q_l vs. temperature for embedded sample cured at 275 °C.	120
5.26	1/ Q_l vs. temperature for non-embedded sample cured at 225 °C.	121
5.27	1/ Q_l vs. temperature for non-embedded sample cured at 250 °C.	122
5.28	1/ Q_l vs. temperature for non-embedded sample cured at 275 °C.	122
5.29	1/ Q_l vs. temperature for Al ₂ O ₃ /Nb/Al ₂ O ₃ sample cured at 225 °C.	123

5.30	$1/Q_l$ vs. temperature for $\text{Al}_2\text{O}_3/\text{Nb}/\text{Al}_2\text{O}_3$ sample cured at 250 °C.	124
5.31	$1/Q_l$ vs. temperature for $\text{Al}_2\text{O}_3/\text{Nb}/\text{Al}_2\text{O}_3$ sample cured at 275 °C.	124
5.32	Image of a flow chart showing the steps followed to separate dielectric and conductor loss.	125
5.33	$1/Q_D$ vs. frequency for embedded sample cured at multiple temperatures. . . .	126
5.34	$1/Q_D$ vs. frequency for non-embedded sample cured at multiple temperatures. .	127
5.35	$1/Q_D$ vs. temperature for $\text{Al}_2\text{O}_3/\text{Nb}/\text{Al}_2\text{O}_3$ sample cured at multiple temperatures.	128
5.36	$\tan\delta$ vs. frequency for embedded sample cured at multiple temperatures.	129
5.37	$\tan\delta$ vs. frequency for non-embedded sample cured at multiple temperatures. . .	130
5.38	$\tan\delta$ vs. temperature for $\text{Al}_2\text{O}_3/\text{Nb}/\text{Al}_2\text{O}_3$ sample cured at multiple temperatures.	131
5.39	$1/Q_c$ vs. frequency for embedded sample cured at multiple temperatures.	132
5.40	$1/Q_c$ vs. frequency for non-embedded sample cured at multiple temperatures. .	133
5.41	$1/Q_c$ vs. frequency for $\text{Al}_2\text{O}_3/\text{Nb}/\text{Al}_2\text{O}_3$ sample cured at multiple temperatures.	134
5.42	$1/Q_c$ vs. frequency for all resonator structures cured at 225 °C.	135
5.43	$1/Q_c$ vs. frequency for all resonator structures cured at 250 °C.	136
5.44	$1/Q_c$ vs. frequency for all resonator structures cured at 275 °C.	137
5.45	A 3D model of the test fixture with flexible sample and SMA connectors on each end used to apply 0.5 kG of magnetic field on the resonator samples.	140

5.46	Flexible Nb resonator assembly with Southwest Microwave, Inc SMA end-launch connectors mounted, attached to a 3D printed magnetic test fixture to apply 0.5 kG of magnetic field on the sample under test.	140
5.47	A 3D model of the test fixture with flexible sample and SMA connectors on each end used to apply 2 kG of magnetic field on the resonator samples.	141
5.48	Flexible Nb resonator assembly with Southwest Microwave, Inc SMA end-launch connectors mounted, attached to a 3D printed magnetic test fixture to apply 2 kG of magnetic field on the sample under test.	141
5.49	A 3D model of the test fixture with flexible sample and SMA connectors on each end used to apply 4 kG of magnetic field on the resonator samples.	142
5.50	Flexible Nb resonator assembly with Southwest Microwave, Inc SMA end-launch connectors mounted, attached to a 3D printed magnetic test fixture to apply 4 kG of magnetic field on the sample under test.	142
5.51	LHe dewar.	143
5.52	$1/Q_l$ vs. T/T_c for non-embedded sample. The sample was baked before making measurements.	144
5.53	$1/Q_l$ vs. T/T_c for non-embedded sample. The sample was NOT baked before making measurements.	145
5.54	$1/Q_D$ vs. frequency for non-embedded sample.	146
5.55	$1/Q_D$ vs. frequency for non-embedded sample. NB represents not baked and B represents baked.	147
5.56	Percentage change of $\Delta(1/Q_D)$ vs. frequency for non-embedded sample.	148

5.57 $\tan\delta$ vs. frequency for non-embedded sample.	149
5.58 $\Delta\tan\delta$ vs. frequency for non-embedded sample. NB represents not baked and B represents baked.	150
5.59 Percentage change of $\Delta\tan\delta$ vs. frequency for non-embedded sample.	151
5.60 $1/Q_c$ vs. frequency for non-embedded sample. NB represents not baked and B represents baked.	152
5.61 $1/Q_c$ vs. frequency for non-embedded sample. NB represents not baked and B represents baked.	153
5.62 Percentage change of $\Delta(1/Q_c)$ vs. frequency for non-embedded sample.	154
5.63 $1/Q_l$ vs. T/T_c for embedded sample. The sample was baked before making measurements.	155
5.64 $1/Q_l$ vs. T/T_c for embedded sample. The sample was NOT baked before making measurements.	156
5.65 $1/Q_D$ vs. frequency for embedded sample.	157
5.66 $1/Q_D$ vs. frequency for embedded sample. NB represents not baked and B represents baked.	158
5.67 Percentage change of $\Delta(1/Q_D)$ vs. frequency for embedded sample.	159
5.68 $\tan\delta$ vs. frequency for non-embedded sample.	160
5.69 $\Delta\tan\delta$ vs. frequency for non-embedded sample. NB represents not baked and B represents baked.	161
5.70 Percentage change of $\Delta\tan\delta$ vs. frequency for non-embedded sample.	162

5.71	1/ Q_c vs. frequency for embedded sample. NB represents not baked and B represents baked.	163
5.72	1/ Q_c vs. frequency for embedded sample. NB represents not baked and B represents baked.	164
5.73	Percentage change of $\Delta(1/Q_c)$ vs. frequency for embedded sample.	165
5.74	Surface resistance vs. temperature for embedded sample cured at 225 °C.	168
5.75	Surface resistance vs. temperature for embedded sample cured at 250 °C.	168
5.76	Surface resistance vs. temperature for embedded sample cured at 275 °C.	169
5.77	Surface resistance vs. temperature for non-embedded sample cured at 225 °C.	170
5.78	Surface resistance vs. temperature for non-embedded sample cured at 250 °C.	170
5.79	Surface resistance vs. temperature for non-embedded sample cured at 275 °C.	171
5.80	Surface resistance vs. temperature for Al ₂ O ₃ /Nb/Al ₂ O ₃ sample cured at 225 °C.	172
5.81	Surface resistance vs. temperature for Al ₂ O ₃ /Nb/Al ₂ O ₃ sample cured at 250 °C.	172
5.82	Surface resistance vs. temperature for Al ₂ O ₃ /Nb/Al ₂ O ₃ sample cured at 275 °C.	173
5.83	Residual resistance vs. frequency for embedded resonator structure cured at multiple temperatures.	174
5.84	Residual resistance vs. frequency for non-embedded resonator structure cured at multiple temperatures.	175
5.85	Residual resistance vs. frequency for embedded resonator structure with a barrier layer of Al ₂ O ₃ cured at multiple temperatures.	176

5.86	BCS resistance vs. frequency for embedded resonator structure cured at multiple temperatures. The plot shows measurement at 4.2 K.	177
5.87	BCS resistance vs. frequency for non-embedded resonator structure cured at multiple temperatures. The plot shows measurement at 4.2 K.	178
5.88	BCS resistance vs. frequency for embedded resonator structure with a barrier layer of Al ₂ O ₃ cured at multiple temperatures. The plot shows measurement at 4.2 K.	179
5.89	BCS resistance vs. frequency for all resonator structures cured at 225 °C.	180
5.90	BCS resistance vs. frequency for all resonator structures cured at 250 °C.	181
5.91	BCS resistance vs. frequency for all resonator structures cured at 275 °C.	182
A.1	1/Q _l vs. resonant frequency for resonators with different linewidths at different temperatures. Square = 50 μm, triangle = 100 μm, star = 150 μm, circle = ADS simulation with tan δ = 0 and zero conductor loss.	196
B.1	1/Q _l vs. Temperature plot before and after baking of an embedded sample at 250 °C.	198
B.2	1/Q _l vs. Temperature plot before and after baking of an embedded sample at 250 °C on a log scale.	199
B.3	1/Q _l vs. Temperature plot before and after baking of non-embedded sample at 250 °C.	200
B.4	1/Q _l vs. Temperature plot before and after baking of non-embedded sample at 250 °C on a log scale.	201

B.5	$1/Q_l$ vs. Temperature plot before and after baking of $\text{Al}_2\text{O}_3/\text{Nb}/\text{Al}_2\text{O}_3$ sample at 250 °C.	202
B.6	$1/Q_l$ vs. Temperature plot before and after baking of $\text{Al}_2\text{O}_3/\text{Nb}/\text{Al}_2\text{O}_3$ sample at 250 °C on a log scale.	203
C.1	Traveler for T_c and I_c measurements of Nb.	205
C.2	Resonator Traveler-1/2.	206
C.3	Resonator Traveler-2/2.	207
C.4	stripline Traveler-1/4.	208
C.5	stripline Traveler-2/4.	209
C.6	stripline Traveler-3/4.	210
C.7	stripline Traveler-4/4.	211
C.8	Different barrier layer to protect Nb.	212
C.9	Different curing temperatures of PI-2611.	213
C.10	Different barrier layer after curing AL-X.	214

List of Tables

2.1	T_c and I_c at 4.2 K for different samples.	37
3.1	Thickness, Sheet resistance, Superconducting transition temperature and Critical current comparison for different Ar pressures.	54
3.2	Thickness, Sheet resistance, Superconducting transition temperature and critical current comparison for different power levels with 4 mTorr Ar pressure.	59
3.3	Sheet resistance, Superconducting transition temperature and Critical current comparison for 4 mTorr Ar pressure level for all Al/Nb/Al films.	61
4.1	Comparison of T_c and I_c for different anti-pad widths of microstrips.	90

List of Abbreviations

λ_L	London penetration depth
μ_0	Permeability of free space
ALD	Atomic layer deposition
Ar	Argon
BCS	Bardeen Cooper Schrieffer
DC	Direct current
EBPVD	Electron beam physical vapor deposition
I_c	Critical current
k_b	Boltzmann constant
LHe	Liquid helium
PI	Polyimide
Q_D	Quality factor due to dielectric
Q_{cp}	Quality factor due to coupling
Q_c	Quality factor due to conductor
Q_l	Loaded quality factor
Q_r	Quality factor due to radiation
Q	Quality factor

\mathbf{R}_{BCS}	BCS resistance
\mathbf{R}_{res}	Residual resistance
\mathbf{R}_s	Surface resistance
\mathbf{RF}	Radio Frequency
\mathbf{T}_c	Superconducting transition temperature
\mathbf{UBM}	Under bump metallization

Chapter 1

Introduction

1.1 Background and Motivation

In cryogenic systems such as dilution refrigerators, a large number of semi-rigid coaxial cables are used in order to route many RF and microwave signals. These coaxial cables not only add to the thermal load but also causes thermal leaks between various temperature stages. There is a need for densely-integrated SC interconnect technology with high density, low transmission loss, low thermal leakage, and, preferably, electromagnetic (EM) shielding with low cross-talk. These interconnects are expected to find use in cryogenic electronics systems, such as densely-integrated computing systems, where a large number of interconnects is necessary along with consideration of thermal leakage between temperature stages (i.e., between 77 K and 4 K or between 4 K and 100 mK).

In this work, we present high-density and low thermal leakage cables with low cross-section and wider bandwidth. This was achieved by fabricating and characterizing thin-film superconducting flexible cables with controlled impedance on a low-loss dielectric substrate.

In order to protect Nb in a multi-layer superconducting flexible cable configuration, we developed multiple solutions to protect Nb from degradation caused by curing polyimide on top of Nb at elevated temperatures. Low curing temperatures for polymers were explored as alternate solutions to preserve Nb superconductivity. A fully-shielded stripline process, with bottom ground – middle signal – top ground configuration was fabricated to provide better electromagnetic shielding and low cross talk. In order to cancel the impedance mismatch from the connection pads, microstrip transmission lines were fabricated with varying anti-pad size in the ground plane.

To better design and optimize various types of low loss superconducting flexible transmission lines, weakly-coupled SC embedded microstrip transmission lines resonators with different configurations were fabricated and characterized to differentiate conductor and dielectric loss.

1.2 Superconductivity

A Superconductor is an element, alloy or compound in which the electrical resistance drops to zero when the temperature is reduced below a critical value, known as the superconducting transition temperature (T_c) [14]. Unlike other materials in which the resistance show a gradual decrease but does not vanish, in superconductors the resistance is absolute zero as shown in Fig. 1.1. This abrupt drop in resistance is well explained by BCS theory developed by John Bardeen, Leon Cooper and Robert Schrieffer to understand the behavior of superconducting material.

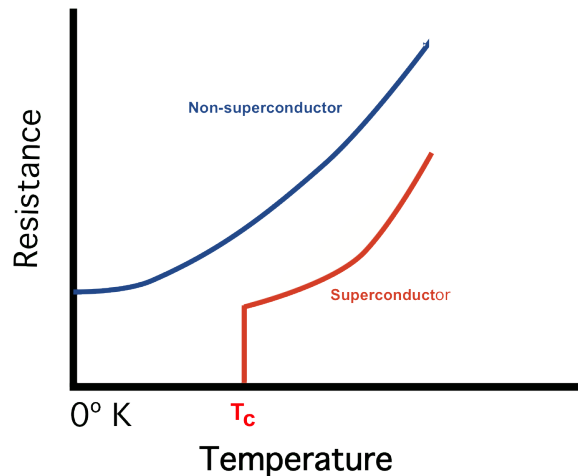


Figure 1.1. Graphical representation of normal metals and superconductors. Adapted from [1].

Superconductors can be classified into various types:

1) Type 1 and type 2 superconductors:

Superconductors are divided into type 1 and type 2 superconductors based on how they behave in the presence of magnetic field. Type 1 usually comprise of pure metals (as shown in Fig. 1.3) which exhibit zero resistivity at low temperatures and are capable of completely

excluding magnetic fields from the interior of superconductors. Type 2 superconductors are usually alloys that have much higher critical current and therefore can carry much higher current densities while still being in a superconducting state. Unlike type 1 superconductor, type 2 superconductor show partial magnetic field expulsion at an intermediate magnetic field strength and show a gradual decrease magnetic field expulsion with increasing magnetic field strength before tuning into a normal conductor (shown in Fig. 1.2).

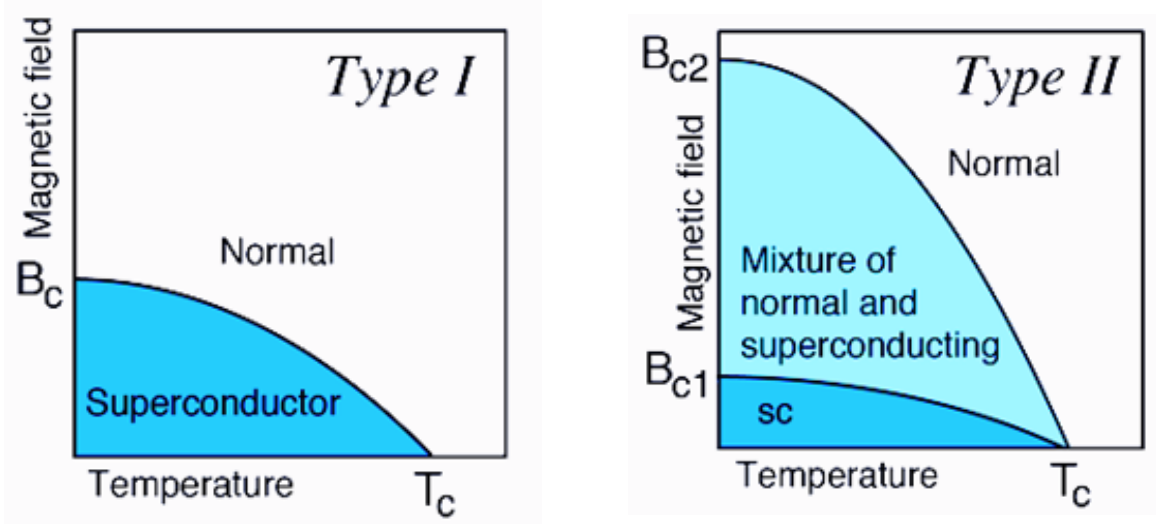


Figure 1.2. Image showing the magnetic phase diagram of type 1 and type 2 superconductors. Adapted from [2]

2) Conventional and unconventional superconductors:

The behavior of conventional superconductors can be explained using BCS theory whereas unconventional superconductors cannot be explained by BCS or related theories.

3) Low temperature and high temperature superconductors:

Elements with superconducting transition temperature below 30 K are known as low temperature superconductor (LTS) and the elements with superconducting transition temperature above 30 K are known as high temperature superconductor (HTS).

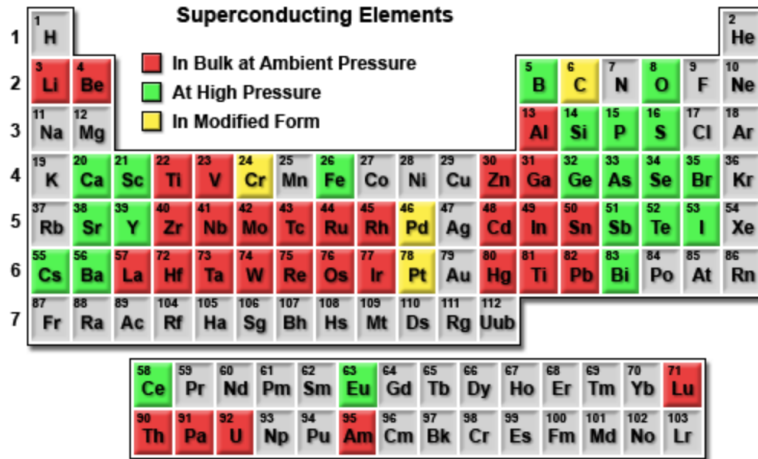


Figure 1.3. Periodic table indicating the superconducting elements. Adapted from [3].

One of the main advantage of using superconductor to transmit microwave signal is its ability to provide low ohmic losses which allows for extremely high efficiency signal transmission. Our goal is to build high density, low thermal leakage cables with small cross section on flexible substrate therefore we designed, fabricated and characterized thin-film transmission lines in microstrip and stripline configurations, as shown in Fig. 1.4.

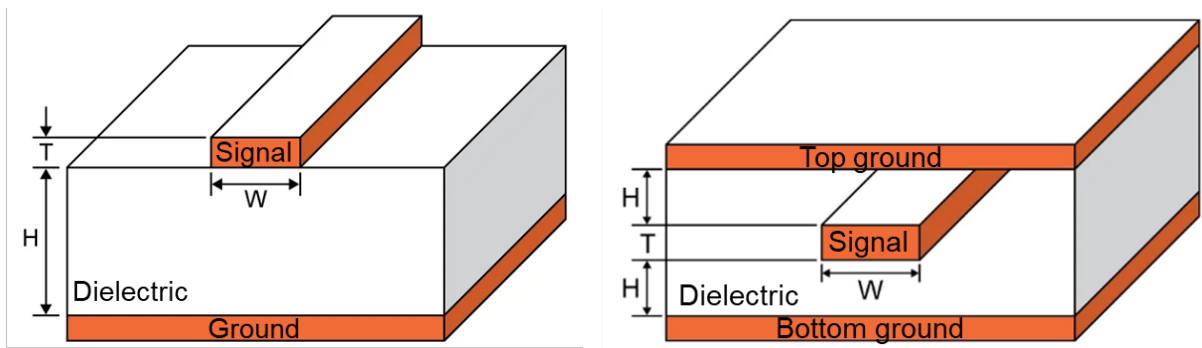


Figure 1.4. Cross-section image of microstrip (left) and stripline (right) structures. Adapted from [4].

1.3 BCS Theory

BCS theory was formulated by John Bardeen, Leon N. Cooper and John R. Schrieffer in 1957 to understand the behavior of superconductors at low temperatures. A key aspect of the theory is pairing of electrons into cooper pairs through slight attraction of electrons related

to lattice vibrations. According to the BCS theory, when a negative charged electron (which act as fermions, due to half integer spin) interact with lattice, it causes vibrations in the lattice structure which leads to emission of phonon. As a result of these vibrations an excess of positive charge ions draws towards the electron. This excess charge attracts the second electron, which absorbs the phonon emitted by the first electron. This interaction of two electrons binds them into a Cooper pairs as shown in Fig. 1.5. Essentially, Cooper pair is a combination of two electrons (that behaves like Bosons and condense into a ground state energy level) with opposite spin and momenta. These Cooper pairs offer no resistance to the flow of the current.

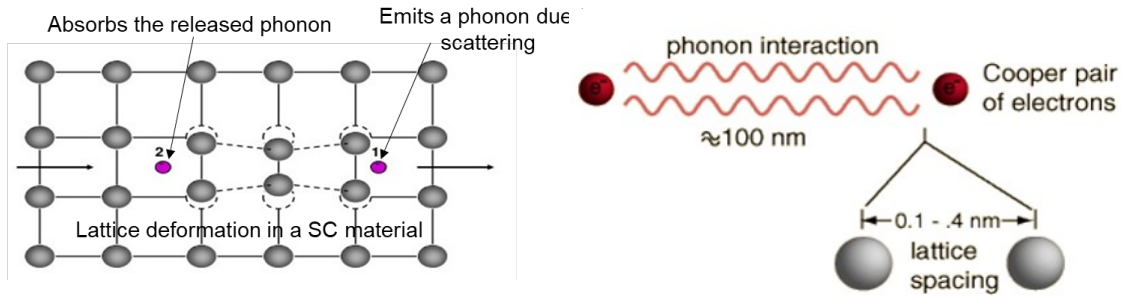


Figure 1.5. Image showing the electron-phonon interaction leading to formation of cooper pairs. Adapted from [5].

1.4 Two Fluid Model

Two fluid model is a very useful model to help us understand the behaviors of superconductors at nonzero temperatures. The electron in a normal metal behaves like free electrons (quasiparticles) in a normal metal i.e. each electron can move independently under the influence of an electric field E , whereas in a superconductor, the electrons are bound together in Cooper pairs. At a certain temperature, T which lies in between absolute 0 and T_c , there will be a mixture of super electrons (Cooper pairs), n_s and normal electrons (quasi-particles), n_n .

$$n_n(T) + n_s(T) = n \quad (1.1)$$

We know from BCS theory that Cooper pairs behaves like Bosons and condense into lowest energy level, thereby creating an energy gap of 2Δ between Cooper pairs (superelectrons) and quasi-particles (normal electrons). The two fluid model realizes superconductors as two parallel channels consisting of quasi-particles and cooper pairs (as shown in Fig. ??) at non-zero temperatures. The quasi-particles are represented by the resistor and the Cooper pairs are represented by the inductor.

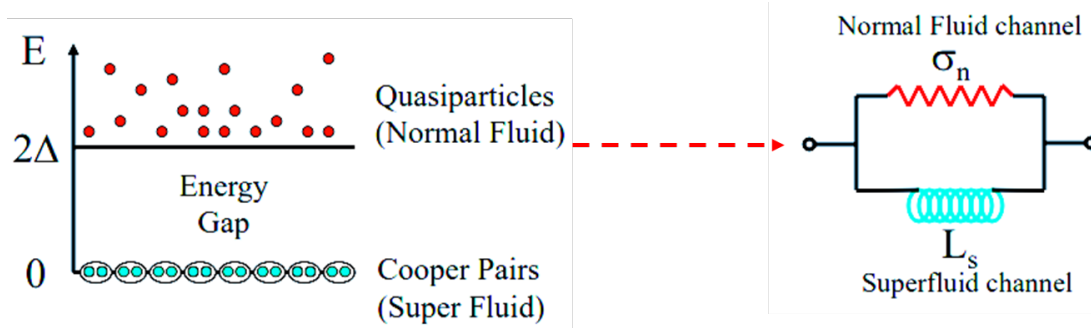


Figure 1.6. BCS energy gap for density of cooper pairs and quasi-particles and two-fluid circuit model for superconductor. Adapted by [6]

In the case of DC, the inductor channel acts as a short, as a result all the current flows through the shorted superfluid channel thereby producing no DC resistance. At low frequencies, most of the current goes through the inductor and some of the current goes through the resistor. At high frequencies, the impedance of the inductor increases and most of the current goes through the resistor channel, which leads to dissipation of energy and breaks Cooper pairs into individual electrons.

Below is the derivation for temperature dependence of n_n and n_s . London penetration depth (denoted by λ_L) represents the distance at which the magnetic field decays in a superconductor. This penetration is governed by the density of n_s . When the superconductor

is cooled below T_c , critical magnetic field gradually increases leading to decrease in the penetration depth. However, when the superconductor is warmed above T_c , critical magnetic field drops to 0, leading to a maximum penetration depth in the superconductor. London penetration depth is expressed as:

$$\lambda_L = \sqrt{\frac{m}{\mu_0 n_s e^2}} \quad (1.2)$$

At a temperature below T_c , Eq. 1.2 can be written as:

$$\lambda(T) = \sqrt{\frac{m}{\mu_0 n_s(T) e^2}} \quad (1.3)$$

At $T = 0$, $n_s = n$ whereas $n_n = 0$. So Eq. 1.3 can be modified as:

$$\lambda(0) = \sqrt{\frac{m}{\mu_0 n e^2}} \quad (1.4)$$

Hence we can write:

$$\frac{n_s}{n} = \left[\frac{\lambda(0)}{\lambda(T)} \right]^2 \quad (1.5)$$

The temperature dependence London penetration depth can be expressed as [7]:

$$\lambda(T) = \lambda(0) \left[1 - \left(\frac{T}{T_c} \right)^4 \right]^{-1/2} \quad (1.6)$$

Using Eq. 1.5 in 1.6, we get:

$$n_s \approx n \left[1 - \left(\frac{T}{T_c} \right)^4 \right] \quad (1.7)$$

Substituting Eq. 1.7 in 1.1 we get:

$$n_n \approx n \left(\frac{T}{T_c} \right)^4 \quad (1.8)$$

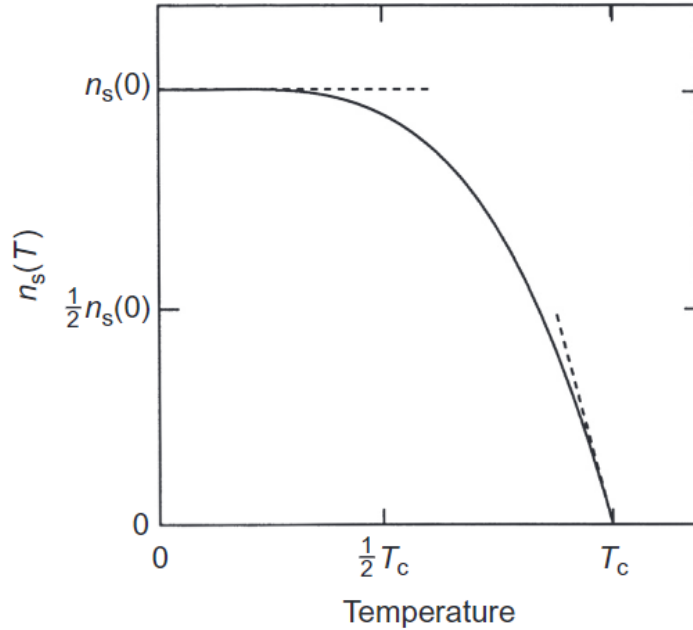


Figure 1.7. n_s vs. temperature as shown in Eq. 1.7. Adapted from [7].

Both n_n and n_s are temperature dependent. Fig.1.7 shows n_s as a function of temperature based on the Eq. 1.7. Eq. 1.8 can be used to estimate the density of super-electrons.

1.5 Superconducting Material Selection: Nb

The key reasons to use Nb was the availability of this material and the deposition system in our fabrication facilities. Nb is a conventional type 2 superconductor and is widely used as a building block in many superconductor applications such as high power accelerator magnets, magnetic resonance imaging, superconducting generators etc. Nb based alloys such as NbTi and Nb₃Sn form the basis of large number of cryogenic cable applications. Nb also offers high thermal conductivity and high melting point (~ 2500 °C). All these qualities make Nb a promising material for use in this study. Nb could be deposited by electron beam physical vapor deposition (EBPVD) or by sputter deposition. In this work we have deposited Nb using a CHA Mark 50 deposition system (shown in Fig. 1.8).



Figure 1.8. CHA Mark 50 metal deposition system.

250 nm thick Nb was used in this work. Nb was deposited using a DC sputter for 30 minutes at an Argon (Ar) pressure of 4 mTorr. The purity of the Nb sputter target used in this work was 99.999%. A vacuum base pressure below 3×10^{-7} Torr was obtained prior to depositing the Nb followed by a Ti evaporation and gettering step, which gave repeatable Nb properties for different samples. A witness sample, 1 cm \times 1 cm Si die with SiO₂, was used to measure the T_c of unpatterned thin film of Nb for this work to ensure good Nb film quality. Typical T_c 's in the range of 8.5 K to 9 K were obtained for various Nb depositions performed in this work.

1.6 Literature Review of Work on Superconducting Flexible Cables and Nb Degradation

Thin film Nb is widely used as a superconducting layer in superconducting electronics (SCE) integrated devices and circuits. Bruijn et al. have described a fabrication process for superconducting, flexible and demountable connector to a kilo-pixel transition edge sensor (shown in Fig. 1.9). The connector part used in this work was made from Nb which retained its superconducting properties and was compatible with the flexible polyimide material processing steps. 400 nm thick SiO_2 buffer layers were used in this work to prevent degradation of Nb. An extra protection to Nb layer from oxidation was provided by using thin tantalum (Ta) layers (as shown in Fig. 1.10). Nb layers are protected against oxidation by thin Ta layers. The connectors were attached to LC filter using a gold (Au) bumping process with under bump metallization of Ti/Au.

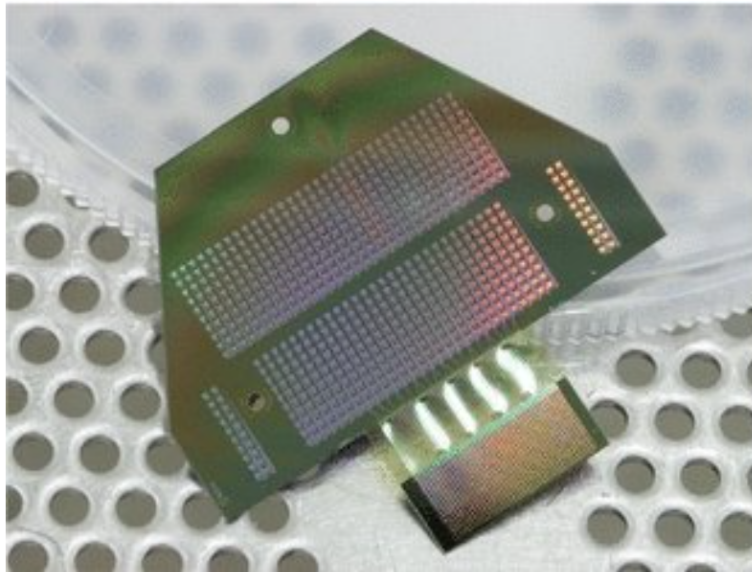


Figure 1.9. Nb based flexible connector attached to LC-filter by a bump array. Adapted from [8].

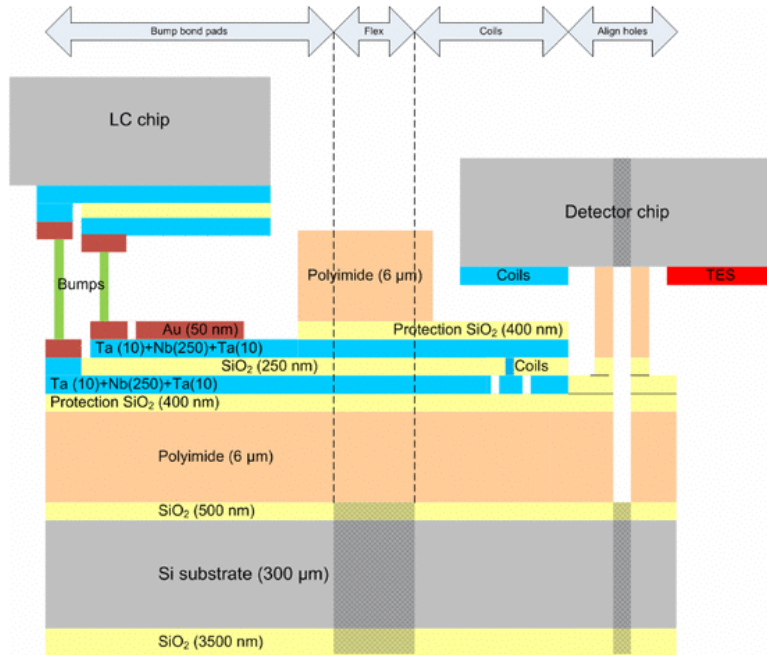


Figure 1.10. Schematic representation of the lithographic fabrication process for the connector, including interfaces with LC filter- and detector-chips. Adapted from [8].

Fig 1.11 shows superconducting transition temperature of two flexible connectors with different trace width of $10 \mu\text{m}$ and $14 \mu\text{m}$. Both Nb connectors achieved superconducting transition temperature of $\sim 7 \text{ K}$.

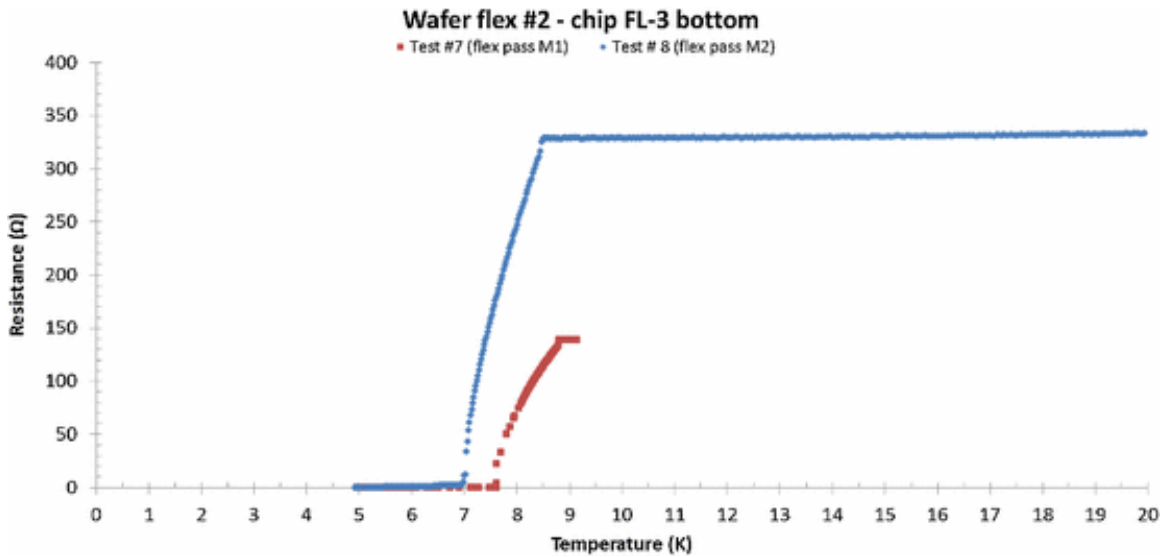


Figure 1.11. Resistance vs. temperature measurement measurement of Nb-based traces across the flexible connector. Track with highest T_c : $14 \mu\text{m}$ wide bottom line. Track with lowest T_c : $10 \mu\text{m}$ wide upper line. Adapted from [8].

Weers et al. have characterized and fabricated Nb flexible cable on Pyralin PI-2611 polyimide substrate suitable for sub-kelvin temperature [9]. Fig 1.12 shows the stack of the Nb flexible cables with titanium (Ti) as an adhesion layer. They also fabricated samples in which an additional Ti layer was used on top of Nb to provide protection from PI-2611 curing at 350 °C.

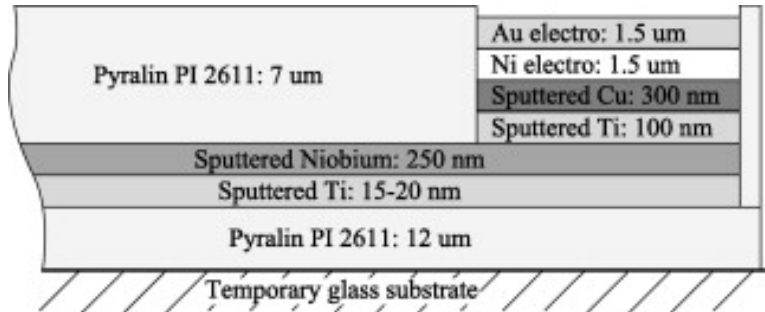


Figure 1.12. Schematic representation of the layer build-up of the flex cable (left) and solder pads (right). Adapted from [9].

Fig. 1.14 shows the transition of a Ti/Nb/Ti flex cable, 25 μm track width which had an RRR of 5. The measurement shows 2 transitions, the first close to the superconducting transition temperature of bulk Nb, the second ~ 7.8 K. The second transition is for only a fraction of the total resistance, possibly related to the SnPb soldered contact areas.

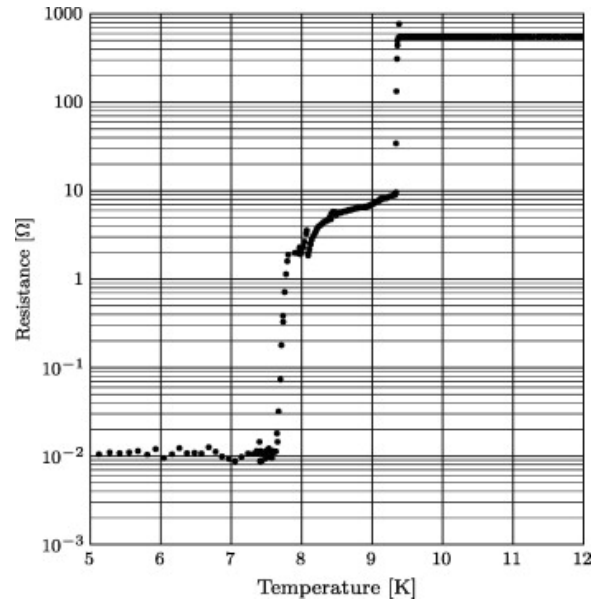


Figure 1.13. Superconducting transition of a Ti/Nb/Ti flex cable, 25 μm track width. Adapted from [9].

In this work, they have also demonstrated a reflow process to solder these flexes directly to PCB's using reflow soldering process (shown in Fig. 1.14)

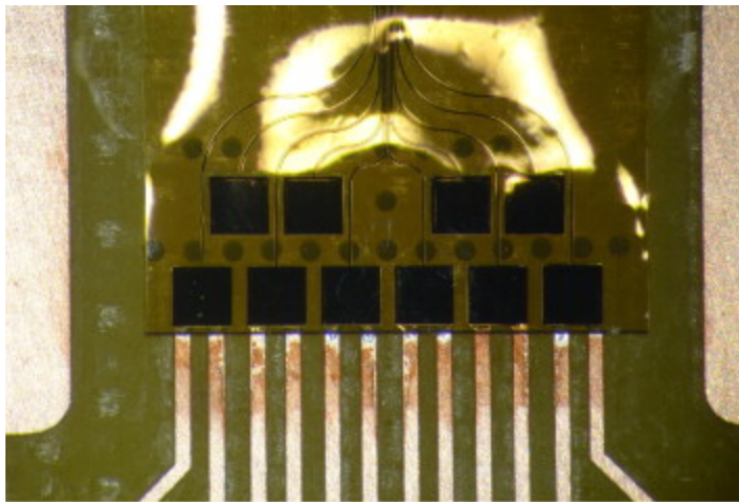


Figure 1.14. Nb flex cable mounted using solder interconnect onto a PCB. Adapted from [9].

The thermal conductivity of Nb on PI-2611 flex cable was measured in the region of 150 mK to 9 K using the setup shown in Fig. 1.15. The upper PCB is thermally anchored to the cold finger of an insertable probe. The bottom PCB is thermally decoupled and includes

a heater. Two RuO₂ SMD resistor thermometers are used to monitor the temperatures T₁ and T₂ of both PCB's.

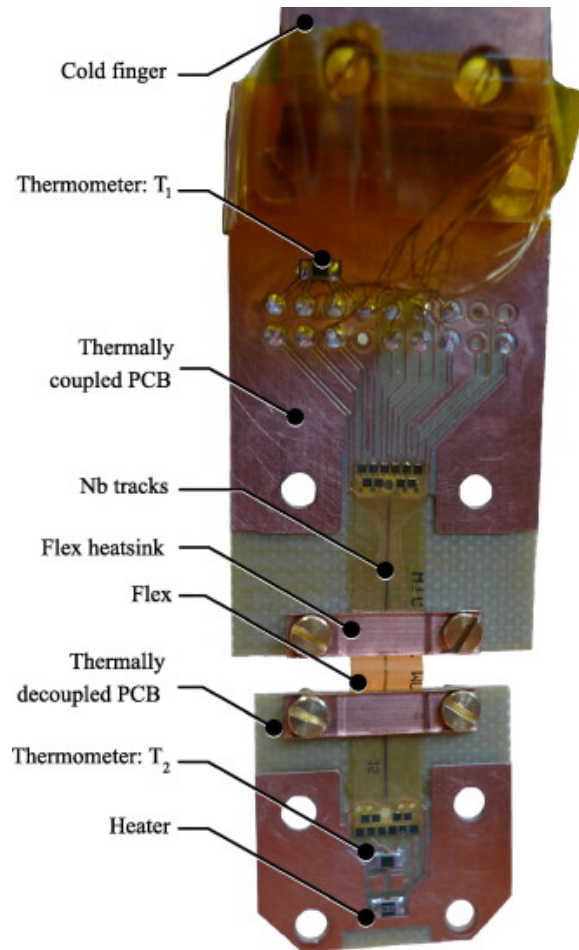


Figure 1.15. Experimental setup used to measure the thermal conductivity of the flex cable. Adapted from [9].

Chapter 2

Multiple Ways to Preserve Nb Superconductivity in Thin-Film Superconducting Flexible Cables

In this section we show multiple ways to protect superconductivity of Nb. Details of the fabrication processes, experimental procedures and performance results are presented in order to provide insight into possible material stack-ups for producing multi-layer Nb-based superconducting flexible cables.

2.1 Preserving Nb Superconductivity by Curing Polymers at Low Temperatures

In this section we have shown that curing polymers above a certain temperature on top of a Nb can adversely affect the superconducting properties including superconducting transition temperature (T_c) and critical current (I_c). We observed a loss in conductivity when polymers were cured on top of Nb at elevated temperatures. Most of the polymers are cured above 250 °C, beyond which the diffusion into the Nb increases and leads to degradation of Nb. Three different polymers: PI-2611, HD-4110 and PI-255 were used in this test.

2.1.1 Low Temperature Curing Tests Using PI-2611 Polyimide

Some of the major benefits of using PI-2611 are low stress, low coefficient of thermal expansion (CTE), low moisture uptake and high modulus for microelectronic application. An aminosilane based adhesion promoter VM-652 was used prior to coating PI-2611 on silicon substrates to improve adhesion. The standard curing temperature for PI-2611 is 350 °C. Multiple samples were measured in order to counter the yield issue and to reproduce the

results. Fig 2.1 shows resistance vs. temperature measurement results showing superconducting transition temperatures for one sample, with and without PI-2611 cured at different temperatures (lower than 350 °C). Minimal degradation in the T_c was seen when the sample was subjected to a curing temperature of 225 °C. However the degradation in T_c is evident when the curing temperature is increased in intervals of 10 °C.

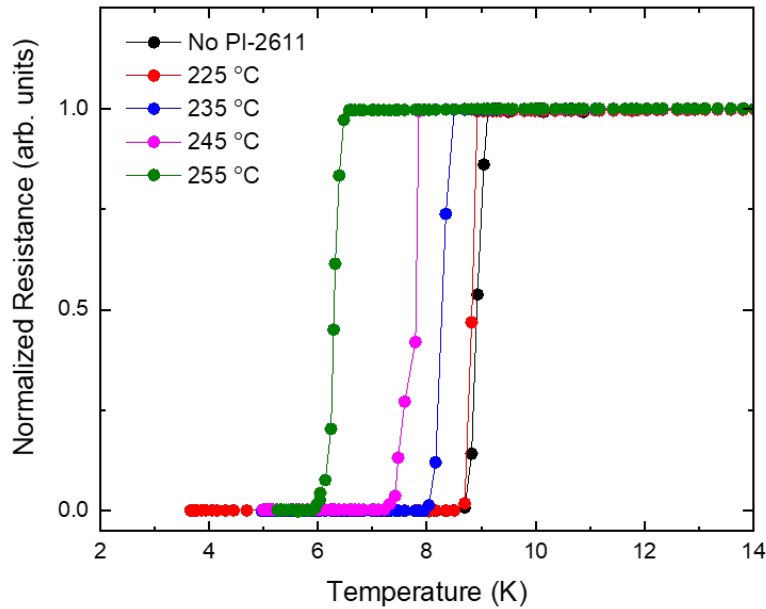


Figure 2.1. Resistance vs. temperature measurement for PI-2611 coated sample cured at different temperatures for one sample.

Fig. 2.2 shows similar trends for another sample and corresponding subsequently-processed versions, which were fabricated and measured in the same way as previous sample. This serves to demonstrate that 225 °C can be used as an alternate curing temperature for PI-2611.

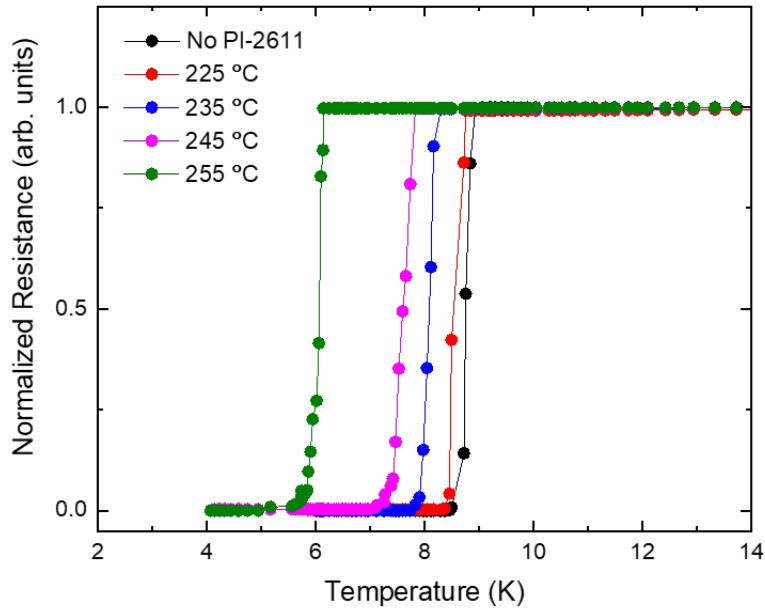


Figure 2.2. Plot of normalized resistance vs. temperature measurement for PI-2611 coated sample cured at different temperatures for a different sample.

Fig 2.3 presents superconducting transition temperature plot of Nb with 20 nm Al capping layers for two independent fabrication runs, before and after over-coating with cured PI-2611 cured at 225 °C. It can be seen that both runs have nearly identical before-and-after T_c values, thereby indicating run-to-run reproducibility and repeatability.

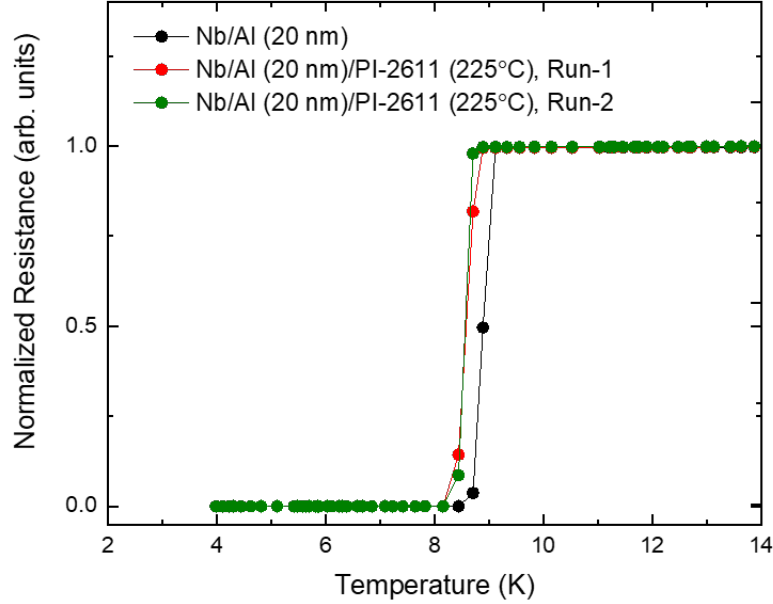


Figure 2.3. Plot of normalized resistance vs. temperature measurement of samples with PI-2611 cured at 225 °C on Nb/Al(20 nm).

2.1.2 Low Temperature Curing Tests Using HD-4110 Polyimide

The photo-definable capability as a spin-on polyimide makes HD-4110 a promising material for various micro-electronic applications. The primary reason for using HD-4100 is that its photo-definable. HD-4100 is an excellent stress buffer and has numerous applications in packaging and flip chip bonding. It is also used to prevent cracking and provide good adhesion to underfill and under bump metallization (UBM) processing steps. The standard curing temperature of HD-4100 is 375 °C. Similar to the case for PI-2611 polyimide, HD-4110 was spun-on and cured at 225 °C on top of Nb. Fig 2.4 shows the superconducting transition temperature of Nb over-coated with HD-4100 cured at 225 °C. An abrupt transition at \sim 8.8 K from normal state to superconducting state can be observed, which indicated that Nb retained its superconducting properties.

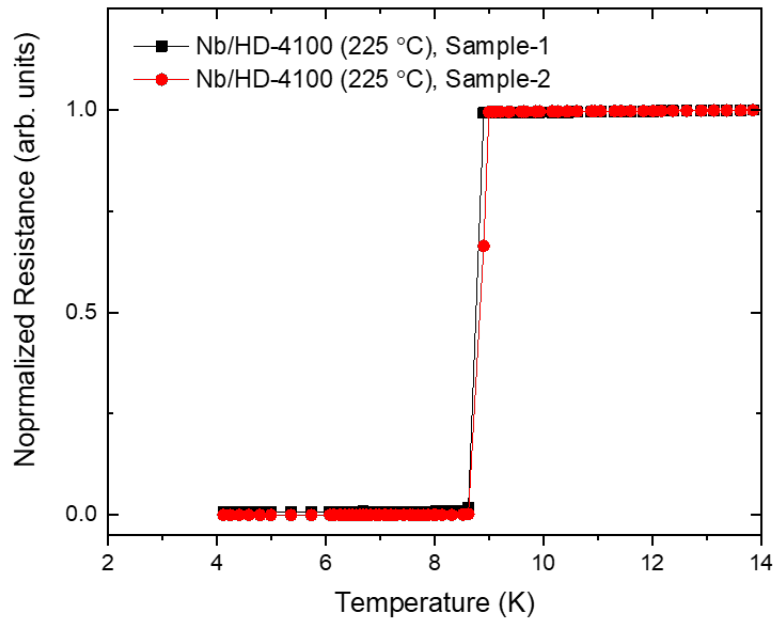


Figure 2.4. Plot of normalized resistance vs. temperature measurement of samples with HD-4110 cured at 225 °C on Nb.

2.1.3 Low Temperature Curing Tests Using PI-2555 Polyimide

PI-2555 is another alternate polymer option from the polyimide family. The key advantage of using PI-255 is its ability to imidize faster at lower temperatures which makes it a good contender for substrates with low temperature tolerance. The curing temperature for PI-2555 is 200 °C. Its most common applications include stress buffer and as inner layer dielectrics over low temperature substrates. Fig 2.5 shows resistance vs. temperature plots for Nb with and without the overcoat of PI-2555. It can be seen that T_c values are nearly identical for both samples, this indicating run-to-run repeatability.

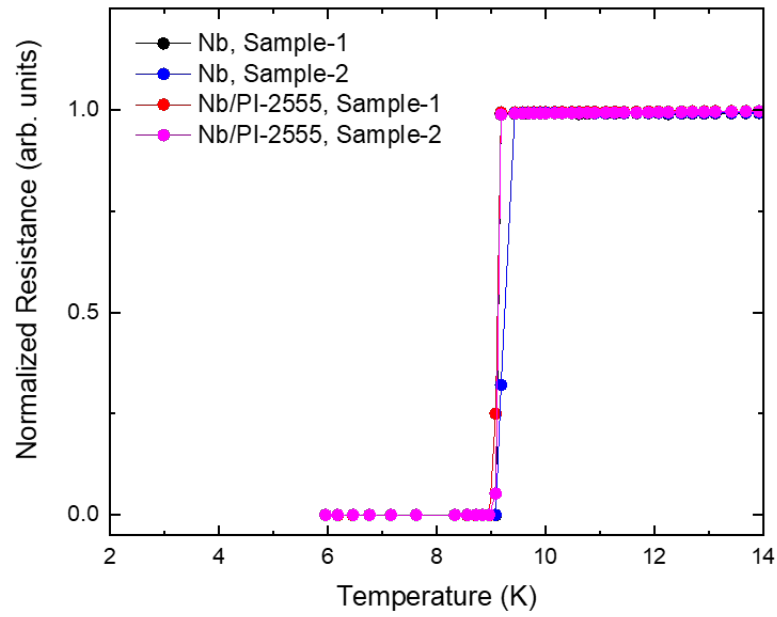


Figure 2.5. Plot of normalized resistance vs. temperature measurement of Nb samples with and without PI-2555 cured at 200 °C.

Fig 2.6 shows resistance vs. temperature plots for Nb with a capping layer of 20 nm thick Al, with and without PI-2555 on two samples. Similar T_c results as shown in Fig 2.5 were observed before and after curing PI-2555 on top at 200 °C for multiple samples.

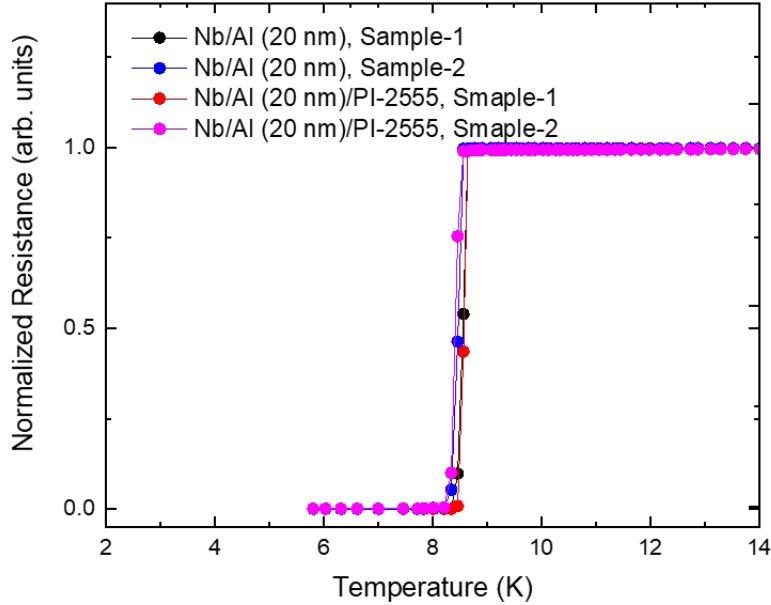


Figure 2.6. Plot of normalized resistance vs. temperature measurement of Nb/Al (20 nm) samples with and without PI-2555 cured at 200 °C.

2.2 Barrier Layers to Protect Nb Superconductivity in Thin Film Superconducting Flexible Cables

In this section we focus on ways to preserve the superconducting properties of Nb thin films for flexible superconducting cables. Polyimide is a promising material for flexible substrates and for embedding superconducting traces. Van Weers et al. [9] and Bruijn et al. [8] have fabricated and characterized the superconducting properties of thin Nb films deposited on and embedded within thin-film polyimide layers, using various protective layers such as Ti, Ta, and SiO₂. They reported significant reductions in the superconducting transition temperature (T_c) of Nb when subjected to a 350 °C polyimide curing cycle, which they attributed to thermal stress. We have fabricated similar structures and observed similar reductions in T_c following curing of an encapsulating polyimide overcoat. We speculate that, in addition to imposing thermal strains, curing the polyimide layer above a certain

temperature leads to diffusion of oxygen, hydrogen, or other degrading materials into the thin Nb films and lines. In an effort to solve this problem, we have studied the effects of metallic capping layers of Al, Cr, and Ta. Additionally, an alternate polymer overcoat (AL-X 2010) was investigated.

2.2.1 Fabrication Process

Since this work is directed at creating embedded superconducting traces, we studied 50 μm wide patterned lines, as opposed to blanket films. The lines had larger probe pads on each end in order to facilitate measurements. The different metals were deposited in a vacuum system capable of both sputter deposition and electron-beam thermal evaporation. All of the tested substrates started as oxidized silicon wafers, onto which 250 nm of Nb was sputter-deposited (DC sputter for 30 minutes in 6.1 mTorr of argon at 1KW). Vacuum base pressures of $\sim 3 \times 10^{-7}$ Torr were attained prior to depositing the Nb, which gave fairly repeatable Nb properties. The capping layer (if any) was then e-beam evaporated without breaking vacuum. After patterning of the conductor traces using a lift-off process, a 10 μm layer of PI-2611 (HD Microsystems) was spin-coated over the test structures and oven-cured at 350 °C in N_2 for one hour. As an alternative to PI-2611, 12 μm of Asahi Glass AL-X2010 was deposited on another set of test structures by spin-coating and oven-curing at 190 °C in N_2 for two hours. Fig. 2.7 shows an image of a fabricated 50 μm wide line (Nb with an Al capping layer) taken with an optical microscope. The left side of the image is where the line meets the probe pads.

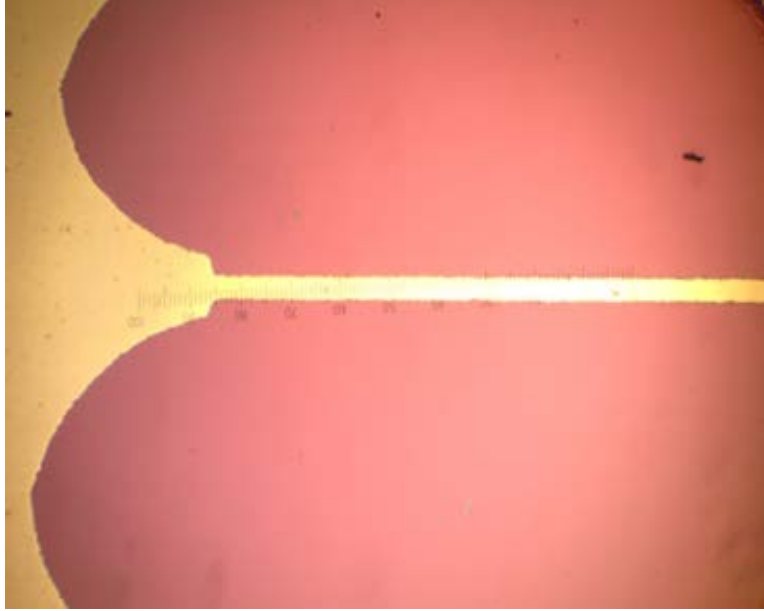


Figure 2.7. Optical image of a fabricated $50\ \mu\text{m}$ wide line with metal stack of Nb (250 nm)/Al (10 nm). A portion of a test probe pad is visible on the left side of the image.

2.2.2 Measurement Setup

Superconducting transition temperature measurements were carried out in a pulse-tube cryostat (shown in Fig. 2.8) with temperature control from $\sim 1.2\ \text{K}$ and up. For each of these systems, the sample is mounted onto a sample holder using a 4-point probe PCB (shown in Fig. 2.9) in order to achieve accurate resistance measurements. Applied currents were maintained below the critical currents of the superconducting films.



Figure 2.8. Pulse-tube cryostat.

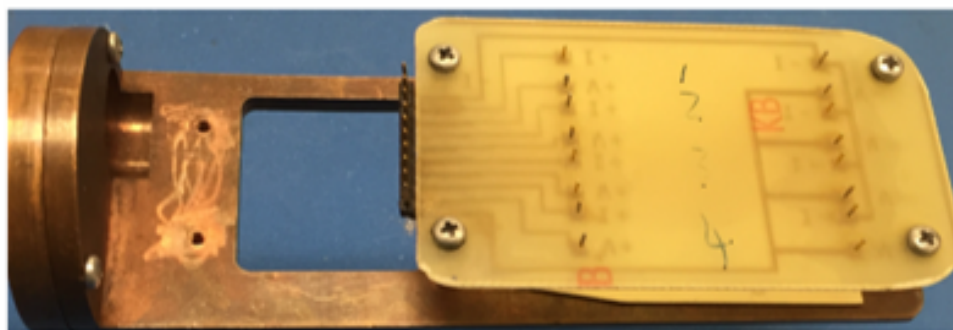


Figure 2.9. PCB mounted onto a Cu sample holder for making 4-point probe resistance measurements low temperatures.

2.2.3 Results and Discussion

We measured the superconducting transition temperature of the 50 μm Nb lines with different metal capping layers of Al, Cr and Ta, which were deposited by electron-beam thermal evaporation. Different capping thicknesses were tested, in the range 10 to 50 nm. We desired to use as thin of a capping layer as possible in order to minimize the impact of the capping layer on the superconducting properties of the underlying Nb. We present results for a comparison of superconducting transition temperatures for Nb lines with various metallic capping layers, with and without different cured polymer layers. In order to better analyze the differences between various layer stacks, the normal-state resistance is normalized to unity in these plots. In Fig. 2.10 we present results for the various capping layers on top of Nb with no polymer overcoat. All of the metal capping layers tested in this section exhibited a fairly abrupt transition from normal to superconducting. Among the capping layers, 10 nm of Cr and 20 nm of Al exhibited the highest T_c values. Following these measurements, we coated 10 μm of PI-2611 on top of the capped samples, cured them at 350 $^\circ\text{C}$ in N_2 , and re-measured T_c (Fig. 2.11). Most of the samples showed significant degradation in T_c , which would be unacceptable for applications such as Josephson logic that are intended to operate at or near 4.2 K. Nonetheless, the 20 nm Al capping layer retained a relatively high T_c (8.5 K, only 0.7 K less than for bulk Nb). Fig. 2.12 shows results for a similar set of test structures with 12 μm of AL-X2010 (instead of PI-2611) deposited and cured on top of the capping layers. We can see that, except for 50 nm of Ta, the T_c of all the capping layers exhibited minimal degradation. This is possibly due to the 190 $^\circ\text{C}$ curing temperature of AL-X2010, which is lower than the 350 $^\circ\text{C}$ used for PI-2611. Based on these results, additional samples were fabricated and tested to check the reproducibility of the superconducting transition temperature of the 20 nm Al capping layer on 250 nm Nb after high temperature curing of PI-2611.

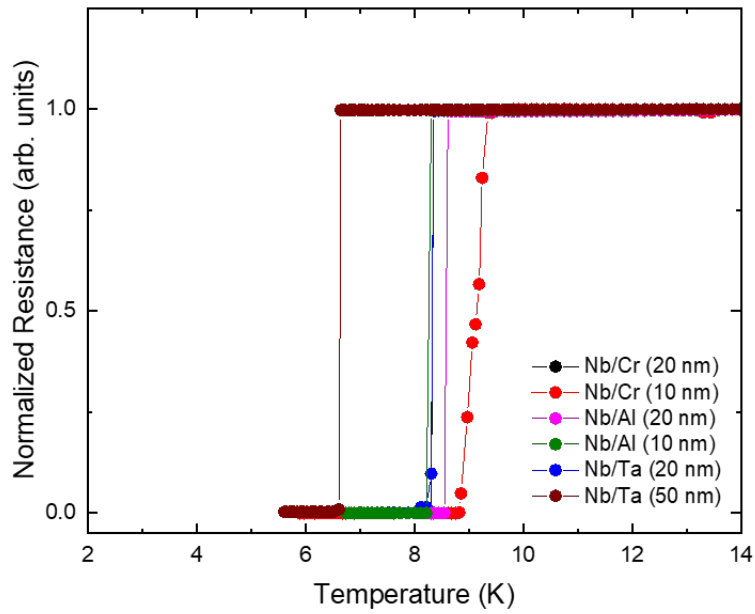


Figure 2.10. Plot of normalized resistance vs. temperature measurement of different types and thicknesses of metallic capping layers with no polymer overcoat.

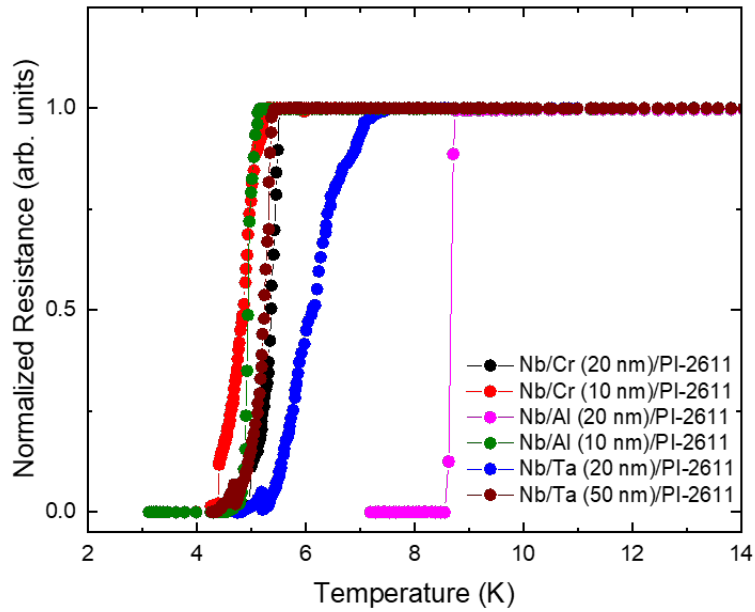


Figure 2.11. Plot of normalized resistance vs. temperature measurement after over-coating metal lines with 10 μm of PI-2611 cured at 350 $^{\circ}\text{C}$.

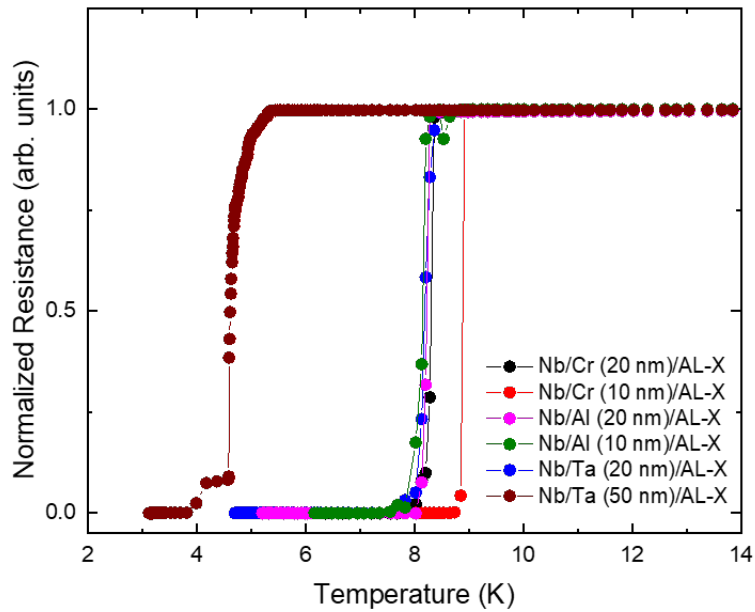


Figure 2.12. Plot of normalized resistance vs. temperature measurement after over-coating metal lines with 12 μm of AL-X2010 cured at 190 $^{\circ}\text{C}$.

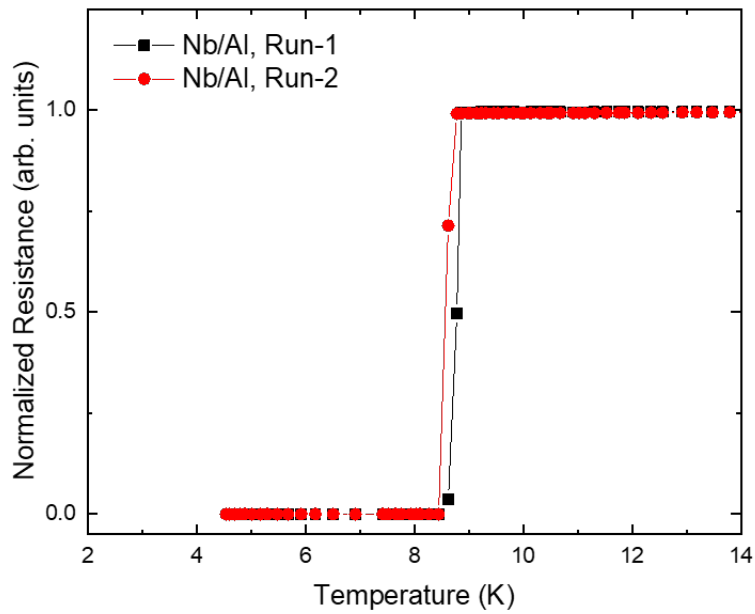


Figure 2.13. Plot of normalized resistance vs. temperature measurement of two independent depositions of 250 nm Nb traces capped with 20 nm Al before applying polyimide.

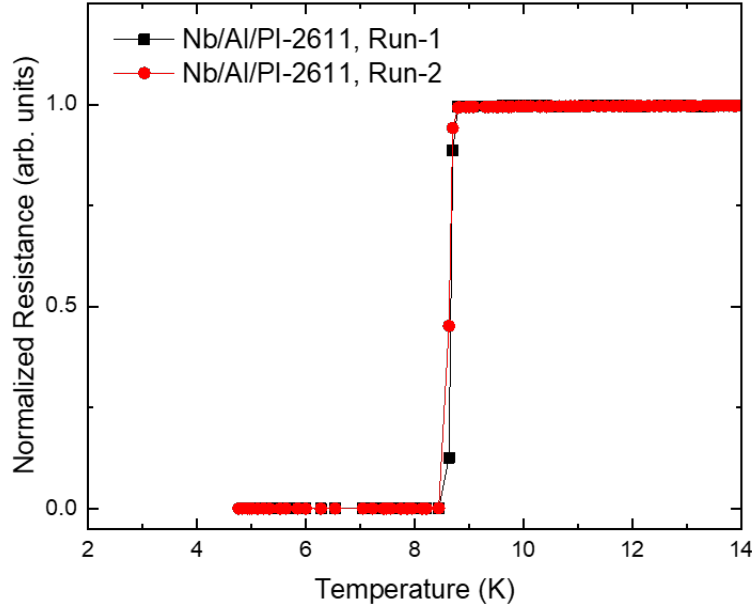


Figure 2.14. Plot of normalized resistance vs. temperature measurement of 250 nm Nb traces capped with 20 nm Al after over-coating with 10 μm of PI-2611 and curing at 350 $^{\circ}\text{C}$.

Fig. 2.13 and Fig. 2.14 presents a comparison of Nb lines with 20 nm Al capping layers for two independent fabrication runs, before and after over-coating with cured PI-2611. It can be seen that both runs have nearly identical before-and-after T_c values of approximately 8.5 K, thereby indicating run-to-run reproducibility within this small set of samples.

The degradation of 50 μm wide, 250 nm thick Nb traces was substantially prevented by using 20 nm of Al as a protective capping layer. The aluminum is possibly acting as some combination of a diffusion barrier, an oxygen getter, and a strain buffer.

2.3 Atomic Layer Deposited Materials as Barrier Layers for Preservation of Nb Superconductivity in Multilayered Thin-Film Structures

In this section, we present experimental results on using thin dielectric barrier layers, specifically Al_2O_3 deposited by atomic layer deposition (ALD), to isolate and protect the Nb

from the surrounding materials and sources of contamination, thereby reducing the degradation of the superconducting properties of the Nb during subsequent fabrication steps at temperatures greater than 250 °C.

ALD is a surface-controlled layer-by-layer process that results in the deposition of conformal thin films, one atomic layer at a time. Several groups have previously described and characterized the growth of Al_2O_3 [15–20]. Proslir, et al. have used a thin uniform ALD deposited Al_2O_3 protective layer with subsequent annealing at temperatures ranging from 250 °C to 500 °C in ultra-high vacuum (UHV) to remove the oxides from the inner wall of Nb cavities and to diffuse oxygen into the bulk Nb [21]. Al_2O_3 deposited by ALD is dense, stable and provides excellent dielectric passivation properties on metallic surfaces [22–24]. High quality Al_2O_3 layers can be deposited using thermal ALD at a relatively low process temperature, below 250 °C. These qualities make Al_2O_3 a promising material to be used as a protective layer to preserve Nb superconductivity. We note that our choice to use Al_2O_3 was due to the above qualities in addition to the availability of this material and thermal ALD system in our fabrication facilities. Other dielectric materials, such as TiO_2 , or alternating stacks of similar dielectric materials, may provide equal or better results and are worth exploring. The incorporation of a barrier layer that protects the superconducting properties of Nb can relax the need for the use of lower temperature fabrication processes and open up possibilities for use of different processes or alternative (more desirable) materials.

In the past, we found that using a lower curing temperature (i.e., lower than the temperature recommended by the manufacturer of HD-4110) of 225 °C can be used to protect the superconductivity of Nb, although it is possible that the polyimide layer is not fully curing at the lower temperature, which could present mechanical robustness or stress concerns during subsequent fabrication steps or during use [25]. In the next sections, we describe the fabrication processes, measurement methods, setup and results.

2.3.1 Fabrication Process

The test structures used in this section consisted of DC electrical measurement structures with 50 μm wide patterned Nb lines, as opposed to blanket films, in order to represent patterned conductor traces that one may find in an integrated superconducting electronics circuit. The test structures also had larger probe pads on each end in order to facilitate four point electrical measurements (shown in Fig. 2.17). Samples that incorporated Al_2O_3 had the film deposited by means of thermal ALD at 200 $^\circ\text{C}$ using trimethylaluminum (TMA) and H_2O as precursors, in a system similar to a Veeco (previously Cambridge Nanotech or Ultratech as shown in Fig. 2.15) Savannah thermal ALD system at a growth rate of 1.5 \AA per cycle. TMA was pulsed first on the sample surface, the excess TMA that is not chemisorbed by the surface is pumped out of the chamber using nitrogen, which acts as a carrier and purge gas. The dissociative chemisorption of TMA forms AlCH_3 on the surface of the sample. The TMA pulse is followed by an H_2O pulse, which reacts with the surface CH_3 to form CH_4 as a reaction byproduct and results in a hydroxylated Al_2O_3 layer. Fig. 2.16 illustrates the whole deposition process for coating Al_2O_3 onto sample surface.

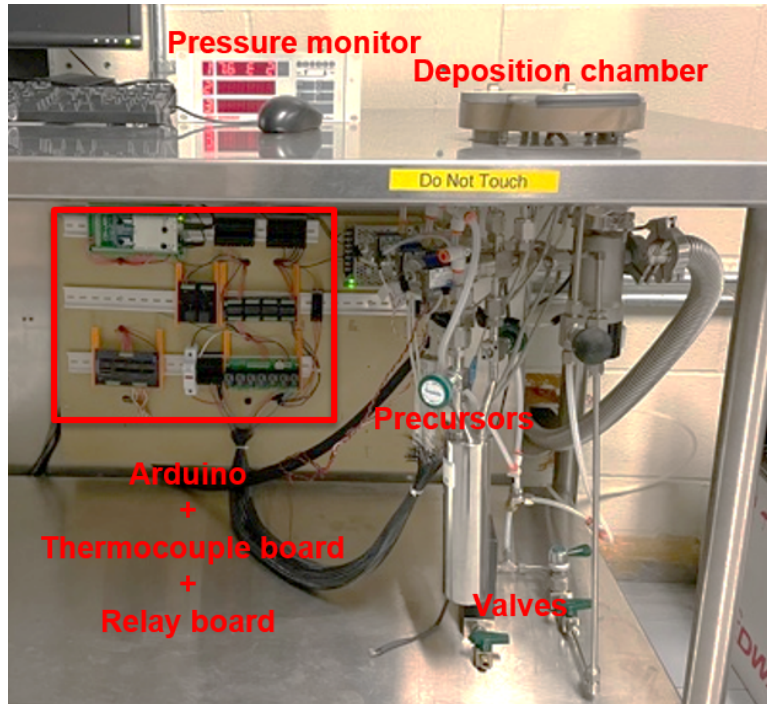


Figure 2.15. Image of the thermal ALD system including the deposition chamber, pressure monitor, precursors, valves and other electrical components.

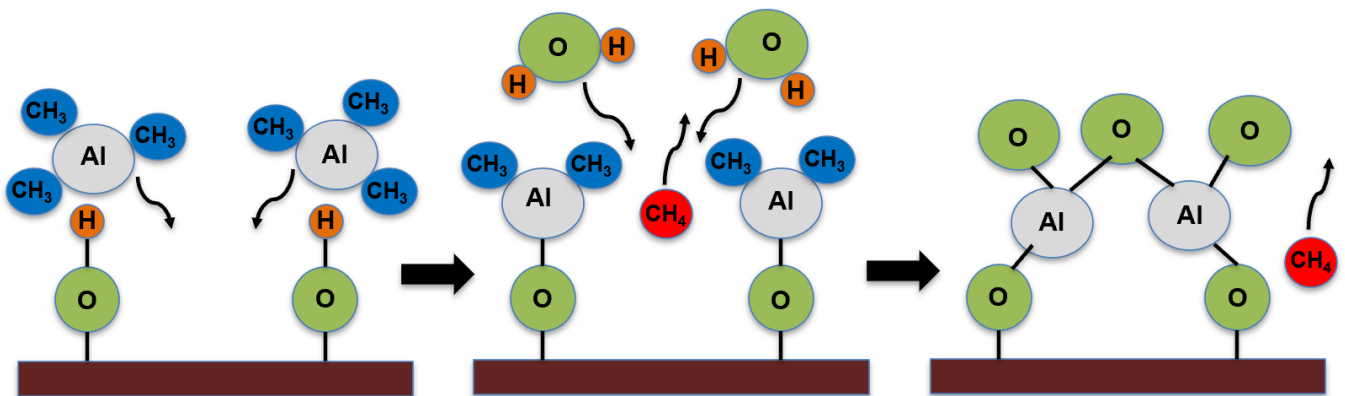


Figure 2.16. Schematic showing the detailed step-by-step process for depositing one atomic layer of Al₂O₃ on a substrate using the precursors (TMA and H₂O).

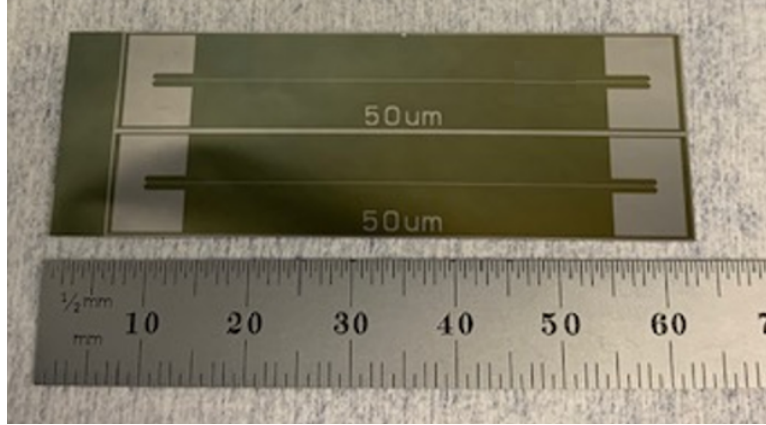


Figure 2.17. 50 μm wide Nb lines on Si substrate with pads on each side to make 4-point probe measurement.

For each sample, 250 nm thick Nb was sputter-deposited (DC sputter for 30 minutes in 4 mTorr of Ar at 1 KW) and subsequently subjected to a conventional lift-off process to define the Nb pattern [26]. The purity of the Nb sputter target used for deposition was 99.999%. A vacuum base pressure below 3×10^{-7} Torr was obtained prior to depositing the Nb in our CHA Mark 50 system with sufficient pumpdown followed by a Ti evaporation and gettering step, which gave repeatable Nb properties for different samples. Nb films were deposited in the same run for all the samples used in this work to allow more straightforward comparison between samples subjected to different subsequent fabrication processes. A nominal thickness of 250 nm (± 10 nm) was used for all samples. A witness sample, 1 cm \times 1 cm Si die with SiO_2 , was used to measure the T_c of an unpatterned thin film of Nb. The T_c and RRR of the Nb on the witness sample were found to be ~ 8.9 K and 3.60, respectively. Fig. 2.17 shows image of a diced Nb sample used in this section without PI and Al_2O_3 overcoat. For samples that received subsequent processing, small Kapton tape “dots” were placed onto the connection pad area, followed either by another layer of Al_2O_3 and/or polyimide, on top of the Nb.

In order to compare the effect of Al_2O_3 as a protective barrier layer we fabricated multiple stack ups: one comprised of bare Nb with no capping layer of Al_2O_3 (shown in Fig. 2.18) and the other comprising barrier layers on both sides of Nb (shown in Fig. 2.19).



Figure 2.18. Schematic cross-section of 250 nm Nb sputter deposited on bare Si (Sample 1(a)).

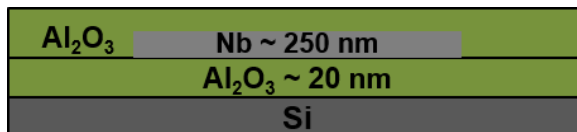


Figure 2.19. Schematic cross-section of 250 nm Nb sandwiched between two Al₂O₃ layers (Sample 2 (a)).

20 nm thick Al₂O₃ layers were used for this work. We began with somewhat thin barrier layers, with the expectation that it would minimize the impact of the barrier layer on the superconducting properties of the underlying Nb. After testing samples without a polyimide topcoat, the same samples were then over-coated with a polyimide layer as shown in Fig. 2.20 and 2.21. It is important to note that the stacks-ups shown in Fig. 2.20 and 2.21 were the same samples shown in Fig. 2.18 and 2.19 that were subjected to further processing, thereby allowing a direct comparison and a determination of the impact of the subsequent processing. The polyimide used in this work was HD-4110 from HD Microsystems. The Kapton “dots” were removed before curing the top HD-4110, in order to create openings for electrical contact.

We note that all the samples were kept in a nitrogen dry box desiccator during subsequent fabrication steps to prevent oxidation of Nb surfaces. Nb was exposed to the lab atmosphere and is expected to form native oxide, it has not been characterized in this section but will be explored in our future experiments.

2.3.2 Measurement Methods and Setup

We measured superconducting transition temperatures (T_c) and critical current (I_c) of multiple samples. The measurements were carried out in a pulse-tube based closed cycle cryostat (Cryo Industries of America), with temperature control from ~ 1.2



Figure 2.20. Schematic cross-section of 250 nm Nb over-coated with 20 μm HD-4110 (Sample 1(b)).

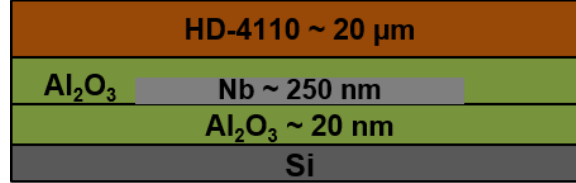


Figure 2.21. Schematic cross-section of 250 nm Nb capped with Al₂O₃ and over-coated with HD-4110 (Sample 2 (b)).

K and up. The temperature was measured using LakeShore 335 temperature controller. Each sample was mounted onto a sample holder that allows 4-point probing of the test structure, using pogo pins, in order to achieve accurate resistance measurements for samples with a wide range of resistance values. Samples were measured in vacuum and the sample holder was instrumented with temperature measurement diodes for accurate temperature measurement. Critical current was measured using a Keithley 2400 source meter. A micro-Ohm meter (Keysight 34420A) was used to measure the resistance values for determination of superconducting transition temperature. Residual resistance ratio (RRR) was obtained by taking the ratio of resistance at 300 K and at 4.2 K.

2.3.3 Results and Discussion

In this section we present results comparing the effectiveness of using Al₂O₃ as barrier layer to protect thin and narrow Nb traces during elevated temperature polyimide curing processes.

Fig. 2.22 presents results of normalized trace resistance vs. sample temperature measurements showing superconducting transition temperature for Nb lines with and without a cured HD-4110 layer on top of the Nb (Samples 1(a) and 1(b) shown in Fig. 2.18 and 2.20). The transition from normal to superconducting state of the Nb as temperature was reduced exhibited a fairly abrupt transition, as can be seen from Fig. 2.22 for the sample without

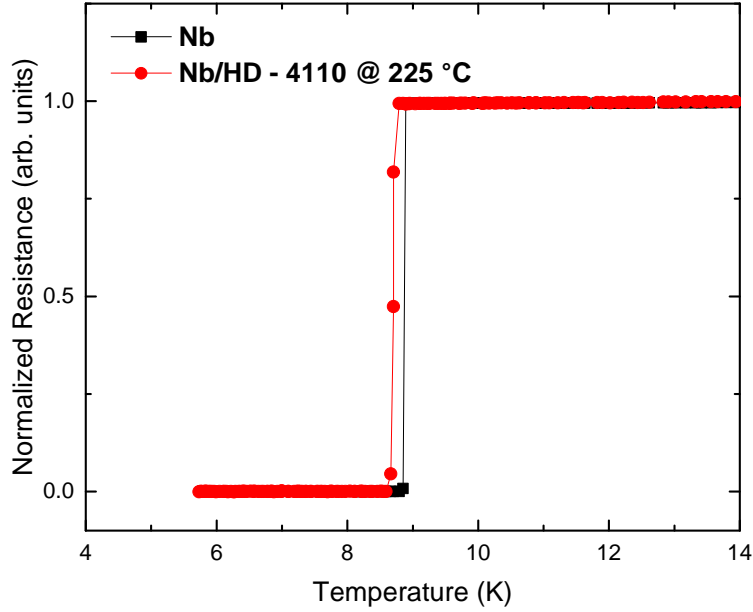


Figure 2.22. Plot of normalized resistance vs. temperature showing superconducting transition temperature of Sample 1(a) without over-coated HD-4110 and of same sample (now Sample 1(b)) with over-coated HD-4110 cured at 225 °C.

an HD-4110 overcoat. The sample was then coated with HD-4110 on top of the Nb signal line and cured at 225 °C in a N₂ atmosphere and subsequently characterized a second time. We note a small amount of degradation (i.e., reduced T_c) is observed in the superconducting transition temperature. Minimal degradation can also be seen in I_c and RRR measurements. After curing HD-4110 at 225 °C, I_c dropped from 186 mA to 182 mA and RRR dropped from 3.58 to 3.34. On the same sample when the HD-4110 was subsequently cured at 375 °C, no electrical connection was found between the pads on the line, hence no transition plot is shown. This is evidence for full degradation of the Nb leading to a loss of superconductivity and possibly full oxidation of the Nb trace caused by curing the polyimide layer at 375 °C.

Fig. 2.23 shows normalized trace resistance vs. sample temperature measurement results showing superconducting transition temperatures for Sample 2, which has Nb lines with Al₂O₃ barrier layers, with and without HD-4110 (i.e., Samples 2(a) and (b) in Figure 2.19 and 2.21). Very little degradation in the T_c was observed on the sample when it was subjected

to a cure temperature of 225 °C. The same sample was then cured at 375 °C and remeasured to determine T_c . The sample retained a relatively high T_c of 8.1 K (0.6 K less than pristine bare Nb), but much higher than the case of the sample without the Al_2O_3 layers. I_c and RRR of the sample were measured before and after curing HD-4110 on top of the sample. The I_c and RRR for the sample prior to HD-4110 deposition were 250 mA and 3.55, respectively. After curing at 225 °C, the I_c dropped to 182 mA and RRR dropped to 3.52. After curing at 375 °C, the I_c dropped to 75 mA and RRR dropped to 3.22. Though there was a reduction in the T_c and RRR, and significant degradation in the I_c for the sample cured at 375 °C, the Nb retained superconductivity and appears to have been fairly-well protected by the ALD-deposited Al_2O_3 barrier layers.

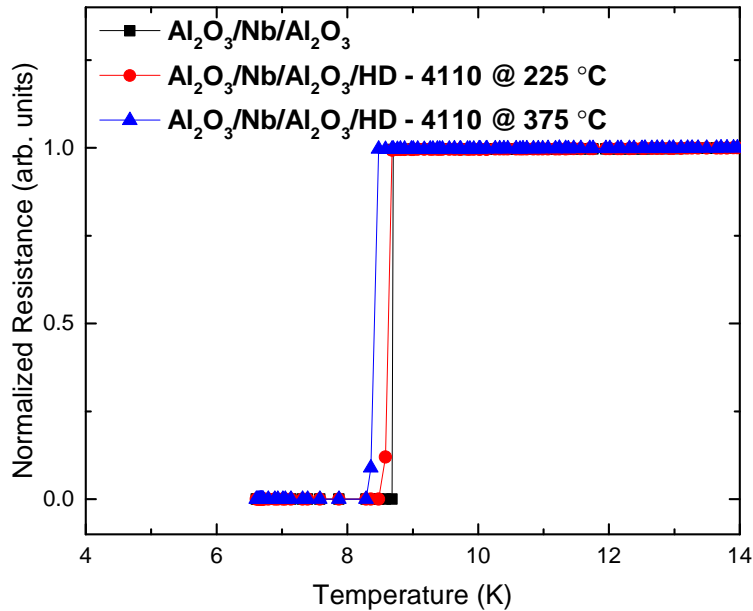


Figure 2.23. Plot of normalized resistance vs. sample temperature showing superconducting transition temperatures of Sample 2(a) with $\text{Al}_2\text{O}_3/\text{Nb}/\text{Al}_2\text{O}_3$ without over-coated HD-4110 and of same sample (now Sample 2(b)) with over-coated HD-4110 and cured at different temperatures (225 °C and 375 °C).

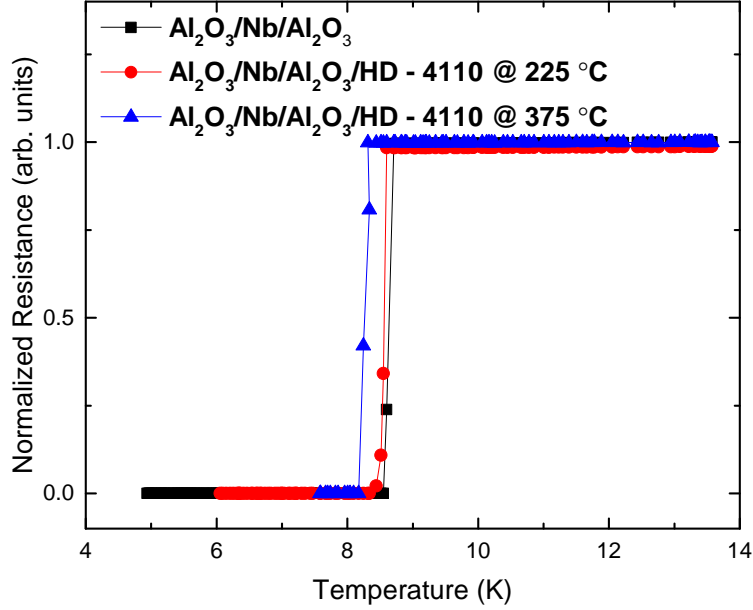


Figure 2.24. Plot of normalized resistance vs. sample temperature showing superconducting transition temperatures of Sample 3 with $\text{Al}_2\text{O}_3/\text{Nb}/\text{Al}_2\text{O}_3$ without over-coated HD-4110 and of same sample with over-coated HD-4110 and cured at different temperatures (225 °C and 375 °C).

Fig. 2.24 shows similar trends for Sample 3 and corresponding subsequently-processed versions, which were fabricated and measured in the same way as Sample 2. This serves to demonstrate a promising level of repeatability of this process and fabricated structures.

Table 2.1. T_c and I_c at 4.2 K for different samples.

PI	Sample 1		Sample 2		Sample 3	
	T_c	I_c	T_c	I_c	T_c	I_c
Before HD-4110	8.9 K	186 mA	8.7 K	250 mA	8.6 K	222 mA
HD-4110 - 225 °C	8.6 K	182 mA	8.5 K	182 mA	8.5 K	176 mA
HD-4110 - 375 °C	X	X	8.1 K	75 mA	8.2 K	65 mA

Table 2.1 summarizes all of the results of this study for the different versions of the 3 samples, which were tested initially, after deposition and curing of HD-4110 at 225 °C, and then after cure at 375 °C.

2.4 Nb Embedded Structures Using Al Barrier Layer and Low Temperature Cured Polyimide

In the previous section we have demonstrated that curing PI-2611 at 225 °C had minimal effect on Nb superconducting properties. In this section we have fabricated embedded structures with top PI-2611 layer cured at low temperature. The stack up of the embedded structure includes a 10 μm thick dielectric layer of PI-2611 on top of silicon onto which 250 nm of Nb was sputter-deposited (DC sputter for 30 minutes). After using the lift off process to pattern 250 nm thick Nb another 10 μm thick encapsulating layer of PI-2611 was cured on top. The bottom PI-2611 was cured at 350 °C and the top PI-2611 layer was cured at 225 °C. Since there is no Nb underneath the bottom PI-2611 layer therefore it was cured at 350 °C. Whereas the second layer of PI-2611 is on top of Nb and is therefore cured at 225 °C in order to prevent diffusion of PI-2611 into Nb. Fig. 2.25 shows the image of a released Nb sample encapsulated between two PI-2611 layers. Fig. 2.26 shows the superconducting transition temperature values of four samples measured using PT. Multiple samples were measured to counter the yield issue and to check the repeatability for the process. It can be seen that all the samples have similar superconducting transition temperatures of ~ 7.1 K.

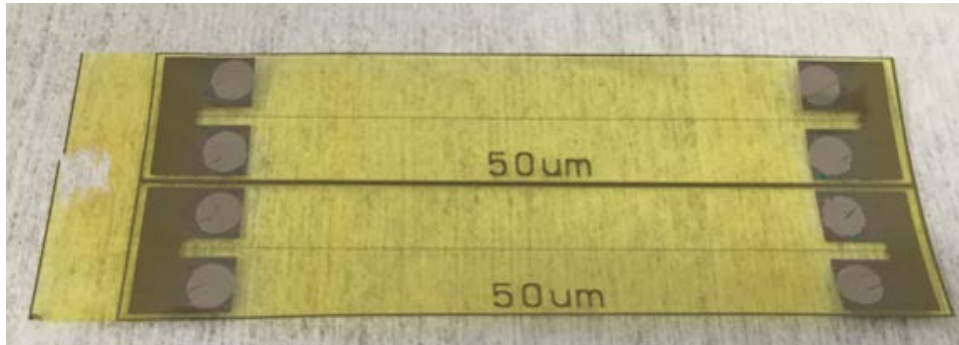


Figure 2.25. Image of a released PI-2611/Nb/PI-2611 sample.

Previously, we have shown that 20 nm of Al is an optimum barrier layer to prevent degradation of polyimide impurities into Nb film leading to loss of superconductivity. In order to test the effectiveness of 20 nm Al capping layer in embedded samples and compare

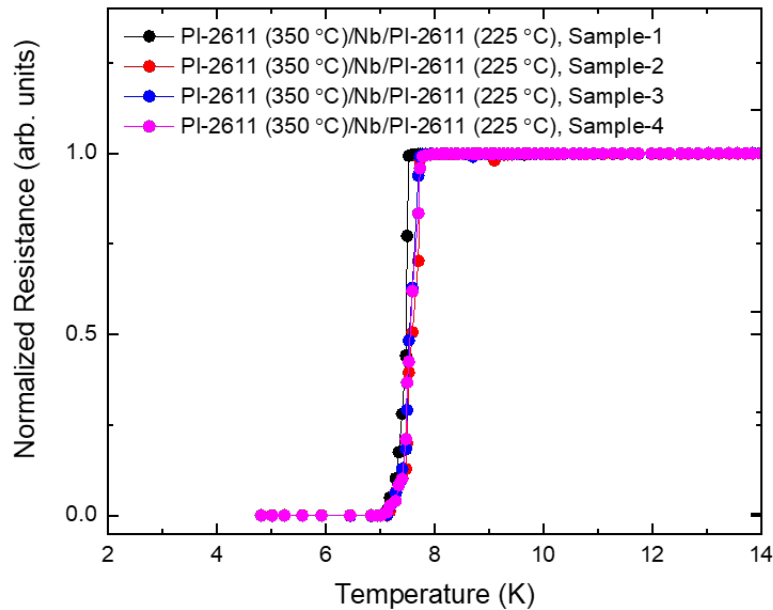


Figure 2.26. Plot of normalized resistance vs. temperature measurement of PI-2611/Nb/PI-2611 samples with bottom PI-2611 cured at 350 °C and top PI-2611 cured at 225 °C.

the results, two samples were fabricated and released in which Nb (sputter deposited) and a capping layer of 20 nm Al (e-beam evaporated) on top of it was encapsulated between two PI-2611 layers. To be consistent, curing temperatures of the bottom and top layers of PI-2611 were kept same as in the previous case i.e. 350 °C and 225 °C for the top and bottom layer respectively. Fig. 2.27 shows the image of a released embedded sample in which Nb with a capping layer of Al is embedded between two PI-2611 layers.

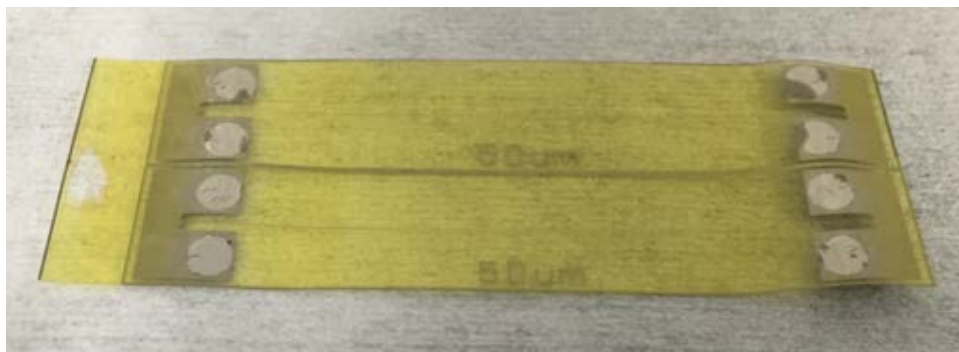


Figure 2.27. Image of a released PI-2611/Nb/Al(20 nm)/PI-2611 embedded sample.

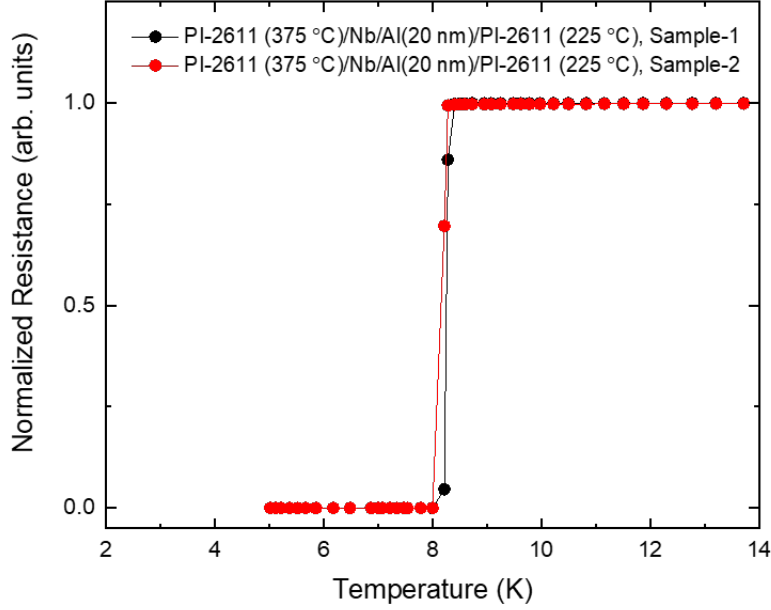


Figure 2.28. Plot of normalized resistance vs. temperature measurement of PI-2611/Nb/Al(20 nm)/PI-2611 samples with bottom PI-2611 cured at 350 °C and top PI-2611 cured at 225 °C.

We observed that 20 nm of Al acts as a good barrier layer when encapsulated between two PI-2611 layers. An increase in superconducting transition temperature was observed from ~ 7.1 K in case of embedded Nb to ~ 8 K in case of embedded Nb with 20 nm Al capping layer as shown in Fig. 2.28. Having a capping layer between Nb and top PI-2611 layer significantly prevents degradation of Nb, but its still in direct contact with the PI-2611 at the bottom. So in order to further encapsulate the Nb and to minimise the degradation of Nb by reducing its contact from the bottom PI-2611 layer, we deposited 20 nm thick Al underneath the Nb layer. Fig. 2.29 shows the released sample with 20 nm of Al on both top and bottom of Nb, sandwiched between two layer of PI-2611. Fig. 2.30 shows the superconducting transition temperature plot of four samples measured with Al(20 nm)/Nb/Al(20 nm) encapsulated between two PI-2611 layers. It can be seen that all the samples have similar transition temperatures. It also shows that this process is repeatable since all the four samples showed similar results. Moreover an increase in T_c is observed (\sim

8.5 K) when 20 nm of Al capping layer is used both at top and bottom of Nb as opposed to only one Al (20 nm) layer ($T_c \sim 8$ K) on top of Nb.

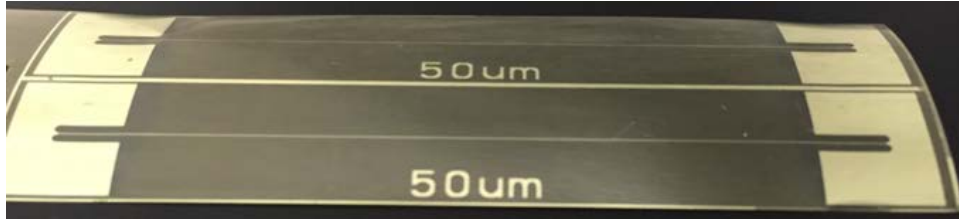


Figure 2.29. Embedded PI-2611/Al(20 nm)/Nb/Al(20 nm)/PI-2611 released.

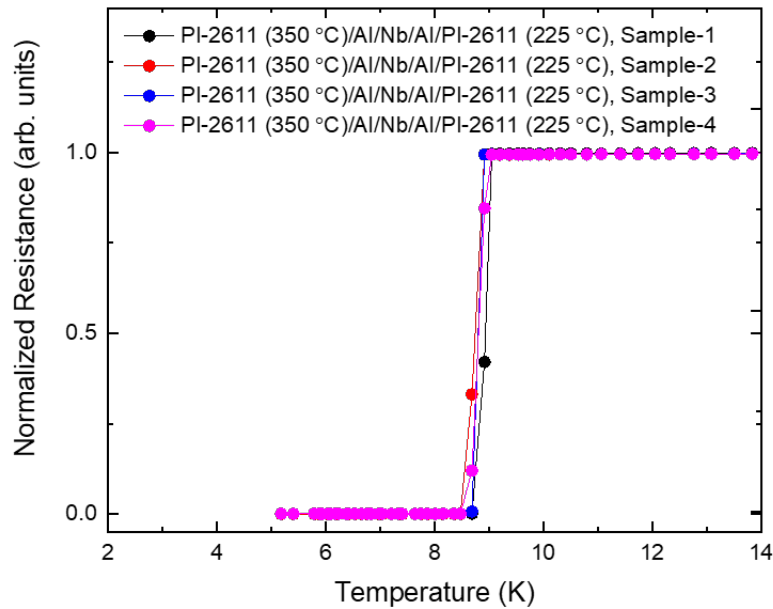


Figure 2.30. Plot of normalized resistance vs. temperature measurement of PI-2611/Al(20 nm)/Nb/Al(20 nm)/PI-2611 samples with bottom PI-2611 cured at 350 °C and top PI-2611 cured at 225 °C.

Multiple material stack-ups have been investigated with a goal to protect the superconducting properties of Nb thin films. The degradation of Nb was significantly decreased by using 20 nm of Al as diffusion barrier layer. We were also able to demonstrate that curing polyimide at lower temperatures leads to less interaction with the material that diffuses into

Nb at higher temperatures. This was shown by using AL-X which is cured at 190 °C, PI-2611 cured at 225 °C and HD-4100 cured at 225 °C on top of Nb. We also show that curing polyimide above 250 °C can deteriorate superconducting properties including T_c . Furthermore, our results show that these processes are repeatable and reproducible through multiple samples.

2.5 Secondary Ion Mass Spectroscopy (SIMS) Study for Nb Degradation

SIMS has been widely used as a key technique to extract depth profiles of elemental and molecular composition with high spatial resolution. The basic principle of SIMS involves bombardment of the sample surface by an ion beam, either positive or negative stream of ions, leading to ejection of secondary ions (as shown in Fig. 2.31). These ions are then analyzed (mass to charge ratios) by a mass spectrometer to determine the elemental composition of the surface. The recent developments in SIMS technology such as cluster ion beams ensures high performance of organic compounds and biological materials [27–30].

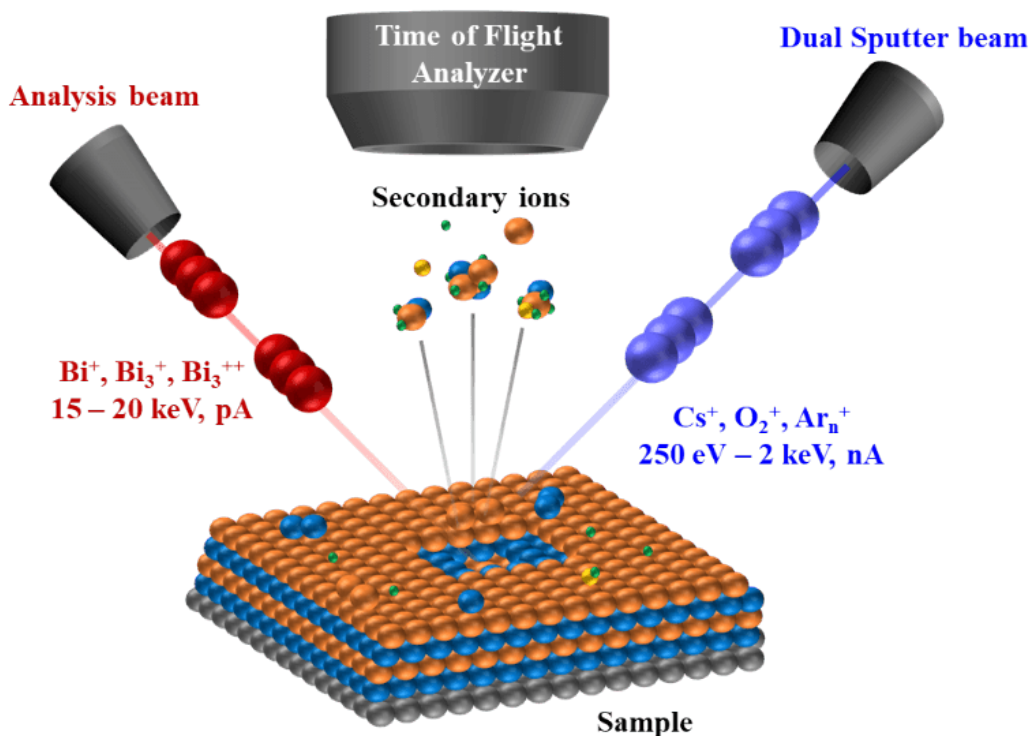


Figure 2.31. adapted from [10].

In this section, SIMS was performed to investigate the morphology of Nb stack ups as a result of curing polyimide on top of it at high temperatures. Four different stack-ups were explored. In order to understand the cause of degradation in Nb with PI cured at elevated temperatures, one of the sample consisted of Nb with PI cured at 375 °C whereas the other consisted of PI cured at 225 °C on top of Nb. The remaining two samples were prepared with barrier layers of Al and Al₂O₃ on both sides of Nb, with PI cured at 375 °C. These samples were built to study the effect of different barrier layers to prevent Nb degradation after curing PI on top.

2.6 Sample Preparation and Measurement Results

500 μm thick silicon substrates with a thin oxide layer (~ 50 nm) were used to fabricate all the different stack-ups. A bulk layer of Nb was sputter deposited using DC sputter to a thickness of 250 nm. For samples involving barrier layers, Al was e-beam evaporated in the same deposition chamber without braking vacuum whereas Al₂O₃ was ALD deposited. A typical thickness of 20 nm was used for the barrier layers. A 20 μm thick layer HD-4110 was spun coated and cured at 375 °C and 225 °C on top of the conductor.

After curing HD-4110 on top, a hole of diameter ~ 1500 μm was etched in Si using deep reactive ion etching. This hole was used to provide the spatial resolution for the primary ion beam to penetrate into the sample surface. Extreme attention was given to the sample preparation in order to prevent any kind of contamination. Fig. 2.32 shows the image of the opening in Si on the back side of the sample with stack up of Nb/PI (375 °C).

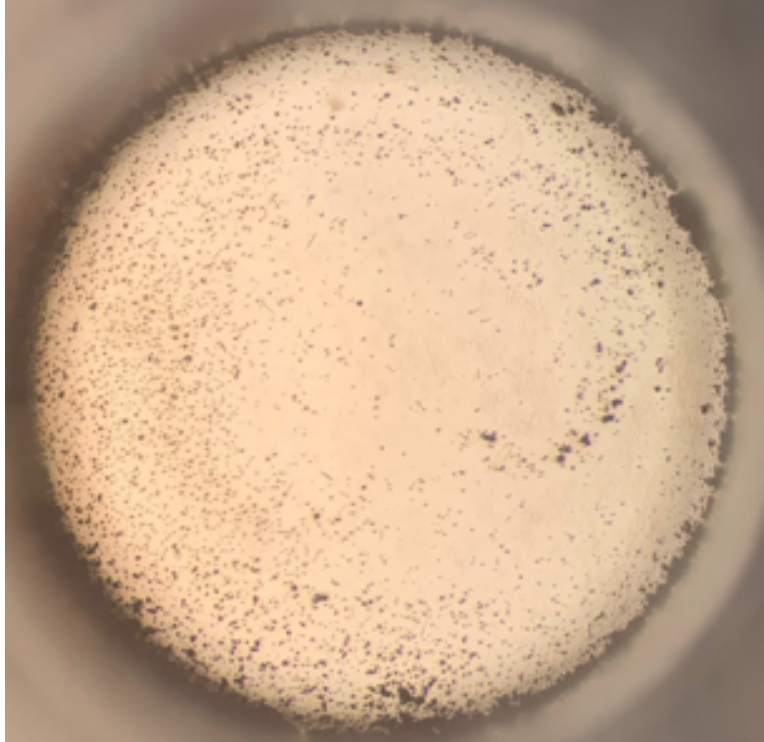


Figure 2.32. Image of the etched area in Si of Nb/PI (375 °C) sample.

Fig. 2.33 shows the image of the opening in Si on the back side of the sample with stack up of Nb/PI (225 °C).

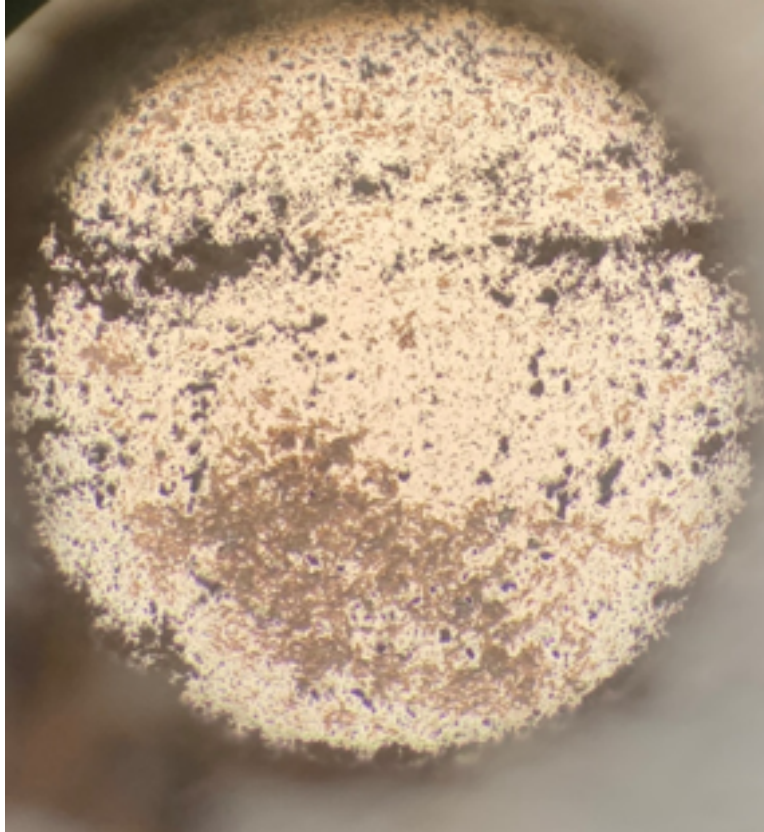


Figure 2.33. Image of the etched area in Si of Nb/PI (225 °C) sample.

Fig. 2.34 shows the image of the opening in Si on the back side of the sample with stack up of Al/Nb/Al/PI (375 °C).

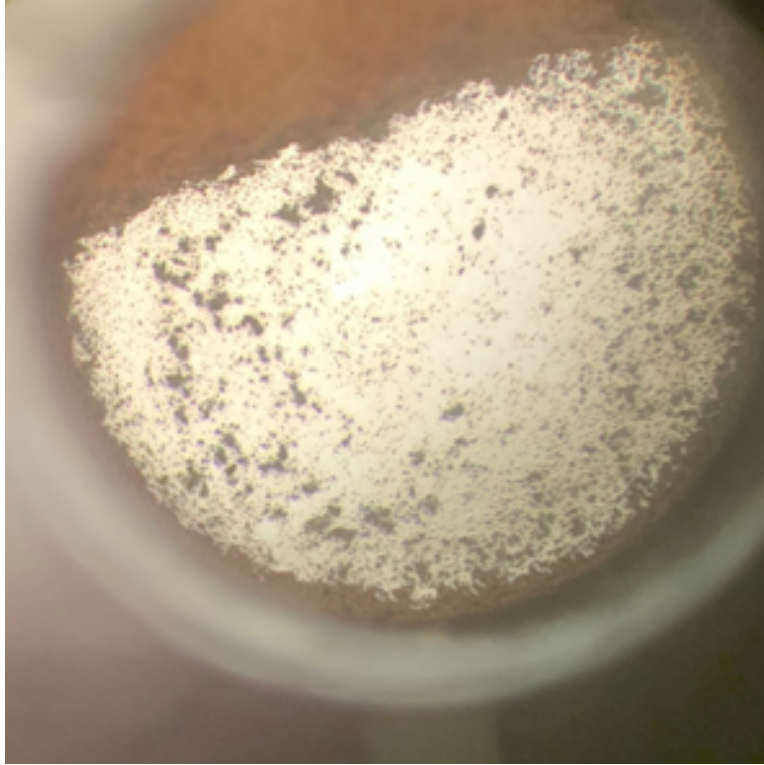


Figure 2.34. Image of the etched area in Si of Al/Nb/Al/PI (375 °C) sample.

Fig. 2.35 shows the image of opening in Si on the back side of the sample with stack up of $\text{Al}_2\text{O}_3/\text{Nb}/\text{Al}_2\text{O}_3/\text{PI}$ (375 °C).

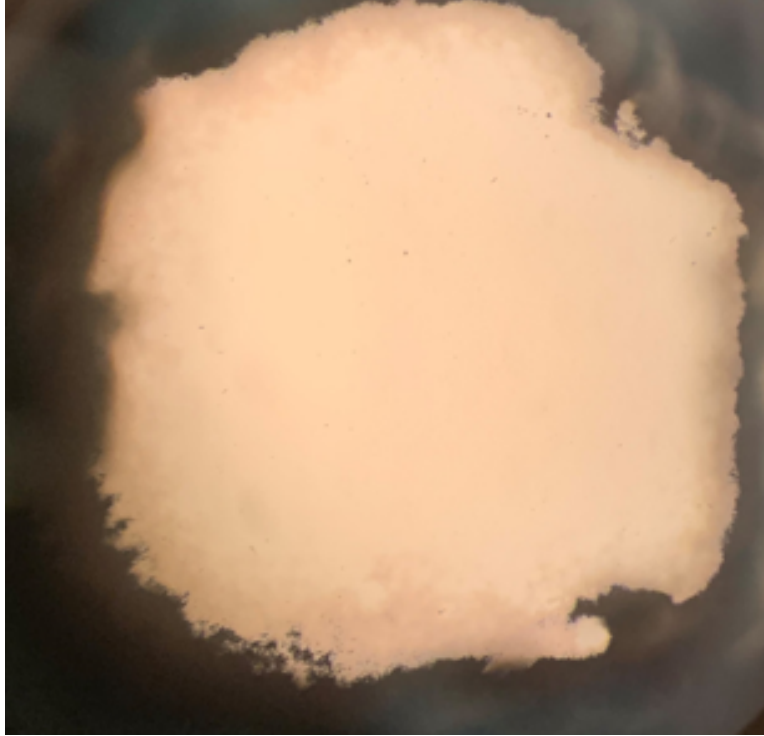


Figure 2.35. Image of the etched area in Si of $\text{Al}_2\text{O}_3/\text{Nb}/\text{Al}_2\text{O}_3/\text{PI}$ (375 °C) sample.

2.6.1 SIMS Analysis on Nb/PI (375 °C)

Fig. 2.36 shows the sputtering time dependent intensity of secondary ion intensity and the corresponding cross-section. The interface of interest is highlighted in red in the cross-section image. The diffusion of O_2 into Nb can be clearly seen from the plot. This diffusion leads to degradation of Nb and adversely affects the superconducting properties of Nb.

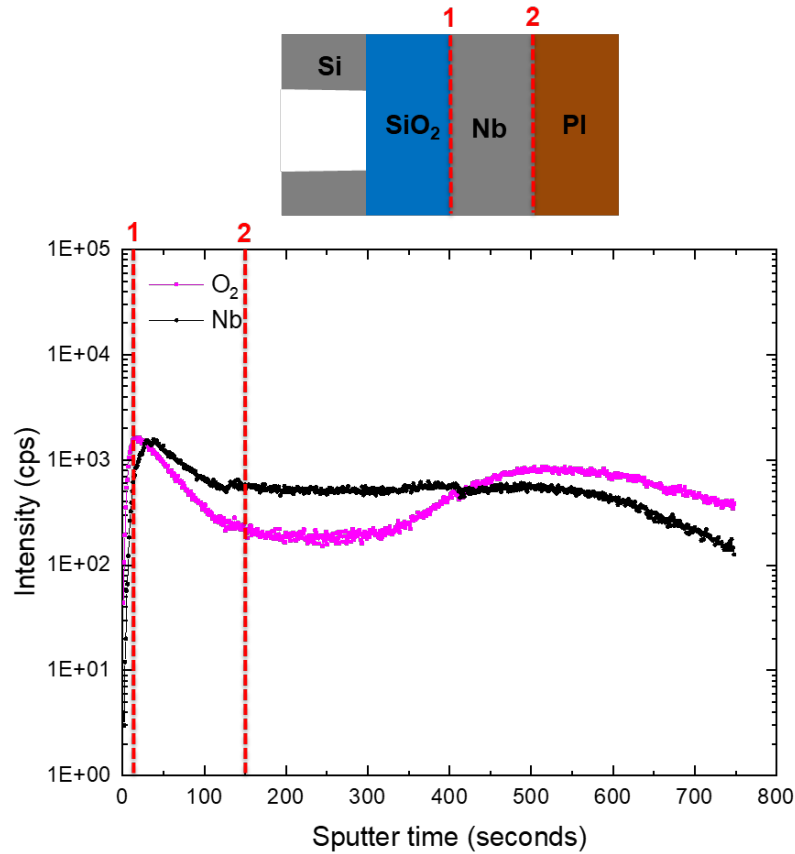


Figure 2.36. Depth profile for Nb/PI (375 °C) structure. The interfaces of interest are highlighted in red.

2.6.2 SIMS Analysis on Nb/PI (225 °C)

Fig. 2.37 shows the sputtering time dependent intensity of secondary ion intensity and the corresponding cross-section. The interface of interest is highlighted in red in the cross-section image. No diffusion of O₂ into Nb was observed, due to curing PI (HD-4110) at lower temperature of 225 °C.

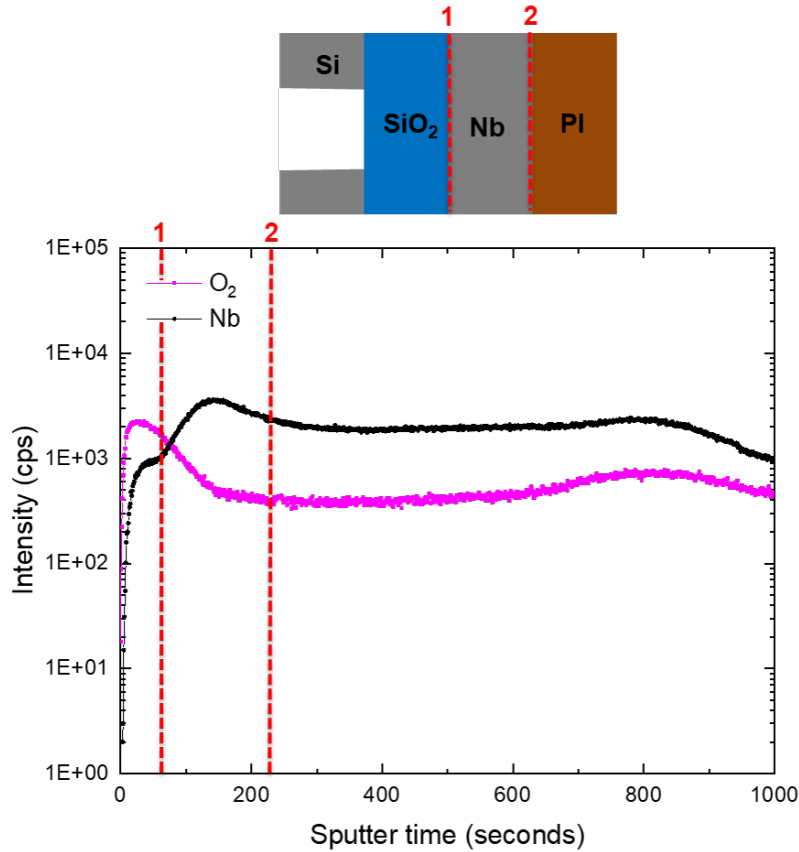


Figure 2.37. Depth profile for Nb/PI (225 °C) structure. The interfaces of interest are highlighted in red.

2.6.3 SIMS Analysis on Al/Nb/Al/PI (375 °C)

Fig. 2.38 shows the sputtering time dependent intensity of secondary ion intensity and the corresponding cross-section. The interface of interest is highlighted in red in the cross-section image. The interface 1 and 3 can be clearly seen by the increase in the signal intensity of Al and O₂, this maybe due to formation of a thin oxide layer on top of Al. The interaction of O₂ with Nb can be seen at interfaces 3 and 4, but an increase in Al intensity can also be observed at those interfaces. This shows that Al acts a promising barrier layer between Nb and PI and reduces the O₂ interaction with Nb, thereby protecting superconducting properties of Nb.

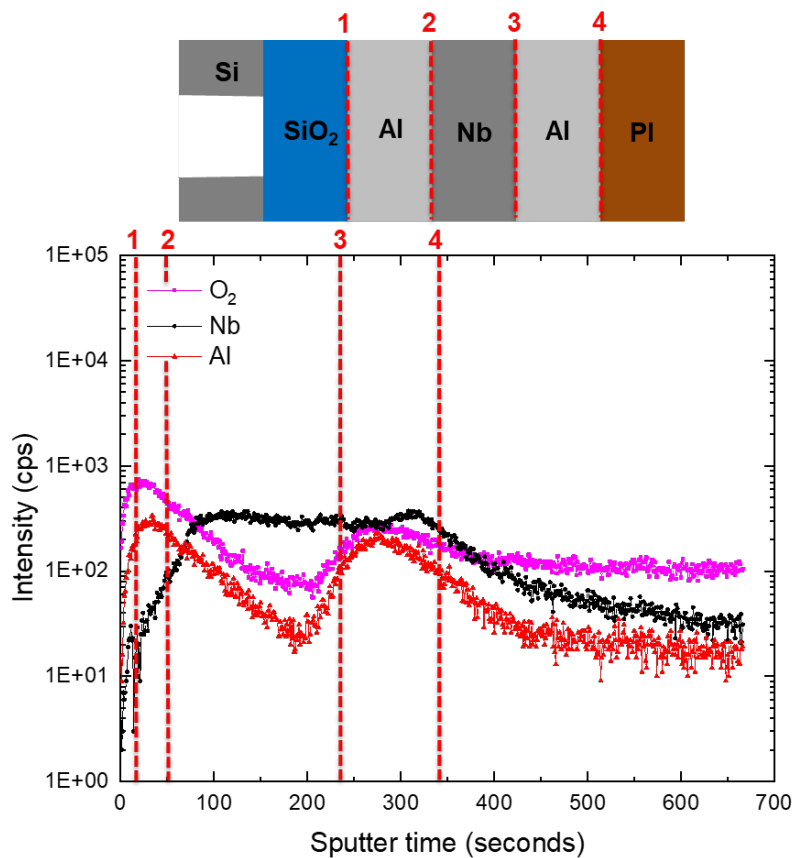


Figure 2.38. Depth profile for Al/Nb/Al/PI (375 °C) structure. The interfaces of interest are highlighted in red.

2.6.4 SIMS Analysis on Al₂O₃/Nb/Al₂O₃/PI (375 °C)

Fig. 2.39 shows the sputtering time dependent intensity of secondary ion intensity and the corresponding cross-section. The interface of interest is highlighted in red in the cross-section image. Similar to the previous case, interface 1 and 3 can be clearly visualized due to increase in the signal intensity of Al₂O₃. An increase in the O₂ intensity can be seen at interface 1 and 3 but a step increase in Al₂O₃ signifies limited interaction of Nb with O₂. Hence Al₂O₃ acts as an effective barrier layer and preserves Nb superconductivity.

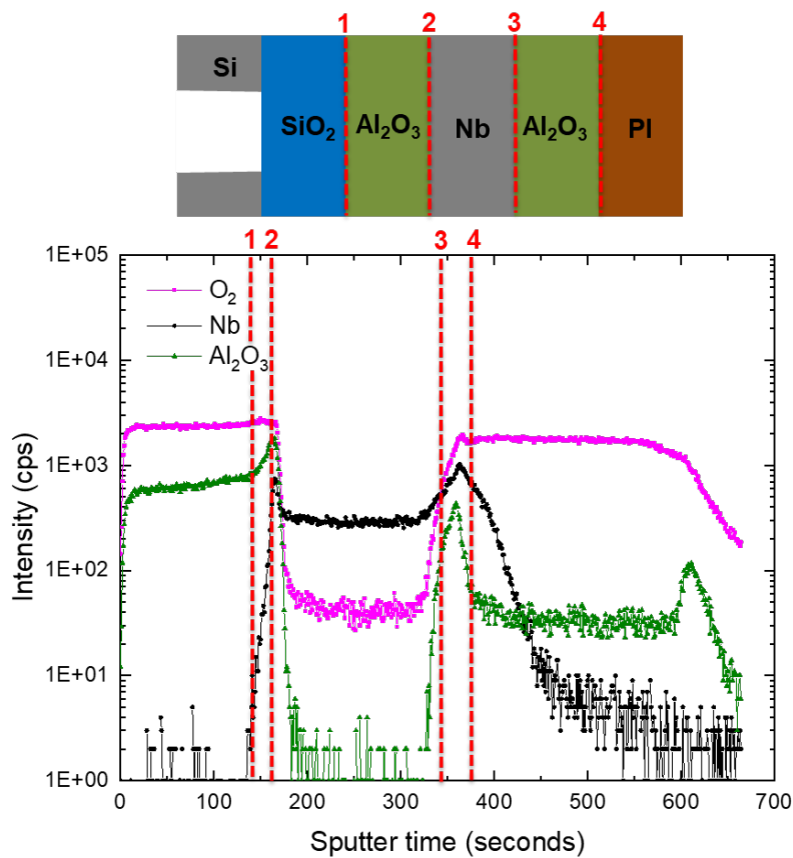


Figure 2.39. Depth profile for $\text{Al}_2\text{O}_3/\text{Nb}/\text{Al}_2\text{O}_3/\text{PI}$ (375°C) structure. The interfaces of interest are highlighted in red.

In this section, multiple samples were investigated with a goal to understand the underlying conditions leading to Nb degradation at elevated temperatures. It was readily apparent that the degradation of Nb was prevented by curing PI at lower temperature (225°C) and by using barrier layers of Al and Al_2O_3 , which acts as a diffusion barrier and oxygen getter against degradation caused by curing PI at elevated temperature of 375°C .

2.6.5 Acknowledgement

The author would like to acknowledge Steve Novak and Satyavolu Papa Rao from SUNY Polytechnic Institute for their help with SIMS measurements.

Chapter 3

Minimizing Film Stress and Degradation in Thin-Film Nb Superconducting Cables

Film stress plays a vital role in the superconducting material properties of Nb thin films. One of the major reasons for film stress is because film depositions are usually made above room temperature on top of a substrate with different coefficient of thermal expansion. Previous research efforts by other groups have focused on ion gun processing, substrate fixturing and wafer preparation in order to minimize film stress. Bass et al. [31] have discussed the role of wafer preparation on the stress of Nb thin films. They have shown the effect of ex-situ substrate cleaning and in-situ ion cleaning on Nb film stress. Liu et al. [32] focused on substrate material to minimize Nb stress. They have shown that a Nb film deposited on oxidized Si is smoother and has larger crystallite size as compared to film deposited on bare Si substrates. They also found that the Nb films deposited on oxidized Si had a better quality than on bare Si. Hoffman [33] has made an extensive study of stresses in magnetron sputtered thin films, and observed that the film stress transitions from compressive to tensile as Ar pressure is increased. The transition pressure is a function of atomic mass of the sputtered material as well as other parameters. In this section we have characterized the transition pressure for 250 nm thick Nb films on flexible Kapton substrates in a particular sputtering system, and have shown that neutral stresses can be achieved at room temperature, suitable for fabrication of superconducting flexible circuits. We explored the impact of Ar pressure during Nb sputtering on the quality of Nb thin films. By varying the Ar pressure during sputter depositions, we have produced both tensile and compressive films in order to find the pressure that yields a balanced stress Nb film on Kapton. In order to see the effect of varying Ar pressure on the Nb film, all other deposition parameters such as base pressure, ion milling, RF power and thickness were held constant. A balanced stress Nb film was also

tested with a thin Al barrier layer (10's of nm) to preserve Nb superconductivity during subsequent fabrication steps.

3.1 Fabrication and Measurement setup

We used 50 μm wide photo-lithographically patterned lines with larger probe pads on each end in order to facilitate measurements. The different metals were deposited in a CHA Mark 50 deposition system capable of both sputter deposition and electron-beam thermal evaporation. The test samples included patterned samples to measure superconducting transition temperature (T_c) and critical current (I_c), oxidized silicon coupons to measure sheet resistance and 50 μm thick Kapton substrates to detect the film stress based on curling of the Kapton. The Kapton sample was 50 μm thick and flat to start, in order to see the effect of different Ar pressure on the whole structure (Nb/Kapton). Other substrates started as oxidized silicon wafers (except for Kapton) onto which 250 nm of Nb was sputter-deposited (DC sputter for 30 minutes). Vacuum base pressures of 3.5×10^{-7} Torr were attained prior to depositing the Nb, which provided repeatable Nb properties in previous experiments. For samples with Al, Al was e-beam evaporated without breaking vacuum. Ar pressures tested were in the range of 2 to 8 mTorr. A power of 1 kW and RF power density of ~ 0.008 kW/cm² was used for all Ar pressures.

Superconducting superconducting transition temperature measurements were carried out in a pulse-tube based cryostat with temperature control from 1.2 K and up. For each of these tests, the sample is mounted onto a sample holder that allows 4-point probing of the test structure in order to achieve accurate resistance measurements.

3.2 Stress of Nb on Kapton

Different Ar pressures in the range of 2 to 8 mTorr were investigated. The effect of varying Ar pressure for Nb films deposited on Kapton is shown qualitatively in Fig. 3.1, based on the direction and degree of sample curling.

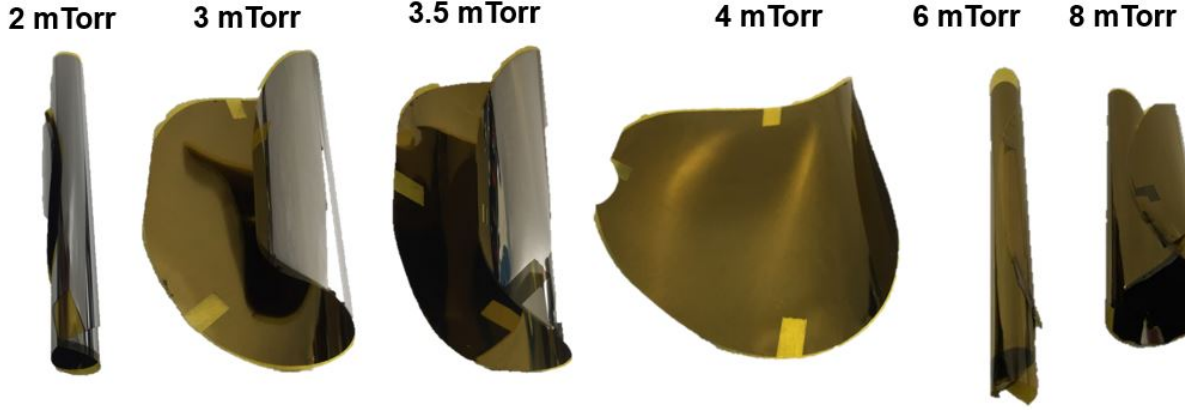


Figure 3.1. Images of 250 nm thin-film Nb deposited using different Ar pressures on 50 μm thick Kapton substrates, exhibiting different stress characteristics.

It can be seen from Fig. 3.1 that Ar pressures lower than 4 mTorr produced compressive films whereas pressures higher than 4 mTorr resulted in a tensile film.

Table 3.1. Thickness, Sheet resistance, Superconducting transition temperature and Critical current comparison for different Ar pressures.

Ar pressure (mTorr)	Thickness (nm)	Sheet resistance (Ω/\square)	T_c (K)	I_c (mA)	Nb Stress
2	220 ± 10	1.10	8.5	82	Compressive
3	235 ± 10	1.10	8.4	130	Compressive
3.5	240 ± 10	0.98	8.5	130	Compressive
4	240 ± 10	0.98	8.9	194	Slightly Compressive
6	235 ± 10	1.10	8.9	158	Tensile
8	240 ± 10	1.60	8.7	134	Tensile

Table. 3.1 compares the thickness, sheet resistance, superconducting transition temperature, critical current and stress state corresponding to specific Ar pressure. It can be seen that 4 mTorr and 6 mTorr have the highest I_c of 194 mA and 158 mA respectively. We also observed that both of these cases have a T_c of 8.9 K which is highest as compared to other Ar pressures. It can also be seen that by changing the Ar pressure the thickness of Nb film changes. The thickness was measured at multiple places along the 50 μm patterned lines. The thickness corresponding to 4 mTorr Ar pressure is ~ 240 nm which is very close to the expected thickness of 250 nm.

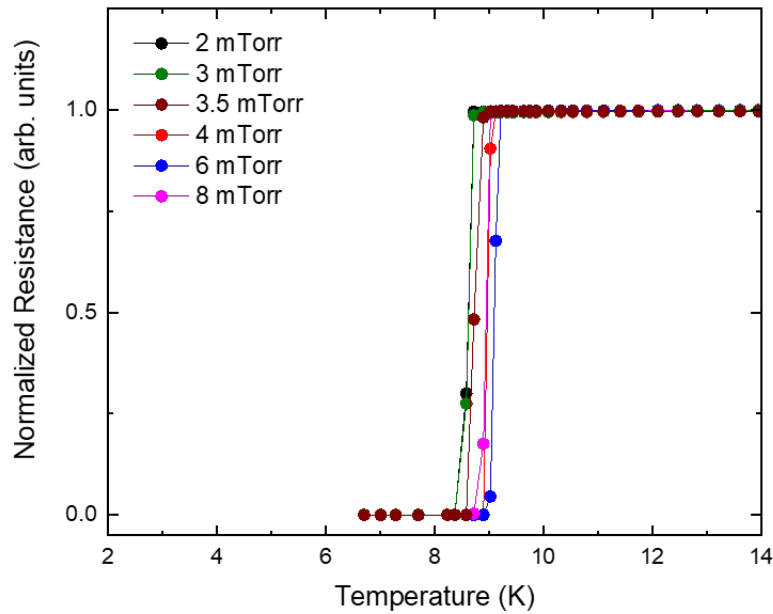


Figure 3.2. Plot of normalized resistance vs. temperature measurement comparison of ~ 250 nm Nb deposited on $50 \mu\text{m}$ thick Kapton using different Ar pressures. The sputtering power used was 1 kW over a target area of $\sim 127 \text{ cm}^2$.

Fig. 3.2 shows the superconducting transition temperature plots for all Ar pressures. It can be seen that the DC samples corresponding to all the Ar pressures have a clean transition, while a 4 mTorr Ar pressure resulted in the highest superconducting transition temperature of ~ 8.9 K. From all of the results, we settled on an Ar pressure of 4 mTorr for deposition of 250 nm thick Nb on $50 \mu\text{m}$ thick Kapton.

3.2.1 Test Results for Different Power Levels - 0.75 kW and 1.25 kW

Different power levels were tested with Ar pressure of 4 mTorr in order to study the effect of power on the stress and superconducting properties of Nb. As shown previously, The test samples included patterned samples to measure superconducting transition temperature (T_c) and critical current (I_c), oxidized silicon coupons to measure sheet resistance and $50 \mu\text{m}$ thick Kapton substrates to detect the film stress based on curling of the Kapton. Fig. 3.3 shows the plot of superconducting transition temperature of 4 samples deposited using

a power of 0.75 kW with 4 mTorr Ar pressure. Fig. 3.4 shows the corresponding image of Kapton with slightly compressive stress.

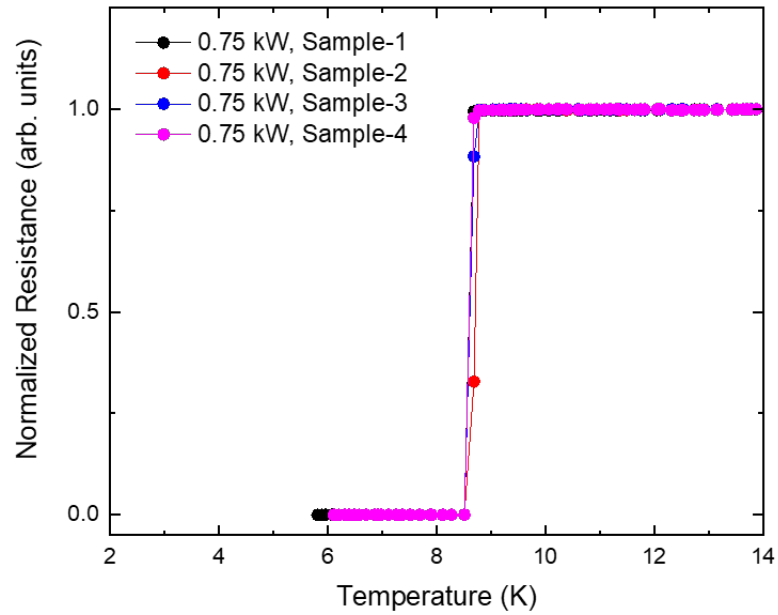


Figure 3.3. Plot of normalized resistance vs. temperature measurement of Nb deposited using Ar pressure of 4 mTorr and power of 0.75 kW.

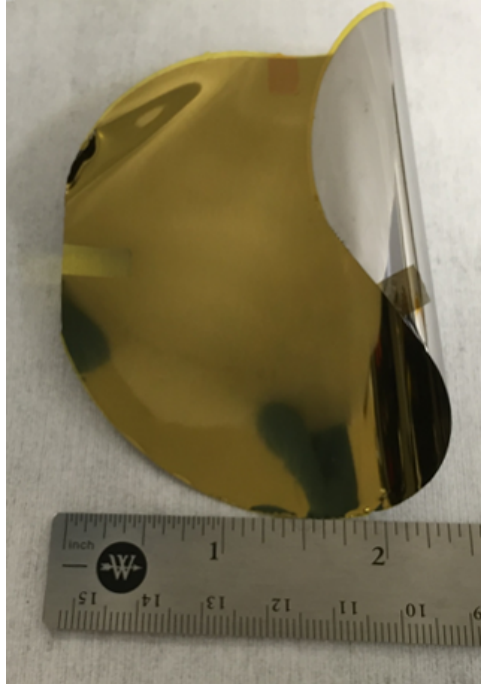


Figure 3.4. Image of Nb deposited on Kapton substrate using Ar pressure of 4 mTorr and power of 0.75 kW exhibiting slightly compressive stress.

Fig. 3.5 shows the plot of superconducting transition temperature of 4 samples deposited using a power of 1.25 kW with 4 mTorr Ar pressure. Fig. 3.6 shows the corresponding image of Kapton indicating compressive stress.

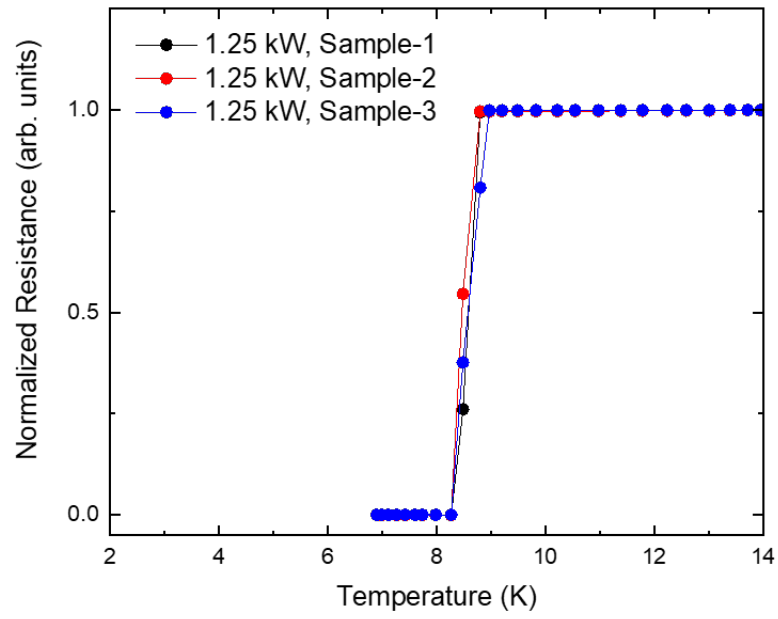


Figure 3.5. Plot of normalized resistance vs. temperature measurement of Nb deposited using Ar pressure of 4 mTorr and power of 1.25 kW.

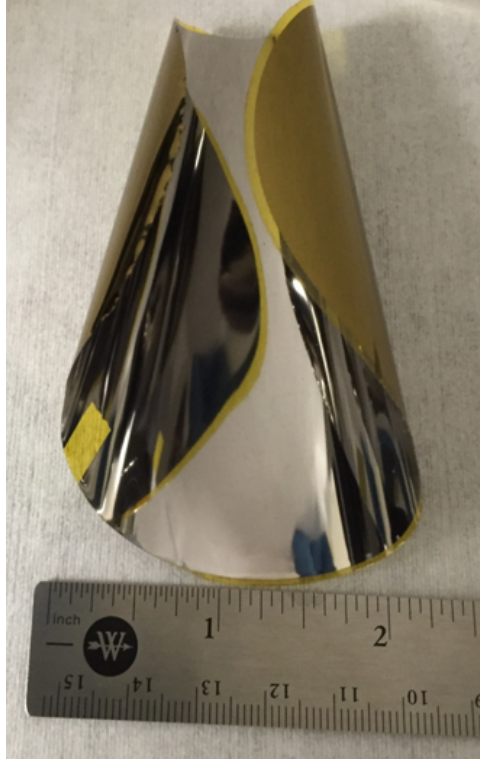


Figure 3.6. Image of Nb deposited on Kapton substrate using Ar pressure of 4 mTorr and power of 1,25 kW exhibiting compressive stress.

Table 3.2. Thickness, Sheet resistance, Superconducting transition temperature and critical current comparison for different power levels with 4 mTorr Ar pressure.

Ar pressure (mTorr)	Thickness (nm)	Power (kW)	Sheet resistance (Ω/\square)	T_c (K)	I_c (mA)	Film stress
4	180 ± 10	0.75	1.41	8.5	95	Compressive
4	240 ± 10	1.00	0.98	8.9	194	Slightly Compressive
4	275 ± 10	1.25	0.83	8.4	115	Tensile

Table. 3.2 compares the thickness, sheet resistance, superconducting transition temperature, critical current and film stress corresponding to 4 mTorr Ar pressure for varying power levels - 0.75 kW, 1 kW and 1.25 kW. A significant variation was observed as an effect of changing the power. 0.75 kW of power yielded a thickness of ~ 180 nm whereas 1.2 kW of power yielded a thickness of ~ 275 nm. Both of these thickness values indicate significant amount of variation from the expected thickness of ~ 250 nm, which was obtained by using 1 kW of power. Also a notable amount of reduction in T_c and I_c was observed for power levels of 0.75 kW and 1.25 kW as compared 1 kW power level.

Since 4 mTorr Ar pressure produced the least stress Nb film and has the highest T_c and I_c therefore it was considered the optimum Ar pressure to get balanced stress Nb film with best superconducting properties.

3.3 Stress of Al/Nb/Al Film on Kapton

In order to minimize degradation of Nb superconducting properties while curing subsequently deposited polyimide layers, a barrier layer of Al may be used [25]. The sputtering parameters used for Nb deposition were 0.008 kW/cm^2 power density and 4 mTorr Ar pressure, since this produced the most balanced stress Nb film. Al was e-beam evaporated in the same vacuum chamber. 250 nm and 20 nm of thickness was used for Nb and Al, respectively.

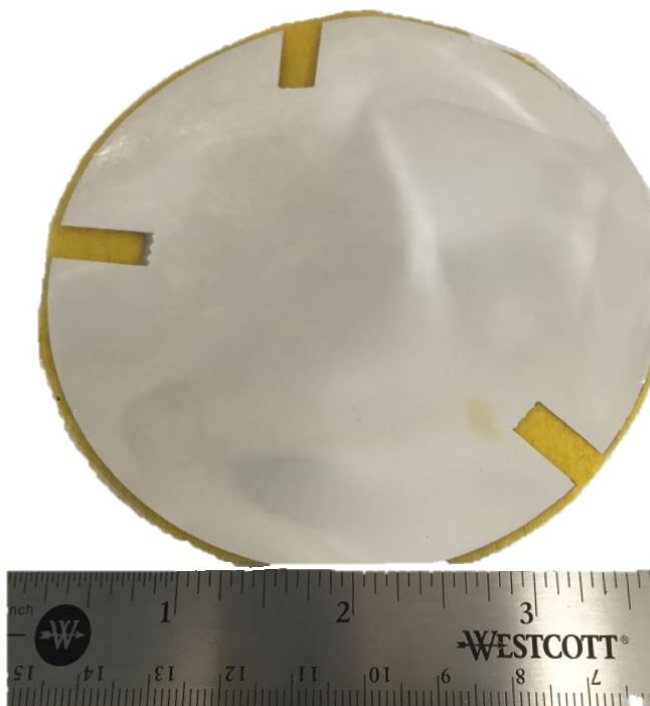


Figure 3.7. Image of metal stack Al (20 nm)/ Nb (250 nm)/ Al (20 nm) on a $50 \mu\text{m}$ thick Kapton substrate. Nb was deposited using 4 mTorr Ar pressure. The room temperature stress on Kapton was approximately neutral as exhibited by the flatness of the free (unmounted) sample.

Fig. 3.7 shows image of an unmounted Kapton with a deposited Al/Nb/Al film. It can be seen that the Kapton is essentially flat, showing balanced stress for this sample and deposition conditions.

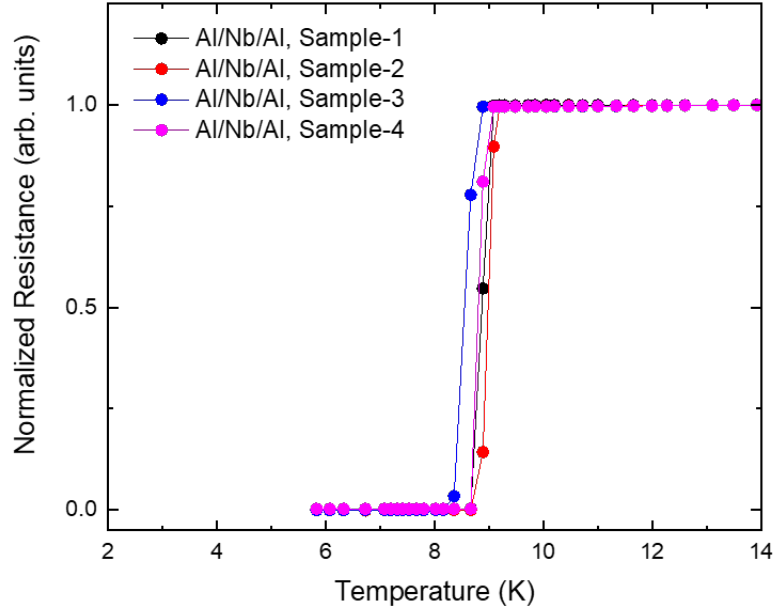


Figure 3.8. Plot of normalized resistance vs. temperature measurement comparison of metal stack Al(20 nm)/Nb (250 nm)/Al (20 nm). Nb was deposited using 4 mTorr Ar pressure.

Fig. 3.8 shows superconducting transition temperature plots for all four samples. It can be seen that all four samples have the same superconducting transition temperature of 8.6 K. This test shows the performance and consistency of the Al/Nb/Al deposited film.

Table 3.3. Sheet resistance, Superconducting transition temperature and Critical current comparison for 4 mTorr Ar pressure level for all Al/Nb/Al films.

Sample no.	Sheet resistance (Ω/\square)	T_c (K)	I_c (mA) for 50 μm wide line
1	0.57	8.6	242
2	0.57	8.6	205
3	0.57	8.6	235
4	0.57	8.6	230

Table 3.3 shows the sheet resistance, superconducting transition temperature and critical current for four different samples with Al/Nb/Al films that were deposited with the same

deposition parameters, but in four different runs. All four samples have the same sheet resistance with an average critical current of ~ 228 mA.

We successfully balanced the stress in Nb films deposited on flexible Kapton substrates. We evaluated the impact of Ar pressure level in terms of stress, thickness and sheet resistance. Nb deposited using a power of ~ 0.008 kW/cm² and Ar pressure of 4 mTorr produced films with the most balanced (neutral) stress and the highest T_c of 8.9 K and I_c of 194 mA, as compared to other pressures tested. Moreover we have used the low stress Nb deposition parameters to explore stress in and performance of Al/Nb/Al films. We have produced near zero stress Al/Nb/Al/Kapton structures with T_c as high as 8.6 K and I_c as high as 242 mA for 50 μ m wide lines and ~ 250 nm thick lines.

Chapter 4

Design, Fabrication and Characterization of Superconducting Flexible Stripline Transmission Line and Resonators

4.1 Introduction

Significant progress has been made towards dense and multi-layer interconnect technologies for cryogenic electronic systems [8,9,34–37]. Though the fabrication process is substantially more involved, one of the major reasons to pursue stripline transmission lines is for enhanced impedance control, electromagnetic shielding and reduced cross-talk compared to microstrip transmission line configurations. Our previous work on related technologies demonstrated that multiple layers of polyimide can be used to embed superconducting traces and, if performed properly, can result in improvements in the robustness of the devices [25,36].

The polyimide used in this section are HD-4100 and HD-4110 (from HD Microsystems). A drawback of using polyimide for passivation, embedding, or for multi-layer stacks with Nb superconducting traces is the undesired interaction of the Nb and polyimide during the polyimide curing process at high temperatures, which leads to degradation, variation or loss of Nb superconducting properties.

Multiple material stack-ups have previously been investigated with a goal to protect the superconducting properties of Nb thin films when the Nb may be subjected to subsequent higher-temperature process steps (such as for curing of polyimide). Al was used in this work because it was readily available and straightforward to use without breaking vacuum in our deposition system. We found that the degradation of Nb traces was substantially reduced by using 20 nm of Al as protective layers [25]. We also found that curing above a certain temperature on top of a Nb layer can adversely affect the superconducting properties including superconducting transition temperature (T_c) and critical current (I_c) [38]. In this

section, we used two approaches to protect the Nb superconductivity: inclusion of thin Al layers between the Nb and PI and using a lower curing temperature for the PI.

In the following sections we describe the stripline fabrication processes and measurement procedures in more detail. We have measured DC properties, including T_c and I_c , of the stripline transmission lines. We also present the microwave performance of Al/Nb/Al flexible superconducting stripline transmission lines measured at 4.2 K. We describe and analyze the performance of similarly-fabricated stripline transmission line resonators and extract effective parameters using the sensitive resonator measurements.

4.2 ADS Layout of Stripline Transmission Line and Transmission Line Resonator

The ADS layout of 25 cm long stripline transmission line, 13 cm long stripline transmission line resonator and 7 cm long embedded microstrip transmission line is shown in Fig. 4.1. Fig. 4.2 shows close-up view of the layout of stripline transmission line and transmission line resonator.

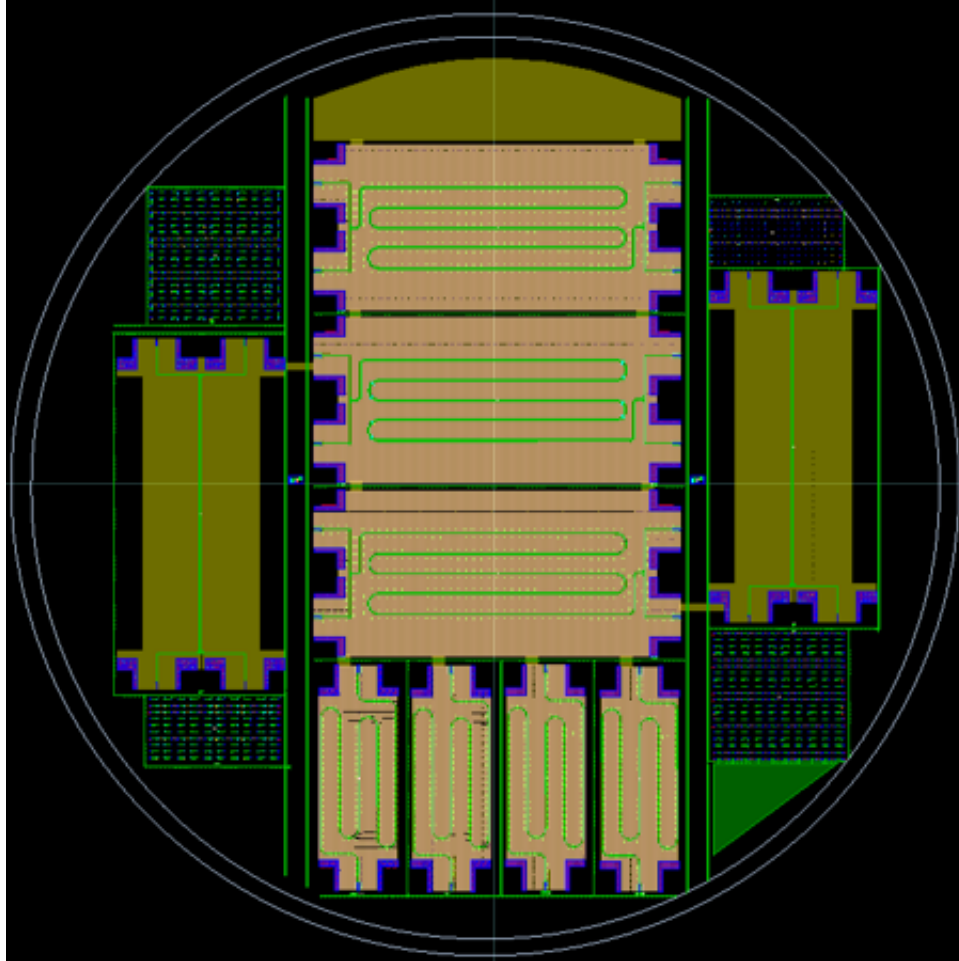


Figure 4.1. ADS layout of stripline transmission line and transmission line resonators on a 150 mm diameter Si wafer. The layout includes 3 stripline transmission lines (centre), 4 stripline transmission line resonators (bottom), 2 microstrip transmission line (one on each side) and via chains structures.

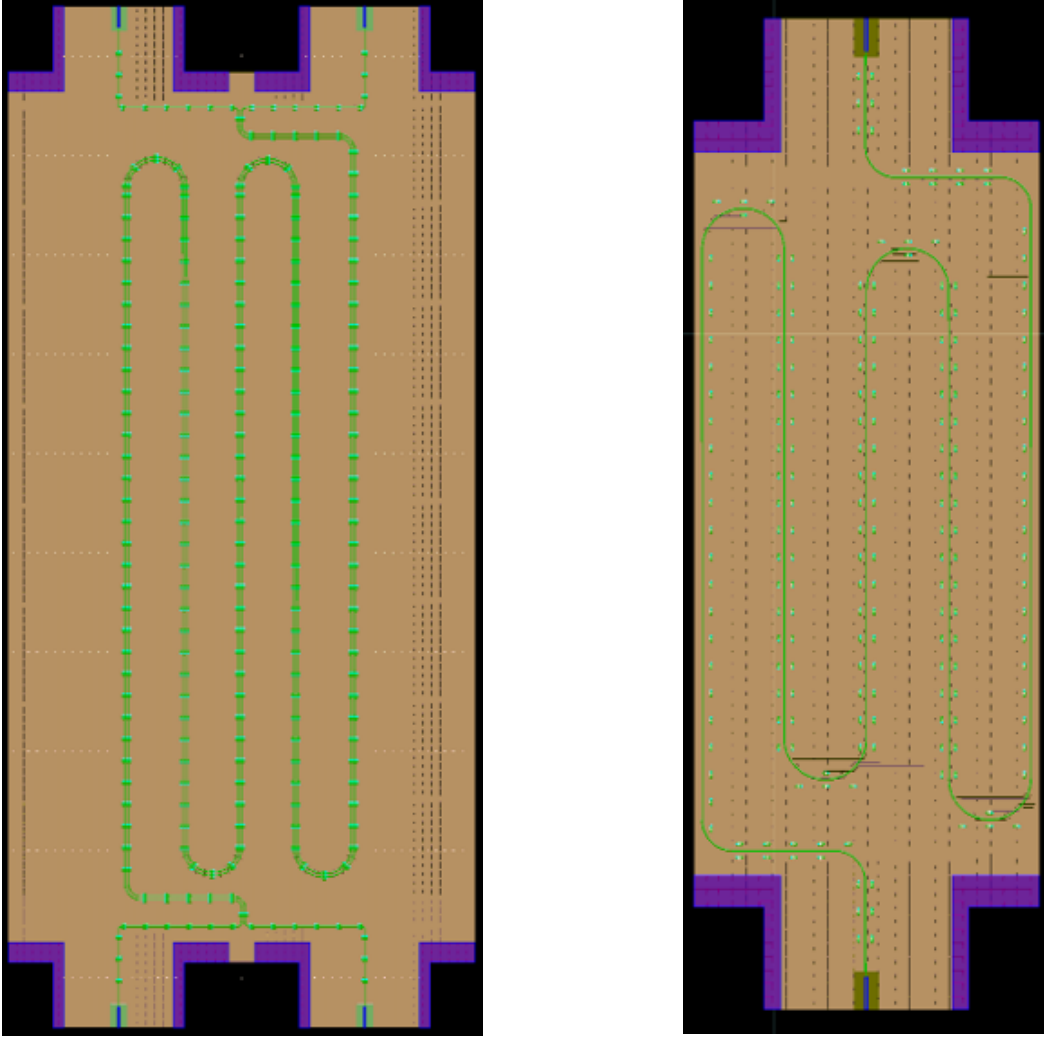


Figure 4.2. ADS layout of a stripline transmission line (left) and transmission line resonator (right).

4.3 Fabrication Process

The fabrication procedure is outlined in Fig. 4.3. To start, on a silicon handle wafer, a release layer of 50 nm thick Cr followed by 200 nm thick Al was deposited. A 10 μm layer of HD-4100 was spin coated and cured in a nitrogen (N_2) ambient oven at 375 $^\circ\text{C}$ for one hour. A ground plane metallization stack of Al(20 nm)/Nb(250 nm)/Al(20 nm) was deposited on top of HD-4100. Nb was sputter-deposited (DC sputter for ~ 30 minutes) with a power of $\sim 8 \text{ W}/\text{cm}^2$ and Ar pressure of 4 mTorr to a thickness of $\sim 250 \text{ nm}$ [26, 32, 33, 39]. Each Al layer was electron-beam evaporated in the same vacuum chamber,

during the same pump-down, without breaking vacuum, to a thickness of ~ 20 nm. Small openings (catch pads for electroplated Cu vias) were photolithographically-defined, using a photoresist lift-off process, on top of the ground plane. These areas were then deposited with 50 nm thick Ti, followed by 200 nm thick Cu, as shown in step 4 of Fig. 4.3. A $20 \mu\text{m}$ layer of HD-4110 was deposited by spin coating, patterned by photolithography to re-open the via catch-pad areas and then cured at 225°C (shown in Fig. 4.4). This HD-4110 layer is the first dielectric layer, between the ground plane and signal trace layer. The main reason to cure HD-4110 at 225°C is to limit the temperature to which the underlying Nb is exposed and thereby protect the superconductivity of Nb when embedded with polyimide [36]. Using the Nb ground plane for a conductive path, the open areas in HD-4110 were then electroplated with Cu to form bottom ground-to-signal layer vias. This was followed by depositing an Al(20 nm)/Nb(250 nm)/Al(20 nm) signal trace layer, which was patterned using a conventional lift-off process, as shown in step 6 of Fig. 4.3. The stripline trace had a line width of $24 \mu\text{m}$, which yielded a characteristic impedance of $\sim 50 \Omega$. A second layer of catch-pads were again defined on top of Al/Nb/Al and deposited with Ti/Cu. A second layer of HD-4110 was deposited by spin coating, patterned and cured at 225°C for a nominal thickness of $20 \mu\text{m}$. Cu vias were again electroplated on top of the Ti/Cu catch-pad layer to continue formation of the ground-layer via stack (shown in Fig. 4.5). We note that the signal layer did not have vias, was protected and opened during processing, in a manner that allowed connector pins to make contact to the lines once the fabrication was completed. A top ground layer of Al(20 nm)/Nb(250 nm)/Al(20 nm) was then deposited on top of the second layer of HD-4110, as shown in step 9 of the fabrication procedure presented in Fig. 4.3. The top ground was covered with an encapsulation layer of HD-4100 cured at 225°C to a thickness of $4 \mu\text{m}$. Signal connection pads (50 nm Ti followed by 250 nm Au) were then deposited on top of the exposed signal trace ends and in patterned encapsulation layer regions for connection to the ground layers, as shown in step 10 of Fig. 4.3. Fig. 4.6 shows the image after deposition of UBM on one end of the stripline transmission line sample. The

samples were then released in a NaCl solution using anodic dissolution to provide individual flexible structures [35,40].

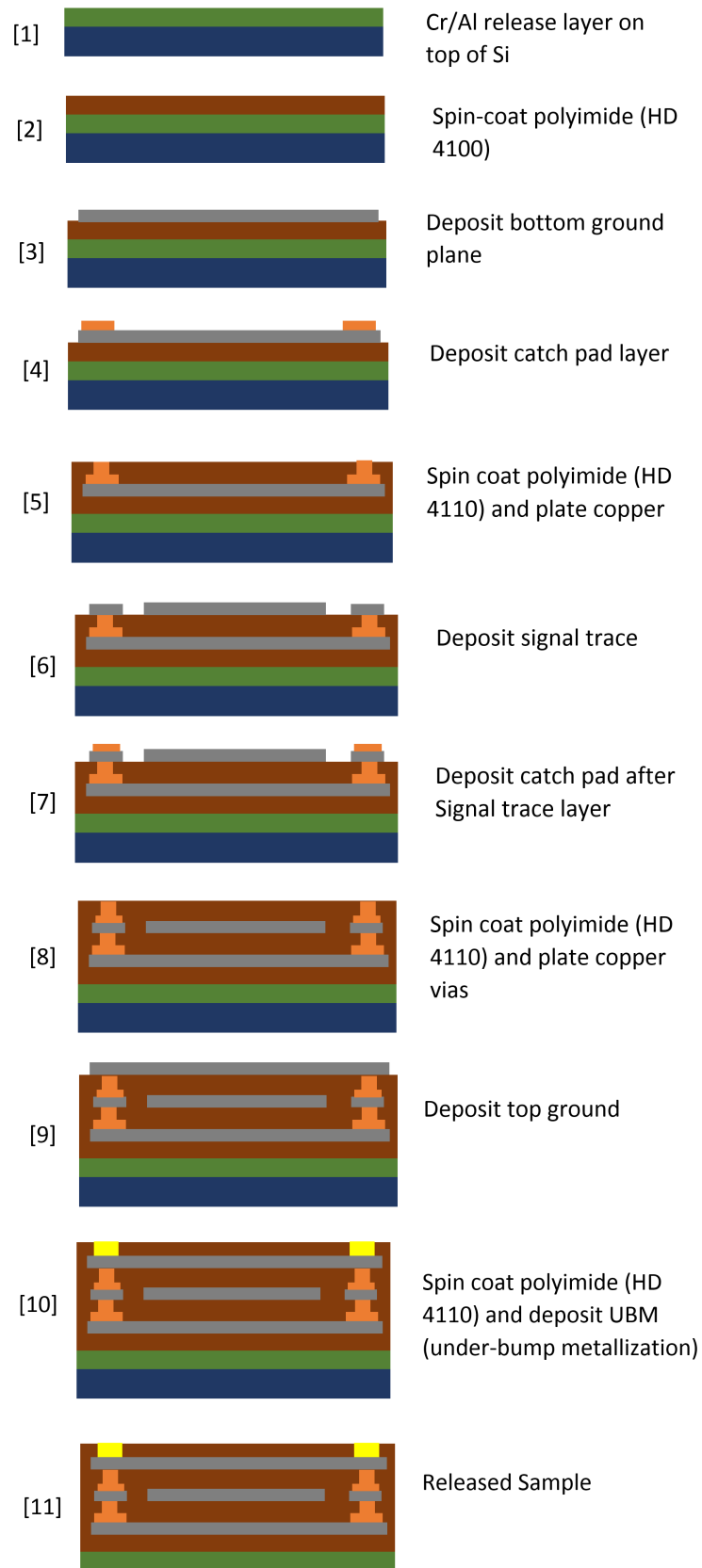


Figure 4.3. Schematic sample cross-sections at various points during fabrication, showing key fabrication process steps for superconducting stripline transmission lines.

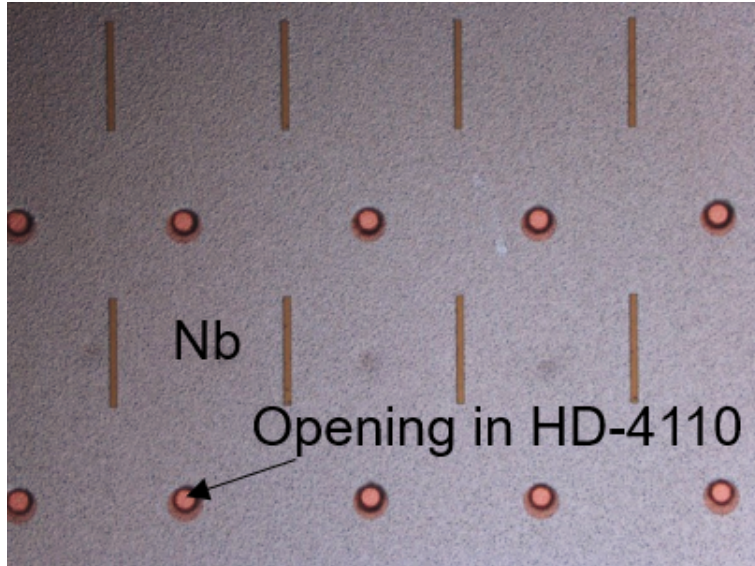


Figure 4.4. Wafer level image of the stripline transmission line after spin-coating HD-4110 and creating openings to catch-pad for plating.

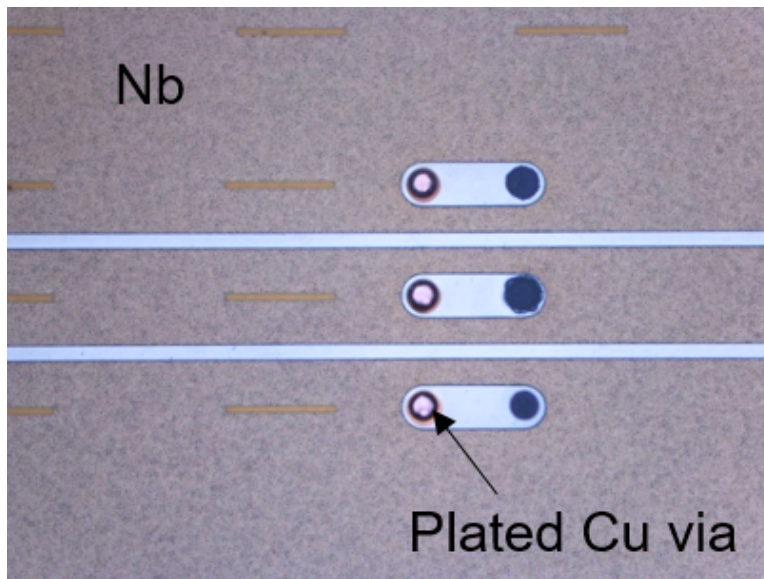


Figure 4.5. Wafer level image of the stripline transmission line after spin-coating HD-4110 on top of signal layer and plating Cu through the openings in HD-4110 to connect bottom and top ground layers.

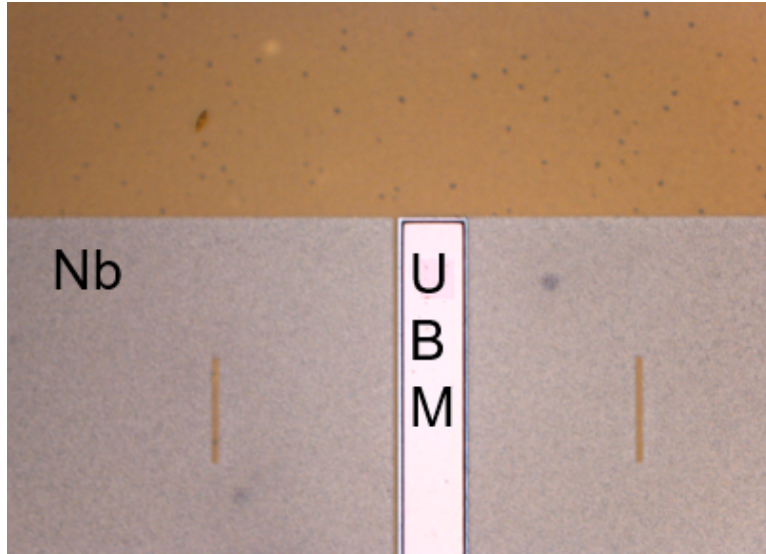


Figure 4.6. Wafer level image of the stripline transmission line after depositing UBM (Ti/Cu/Au) layer to make connections for signal and ground layer.

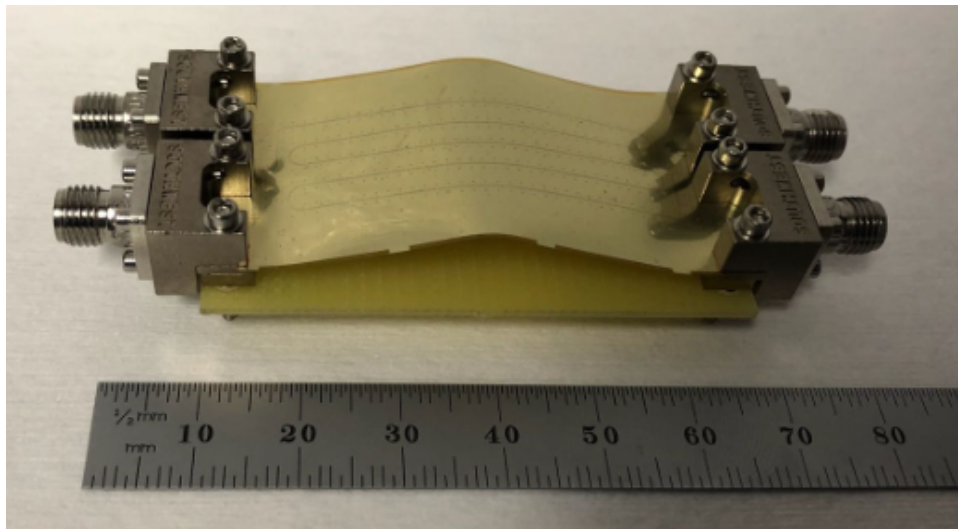


Figure 4.7. Flexible Al/Nb/Al stripline transmission line (25 cm long, meandered), with Southwest Microwave, Inc. SMA end-launch connectors attached and mounted to a PCB support board. Note that two transmission lines, involving four external connections, are connected in this structure. The design provides meandered lines that are in close proximity over a substantial portion of their length and is also used for cross-talk characterization.

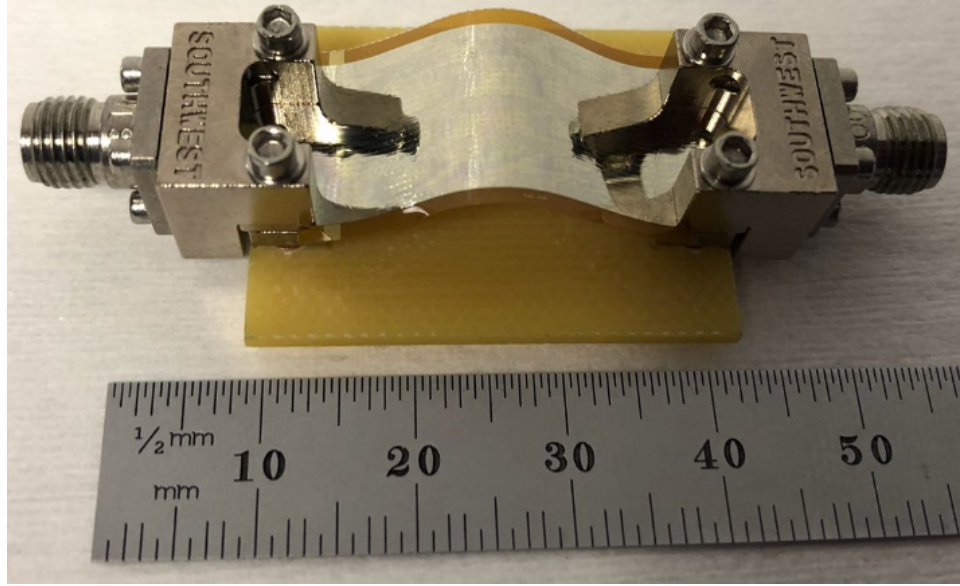


Figure 4.8. Flexible Al/Nb/Al stripline transmission line resonator (13 cm length for resonant section), with Southwest Microwave, Inc. SMA end-launch connectors attached and mounted to a PCB support board.

4.4 Measurement Methods

End-launch SMA connectors from Southwest Microwave, Inc. were used for electrical connections for DC and RF measurements. A blank piece of printed circuit board (PCB) was used to support the sample to prevent it from breaking with the heavy end-launch connectors attached. Fig. 4.7 shows an assembled stripline transmission line sample with four connections to two closely-spaced lines (100 μm spacing with no vias between the lines). Fig. 4.8 shows an assembled stripline transmission line resonator sample used to characterize the microwave loss properties of structures fabricated using the multi-layer fabrication process.

A pulse tube (PT) cryostat with stainless steel cryogenic RF coaxial cables was used for measurements above $\sim 1.2\text{K}$ (shown in Fig. 4.9). The resonators were baked at 90°C prior to loading in the pulse tube cryostat for measurements. For DC measurements, to obtain critical current I_c and superconducting transition temperature T_c , 2-wire measurements at multiple temperatures were made in the PT. A micro-Ohm meter (Keysight 34420A) was used to measure resistance values for obtaining T_c . Critical current measurements were

made in the set-up using a Keithley 2400. S-parameters were measured using an Agilent (Keysight) N5227A PNA (shown in Fig. 4.10). The transmission lines were measured in LHe at frequencies up to 10 GHz. Since these lines had a very low loss, a careful calibration was necessary. We used a short-open-load-reciprocal through calibration method that has been previously discussed [35]. Measurements were performed with an RF power of -20 dBm out of the PNA. The transmission line resonators were measured at different temperatures (above 1.2 K) up to ~ 14 GHz in the PT system.



Figure 4.9. A stripline transmission line sample mounted on a sample holder, connected to cryogenic cables, for use in the PT system.

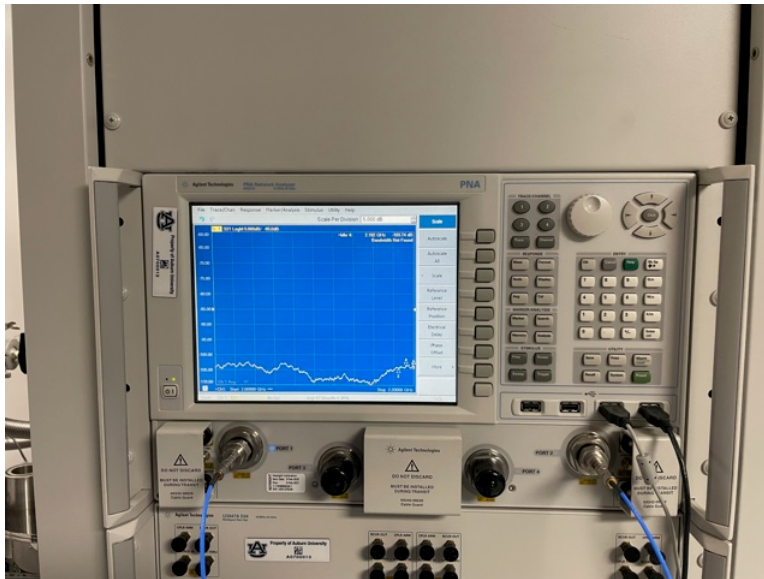


Figure 4.10. Agilent (Keysight) N5227A network analyzer with multiple ports.

4.5 Results and Discussion

In this section we present the characterization results for flexible superconducting stripline transmission lines and resonators. Multiple stripline transmission lines were measured to characterize DC properties. Microwave performance was measured, including RF cross-talk performance, for the transmission lines. To explore the microwave loss properties in further detail, weakly-coupled stripline resonators, with high quality factors, were used and corresponding results are also presented in this section.

4.5.1 DC Properties of Stripline Transmission Lines

superconducting transition temperature (T_c) and critical current (I_c) measurements were carried out, as described in the previous section. Both signal and ground exhibit complete transition at 8.8 K and 8.6 K, respectively. Fig. 4.11 shows superconducting transition temperature T_c plots for the signal traces of stripline transmission lines. A total of eight stripline transmission line samples were measured. It can be seen from Fig. 4.11 that all the stripline transmission lines have a clean transition to the superconducting state and resulted in a superconducting transition temperature of ~ 8.8 K. Fig. 4.12 is the T_c plot for the ground plane of the respective stripline transmission line sample. The T_c for both the signal line and ground plane is close to the Nb bulk value of ~ 9.2 K and demonstrates that the Al/Nb/Al signal layer has survived the multiple subsequent, elevated temperature, fabrication processes.

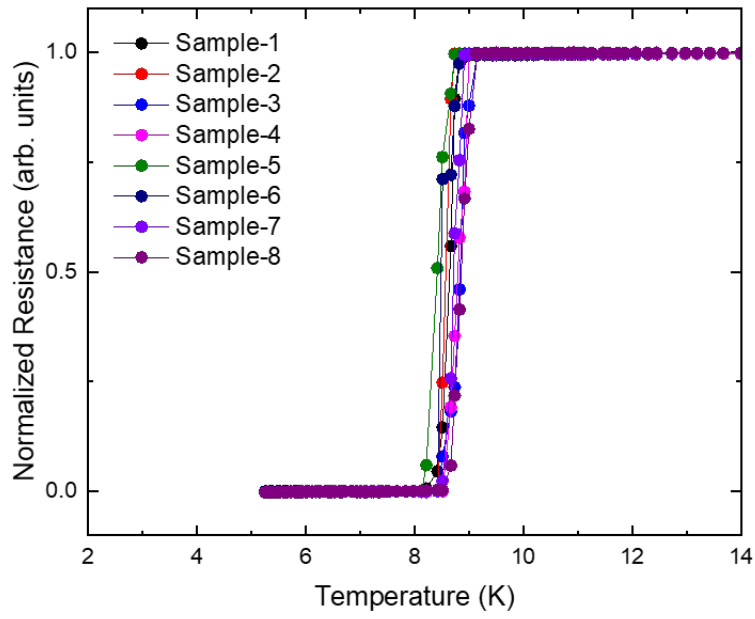


Figure 4.11. T_c measurement results for flexible stripline transmission lines measured in a pulse tube cryostat.

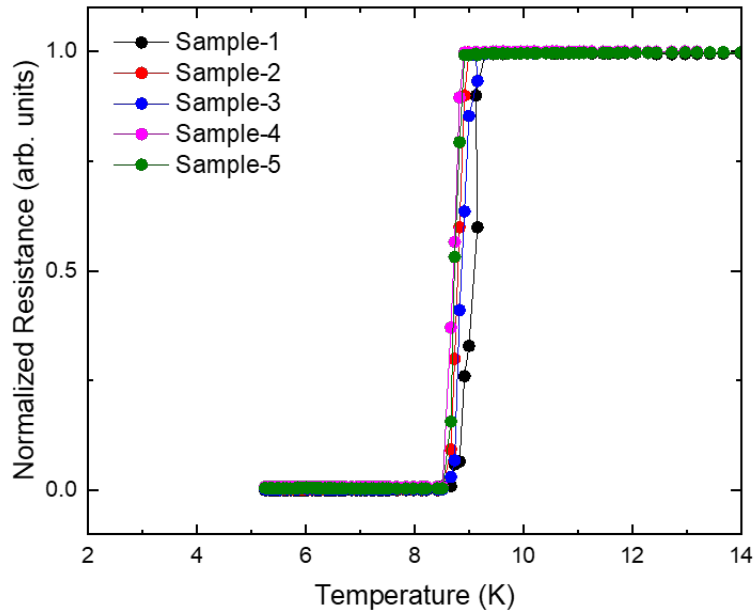


Figure 4.12. T_c measurement results for the stripline ground plane measured in a pulse tube cryostat.

Fig. 4.13 shows a box plot of I_c measurement results for multiple stripline transmission lines. I_c results from measurements in the cryostat at different temperatures are compared with the values obtained in a LHe dewar. The I_c values from measurements immersed in LHe (in a dewar) were $\sim 2\times$ higher than those for the same structures measured in the PT system.

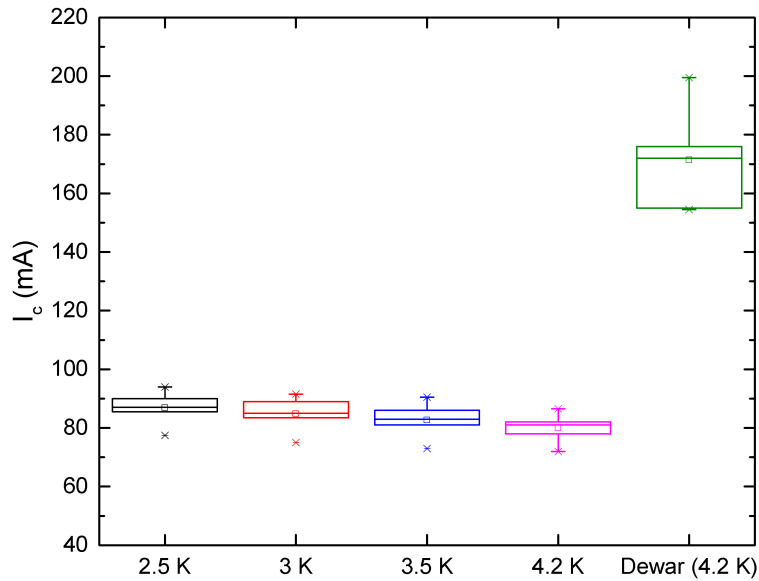


Figure 4.13. I_c measurement results for flexible stripline transmission lines measured in a pulse-tube (PT) cryostat at different temperatures or in a LHe dewar at 4.2 K.

4.5.2 Microwave Measurement of Stripline Transmission Lines

S-parameter measurement results, for a sample measured at 4.2 K (in LHe), are shown for S_{11} in Fig. C.10 and for S_{21} in Fig. 4.15, along with corresponding Keysight ADS simulations. S_{11} shows a reasonable impedance match over the tested frequency range, with increasing reflection and a divergence from simulated response at higher frequencies. Better match should be achievable with either better trace linewidth control or dielectric thickness control. For the S_{21} data shown in Fig. 4.15, we see this structure has a very low loss and exhibits

an oscillatory nature that is caused by the low loss combined with capacitive discontinuities at each end of the transmission line due to connections to the signal pin pad. Fig. 4.16 shows the insertion loss per unit length for seven stripline transmission line samples. We achieved repeatable loss per unit length (lower than 0.05dB/cm) for all the stripline samples. We have previously described these considerations and refer the reader to the corresponding paper [35].

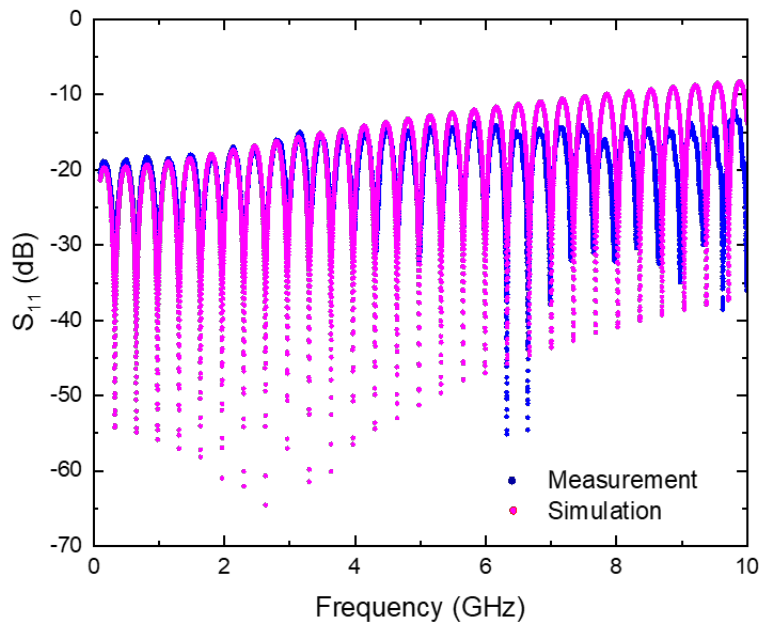


Figure 4.14. S_{11} of a 25 cm long flexible superconducting stripline transmission line measured in a LHe dewar ($T = 4.2$ K). ADS simulation result is also shown.

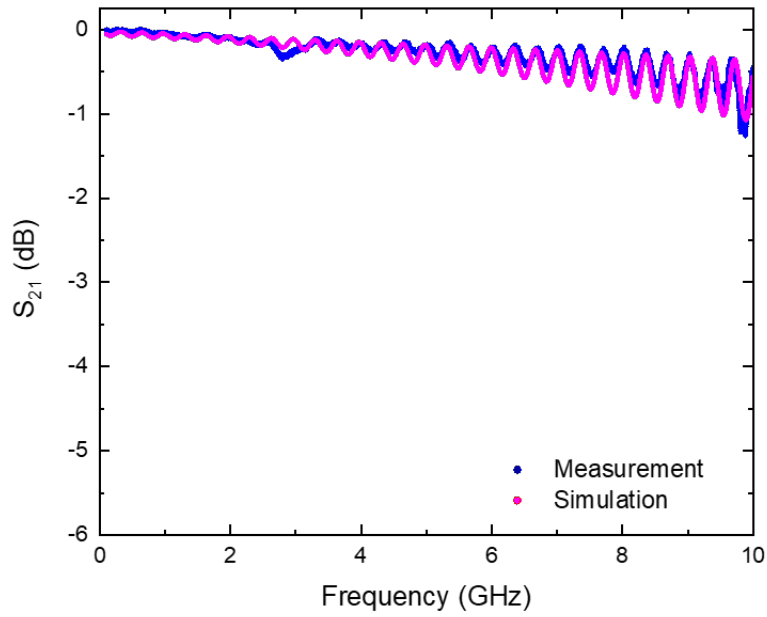


Figure 4.15. S_{21} of a 25 cm long flexible superconducting stripline transmission line measured in a LHe dewar (4.2 K). ADS simulation result is also shown.

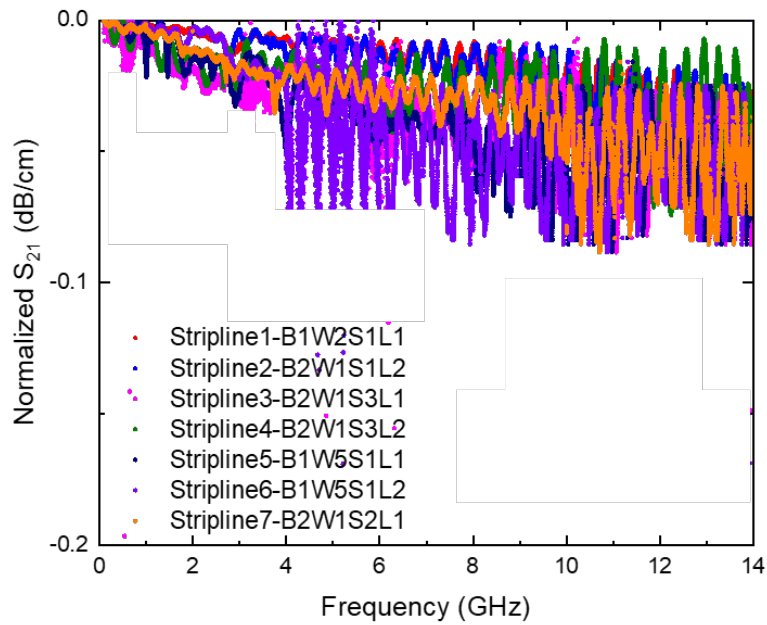


Figure 4.16. S_{21} per unit length of a 25 cm long flexible superconducting stripline transmission line measured in a LHe dewar (4.2 K).

Cross-talk is a critical signal integrity issue, especially in high density, high speed and high frequency design. While stripline geometries provide shielding from external signals, they can exhibit significant cross-talk if not properly designed. Fig. 4.32 shows results for a cross-talk measurement between port 1 and port 3, adjacent ports on the same side of the sample, corresponding to near-end cross-talk. Fig. 4.33 shows results for a cross-talk measurement between port 1 and port 4, i.e., ports on opposite sides of the sample, corresponding to far-end cross-talk. For comparison, we also include simple cross-talk simulation results, simulated using Keysight ADS, which don't include connector effects. There is a reasonable match between simulation and measurement for the cross-talk results. Furthermore, the cross-talk level is typically near or below -60 dB up to at least 10 GHz.

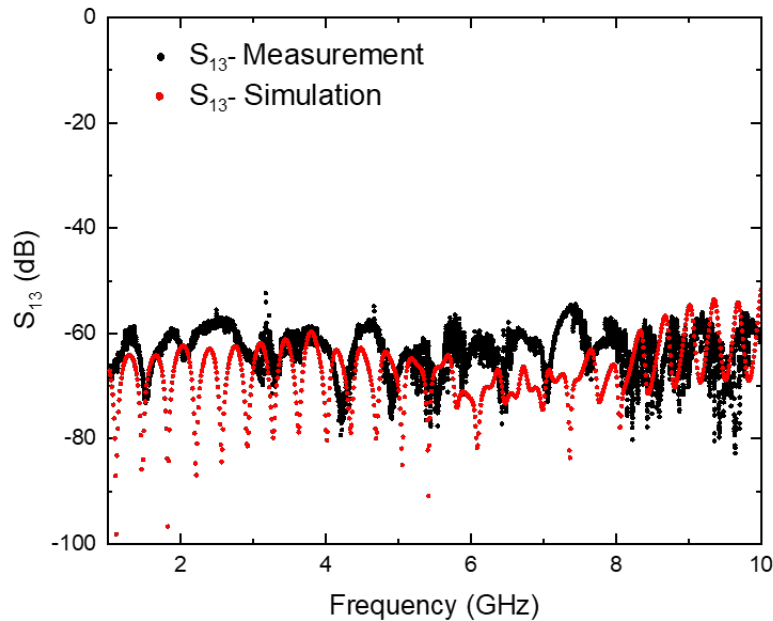


Figure 4.17. Near end cross-talk measurement and simulation of Al/Nb/Al stripline transmission line cables at 4.2 K.

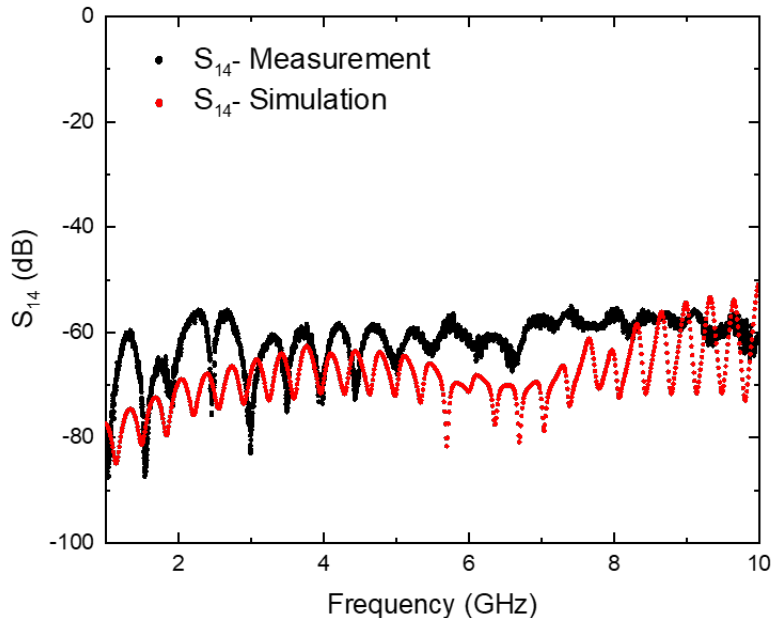


Figure 4.18. Far end cross-talk measurement and simulation of Al/Nb/Al stripline transmission lines at 4.2 K.

4.5.3 Microwave Characterization of Stripline Resonators

Weakly-coupled superconducting resonators can provide a sensitive measurement of the low loss properties of the superconductor and dielectric materials. We have previously used SC resonators to characterize the loss properties of polyimide in microstrip configurations [34, 36, 37]. For series (or through) resonators, S_{21} (and S_{12}) contain the needed resonance information. S_{21} was measured at multiple temperatures up to 14 GHz, as described above. A convenient way to plot the resonator response is $1/Q_l$ vs. resonant frequency, where Q_l is the loaded Q value. This is shown in Fig. 4.19 for a stripline resonator. The primary take-away from these results is that quite high quality factors can be obtained for these structures (~ 7000 at 10 GHz and 1.2 K). This demonstrates that multi-layer, low loss, flexible transmission lines can be fabricated in stripline configurations that involve multiple elevated temperature processes after formation of the signal trace. A full analysis of the resonator response is outside the scope of this paper. Methods described in [41] can be used

to distinguish between dielectric and conductor losses, and uncover their temperature and frequency dependencies.

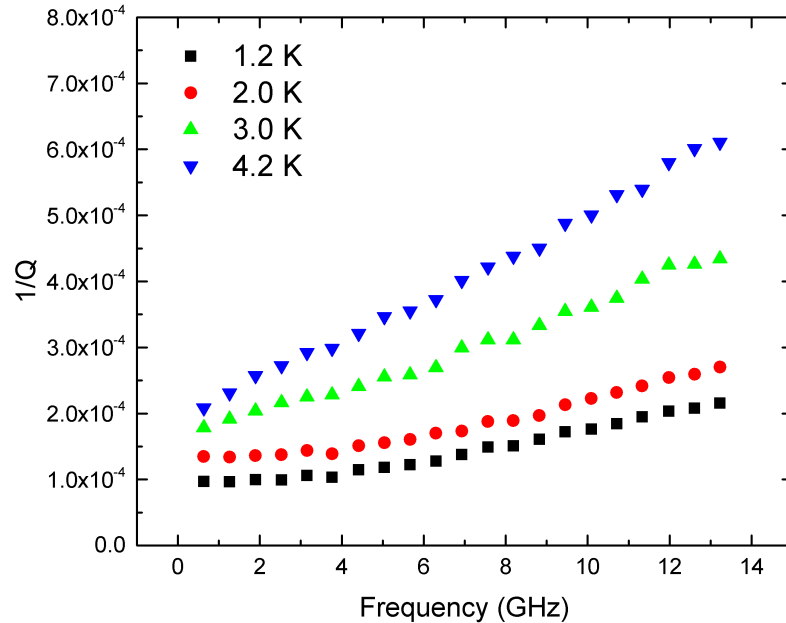


Figure 4.19. $1/Q_l$ vs. resonant frequency comparison of stripline transmission line resonators for measurements at different temperatures.

4.5.4 Conclusion

We presented the fabrication details and characterization results for flexible superconducting stripline transmission lines and resonators. We used thin Al layers on the top and bottom of Nb signal traces to protect the Nb during subsequent fabrication steps. Polyimide curing steps after Nb deposition were also performed at a reduced temperature to alleviate degradation of the Nb superconductivity. Characterization (both DC and RF) of transmission lines showed promising performance. Cross-talk between signal traces was also characterized and showed excellent, low-cross-talk behavior. Furthermore, similarly-fabricated stripline resonators exhibited promisingly high quality factor values. The data presented in this paper provides design guidance for constructing low-loss, flexible thin-film superconducting

interconnects using stripline transmission line configurations. It also provides a solution to robust, multi-layer interconnects, with enhanced shielding and low cross-talk for use in future cryogenic electronics systems.

4.6 Microwave Optimization of Connector Transitions For Superconducting Cables Using Microstrip Transmission Lines

One of the main reason for microwave optimization of connector transition region is to minimize capacitive discontinuities in low loss systems. In this section we have explored embedded microstrip transmission lines using anti-pads on the ground layer. These anti-pads which are essentially an opening in the ground layer (as shown in Fig. 4.20), were designed to counteract the extra capacitance at each end of the transmission line due to connections to the signal pin pad using end-launch SMA connectors.



Figure 4.20. Close-up view of the anti-pad opening in the ground plane.

Fig. 4.21 shows the ADS layout of a 7 cm long microstrip transmission line. The whole mask layout is shown in the previous section.

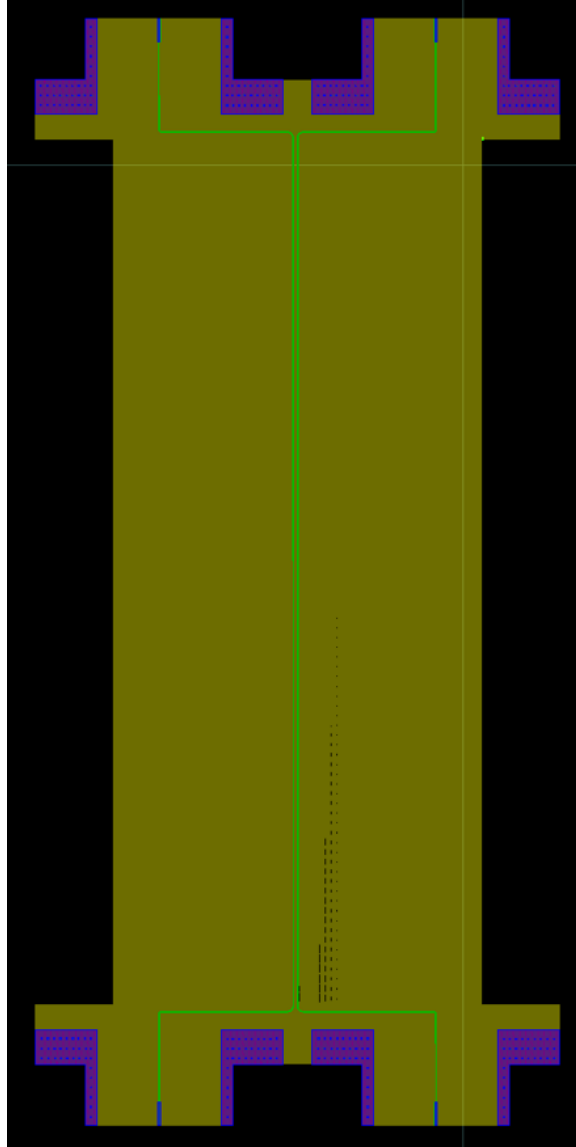


Figure 4.21. ADS layout of a microstrip transmission line.

The width and length of the pin pad is $120 \mu\text{m}$ and $1200 \mu\text{m}$ respectively. In order to optimize the connector transition region, simulations were performed in Sonnet and HFSS. All the anti-pads were designed to have same length of $1200 \mu\text{m}$ but varying widths. Fig. 4.22 demonstrates the insertion loss (S_{21}) upto 14 GHz for varying anti-pad widths obtained from Sonnet. It can be seen that $132 \mu\text{m}$ wide anti-pad provides the lowest insertion loss. Fig. 4.23 shows the insertion loss plot of varying anti-pad widths obtained from HFSS. We note that the anti-pad width of $220 \mu\text{m}$ shows the lowest insertion loss. Based on the

simulation results from Sonnet and HFSS, 132 μm and 220 μm wide anti-pads were designed (as shown in Fig. 4.24) and fabricated for microstrip transmission lines. We also designed an anti-pad width of 176 μm (halfway between 132 μm and 220 μm) , to check if we can detect any trends in the measurements based on the anti-pads widths. The microwave properties of microstrip with varying anti-pad widths is compared with the similarly-fabricated microstrip with of no anti-pad.

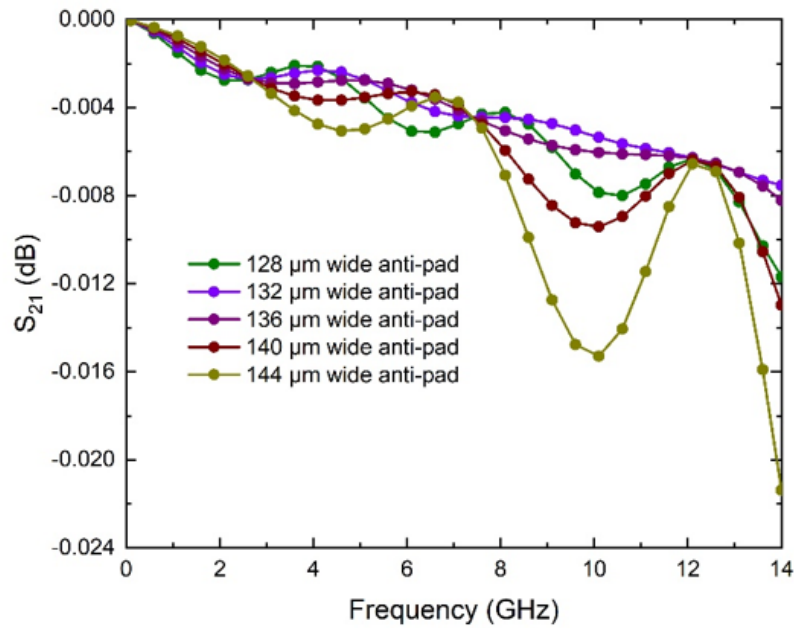


Figure 4.22. S_{21} simulation of 2 cm long microstrip with varying anti-pad widths in Sonnet.

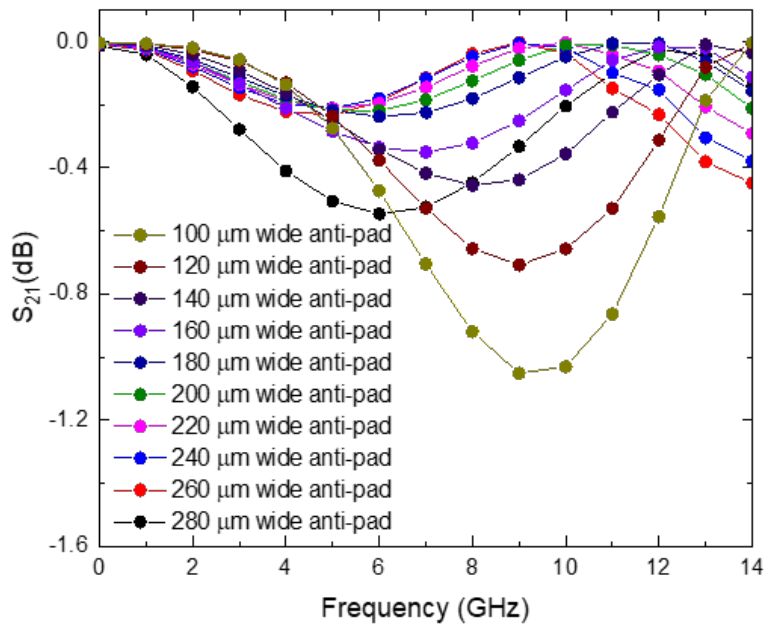
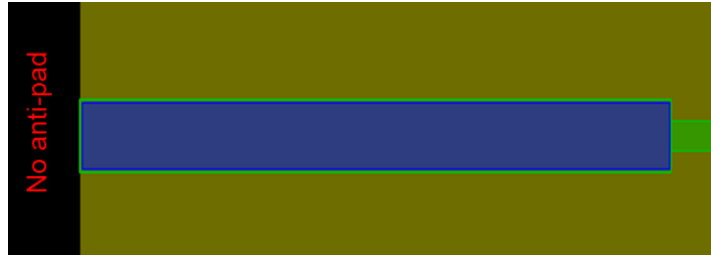
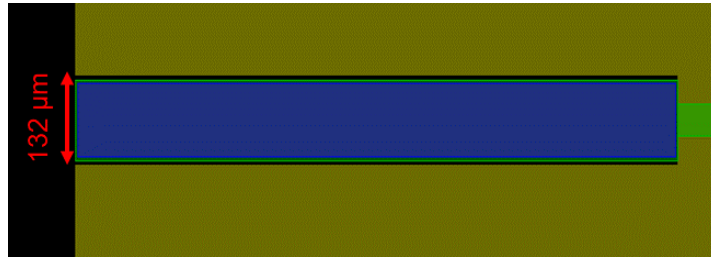


Figure 4.23. S_{21} simulation of 1 cm long microstrip with varying anti-pad widths in HFSS.



(a) Microstrip design with no anti-pad.



(b) Microstrip design with anti-pad width of $132 \mu\text{m}$.



(c) Microstrip design with anti-pad width of $176 \mu\text{m}$.



(d) Microstrip design with anti-pad width of $220 \mu\text{m}$.

Figure 4.24. Image showing the connection regions with varying anti-pad width of $132 \mu\text{m}$, $176 \mu\text{m}$ and $220 \mu\text{m}$ in ground layer.

4.6.1 Fabrication and Measurement Methods

This section describes the fabrication process flow of microstrip transmission line. A release layer of 50 nm thick Cr followed by 200 nm thick Al was deposited onto a silicon handle wafer. HD-4100 was spin coated and cured in N_2 ambient oven at $375 \text{ }^\circ\text{C}$ to achieve a

thickness of $10\ \mu\text{m}$. This was followed by Al(20 nm)/Nb(250 nm)/Al(20 nm) ground layer on top of HD-4100. The ground layer consisted of different width anti-pads ($132\ \mu\text{m}$, $176\ \mu\text{m}$, $220\ \mu\text{m}$ for microstrip transmission line). 250 nm of Nb was sputter deposited (DC sputter for ~ 30 minutes) with a power of $\sim 8\ \text{W}/\text{cm}^2$ and Ar pressure of 4 mTorr [26, 39]. Al capping layers was e-beam evaporated without breaking vacuum to a nominal thickness of $\sim 20\ \text{nm}$. Ti(50 nm)/Cu(200 nm) was then deposited on top of ground layer in small areas (catch pads for electroplated Cu vias) defined by photoresist. HD-4110 was photo-defined in the small catch-pad areas and cured at $225\ ^\circ\text{C}$ in a nitrogen ambient pressure for two hours to obtain a thickness of $20\ \mu\text{m}$. Using the Nb ground plane for a conductive path, the open areas in HD-4110 were then electroplated with Cu to form bottom ground-to-signal layer vias. Signal trace of Al(20 nm)/Nb(250 nm)/Al(20 nm) was deposited using a conventional photolithography process. An encapsulation layer of HD-4100 was coated on top of signal layer and cured at $225\ ^\circ\text{C}$. The samples were then released into flexible substrates in sodium chloride solution using anodic dissolution [40].

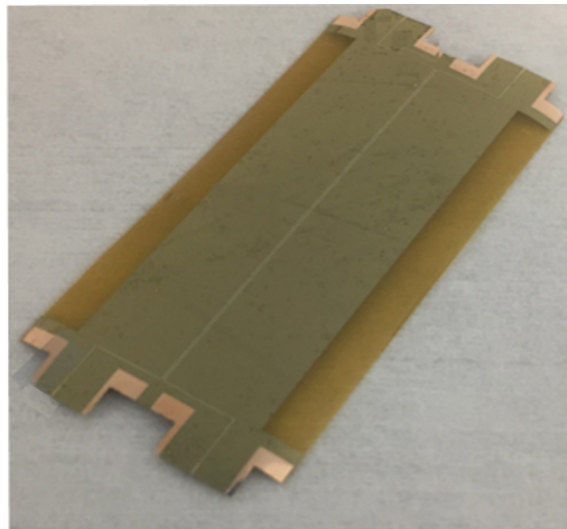


Figure 4.25. Image of flexible Al/Nb/Al microstrip transmission line after release.

End-launch SMA connectors from Southwest Microwave, Inc. were used for electrical connections for DC and RF measurements. Fig. 4.25 shows a released flexible microstrip

transmission line fabricated using the multi-layer fabrication process.

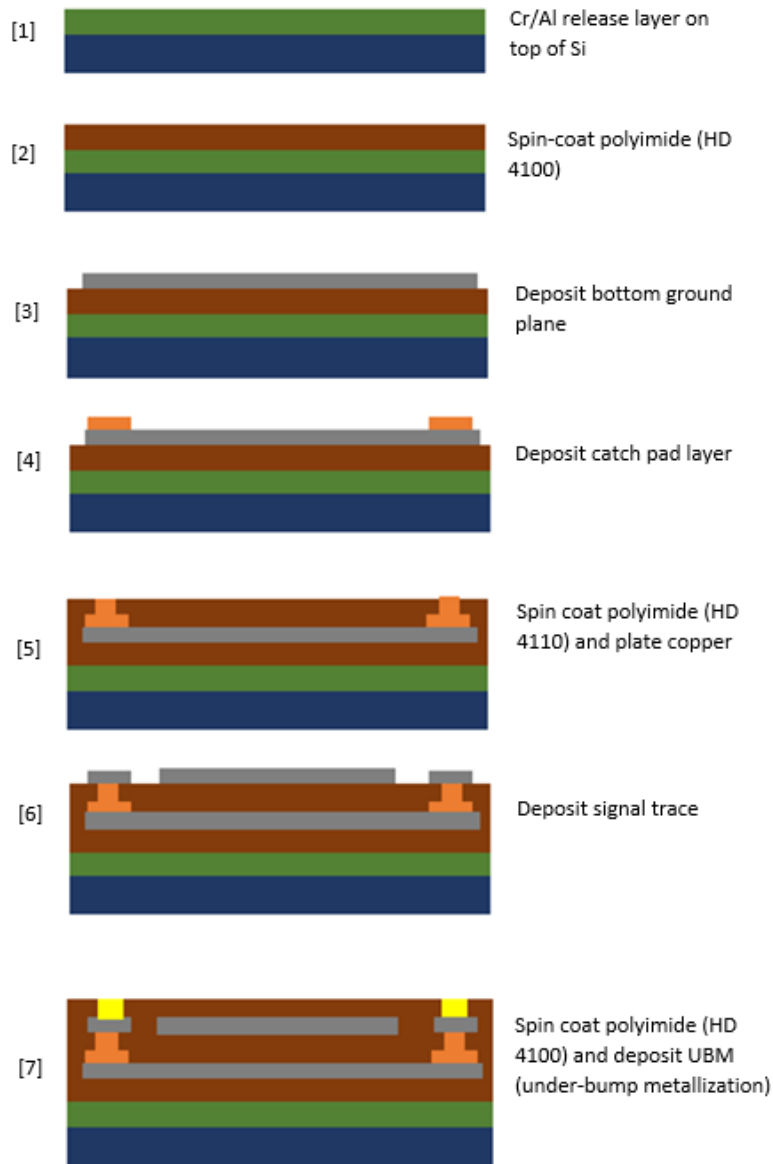


Figure 4.26. Schematic sample cross-section at various points during fabrication, showing key fabrication process steps for superconducting microstrip transmission lines.

4.6.2 DC Measurement Results of Microstrip Transmission Lines

A pulse tube (PT) cryostat with stainless steel cryogenic RF coaxial cables was used for measurements above ~ 1.2 K. For DC measurements, to obtain critical current I_c and superconducting transition temperature T_c , 2 wire measurements at multiple temperatures were made in the PT. A micro-Ohm meter (Keysight 34420A) was used to measure resistance value for obtaining T_c .

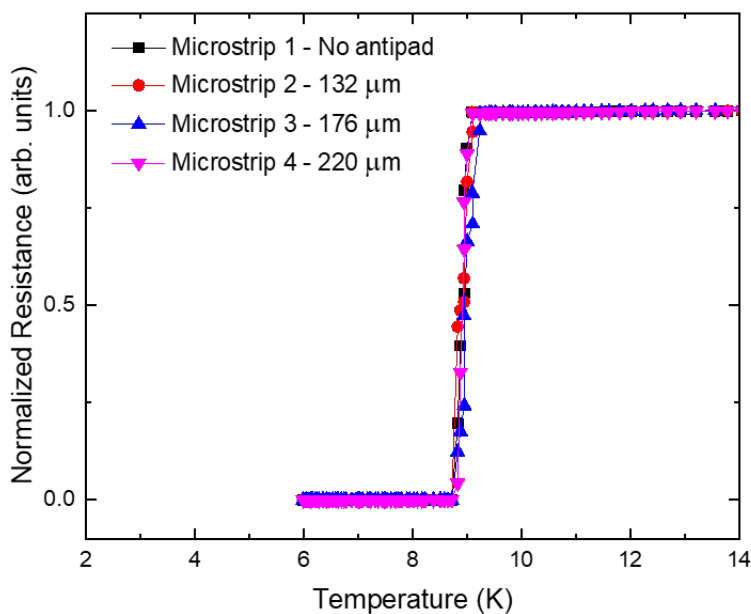


Figure 4.27. T_c measurement results for flexible microstrip transmission lines measured in a pulse tube cryostat.

Fig. 4.27 and Fig. 4.28 shows the superconducting transition temperature (T_c) and critical current plots for signal traces of four microstrip transmission lines. “Microstrip 1” has no anti-pad, “Microstrip 2” has an anti-pad width of $132 \mu\text{m}$, “Microstrip 3” has an anti-pad width of $176 \mu\text{m}$ and “Microstrip 4” has an anti-pad width of $220 \mu\text{m}$. A clean transition can be seen for all the microstrip transmission lines with a T_c of ~ 8.8 K.

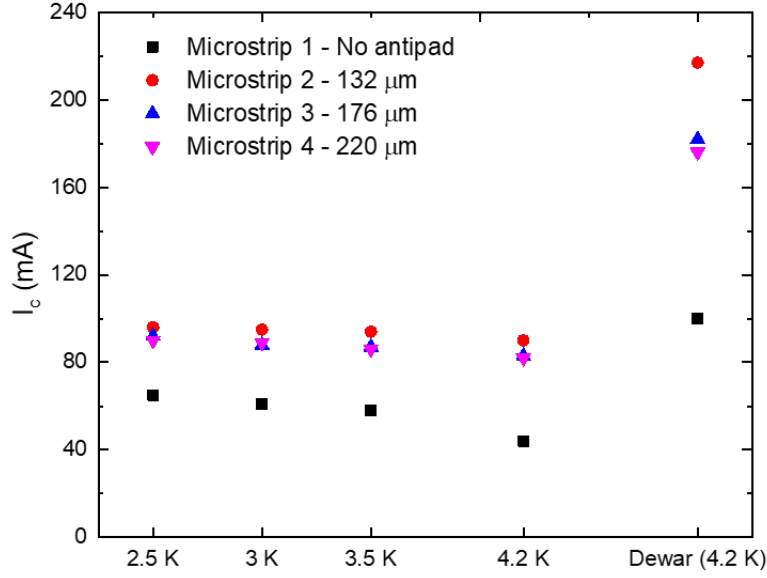


Figure 4.28. I_c measurement results for flexible microstrip transmission lines measured in a pulse tube cryostat.

Table 4.1. Comparison of T_c and I_c for different anti-pad widths of microstrips.

Anti-pad width	T_c (K)	I_c at 2.5 K (mA)	I_c at 3 K (mA)	I_c at 3.5 K (mA)	I_c at 4.2 K (mA)	I_c in dewar (mA)
-	8.1	65	61	58	44	100
132 μm	8.8	96	95	94	90	217
176 μm	8.8	92	88	87	83	182
220 μm	8.8	90	89	86	82	176

Table 4.1 shows the comparison of T_c and I_c for different microstrip versions. All the microstrip versions show a clean transition to the superconducting state. The T_c of the microstrips with anti-pads is ~ 8.8 K, whereas the microstrip with no anti-pad has a slightly lower T_c of 8.1. A similar trend was observed in the I_c measurements as well, where the microstrips with anti-pads show a substantial increase in I_c values compared to the one with no anti-pad. The I_c measurements were carried out in PT cryostat at multiple temperatures - 2.5 K, 3 K, 3.5 K and 4.2 K. These measurements were compared with the ones obtained in LHe dewar.

4.6.3 Microwave Measurement Results of Microstrip Transmission Lines

S-parameter measurement results, for a sample measured at 4.2 K (in LHe), are shown for S_{21} in Fig. 4.29, 4.30 and 4.31 for anti-pad width 132 μm , 176 μm and 220 μm respectively. Fig. 4.32 shows the S_{21} of microstrip transmission line with no anti-pad. S-parameters were measured using an Agilent (Keysight) N5227A PNA. The transmission lines were measured in LHe at frequencies up to 10 GHz. A short-open-load-reciprocal through calibration method (as previously discussed [35]) was performed to measure the microstrip transmission lines. Measurements were performed with an RF power of -20 dBm out of the PNA. A significant reduction in the oscillating behavior can be seen in the S_{21} of microstrips with anti-pads compared to microstrips with no anti-pad. This oscillating behavior is due to the capacitive discontinuities at each end of the line. The resonances observed in the following plots are due to the cross-talk with the neighboring trace.

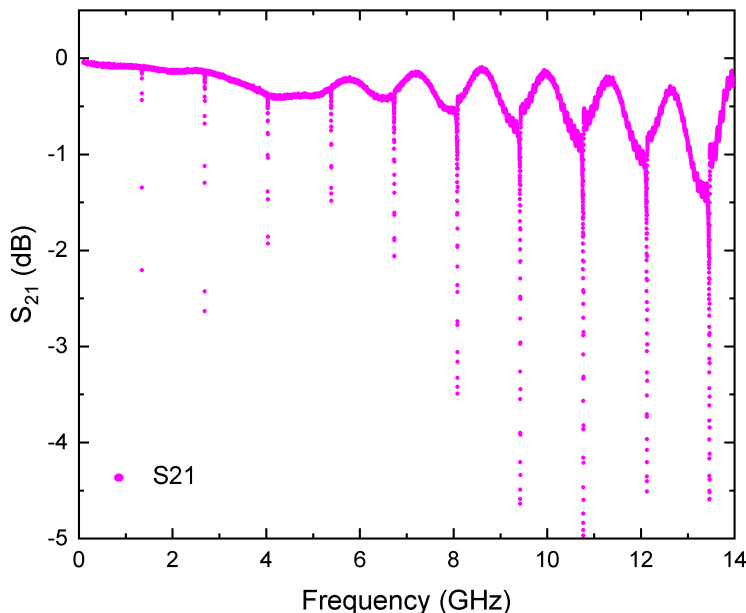


Figure 4.29. S_{21} of a 13 cm long flexible superconducting microstrip transmission line measured in a LHe dewar ($T = 4.2\text{ K}$) with anti-pad width of 132 μm .

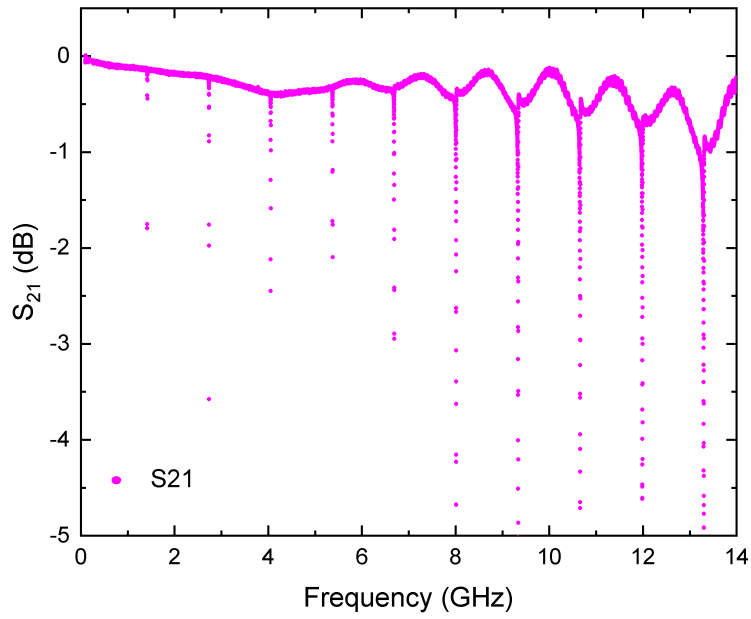


Figure 4.30. S_{21} of a 13 cm long flexible superconducting microstrip transmission line measured in a LHe dewar ($T = 4.2$ K) with anti-pad width of $176 \mu\text{m}$.

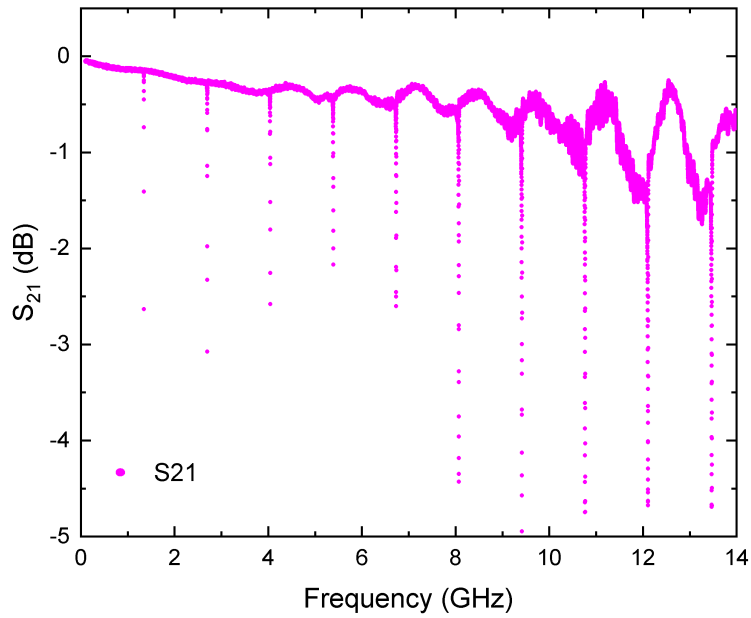


Figure 4.31. S_{21} of a 13 cm long flexible superconducting microstrip transmission line measured in a LHe dewar ($T = 4.2$ K) with anti-pad width of $220 \mu\text{m}$.

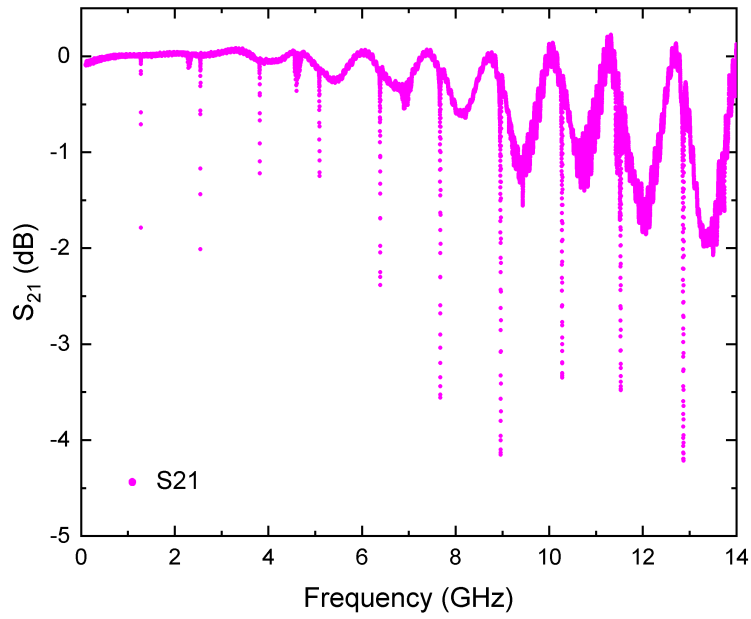


Figure 4.32. S_{21} of a 13 cm long flexible superconducting microstrip transmission line measured in a LHe dewar ($T = 4.2$ K) with no anti-pad.

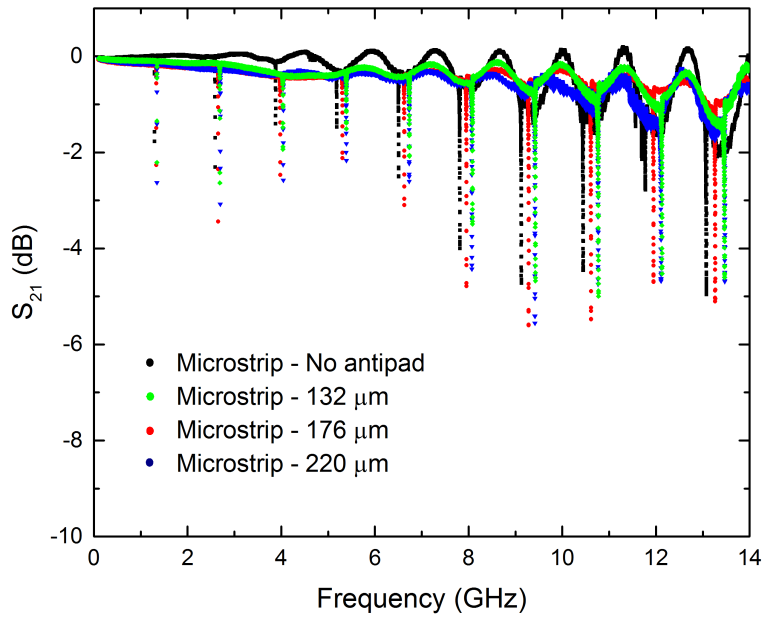


Figure 4.33. Comparison of normalized S_{21} for microstrip transmission lines (with different antipad widths).

Fig. 4.34 shows the peak and trough analysis for the microstrip with anti-pad width of $176 \mu\text{m}$, compared with microstrip with no anti-pad, along with the quadratic fit. The quadratic fits used in the plot are guide for the eye to compare between different anti-pad widths. A higher difference between the peak and trough of the microstrips with no anti-pad can be seen by the quadratic fit as compared to the one with anti-pad. We suspect this difference might be coming due to the extra capacitance at each end of the sample, which, in case of microstrip with anti-pad might be counteracted by the varying anti-pad sizes in the ground layer.

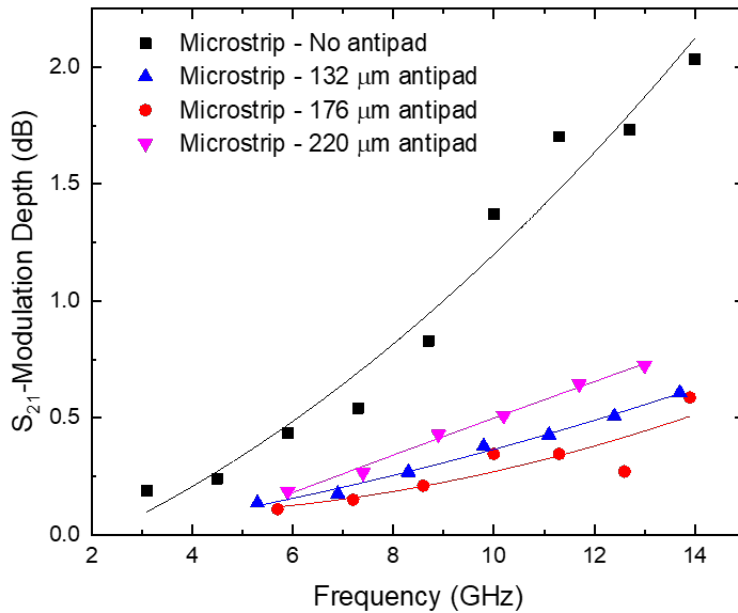


Figure 4.34. Peak and trough analysis, along with corresponding quadratic fit, for microstrip with no anti-pad and microstrip with anti-pad width of $176 \mu\text{m}$.

4.7 Conclusion

In this chapter we have shown a decrease in the oscillating nature of the microstrips with varying anti-pad widths on the ground layer. This oscillating nature is caused by a combination of low loss and capacitive discontinuities at each end for connection to end-launch SMA

connectors. The data presented in this chapter provide guidance to optimize the connector transition region for multi-layer, multi-signal interconnect technology.

Chapter 5

Multiple Approaches to Separate Conductor Loss From Dielectric Loss Using Superconducting Resonator Structures

In the following sections we provide a brief description of resonator including the weakly coupled resonator design and the quality factor calculation carried out in this work. We measured the microwave performance of different resonator structures - embedded, non-embedded and embedded with Al_2O_3 barrier layer at multiple temperatures. We discuss the effect of exposure to elevated temperatures (225 °C, 250 °C and 275 °C) on the microwave performance of different resonator structures.

Different approaches were implemented to extract the dielectric and conductor loss using resonator structures. In the first approach we measured the resonator structures at multiple temperatures and were able to extract the dielectric loss using the exponential drop in the density of normal electrons with lowering temperature. In a different approach we measured resonator structures in varying external magnetic field strengths, which lead to breaking of the Cooper pairs and thereby suppressing T_c . By plotting $1/Q_l$ as a function of T/T_c , the dielectric loss was extracted. Details of the fabrication process, experimental procedures and performance results will be presented in detail in the following sections.

5.1 Resonator Theory

In the presence of an alternating voltage applied across a resistor, capacitor and an inductor, the response of the circuit has a higher amplitude at frequency equal to resonant frequency of the circuit. The electrical response of the circuit depends on the series or parallel combination of the resistor, capacitor and the inductor [12]. In this following sections the characteristic behavior of series and parallel resonant circuit is presented.

5.1.1 Parallel Resonator

A parallel resonator circuit contains a resistor (R), an inductor (L) and a capacitor (C). At resonance frequency, $\omega_0 = 1/\sqrt{LC}$, a current resonance is produced as an effect of circulating current between inductor and capacitor. Fig. 5.1 shows the parallel combination of R, L and C components with current source $i_{in}(t)$ connected across the terminals, $i_o(t)$ is current flowing through the resistor and $v_o(t)$ is the voltage across the circuit.

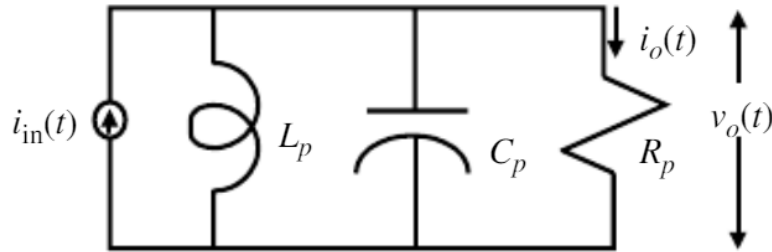


Figure 5.1. Parallel R-L-C circuit. Adapted from [11].

The response curve of impedance vs. frequency is shown in Fig. 5.2

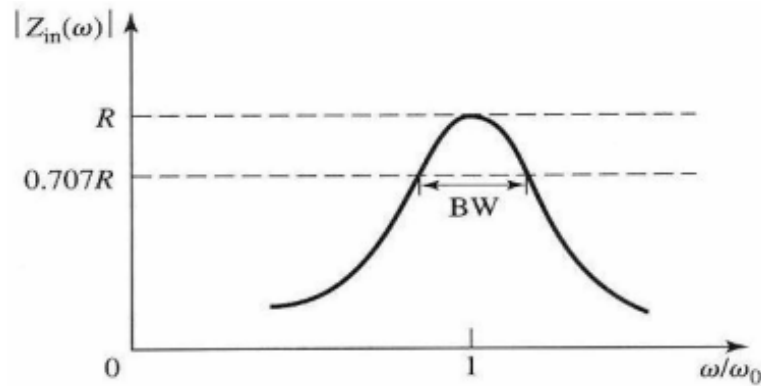


Figure 5.2. Magnitude response of input impedance as a function of frequency. Adapted from [12].

The frequency dependence of input impedance is shown in Fig. 5.2. The impedance across the input terminal can be determined by:

$$Z_{in} = \left(\frac{1}{R} + j\omega C + \frac{1}{j\omega L} \right)^{-1}, \quad (5.1)$$

The power supplied to the resonator is given by:

$$P_{in} = \frac{1}{2}VI = \frac{1}{2} \frac{(V)^2}{Z_{in}} \quad (5.2)$$

Substituting Eq. 5.2 in 5.1, we get the power inserted into parallel RLC circuit as:

$$P_{in} = \frac{1}{2}VI = \frac{1}{2}(V)^2 \left(\frac{1}{R} + j\omega C + \frac{1}{j\omega L} \right) \quad (5.3)$$

The power dissipation by the resistor is given by:

$$P_{loss} = \frac{1}{2}|I^2|R \quad (5.4)$$

5.1.2 Series Resonator

The series resonator circuit consists of R, L and C components in a single loop. In a series resonator circuit inductive and capacitive reactance are equal in magnitude. The frequency at which this occurs is called resonant frequency. Fig. 5.3 shows schematic of a series RLC circuit.

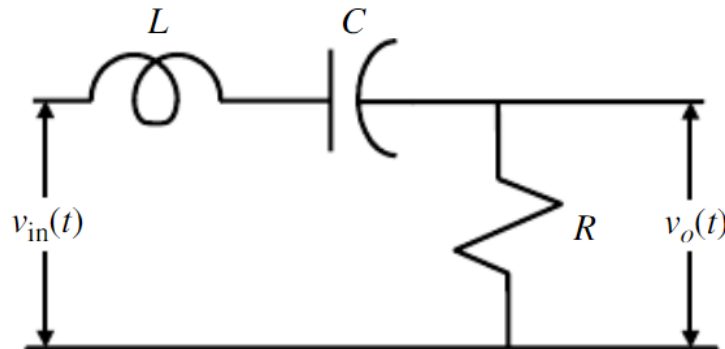


Figure 5.3. Series RLC circuit. Adapted from [11]

A typical response for input impedance is illustrated in Fig. 5.4.

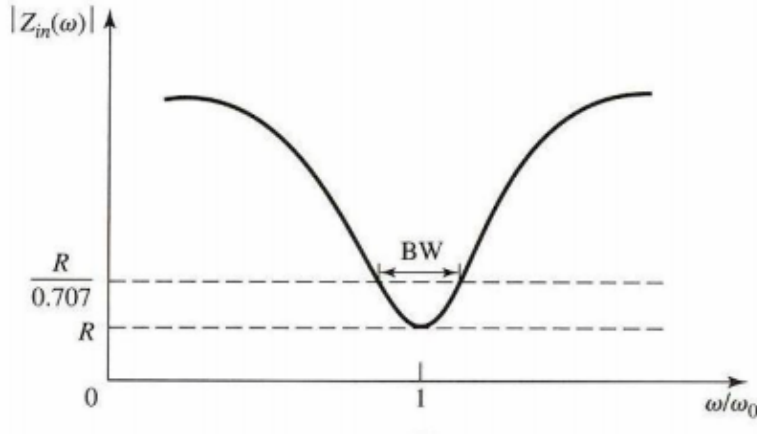


Figure 5.4. Magnitude response of input impedance as a function of frequency. Adapted from [12].

The impedance across the input terminal can be determined by:

$$Z_{in} = R + j\omega L - \frac{1}{j\omega C}, \quad (5.5)$$

At resonance frequency, $\omega_0 = 1/\sqrt{LC}$, the power supplied to the resonator is given by:

$$P_{in} = \frac{1}{2}VI = \frac{1}{2}I^2R = \frac{1}{2}Z_{in}[I]^2 \quad (5.6)$$

Substituting Eq. 5.6 in 5.5, we get the input power for the resonator:

$$P_{in} = \frac{1}{2}VI = \frac{1}{2} \left(R + j\omega L + \frac{1}{j\omega C} \right) [I]^2 \quad (5.7)$$

The power dissipation by the resistor is given by:

$$P_{loss} = \frac{1}{2} \frac{|V^2|}{R} \quad (5.8)$$

5.1.3 Quality Factor Calculation

Quality factor (Q) is a dimensionless parameter that indicates the energy loss in a system. In electronic circuits, Q is represented as the ratio of energy stored in a resonator to the energy dissipated to it, per cycle (shown in Eq. 5.9).

$$Q = 2\pi \times \frac{\text{energy stored}}{\text{energy dissipated per cycle}} \quad (5.9)$$

Fig. 5.5 shows the response of current vs. frequency of resonator circuit. The peak of the resonant curve is characterized by the center frequency (f_0). Bandwidth is defined as the total number of cycles below and above the resonant frequency, calculated by subtracting f_1 from f_2 . Q is measured by using 3 dB technique, that essentially shows the point where half the power is dissipated in the circuit.

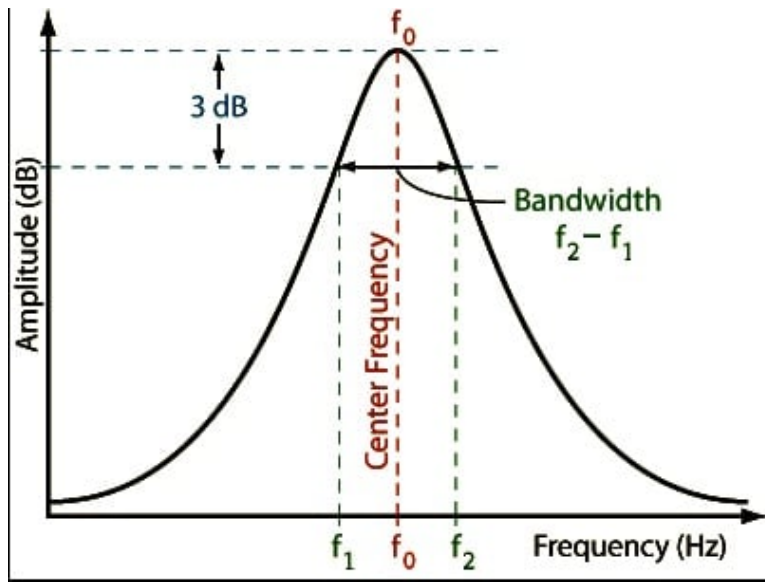


Figure 5.5. Bandwidth of a resonant circuit indicating resonance frequency. Adapted from [13].

$$Q_l = \frac{f_0}{BW_{(-3dB)}} \quad (5.10)$$

Q_l is the loaded Q , f_0 is the center frequency of the resonator and $BW_{(-3dB)}$ is the -3 dB bandwidth as shown in Fig. 5.5. Q_l can further be broken down into:

$$\frac{1}{Q_l} = \frac{1}{Q_c} + \frac{1}{Q_D} + \frac{1}{Q_r} + \frac{1}{Q_{cp}} + \frac{1}{Q_{other}} \quad (5.11)$$

Q_c is related to conductor loss, Q_D is related to dielectric loss, Q_r is related to electromagnetic radiation loss, Q_{cp} is related to coupling loss and Q_{other} is related to other potential (not dominant) sources of loss.

The dielectric loss tangent can be determined from dielectric loss (i.e. $1/Q_D$) using the following equation:

$$Q_D = \frac{1}{\tan\delta} + \left(1 + \frac{1-q}{\epsilon_r}\right) \quad (5.12)$$

5.1.4 Resonator Design

In this work, half wavelength ($l = \lambda/2$), capacitively coupled "thru type" microstrip transmission line resonators (shown in 5.6) have been fabricated and characterized on flexible spin-on polyimide substrates.

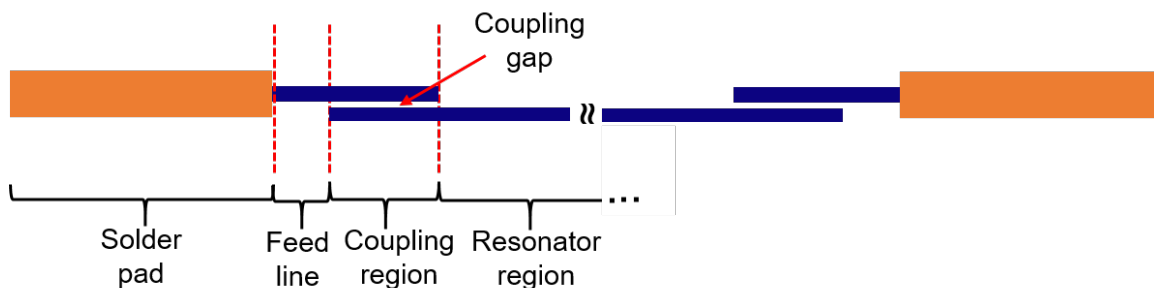


Figure 5.6. Top view of both ends of the microstrip transmission line resonator indicating the coupling region.

In order to provide high sensitivity to the dielectric material, optimization of coupling gap is necessary. If the coupling gap is too small then the loss due to the coupling region will be included in the Q_l whereas if the coupling gap is too large then the resonances may be buried under the noise level of the network analyzer. Hence, the resonators are designed with a coupling length of $300 \mu\text{m}$ and coupling gap of $20 \mu\text{m}$ so that the resonances are above the noise level.

5.2 Fabrication and Microwave Characterization of Flexible Thin Film Nb Resonator Structures

In this section, weakly-coupled Nb resonator samples were measured at multiple temperatures. By changing the measured temperature, we were able to observe the exponential dependence of Q_t on density of normal electrons and superelectrons. The effect of curing Nb samples at elevated temperatures was studied with a goal to protect Nb and to detect the degradation in T_c of Nb after exposure to elevated temperatures. Multiple curing temperatures were explored on fabricated resonators such as 225 °C, 250 °C and 275 °C. Resonator structures with various layer stack ups were studied such as Nb, Nb/PI and $\text{Al}_2\text{O}_3/\text{Nb}/\text{Al}_2\text{O}_3/\text{PI}$. The effectiveness of Al_2O_3 as a barrier layer to protect Nb during subsequent fabrication steps of curing PI on top at elevated temperatures was also studied in this section.

5.2.1 Resonator Fabrication Process

Thin-film wafer-level fabrication processes, as illustrated in Fig. 5.7, were used. Starting with a silicon handle wafer, a release layer stack of 50 nm thick Cr, followed by 200 nm thick Al was deposited. A 20 μm thick layer of HD-4110 (polyimide) was spin coated, photodefined and cured in a nitrogen ambient oven at 375 °C for one hour. Signal traces were defined using photolithography, followed by Nb sputter deposition and subsequent lift-off. The Nb was sputter-deposited (DC sputter for ~ 30 minutes) to a nominal thickness of ~ 250 nm. An Ar pressure of 4 mTorr was used to deposit Nb in our CHA Mark 50 system, yielding a low stress Nb film [26,39]. The signal layer was covered with an encapsulation layer of HD-4100 (a photodefinable polyimide), with a thickness of 4 μm , cured in a nitrogen ambient oven. The HD-4100 layer was cured at 225 °C to protect the superconductivity of Nb during the curing of the embedding polyimide layer [25]. Under bump metallization (UBM) pads were deposited in openings in the HD-4100 encapsulation layer, to make contact to the exposed

signal traces. The UBM stack was formed using 50 nm Ti, followed by 250 nm Au, using standard lift-off processes. The samples were then released using a NaCl anodic dissolution process, producing individual flexible resonator structures [40].

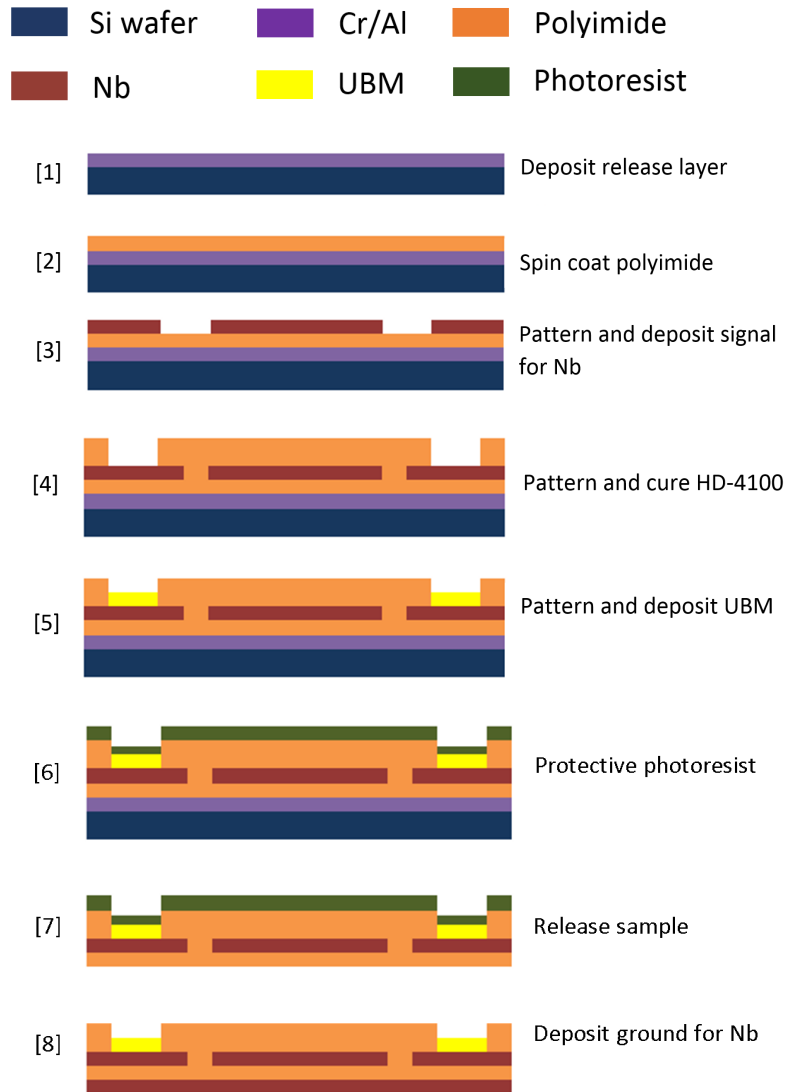


Figure 5.7. Process flow for embedded microstrip transmission line resonator.

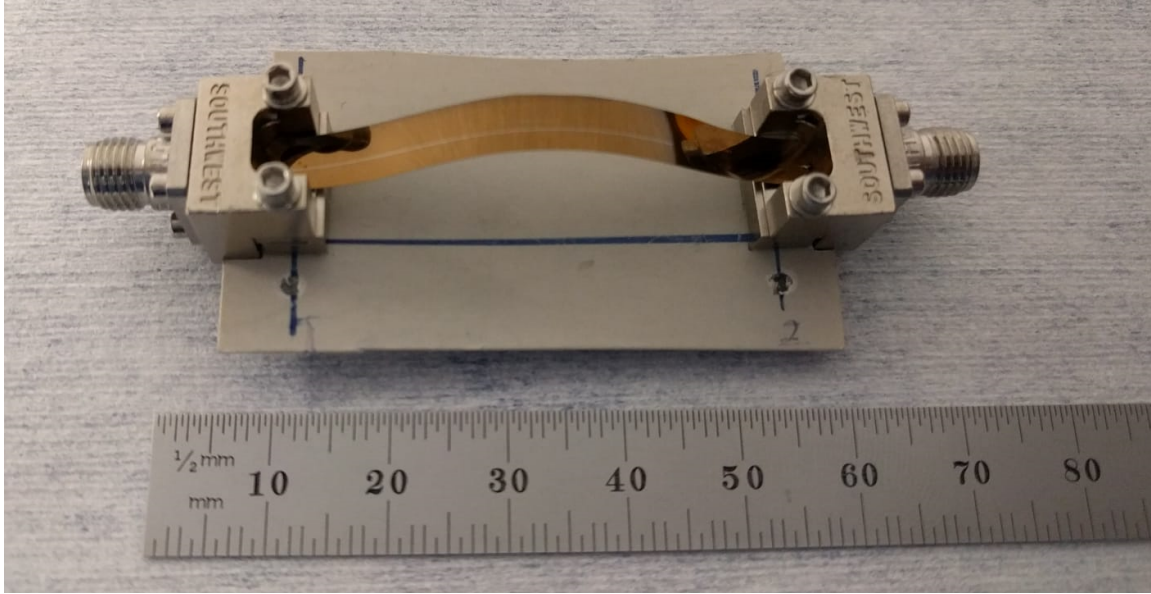


Figure 5.8. Flexible Nb resonator assembly with Southwest Microwave, Inc SMA end-launch connectors mounted, attached to a support board.

5.2.2 Cryogenic and Microwave Measurement Setup

Measurements were performed in a pulse tube based cryostat (from Cryo Industries of America, Inc.) with temperature control from ~ 1.2 K and up. The resonators were baked at 90°C prior to loading in the pulse tube cryostat for measurements. Microwave measurements were made up to ~ 18 GHz, using a Keysight N5227A PNA, at a nominal power out of the PNA of -20 dBm.

End-launch SMA connectors from Southwest Microwave, Inc. were used to connect to and measure the transmission line resonators. Fig. 5.8 shows an assembled flexible microstrip resonator sample, with connectors mounted. A piece of printed circuit board material was used as a support board underneath the sample to support the heavy end-launch connectors.

5.2.3 Design and Characterization of Non-Embedded Resonator Structure at Cryogenic Temperatures

A 3D view of the non-embedded resonator structure is shown in Fig. 5.9. Fig. 5.10 shows S_{21} measurement results of a non-embedded resonator structure over a wide frequency range

(from 1st to 10th mode). Broad frequency sweeps were performed, followed by narrower sweeps at the resonant frequencies, in order to gather sufficient data around the resonances to allow fitting to a Lorentzian curve. Fig. 5.11 shows the S_{21} measurement results of a non-embedded resonator at 2 GHz and the corresponding Lorentz fit. The Lorentz equation is given by:

$$|S_{21}(f)| = A_1 + A_2 f + \frac{|S_{max}(f)| + A_3 f}{\sqrt{1 + 4 \left(\frac{f - f_0}{\Delta f_{Lorentz}} \right)^2}} \quad (5.13)$$

Where f_0 represents the resonant frequency, $\Delta f_{Lorentz}$ represents the bandwidth, A_1 represents the constant background, A_2 represents the slope on the background, A_3 represents the skew and $|S_{max}|$ represents the maximum magnitude [42].

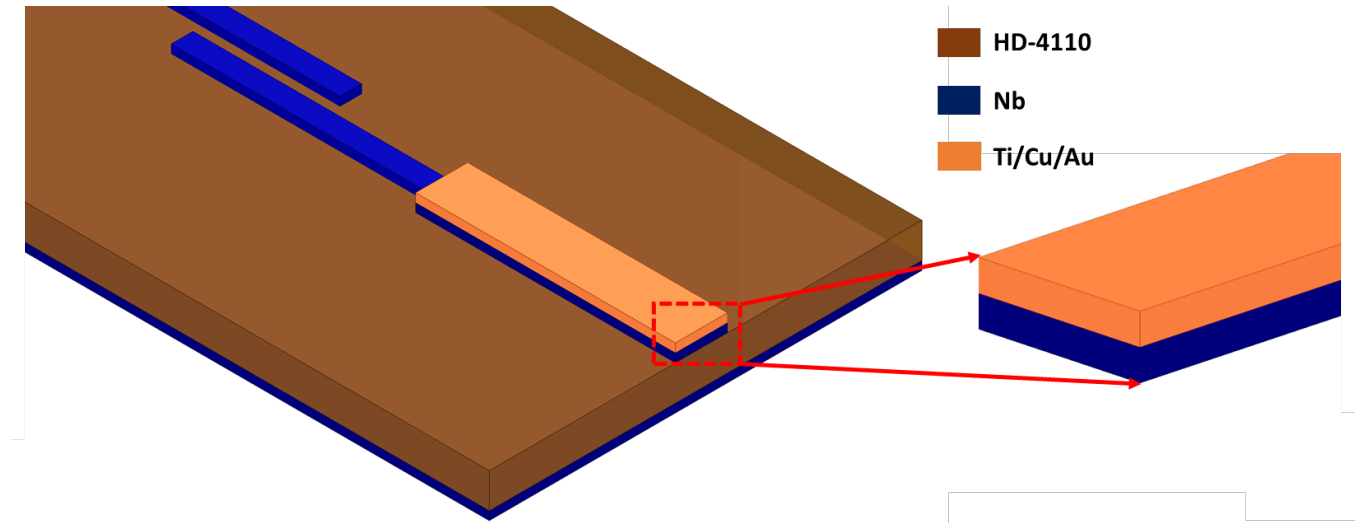


Figure 5.9. 3D view of one end of a non-embedded microstrip resonator structure.

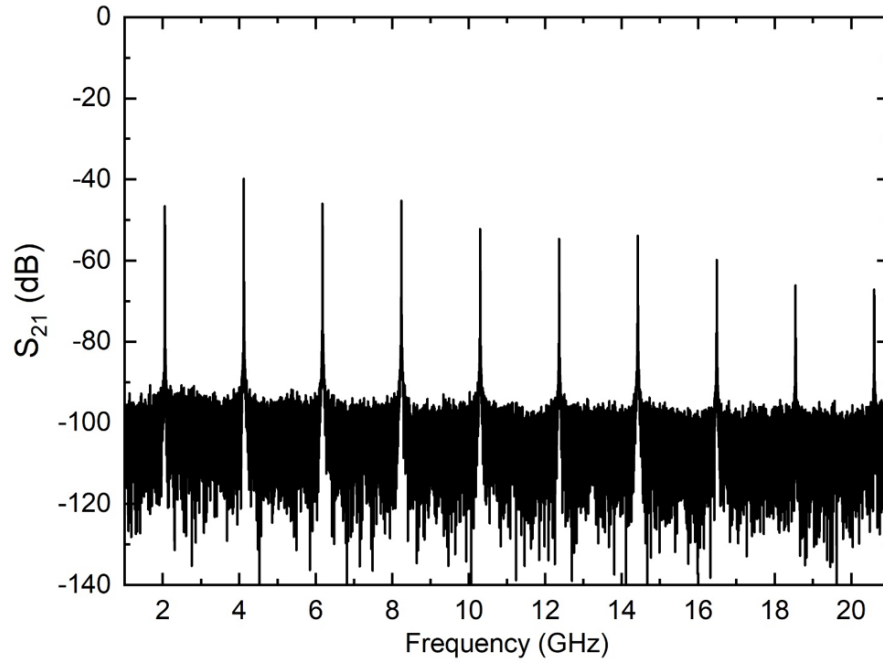


Figure 5.10. S_{21} measurement results of non-embedded resonator structure measured at 4.2 K over a wide frequency range (1 GHz - 21 GHz).

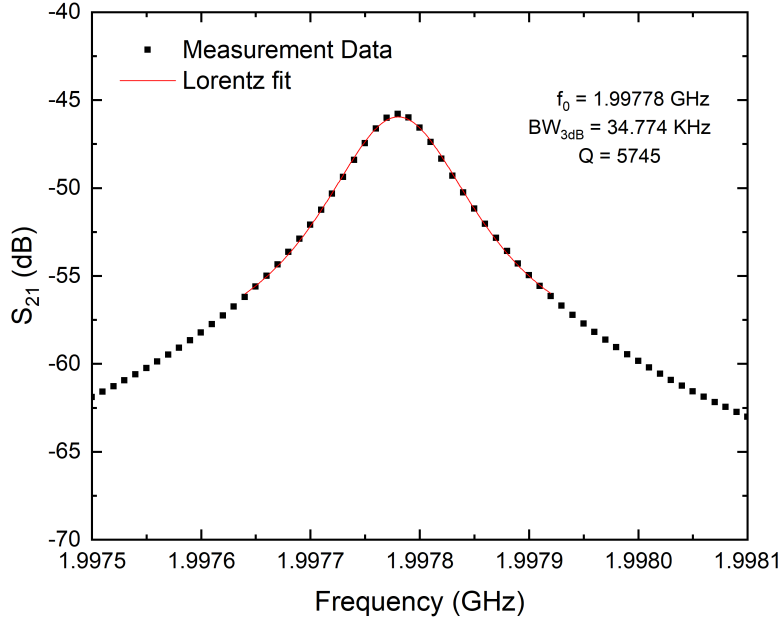


Figure 5.11. Fundamental resonance measurement and the corresponding Lorentz fit for non-embedded resonator structure.

Fig. 5.12 presents results for $1/Q_l$ vs. temperature for the non-embedded (without the top PI overcoat) resonator structure measured at multiple temperatures. We can see that at temperature close to the T_c there is a rapid decrease in value of Q_l leading an sudden increase in $1/Q_l$ values. This is because at temperatures close to T_c there is an increase in the density of normal electrons leading to lower Q_l , whereas when the temperature is lowered the density of normal electrons drops exponentially and Q_l is mainly governed by the density of superelectrons.

In terms of Nb degradation, we can clearly see the degradation in T_c when the sample was exposed to elevated temperatures. The samples was first cured at 225 °C, which resulted in T_c of ~ 9 K. The same sample was then cured at 250 °C which lowered the T_c of the sample to ~ 7.2 K. After curing the same sample at 275 °C, T_c dropped to ~ 5.5 K.

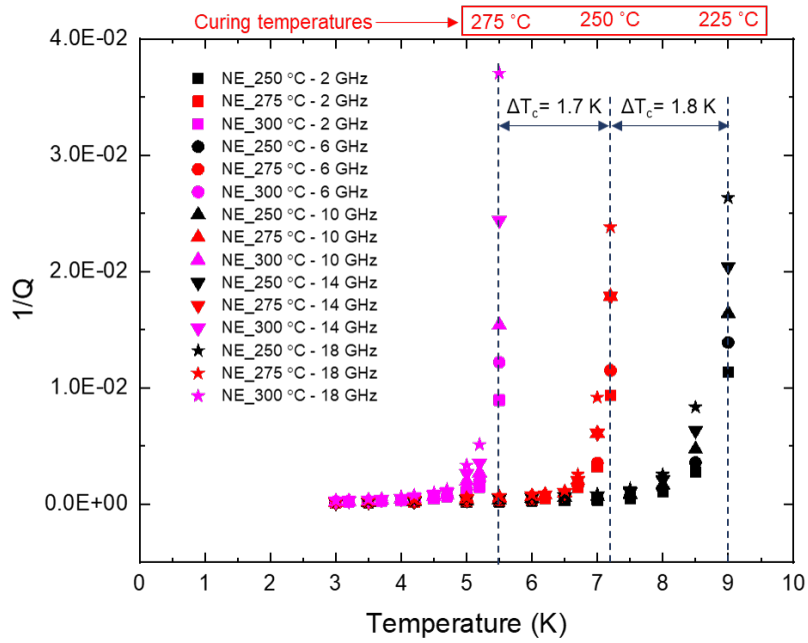


Figure 5.12. $1/Q_l$ vs. temperature plot showing degradation of non-embedded sample after different curing temperatures.

Fig. 5.13 shows the same data from previous plot in log scale to better visualize the overlapped data points.

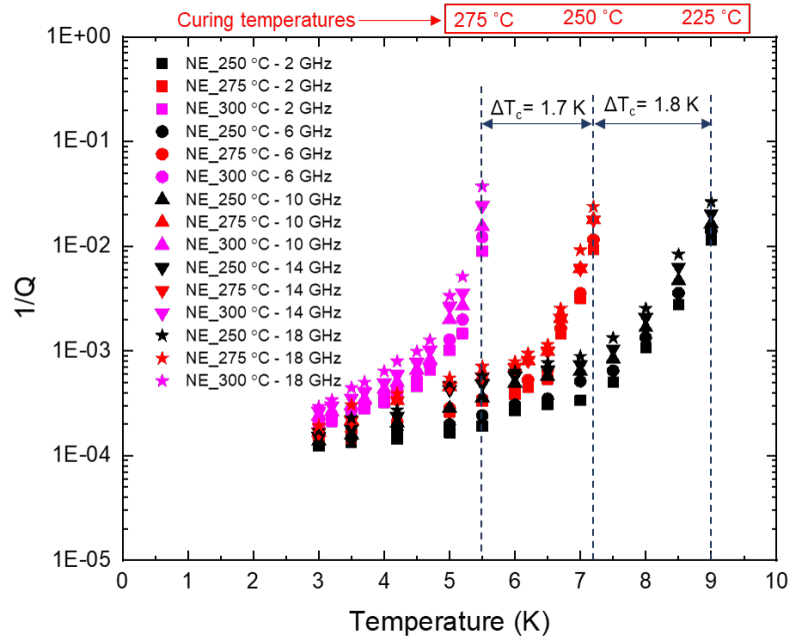


Figure 5.13. $1/Q_l$ vs. temperature plot showing degradation of non-embedded sample after different curing temperatures.

5.2.4 Design and Characterization of Embedded Resonator Structure at Cryogenic Temperatures

A 3D view of the embedded resonator structure is shown in Fig. 5.14. The same procedure was followed in order to obtain the Q_l values for embedded resonator structure, as shown for the case of non-embedded resonator structure.

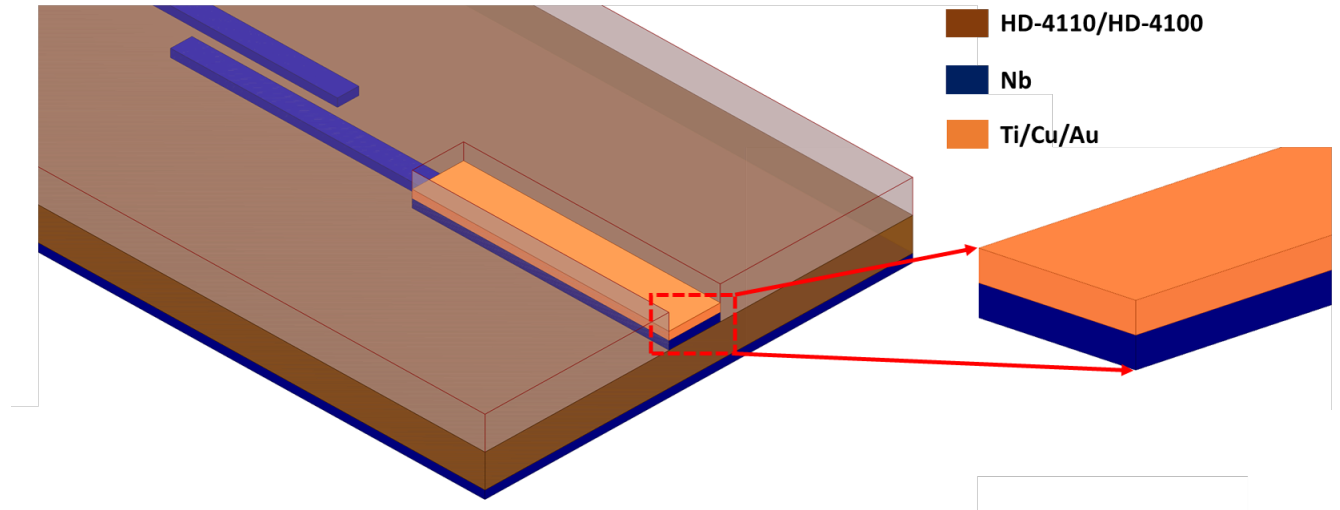


Figure 5.14. 3D view of one end of a embedded microstrip resonator structure.

Fig. 5.15 presents results for $1/Q_l$ vs. temperature for the embedded (without the top PI overcoat) resonator structure measured at multiple temperatures. A similar trend was observed in $1/Q_l$ values at temperatures close to the T_c and at lower temperatures.

A significant amount of degradation was observed in T_c when the sample was exposed to elevated temperatures. The sample was first cured at 225 °C, which resulted in T_c of \sim 8.5 K. The same sample was then cured at 250 °C which lowered the T_c of the sample to \sim 6.5 K. After curing the same sample at 275 °C, T_c dropped to \sim 4.5 K.

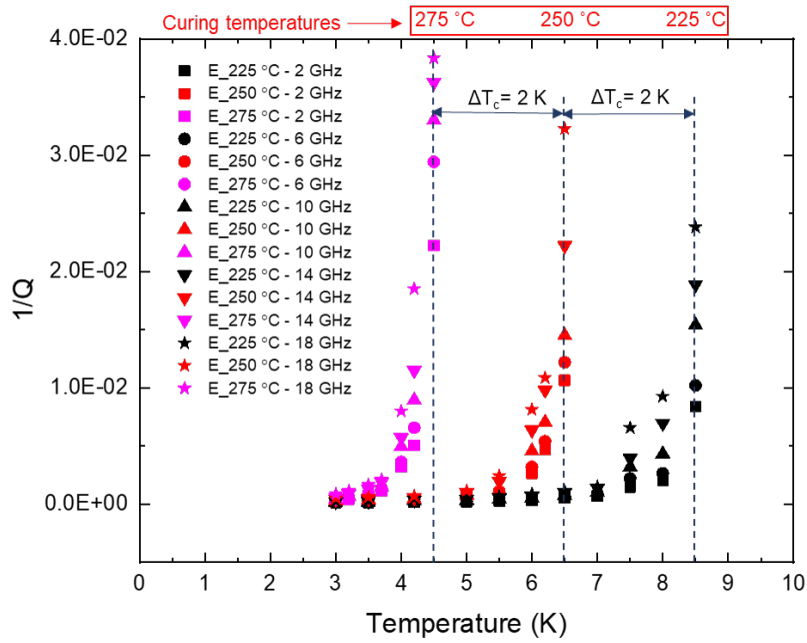


Figure 5.15. $1/Q_l$ vs. temperature plot showing degradation of embedded sample after different curing temperatures.

Fig. 5.16 shows the same data from previous plot in log scale to better visualize the overlapped data points.

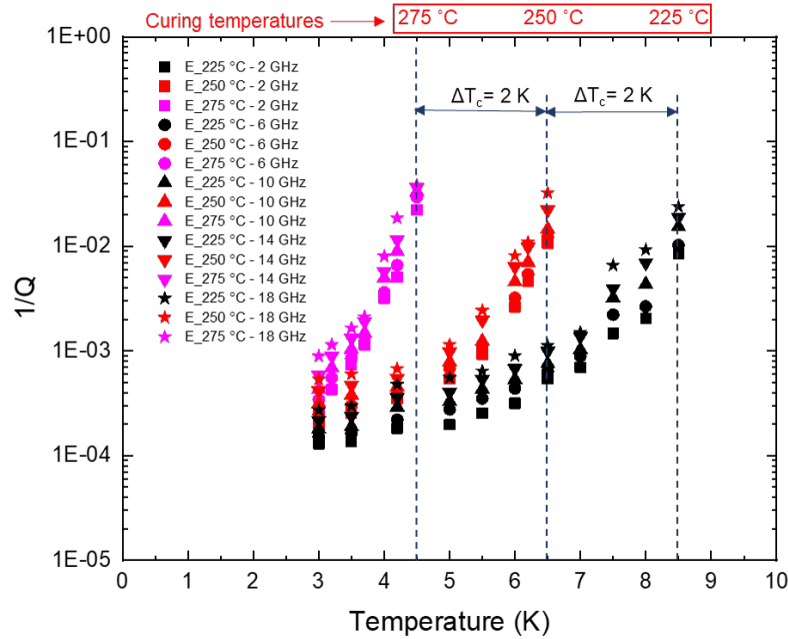


Figure 5.16. $1/Q_l$ vs. temperature plot showing degradation of embedded sample after different curing temperatures.

5.2.5 Design and Characterization of Embedded Resonator Structure With a Barrier Layer of Al_2O_3 at Cryogenic Temperatures

A 3D view of the embedded resonator structure with a thin Al_2O_3 layer is shown in Fig. 5.17. The same procedure was followed in order to obtain the Q_l values for embedded resonator structure with a barrier layer of Al_2O_3 , as shown for the case of non-embedded resonator structure.

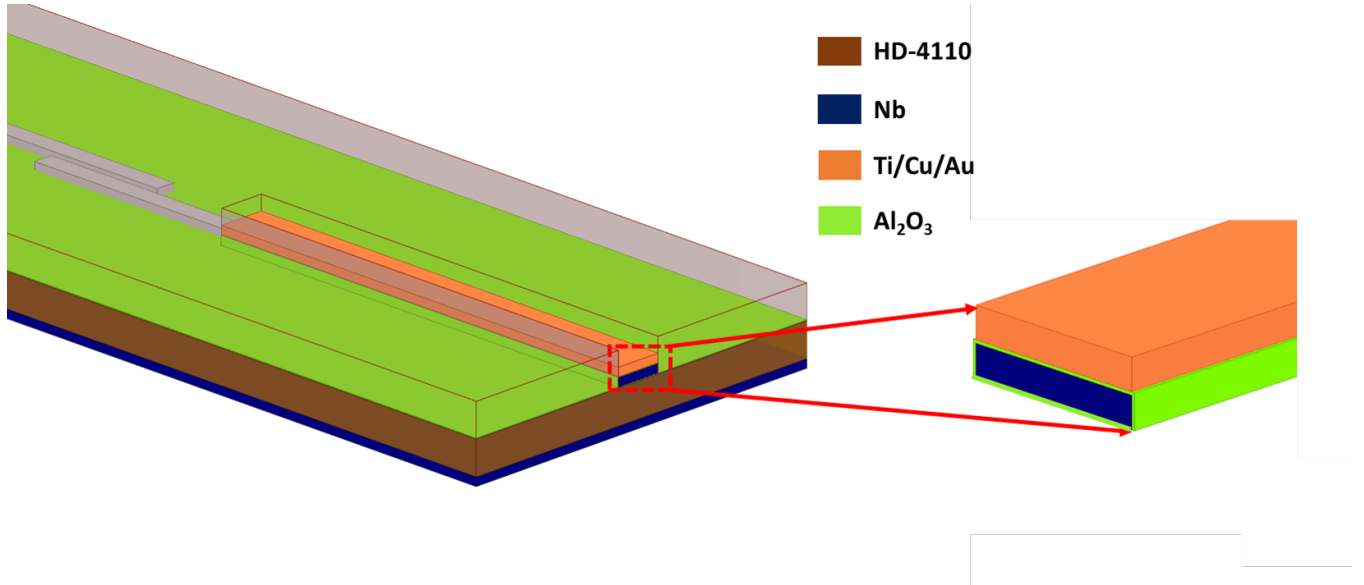


Figure 5.17. 3D view of one end of a embedded microstrip resonator structure with a 20 nm thick Al_2O_3 barrier layer.

Fig. 5.18 shows the results for $1/Q_l$ vs. temperature for the embedded (with the top PI overcoat) resonator structure with a barrier layer of Al_2O_3 measured at multiple temperatures. As seen in the case non-embedded and embedded resonator structures, an abrupt increase in the values $1/Q_l$ was observed near T_c whereas an exponential drop in $1/Q_l$ values was observed at lower temperatures.

Minimal degradation was observed in T_c when the sample was exposed to elevated temperatures. The samples was first cured at 225 °C, which resulted in T_c of ~ 8.5 K. The same sample was then cured at 250 °C which lowered the T_c of the sample to ~ 8.2 K. After curing the sample at 275 °C, T_c dropped to ~ 7.2 K.

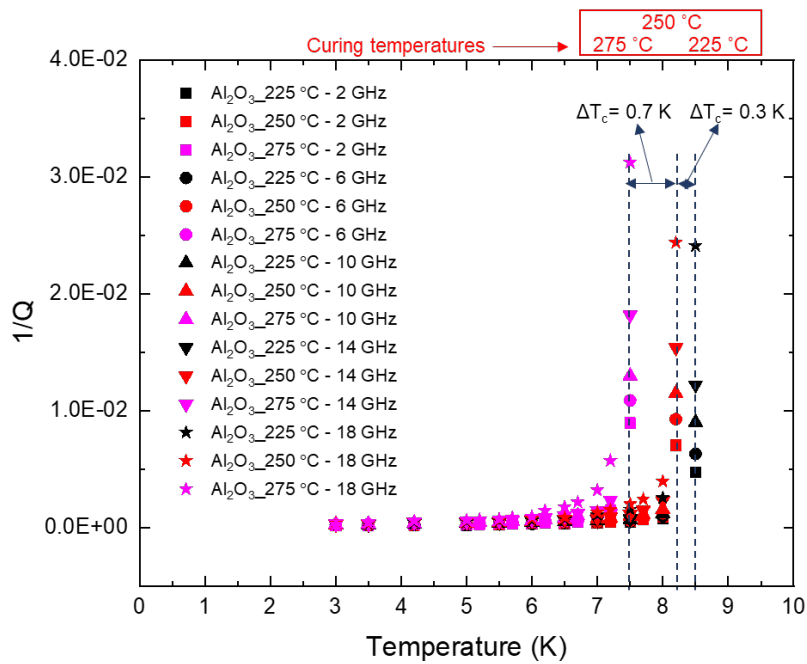


Figure 5.18. $1/Q_l$ vs. temperature plot showing degradation $\text{Al}_2\text{O}_3/\text{Nb}/\text{Al}_2\text{O}_3$ sample after different curing temperatures.

Fig. 5.19 shows the same data from previous plot in log scale to better visualize the overlapped data points.

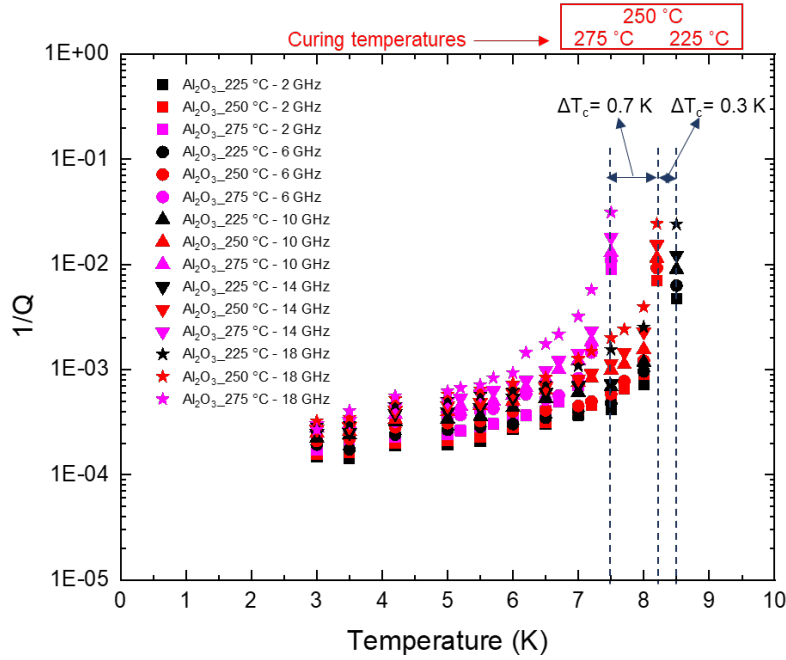


Figure 5.19. $1/Q_l$ vs. temperature plot showing degradation $\text{Al}_2\text{O}_3/\text{Nb}/\text{Al}_2\text{O}_3$ sample after different curing temperatures.

In this section, we have presented the fabrication and microwave characterization of weakly coupled SC transmission line resonators. Different resonator structures were explored - non-embedded, embedded and embedded with Al_2O_3 barrier layer with the goal to protect Nb superconductivity at elevated temperatures. Resonator structures with a 20 nm thick barrier layer of Al_2O_3 have shown the least amount of reduction in the T_c as compared to the other resonator structures. The data shown here provides insight into promising material and stack-up where Nb can be subjected to multiple subsequent high temperature steps.

5.3 Separation of Conductor and Dielectric Losses Using Resonators Measured at Multiple Temperatures

In this section, we have used microstrip SC resonator structures to differentiate the conductor loss and dielectric loss. It is very important to understand the various loss mechanism that contribute to microwave losses in order to design an optimized, low loss structure for use in

quantum computing. Multiple resonator structures were used to separate the internal losses - embedded, non-embedded and embedded with Al₂O₃ barrier layer. The measurement results of all these resonators were shown in the previous section.

Simulations were performed in Ansys HFSS of a 5 cm long Nb microstrip transmission line resonator using the superconducting model provided by HFSS. Fig. 5.20 shows the simulation result of embedded resonator structure and Fig. 5.21 shows the simulation result of non-embedded resonator structure at 2 GHz. For each resonator structure, $1/Q_l$ was plotted at multiple temperatures for varying T_c (based on the T_c degradation observed after exposure the elevated temperatures for the corresponding resonator type, shown in previous section).

The value of loss tangent used for simulations was 2E-4. In order to account for filling factor for microstrip, effective loss tangent was calculated using the following equations.

For $w/h \gg 1$, w represents the trace width and h represents the height of the dielectric.

$$k_{eff} = \frac{k+1}{1} + \frac{k-1}{1} \left[\frac{1}{\sqrt{1 + \frac{12h}{w}}} \right] \quad (5.14)$$

$$q_d = \frac{k_{eff}}{k-1} \quad (5.15)$$

$$\tan\delta_{eff} = \frac{q_d k}{k_{eff}} \tan\delta \quad (5.16)$$

Where w represents the trace width and h represents the height of the dielectric. k and k_{eff} represents the dielectric constant and the effective dielectric constant, respectively. From the above equations, we got $k_{eff}=2.56$, $q_d=0.71$ and $\tan\delta_{eff}=1.78E-4$ for a $50\mu\text{m}$ trace width in a microstrip configuration.

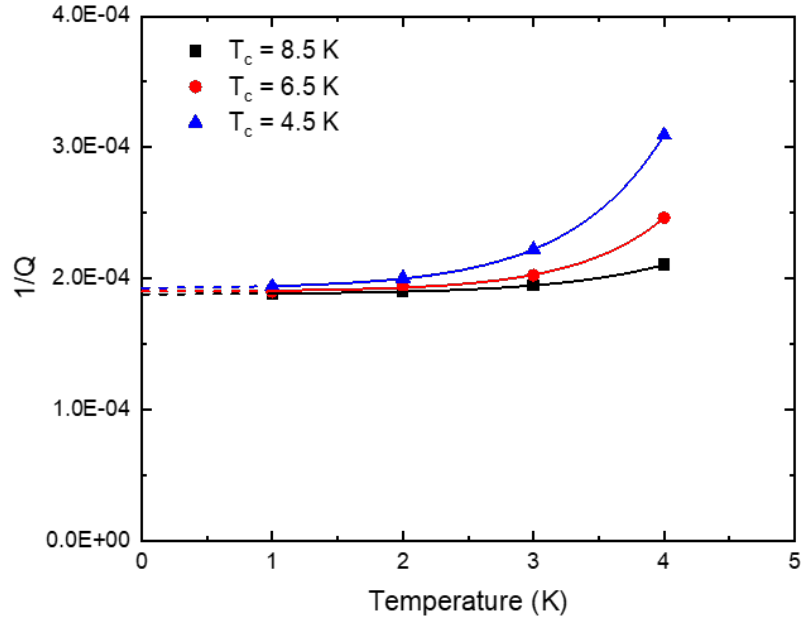


Figure 5.20. Simulation results of embedded resonator structure at multiple temperatures for varying T_c .

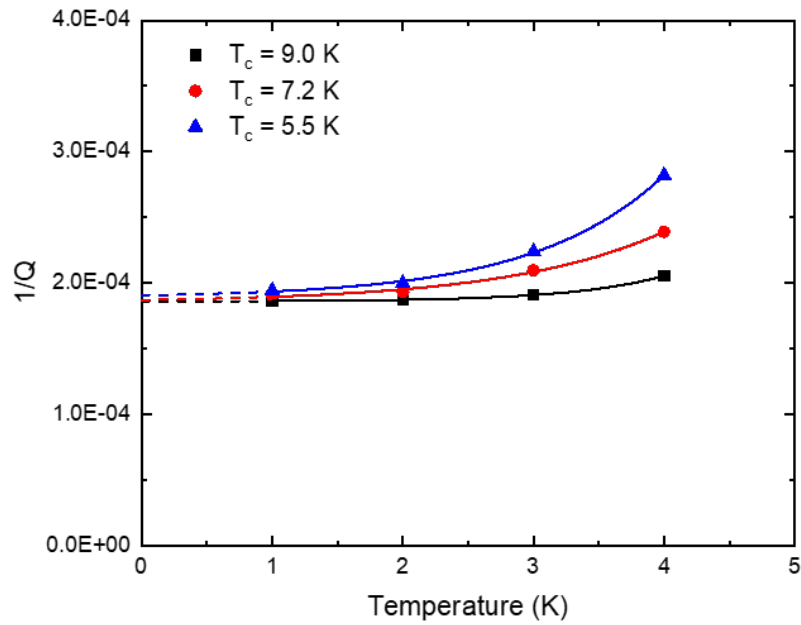


Figure 5.21. Simulation results of non-embedded resonator structure at multiple temperatures for varying T_c .

The fitting for temperature dependence of Q_l was performed using the Eq. 5.17. The intercepts were extracted by extrapolating to $T = 0$ K. These intercepts indicate the dielectric loss (i.e. Q_D) for both resonator structures. For each resonator structure, $\tan\delta$ was calculated using Eq. 5.13.

Embedded		Non-embedded	
T_c	$\tan\delta$	T_c	$\tan\delta$
8.5	1.80E-4	9.0	1.79E-4
6.5	1.84E-4	7.2	1.82E-4
4.5	1.87E-4	6.5	1.85E-4

Figure 5.22. Extracted $\tan\delta$ from embedded and non-embedded resonator structures for varying T_c .

Fig. 5.22 shows the tabulated loss tangent values for both embedded and non-embedded resonator structures. The extracted values of $\tan\delta$ were very close to the actual value of $\tan\delta_{eff}$ (1.78E-4). This shows the promising proof of concept for this approach and hence the same approach was used in the following section to extract the dielectric loss for the three fabricated resonator structures.

5.3.1 Measurement Results and Discussion

According to BCS theory, there is an exponential drop by a factor of $e^{\frac{-\Delta}{k_b T}}$ in the density of normal electron (i.e quasi-particles) as temperature is lowered below $T_c/2$. We have plotted $1/Q_l$ vs. temperature for all resonator structures cured at multiple temperatures. We have used following equation (valid for $T < T_c/2$) for fitting temperature dependence of Q_l .

$$R_s \approx \frac{\omega^2}{T} \exp\left(\frac{-\Delta(T)}{k_b T}\right) \quad (5.17)$$

ω represents the frequency, T represents the measured temperature. $\Delta(T)$ was calculated using the relation shown below:

$$\frac{\Delta(T)}{\Delta(0)} = 1.74 \sqrt{1 - \frac{T}{T_c}} \quad (5.18)$$

k_b is the Boltzman constant and Δ is the gap energy of a superconductor. The excitation energy required to break a Cooper pair is given by:

$$2\Delta = 3.5k_bT_c \quad (5.19)$$

Fig. 5.23, 5.24 and 5.25 shows the measurement results of $1/Q_l$ vs. temperature for embedded resonator structure cured at 225 °C, 250 °C and 275 °C respectively at different frequencies.

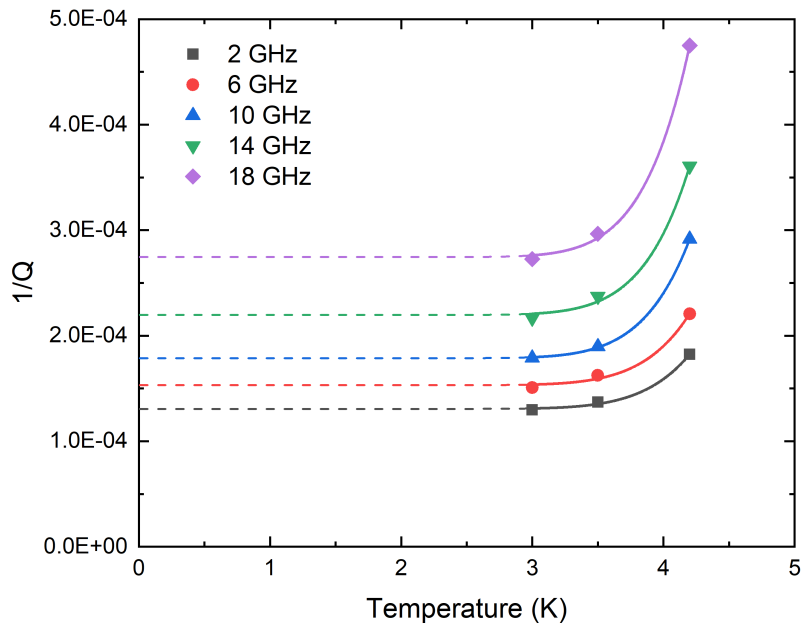


Figure 5.23. $1/Q_l$ vs. temperature for embedded sample cured at 225 °C.

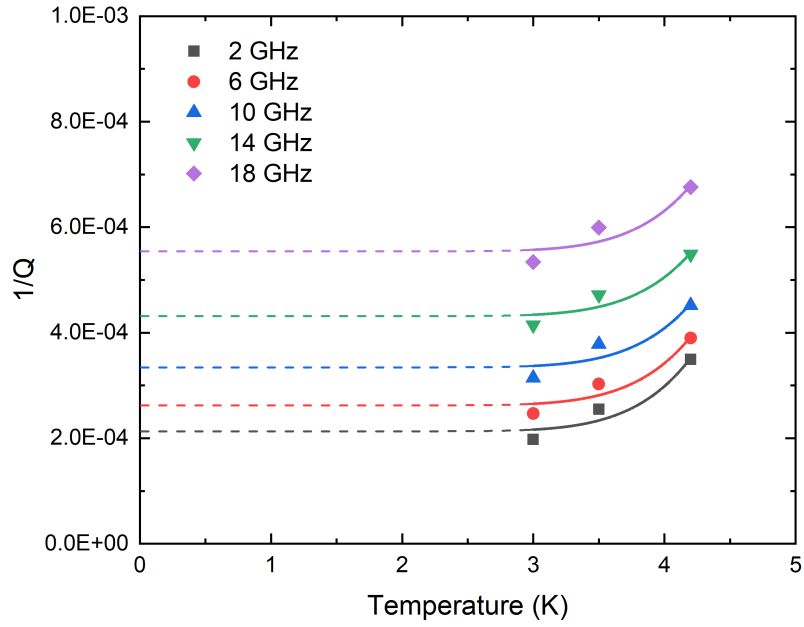


Figure 5.24. $1/Q_l$ vs. temperature for embedded sample cured at 250 °C.

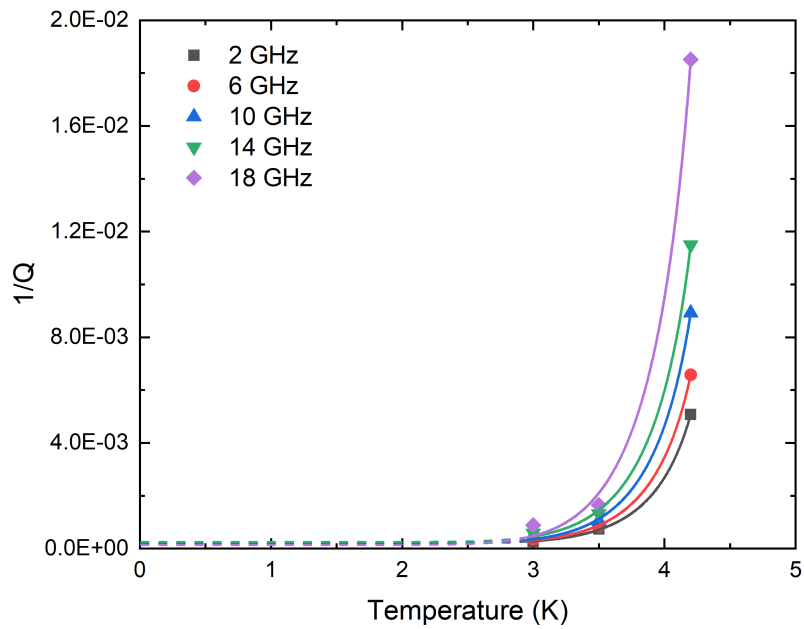


Figure 5.25. $1/Q_l$ vs. temperature for embedded sample cured at 275 °C.

Fig. 5.26, 5.27 and 5.28 shows the measurement results of $1/Q_l$ vs. temperature for non-embedded resonator structure cured at 225 °C, 250 °C and 275 °C respectively at different frequencies.

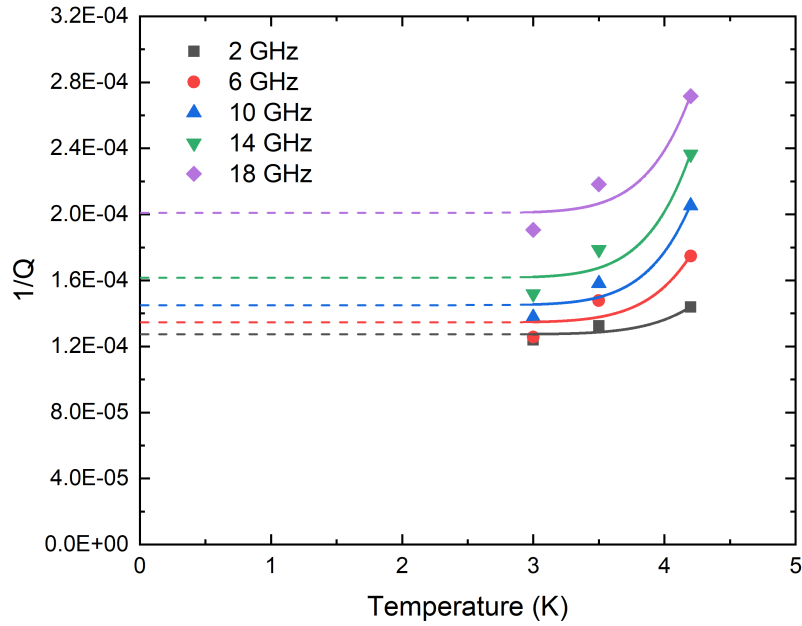


Figure 5.26. $1/Q_l$ vs. temperature for non-embedded sample cured at 225 °C.

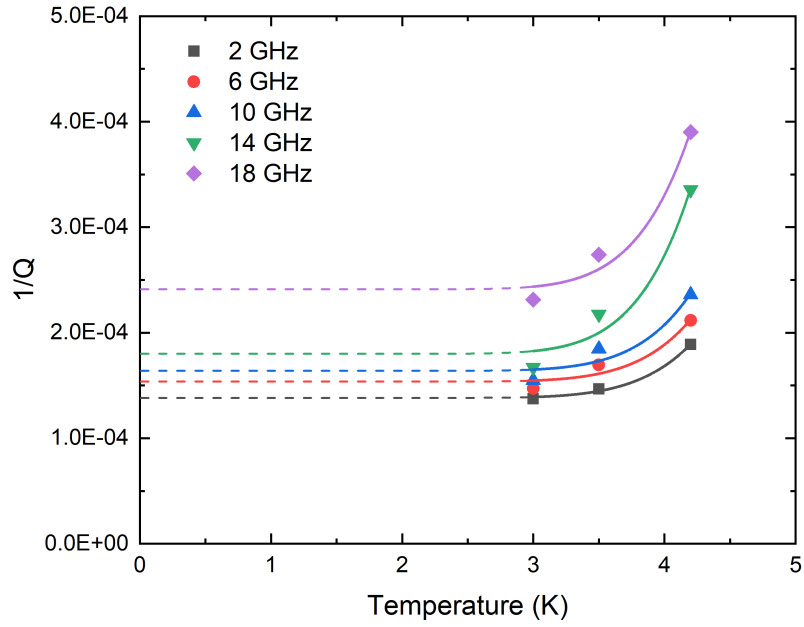


Figure 5.27. $1/Q_l$ vs. temperature for non-embedded sample cured at 250 °C.

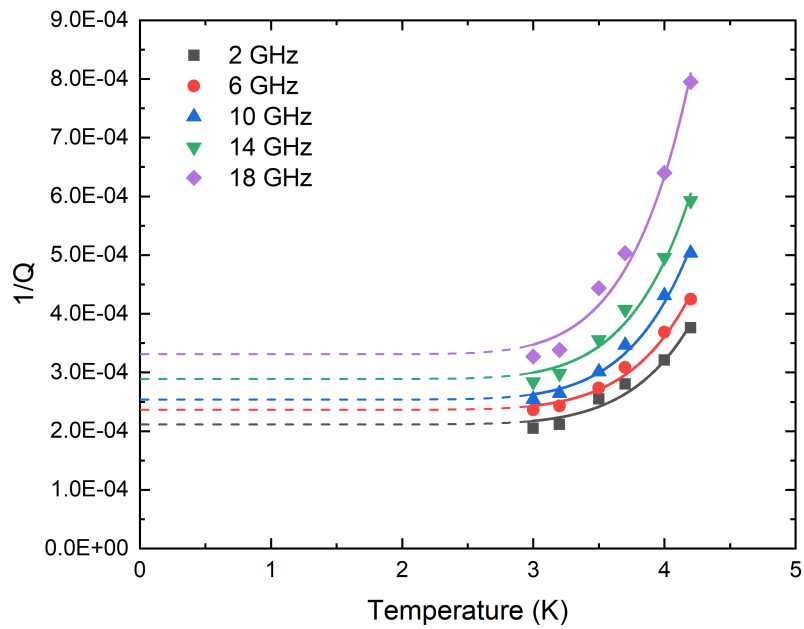


Figure 5.28. $1/Q_l$ vs. temperature for non-embedded sample cured at 275 °C.

Fig. 5.29, 5.30 and 5.31 shows the measurement results of $1/Q_l$ vs. temperature for embedded resonator structure with Al_2O_3 barrier layer cured at $225\text{ }^\circ\text{C}$, $250\text{ }^\circ\text{C}$ and $275\text{ }^\circ\text{C}$ respectively at different frequencies.

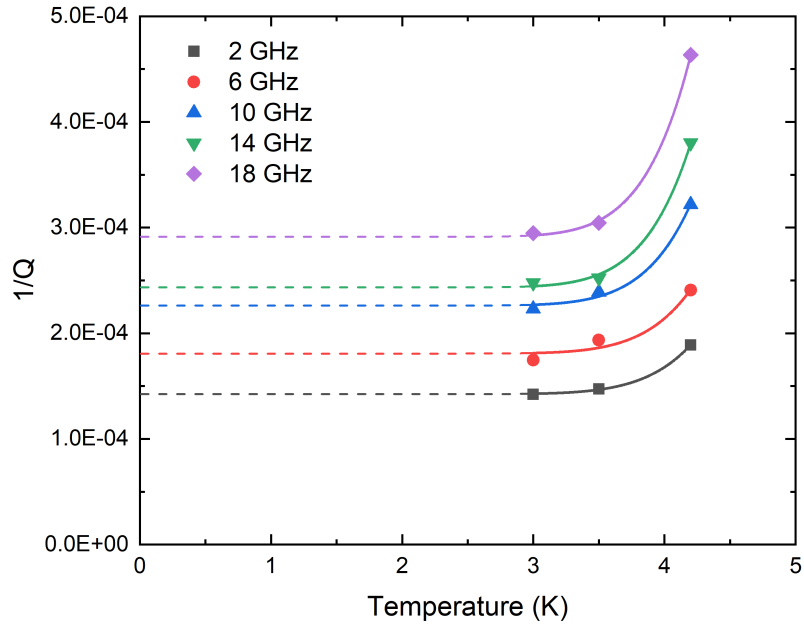


Figure 5.29. $1/Q_l$ vs. temperature for $\text{Al}_2\text{O}_3/\text{Nb}/\text{Al}_2\text{O}_3$ sample cured at $225\text{ }^\circ\text{C}$.

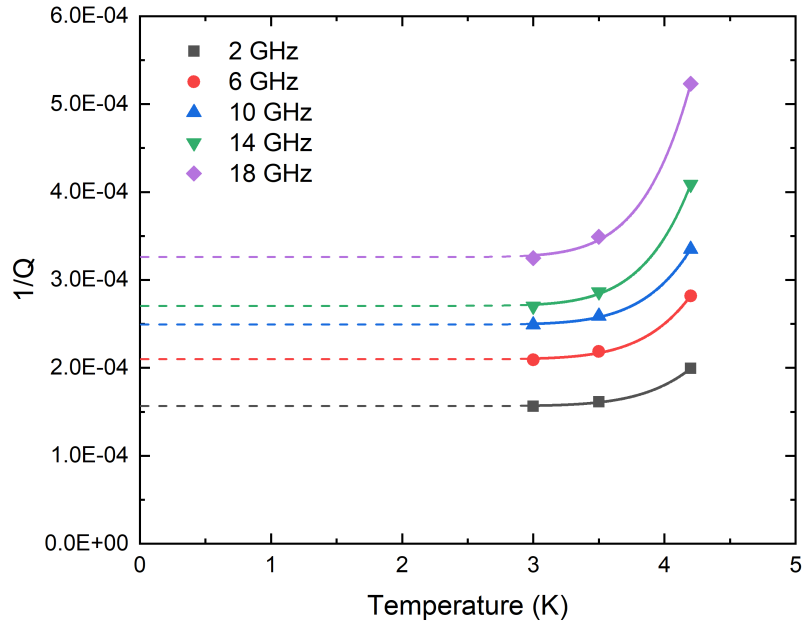


Figure 5.30. $1/Q_l$ vs. temperature for $\text{Al}_2\text{O}_3/\text{Nb}/\text{Al}_2\text{O}_3$ sample cured at 250 °C.

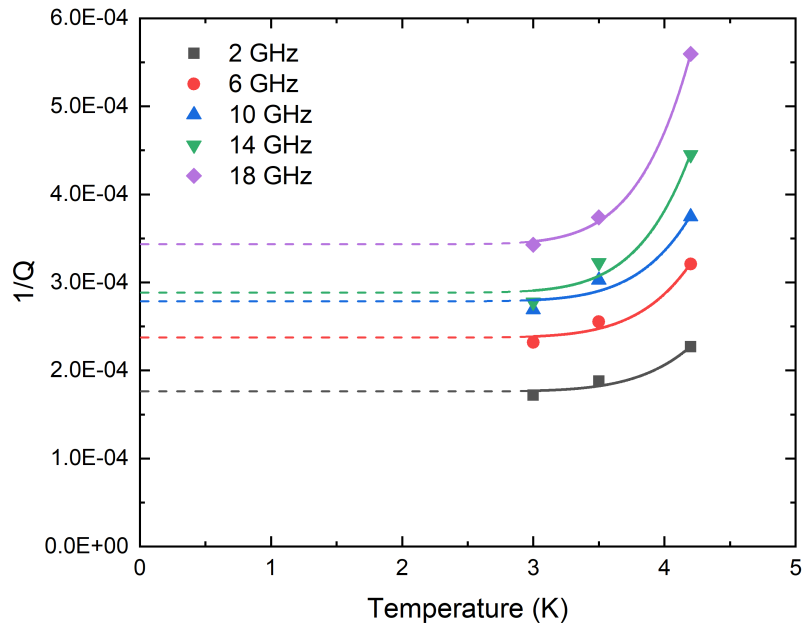


Figure 5.31. $1/Q_l$ vs. temperature for $\text{Al}_2\text{O}_3/\text{Nb}/\text{Al}_2\text{O}_3$ sample cured at 275 °C.

5.3.2 Extraction of Dielectric Loss for Different Resonator Structures

We know that the loaded quality factor Q_l is defined as:

$$\frac{1}{Q_l} = \frac{1}{Q_c} + \frac{1}{Q_D} + \frac{1}{Q_r} + \frac{1}{Q_{cp}} \quad (5.20)$$

Where Q_l is the loaded quality factor and the other terms are quality factors associated with conductor loss (Q_c), dielectric loss (Q_D), radiation loss (Q_r) and coupling loss (Q_{cp}). The resonators used in this work have a small cross-section, therefore we have assumed negligible radiation loss. Weakly coupled resonators yield sufficiently high Q_{cp} , hence $1/Q_{cp}$ can be safely ignored. With these assumptions we modify Eq. 5.20 and express it as:

$$\frac{1}{Q_l} = \frac{1}{Q_c} + \frac{1}{Q_D} \quad (5.21)$$

Exponential extrapolations to $T = 0$ correspond to an “absolute 0 K” case, which should have negligible conductor loss. Therefore, the Q_l values at these intercept points should primarily depend on the dielectric loss (i.e., Q_D). From these intercepts, we can get the frequency dependent dielectric loss and use Eq. 5.21 to extract conductor loss. Fig. 5.32 shows a sequence of steps followed to extract dielectric and conductor loss.

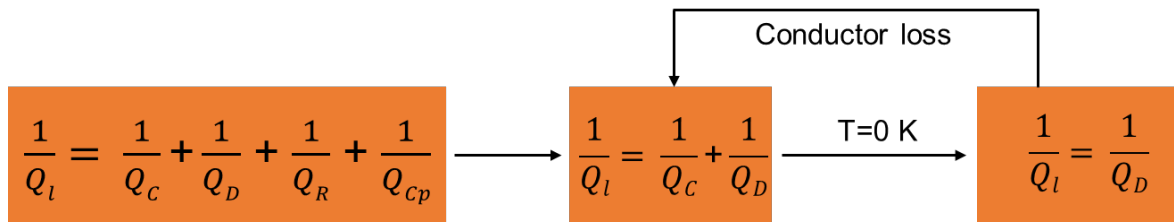


Figure 5.32. Image of a flow chart showing the steps followed to separate dielectric and conductor loss.

Fig. 5.33 shows the measurement results of the $1/Q_D$ vs. frequency for embedded resonator structure cured at 225 °C, 250 °C and 275 °C respectively at different frequencies

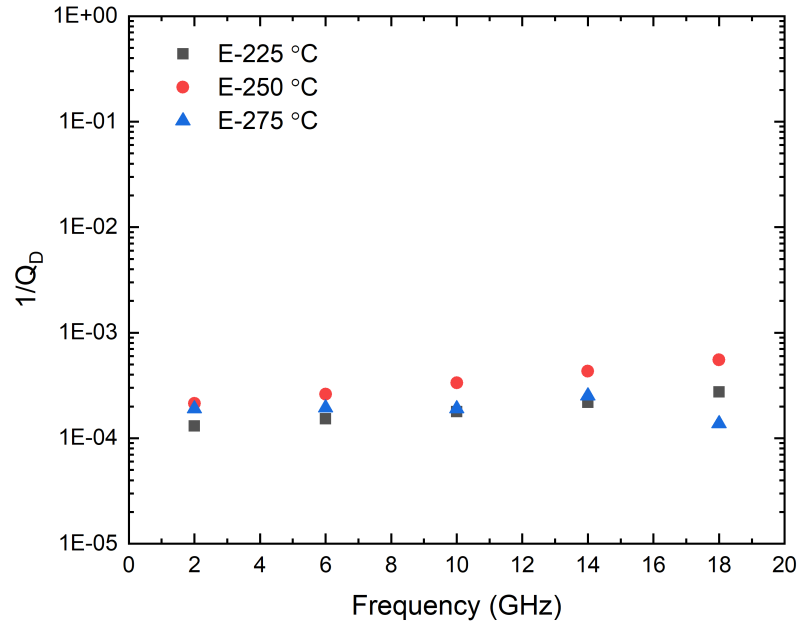


Figure 5.33. $1/Q_D$ vs. frequency for embedded sample cured at multiple temperatures.

Fig. 5.34 shows the measurement results of the extracted $1/Q_D$ vs. frequency for non-embedded resonator cured at 225 °C, 250 °C and 275 °C respectively.

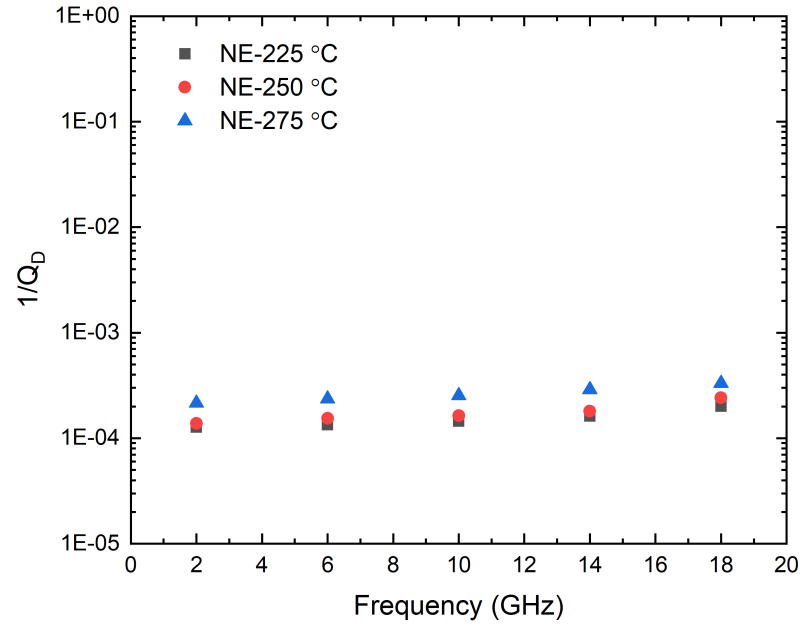


Figure 5.34. $1/Q_D$ vs. frequency for non-embedded sample cured at multiple temperatures.

Fig. 5.35 shows the measurement results of the extracted $1/Q_D$ vs. frequency for embedded resonator with Al_2O_3 barrier layer cured at 225 °C, 250 °C and 275 °C respectively.

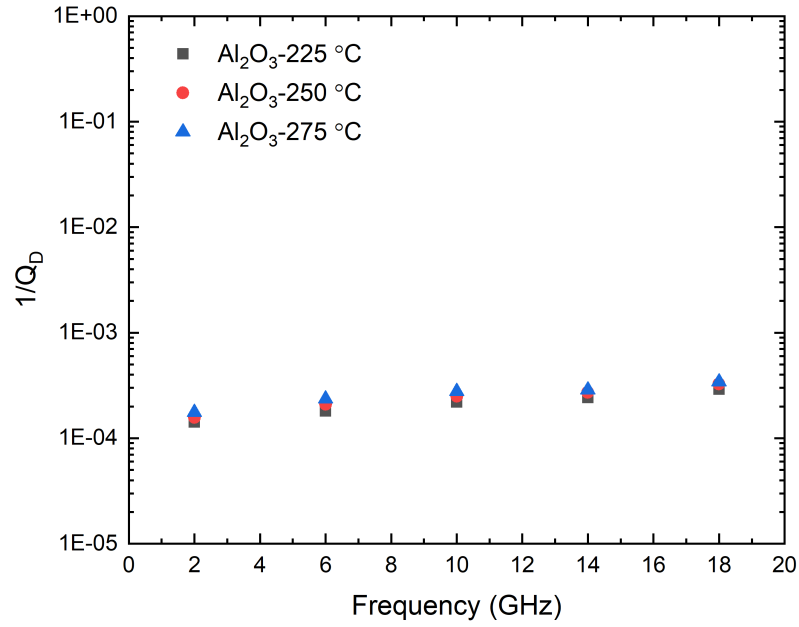


Figure 5.35. $1/Q_D$ vs. temperature for $\text{Al}_2\text{O}_3/\text{Nb}/\text{Al}_2\text{O}_3$ sample cured at multiple temperatures.

The dielectric loss tangent for each resonator structure was calculated using Eq. 5.13. Fig. 5.36 shows the measurement results of the $\tan\delta$ vs. frequency for embedded resonator structure cured at 225 °C, 250 °C and 275 °C respectively at different frequencies.

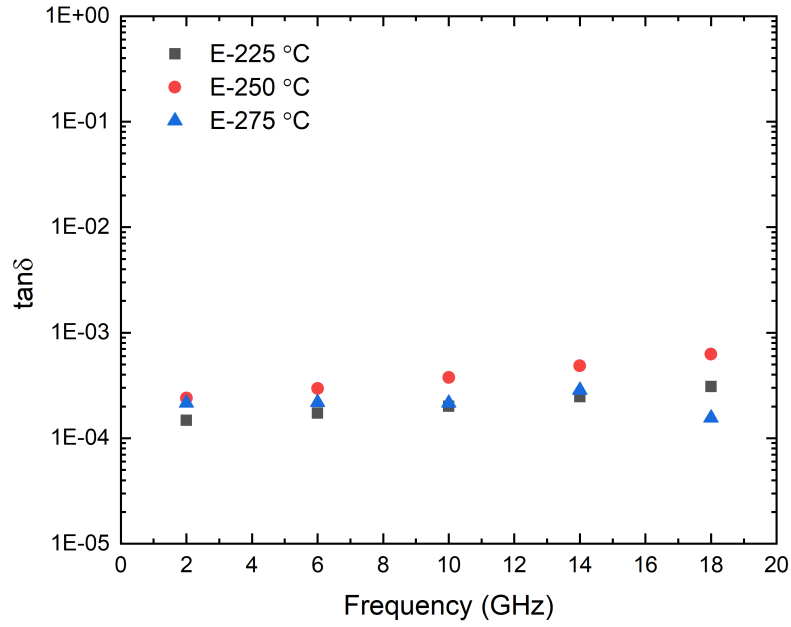


Figure 5.36. $\tan\delta$ vs. frequency for embedded sample cured at multiple temperatures.

Fig. 5.37 shows the measurement results of the $\tan\delta$ vs. frequency for non-embedded resonator cured at 225 °C, 250 °C and 275 °C respectively.

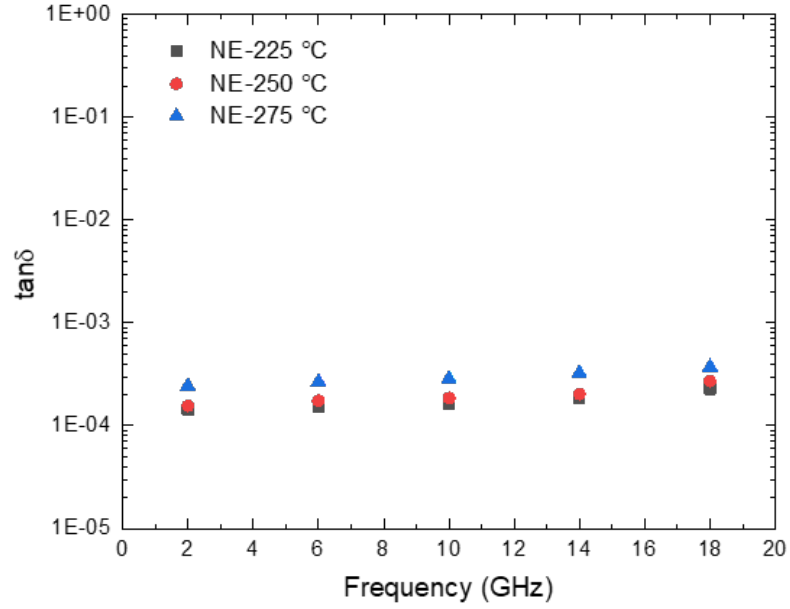


Figure 5.37. $\tan\delta$ vs. frequency for non-embedded sample cured at multiple temperatures.

Fig. 5.38 shows the measurement results of the $\tan\delta$ vs. frequency for embedded resonator with Al_2O_3 barrier layer cured at 225 °C, 250 °C and 275 °C respectively.

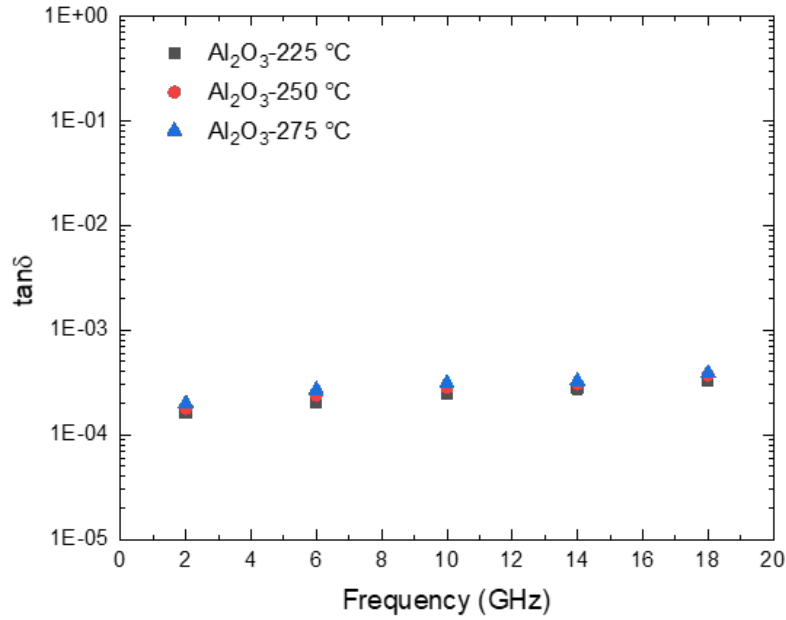


Figure 5.38. $\tan\delta$ vs. temperature for $\text{Al}_2\text{O}_3/\text{Nb}/\text{Al}_2\text{O}_3$ sample cured at multiple temperatures.

5.3.3 Extraction of Conductor Loss for Different Resonator Structures

The $1/Q_c$ was extracted using the Eq. 5.21. Fig. 5.39 shows the measurement results of the extracted $1/Q_c$ vs. frequency for embedded resonator cured at 225 °C, 250 °C and 275 °C respectively.

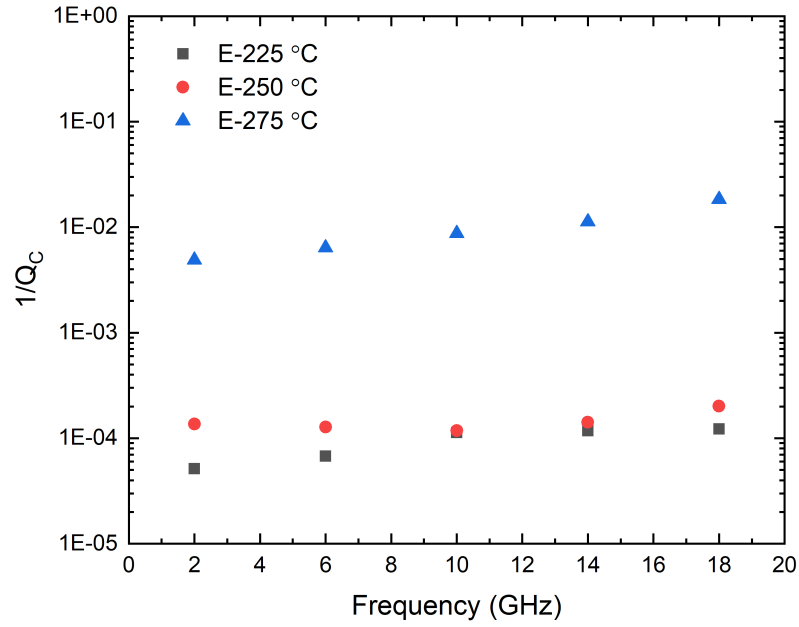


Figure 5.39. $1/Q_c$ vs. frequency for embedded sample cured at multiple temperatures.

Fig. 5.40 shows the measurement results of the extracted $1/Q_c$ vs. frequency for non-embedded resonator cured at 225 °C, 250 °C and 275 °C respectively at different frequencies.

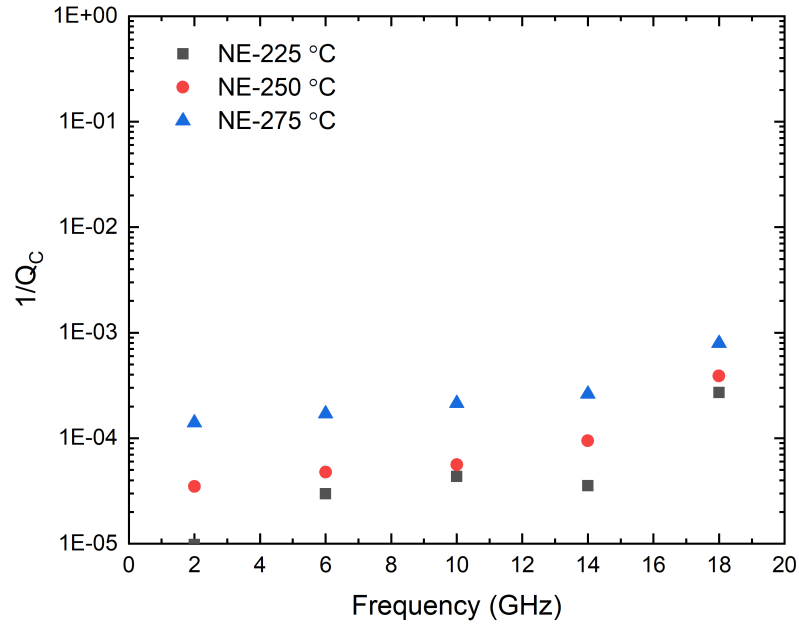


Figure 5.40. $1/Q_c$ vs. frequency for non-embedded sample cured at multiple temperatures.

Fig. 5.41 shows the measurement results of the extracted $1/Q_c$ vs. frequency for embedded resonator with Al_2O_3 barrier layer cured at 225 °C, 250 °C and 275 °C respectively at different frequencies.

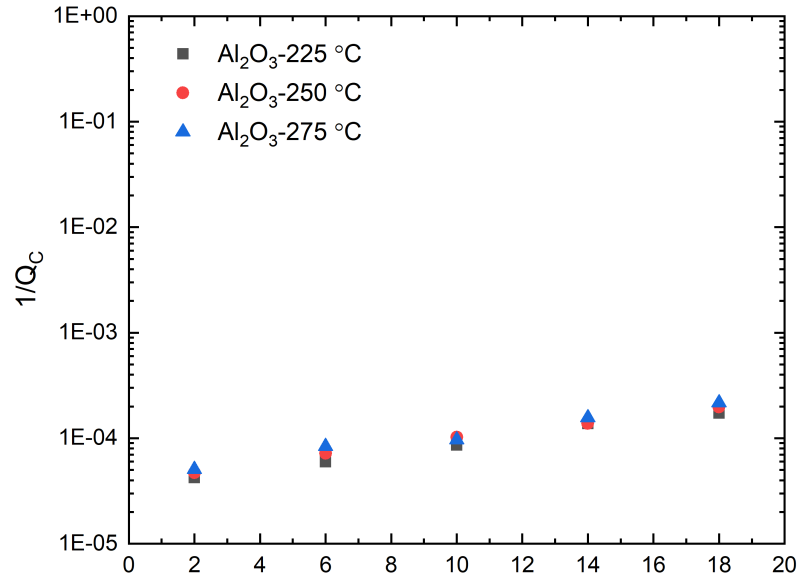


Figure 5.41. $1/Q_c$ vs. frequency for $\text{Al}_2\text{O}_3/\text{Nb}/\text{Al}_2\text{O}_3$ sample cured at multiple temperatures.

The following plots were generated to better compare the conductor loss of all resonator structures at different curing temperatures. Fig. 5.42 shows the measurement results of the $1/Q_c$ vs. frequency for all resonator structures cured at 225 °C.

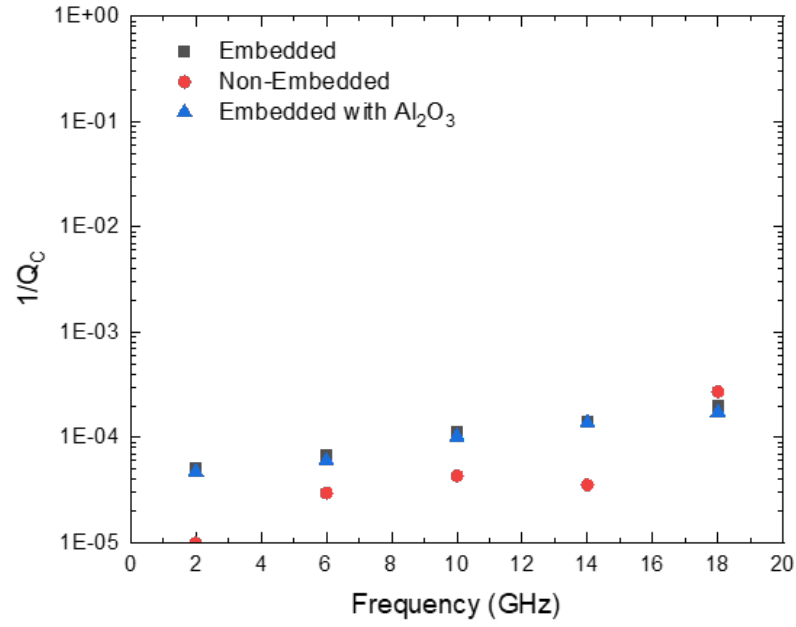


Figure 5.42. $1/Q_c$ vs. frequency for all resonator structures cured at 225 °C.

Fig. 5.43 shows the measurement results of the $1/Q_c$ vs. frequency for all resonator structures cured at 250 °C.

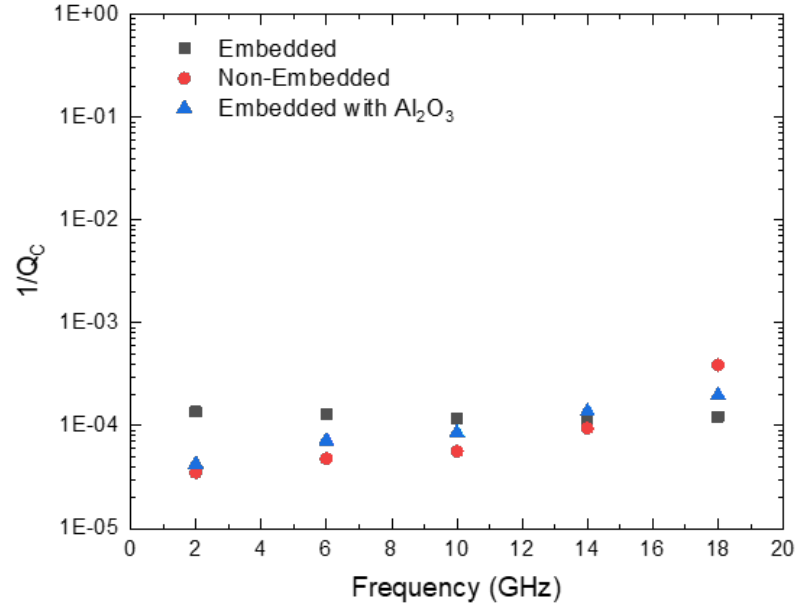


Figure 5.43. $1/Q_c$ vs. frequency for all resonator structures cured at 250 °C.

Fig. 5.44 shows the measurement results of the $1/Q_c$ vs. frequency for all resonator structures cured at 275 °C.

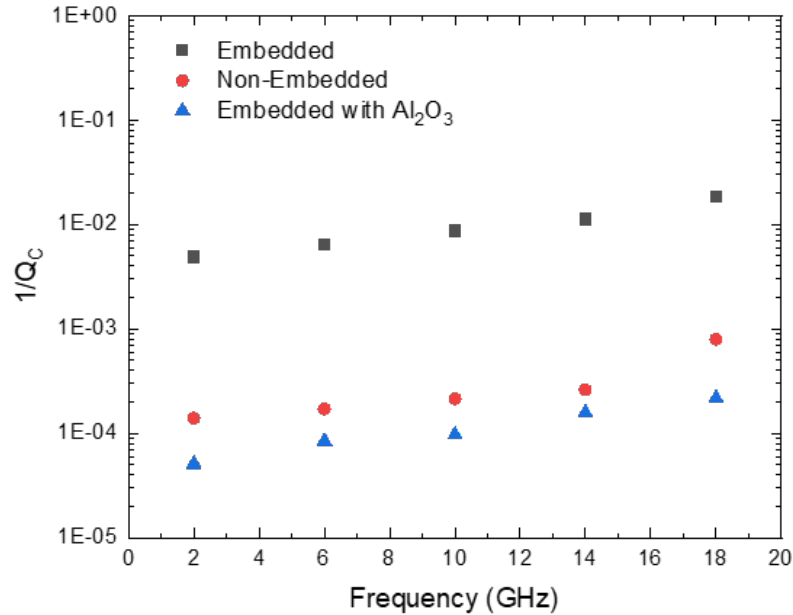


Figure 5.44. $1/Q_c$ vs. frequency for all resonator structures cured at 275 °C.

In this section we have extracted dielectric loss and conductor loss using microstrip resonators measured at multiple temperatures. The impact of curing samples at temperatures - 225 °C, 250 °C and 275 °C on dielectric and conductor loss was studied. It can be seen that at lower curing temperatures of 225 °C and 250 °C, non-embedded samples show the least amount of conductor loss, this may be due to the absence of an encapsulating PI layer on top, which causes degradation in the embedded cases (with and without Al₂O₃ barrier layer). When the same samples were exposed to a curing temperature of 275 °C, significant degradation was observed in embedded and non-embedded resonator structures, whereas the embedded resonator structure with Al₂O₃ barrier layer shows the least amount of degradation. This proves the effectiveness of Al₂O₃ as a promising barrier layer at curing temperatures above 250 °C.

5.4 Separation of Conductor and Dielectric Losses Using an External Magnetic Field on Microstrip Resonators

One of the most common ways to alter the state of superconductor from superconducting state to normal state is by applying an external magnetic field. Several groups have studied the effect of external magnetic field in superconducting radio-frequency (SRF) cavities which are basically resonator structures that allow acceleration of charge particles at high energies [43–49]. The field at which superconductivity is destroyed is called critical magnetic field B_c . Superconductors are divided into two categories: Type I and Type II. Type I superconductors not only behave as perfect conductors but also act as ideal diamagnets. Hence when the temperature is lowered below T_c , in the presence of some applied magnetic field (less than B_c) an induced magnetic field in the opposite direction is created inside the superconductor leading to the expulsion of magnetic flux from the interior of superconductors. Type II superconductors exhibit two critical fields - lower critical field and upper critical field. Below the lower critical field, an induced magnetic field inside the superconductor opposes the applied field, similar to type I. Above the lower critical field, there is slow transition from superconducting state to normal state until upper critical field is reached. This phenomenon is known as Meissner effect. The Nb used in this work falls under the category of Type II. The critical magnetic field is related to temperature by the parabolic law shown below.

$$B_c = B_c(0) \left[1 - \left(\frac{T}{T_c} \right)^2 \right] \quad (5.22)$$

Eq. 5.22 can be inverted to obtain suppressed superconducting transition temperature (T_c) [50]:

$$T_c = T_c(0) \left[1 - \left(\frac{B}{B_c} \right)^2 \right] \quad (5.23)$$

In this section, an external magnetic field was applied to separate internal losses i.e. a combination of conductor loss and dielectric loss using microstrip resonator structures. In

the presence of an external magnetic field, the electrons forming Cooper pairs tend to break due to extra energy provided by the external magnetic field to overcome the energy gap. As a result, the number of normal electrons in the superconductor increases leading to disruption of superconductivity.

We report the microwave performance of non-embedded and embedded transmission line resonator in the presence of external field. Neodymium magnets were used as a source of magnetic field in this section, these magnets are strong permanent magnets and part of the rare-earth magnet family.

5.4.1 Magnetic Test Fixtures

In order to study the effect of magnetic field on superconducting resonator structures, three fixtures were built. Depending upon the proximity of the magnet to the sample, each fixture exhibited different magnetic field strength on the sample.

5.4.1.1 Fixture for Magnetic Field Strength of 0.5 kG

Fig. 5.45 shows the 3D image of the designed fixture used for applying B of 0.5 kG on the sample. The magnet is hidden inside the rectangular cavity as indicated in the image. This was done to apply a constant field on the sample at all times during testing and to prevent it from moving and or falling while performing tests at cryo temperatures. Fig. 5.46 shows the assembled flexible microstrip resonator sample, with end-launch SMA connectors mounted at each end of the sample.

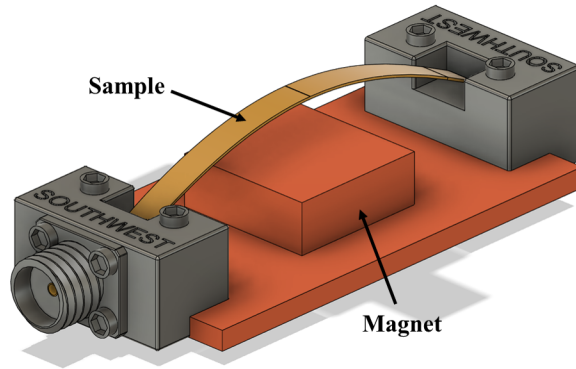


Figure 5.45. A 3D model of the test fixture with flexible sample and SMA connectors on each end used to apply 0.5 kG of magnetic field on the resonator samples.

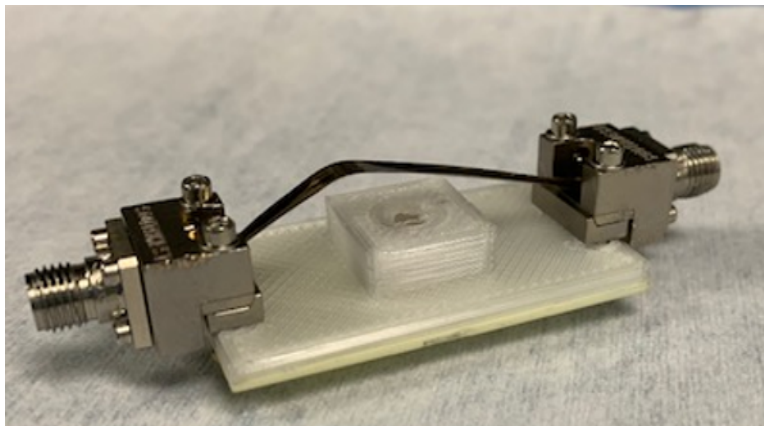


Figure 5.46. Flexible Nb resonator assembly with Southwest Microwave, Inc SMA end-launch connectors mounted, attached to a 3D printed magnetic test fixture to apply 0.5 kG of magnetic field on the sample under test.

5.4.1.2 Fixture for Magnetic Field Strength of 2 kG

Fig. 5.47 shows the 3D image of the designed fixture used for applying B of 2 kG on the sample. Similar to the previous case the magnet is placed inside the cavity as shown in the image. It can be seen that the magnet is moved closer to the sample in this fixture. Hence the magnetic field increased to 2 kG. Fig. 5.48 shows the assembled flexible microstrip resonator sample, with end-launch SMA connectors mounted at each end of the sample.

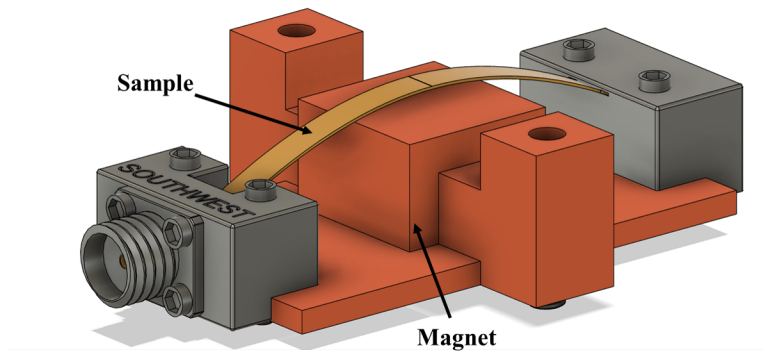


Figure 5.47. A 3D model of the test fixture with flexible sample and SMA connectors on each end used to apply 2 kG of magnetic field on the resonator samples.

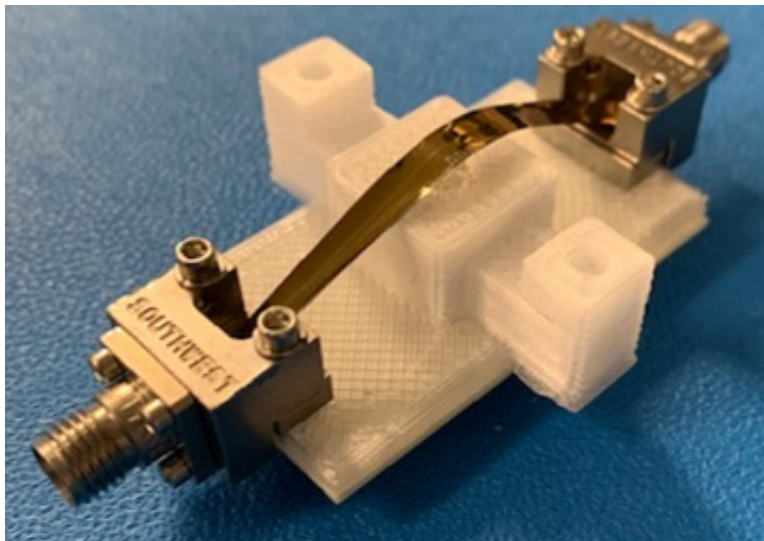


Figure 5.48. Flexible Nb resonator assembly with Southwest Microwave, Inc SMA end-launch connectors mounted, attached to a 3D printed magnetic test fixture to apply 2 kG of magnetic field on the sample under test.

5.4.1.3 Fixture for Magnetic Field Strength of 4 kG

Fig. 5.47 shows the 3D image of the designed fixture used for applying B of 4 kG on the sample. This fixture is a combination of two identical 2 kG fixture parts, one of the part is inverted on top of the other and held down by screws to produce an effective field of 4 kG. Fig. 5.50 shows the assembled flexible microstrip resonator sample, with end-launch SMA connectors mounted at each end of the sample.

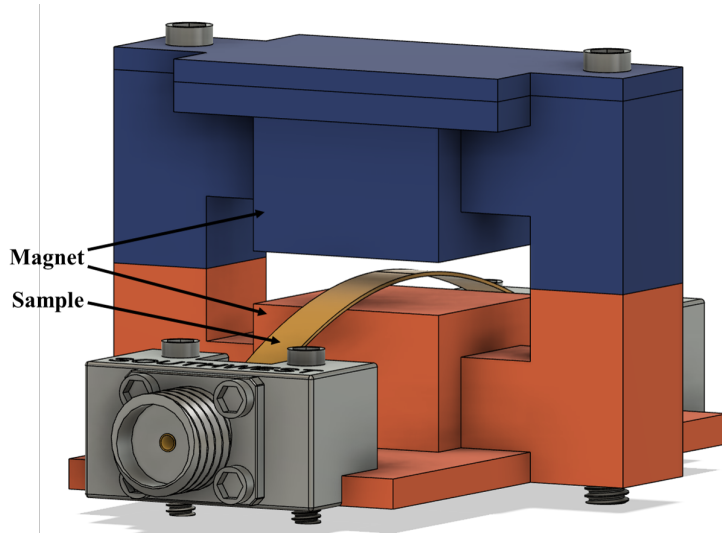


Figure 5.49. A 3D model of the test fixture with flexible sample and SMA connectors on each end used to apply 4 kG of magnetic field on the resonator samples.

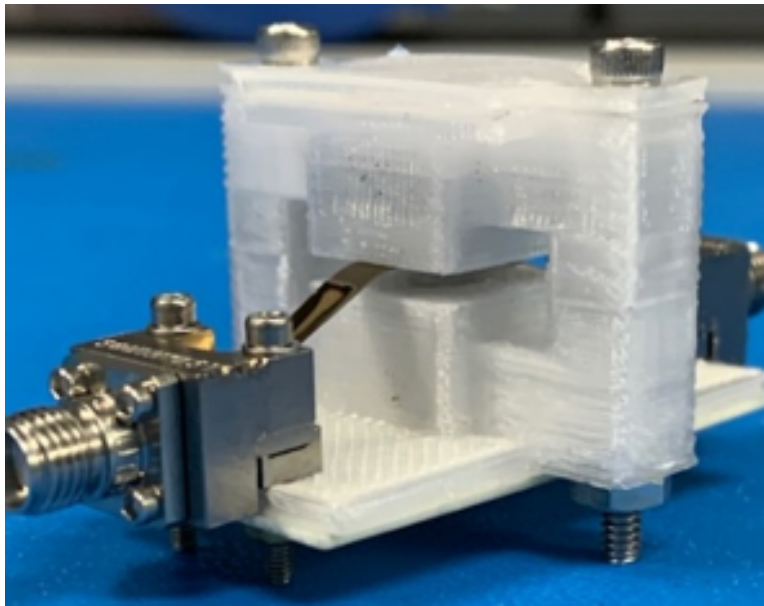


Figure 5.50. Flexible Nb resonator assembly with Southwest Microwave, Inc SMA end-launch connectors mounted, attached to a 3D printed magnetic test fixture to apply 4 kG of magnetic field on the sample under test.

5.4.2 Measurement Setup

Microwave measurements were made up to ~ 10 GHz, using a Keysight N5227A PNA, at a nominal power out of the PNA of, at a nominal power out of the PNA of -20 dBm -20 dBm. Measurements were performed in LHe dewar at 4.2 K (shown in Fig. 5.51).



Figure 5.51. LHe dewar.

5.4.3 Results and Discussion

Using the correlation shown in Eq. 5.23, T_c was calculated for each value of applied magnetic field. T_c values of 8.97 K, 8.46 K and 6.86 K were obtained for magnetic strengths of 0.5 kG, 2 kG and 4 kG respectively. Based on these values, $1/Q_t$ was plotted as a function of T/T_c for a non-embedded sample (shown in Fig. 5.52). The sample was baked at 90 °C in a vacuum oven for 2 hr prior to making measurements, this was done to minimize the humidity effects on the resonator during measurement. An exponential fitting was performed due to the reduction in the number of normal electrons by a factor of $e^{\frac{-\Delta}{k_b T}}$ (as shown in Eq. 5.17).

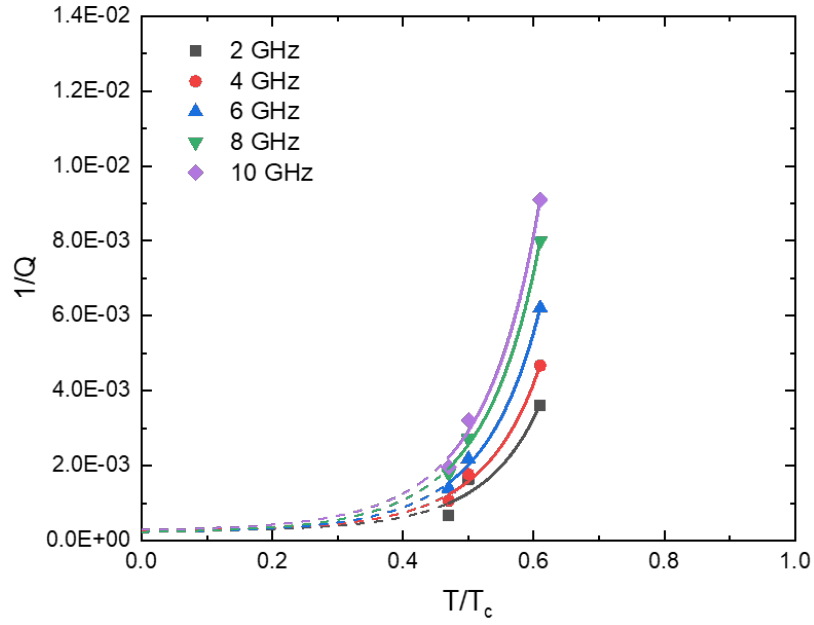


Figure 5.52. $1/Q_l$ vs. T/T_c for non-embedded sample. The sample was baked before making measurements.

The same sample was measured again without baking prior to making measurements. Fig. 5.53 shows the plot of $1/Q_l$ as a function of T/T_c . This was done to measure the change in Q_l value as an effect of humidity.

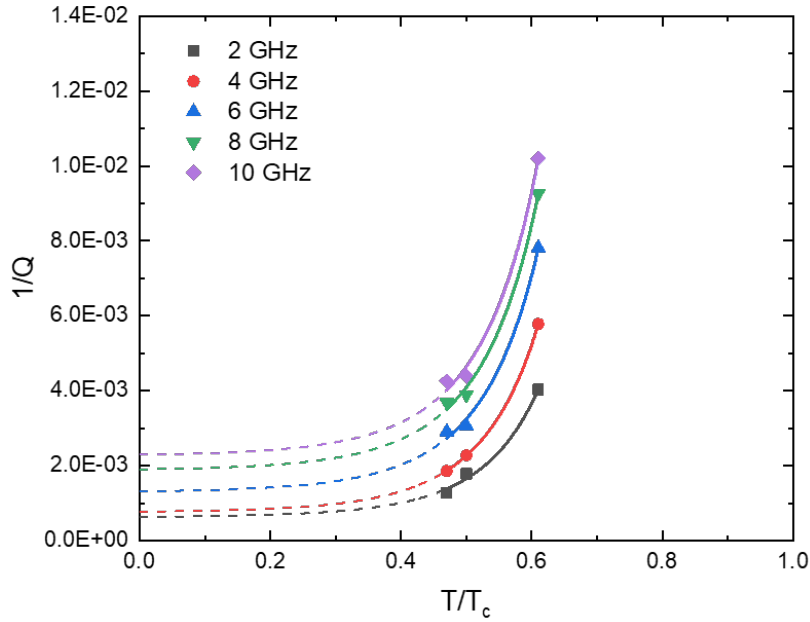


Figure 5.53. $1/Q_l$ vs. T/T_c for non-embedded sample. The sample was NOT baked before making measurements.

By extrapolating the data points shown in previous plot, we obtained the absolute 0 K case. This case represents the Q_l values that primarily depend on the dielectric loss (i.e., $1/Q_D$), with no conductor loss. Fig. 5.54 shows the plot $1/Q_D$ vs. frequency for non-embedded resonators. It is evident from the plot that dielectric loss for the non-baked case is higher than the one for the baked case.

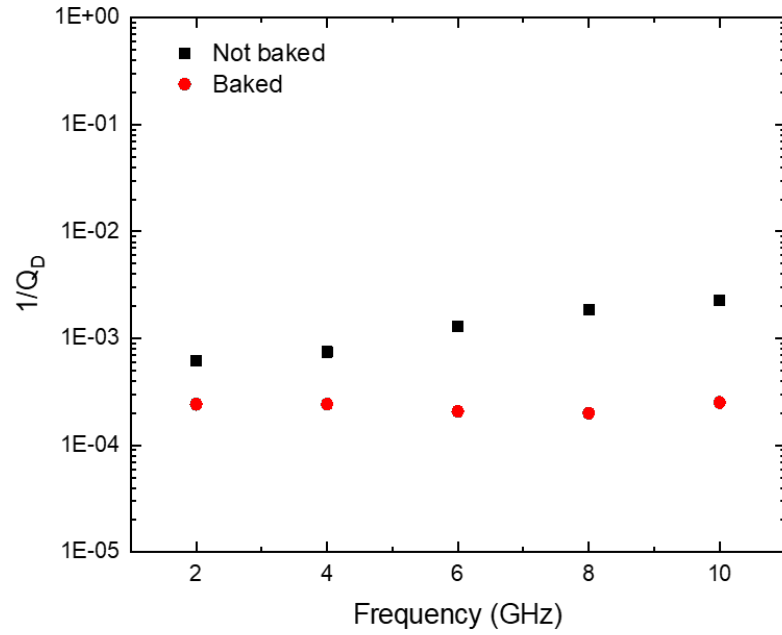


Figure 5.54. $1/Q_D$ vs. frequency for non-embedded sample.

Fig. 5.55 shows the difference in $1/Q_D$ values between the baked and not-baked cases.

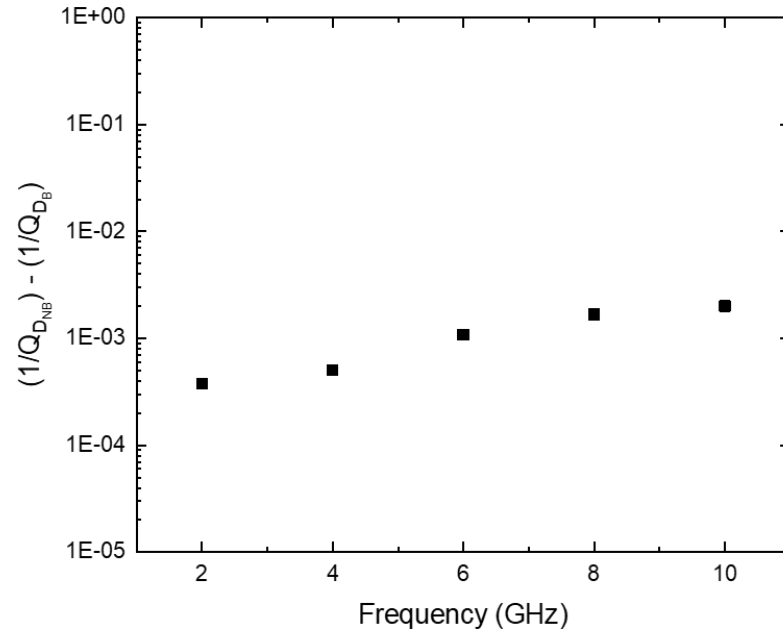


Figure 5.55. $1/Q_D$ vs. frequency for non-embedded sample. NB represents not baked and B represents baked.

Fig. 5.56 shows the percentage change in the dielectric loss as an effect of baking prior to making measurement.

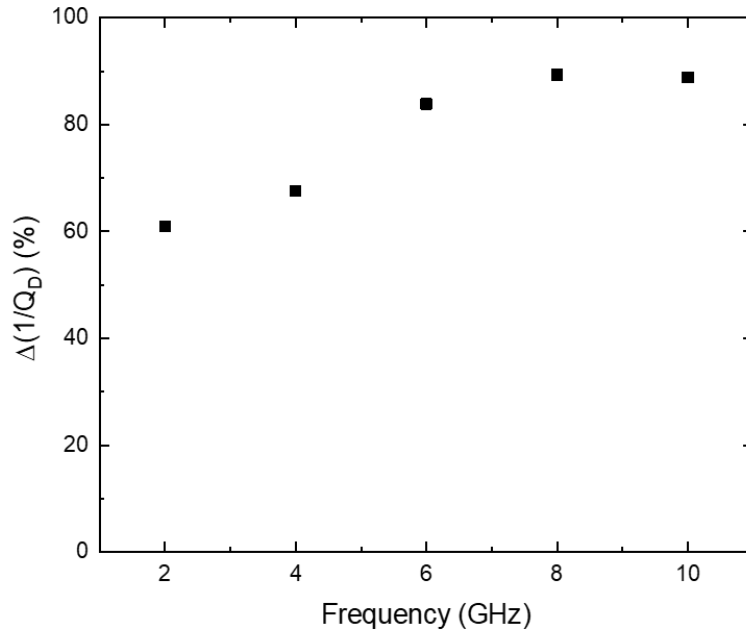


Figure 5.56. Percentage change of $\Delta(1/Q_D)$ vs. frequency for non-embedded sample.

The dielectric loss tangent was calculated from dielectric loss (i.e. $1/Q_D$) using the Eq. 5.13. Fig. 5.57 shows the plot $\tan\delta$ vs. frequency for non-embedded resonators. Similar to the case dielectric loss, the $\tan\delta$ value for the non-baked case is higher than the one for the baked case.

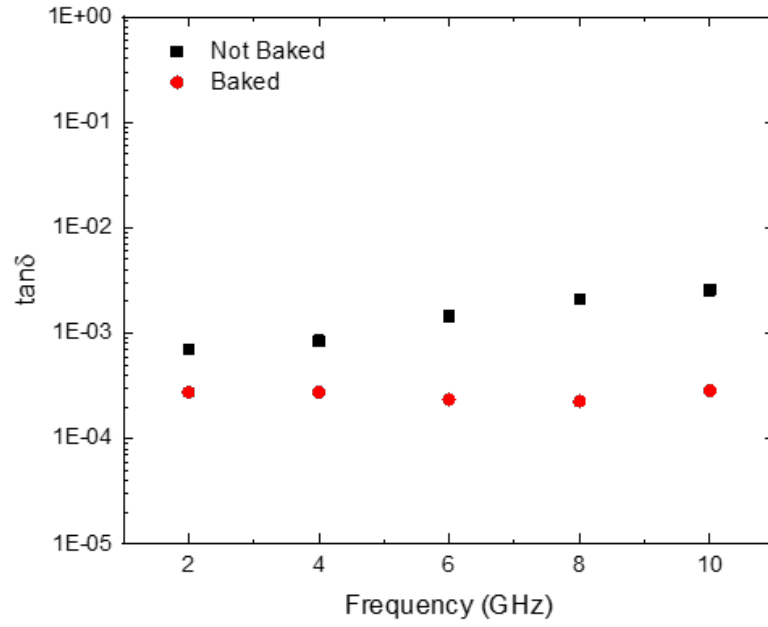


Figure 5.57. $\tan\delta$ vs. frequency for non-embedded sample.

Fig. 5.58 shows the difference in $\tan\delta$ values between the baked and not-baked cases.

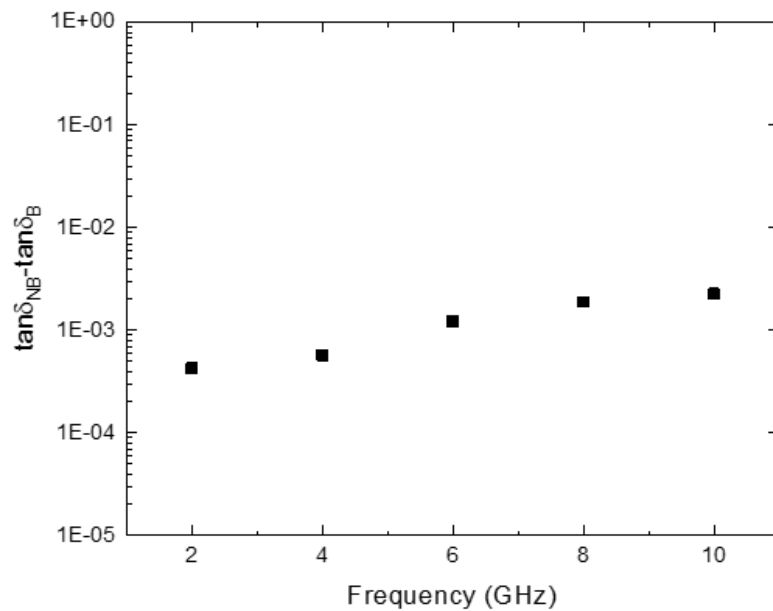


Figure 5.58. $\Delta \tan\delta$ vs. frequency for non-embedded sample. NB represents not baked and B represents baked.

Fig. 5.59 shows the percentage change in the $\tan\delta$ as an effect of baking prior to making measurement.

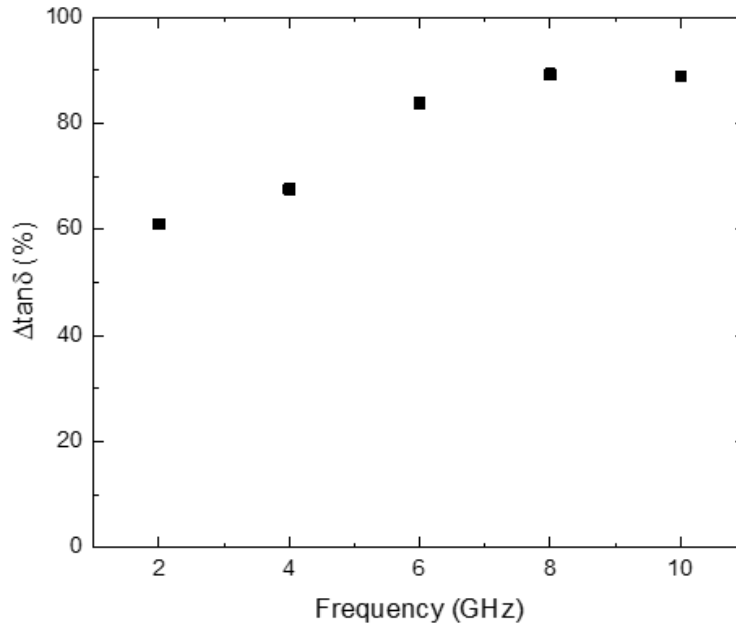


Figure 5.59. Percentage change of $\Delta \tan \delta$ vs. frequency for non-embedded sample.

$1/Q_c$ was calculated using Eq. 5.21. Fig. 5.60 shows the plot of $1/Q_c$ vs. frequency for the non-embedded sample. Minimal change was observed in the conductor loss as an effect of baking the sample.

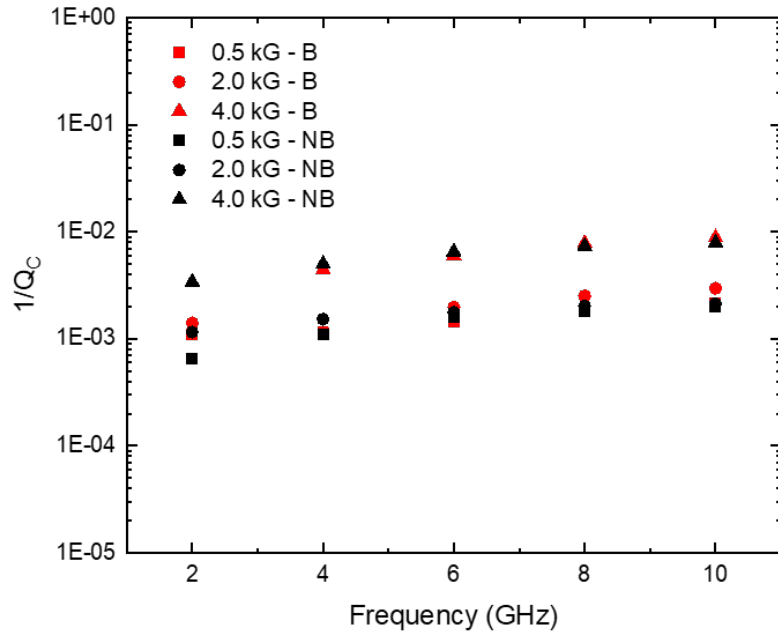


Figure 5.60. $1/Q_c$ vs. frequency for non-embedded sample. NB represents not baked and B represents baked.

Fig. 5.61 shows the difference in $1/Q_c$ values between the baked and not-baked cases for the non-embedded resonator.

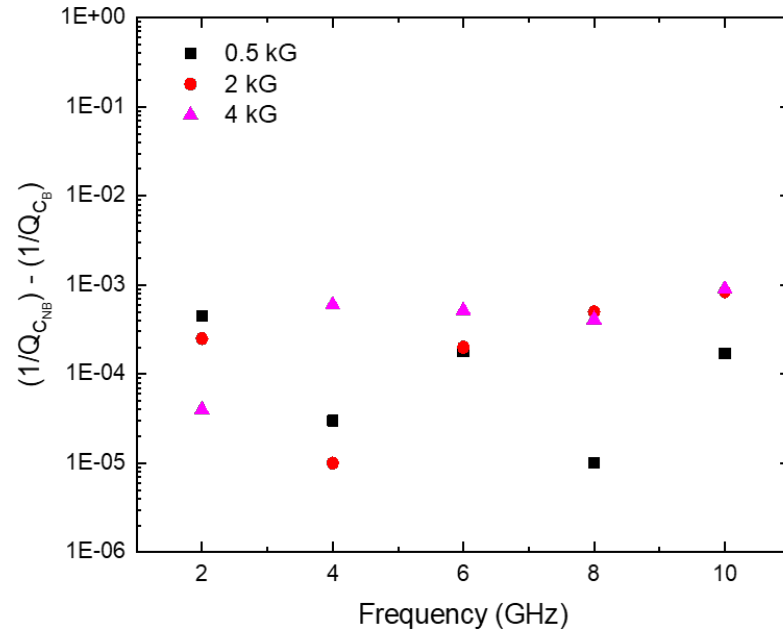


Figure 5.61. $1/Q_e$ vs. frequency for non-embedded sample. NB represents not baked and B represents baked.

Fig. 5.62 shows the percentage change in the conductor loss as an effect of baking prior to making measurement for the non-embedded resonators.

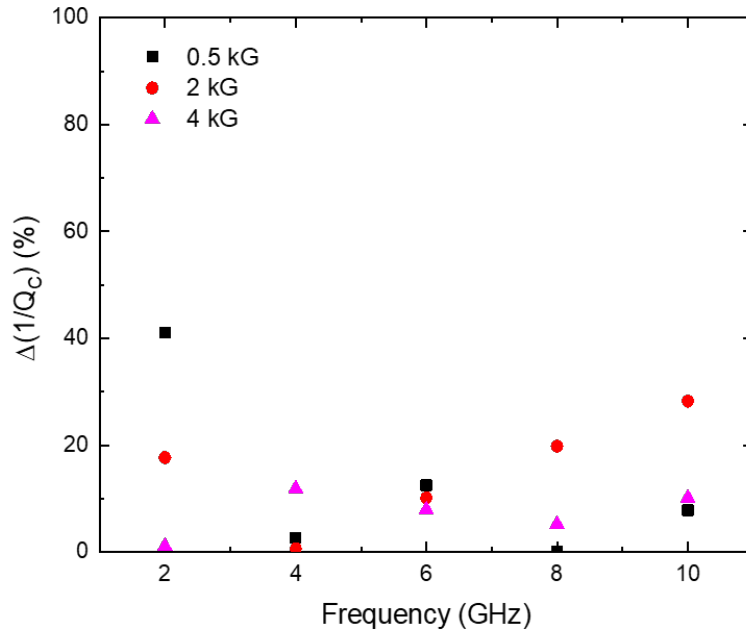


Figure 5.62. Percentage change of $\Delta(1/Q_c)$ vs. frequency for non-embedded sample.

We also studied the effect of varying applied magnetic field on embedded resonator which was fabricated in the similar manner as non-embedded resonator but with an additional top PI encapsulating layer. Embedded resonator structure is more practical and robust as compared to non-embedded resonator structure. The sample was measured in LHe dewar at 4.2 K using all the three magnetic fixtures (shown previously). Fig. 5.63 shows the plot of $1/Q_l$ vs. T/T_c for the embedded resonator at multiple frequencies after baking the sample at 90 °C for 2 hr.

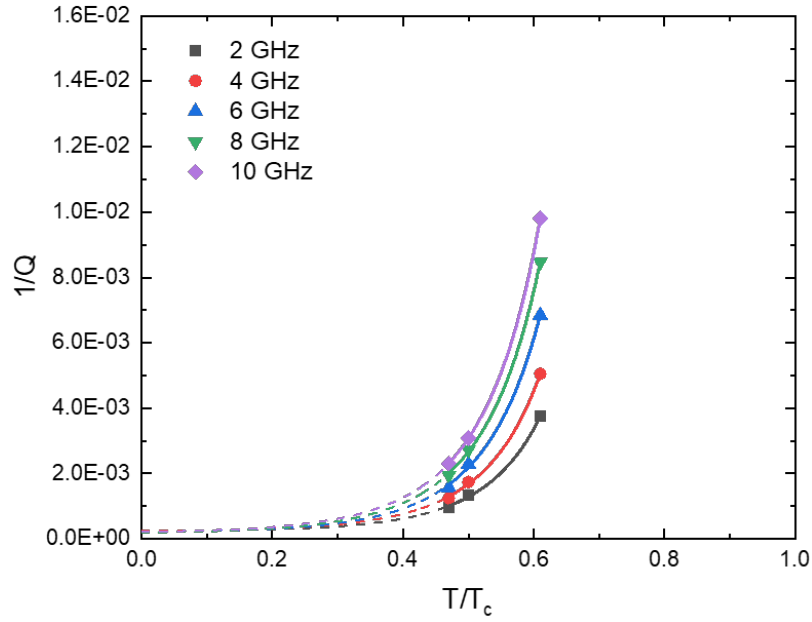


Figure 5.63. $1/Q_l$ vs. T/T_c for embedded sample. The sample was baked before making measurements.

Fig. 5.64 shows the plot of $1/Q_l$ vs. T/T_c for a embedded resonator at multiple frequencies prior to baking the sample.

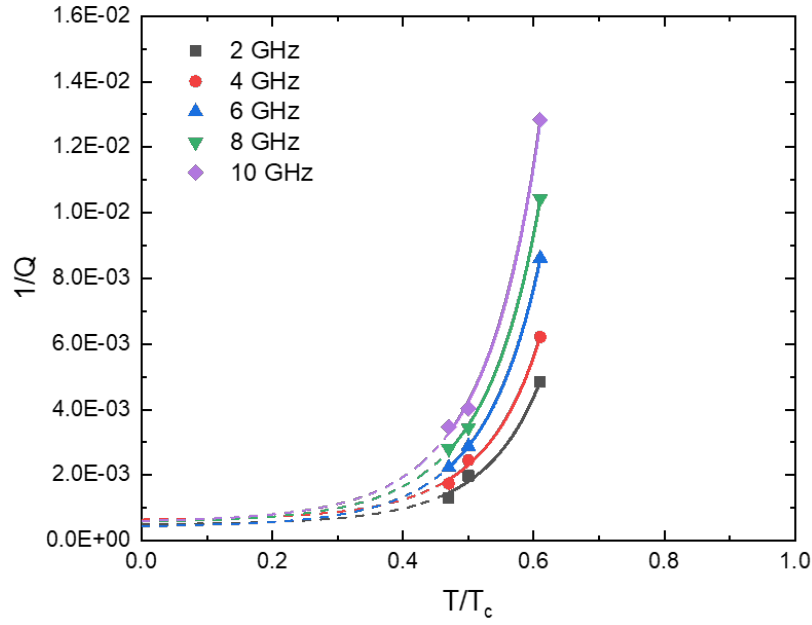


Figure 5.64. $1/Q_i$ vs. T/T_c for embedded sample. The sample was NOT baked before making measurements.

The data points for $1/Q_i$ vs. T/T_c were extrapolated to yield $1/Q_D$ values for different frequencies. Fig. 5.65 shows the plot $1/Q_D$ vs. frequency for the baked and not baked case.

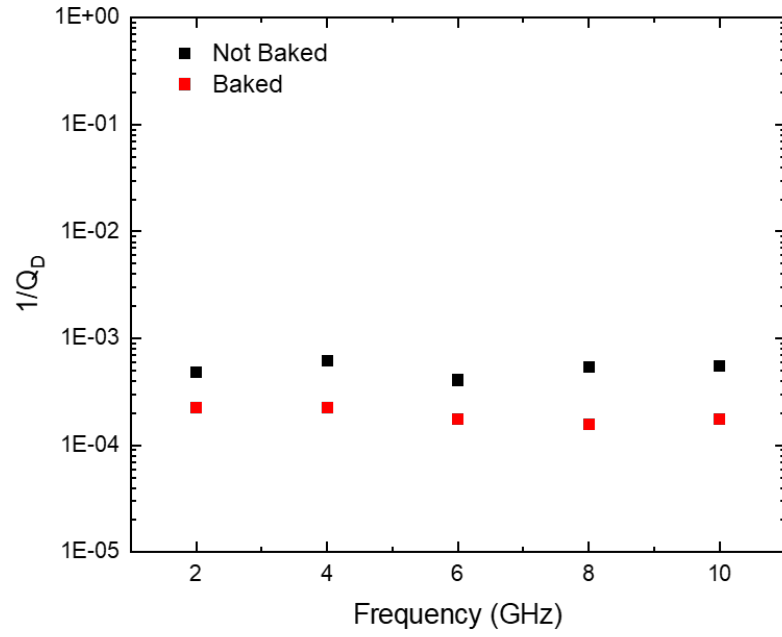


Figure 5.65. $1/Q_D$ vs. frequency for embedded sample.

Fig. 5.66 shows the difference in $1/Q_D$ values between the baked and not-baked cases.

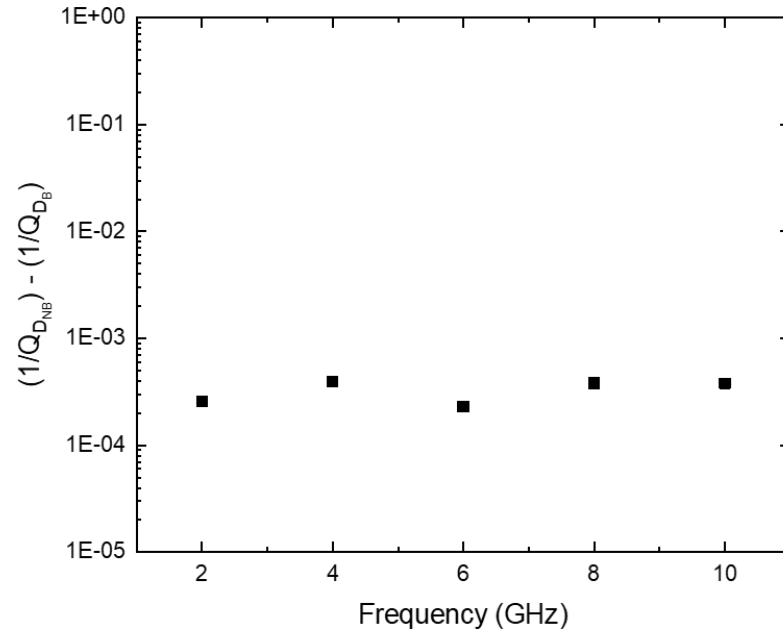


Figure 5.66. $1/Q_D$ vs. frequency for embedded sample. NB represents not baked and B represents baked.

Fig. 5.67 shows the percentage change in the dielectric loss as an effect of baking prior to making measurement.

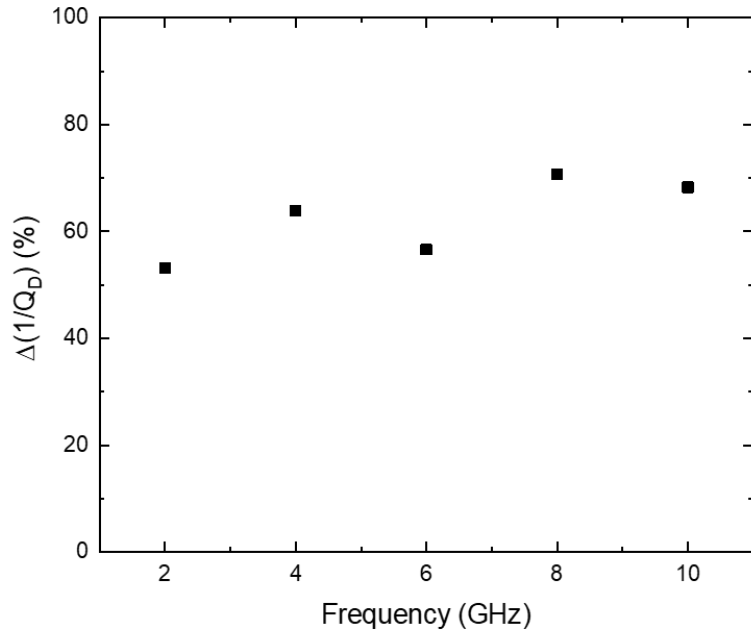


Figure 5.67. Percentage change of $\Delta(1/Q_D)$ vs. frequency for embedded sample.

Using Eq. 5.13 the loss tangent was calculated for embedded resonators. Fig. 5.68 shows the plot $\tan\delta$ vs. frequency for non-embedded resonators.

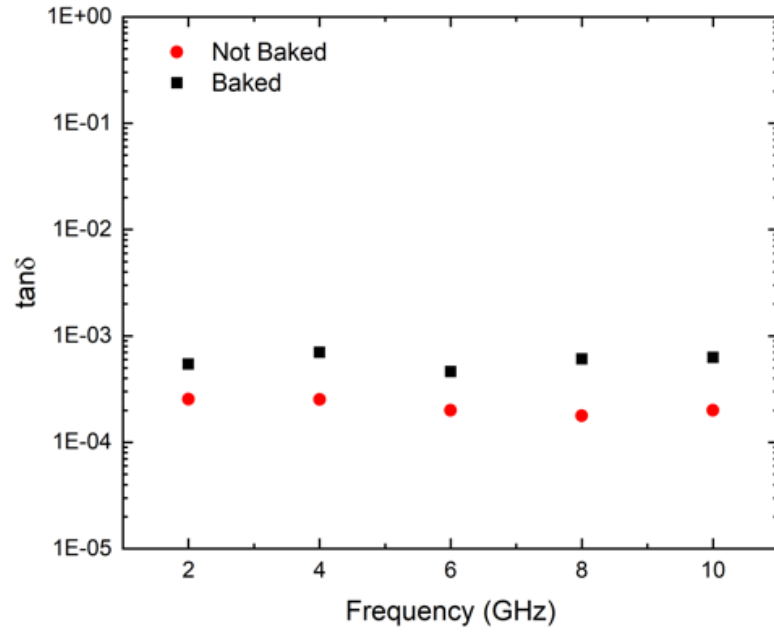


Figure 5.68. $\tan\delta$ vs. frequency for non-embedded sample.

Fig. 5.69 shows the difference in $\tan\delta$ values between the baked and not-baked cases.

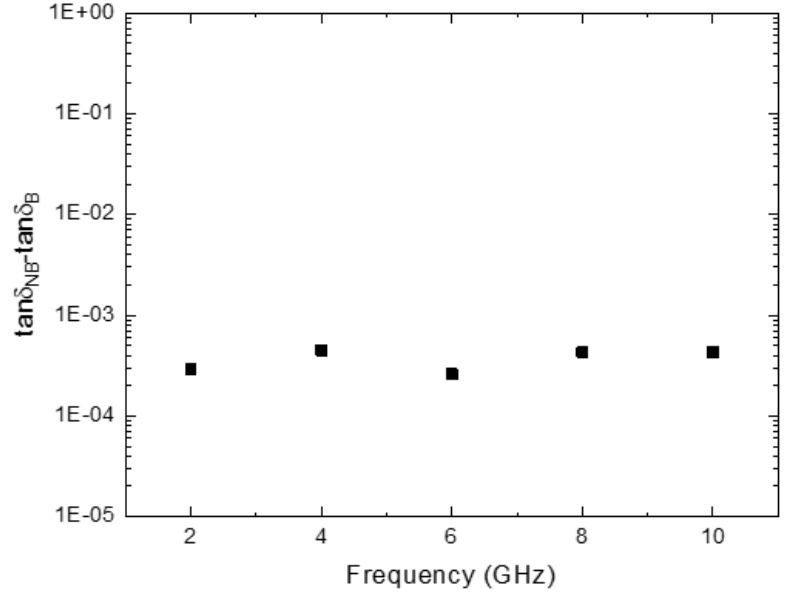


Figure 5.69. $\Delta \tan\delta$ vs. frequency for non-embedded sample. NB represents not baked and B represents baked.

Fig. 5.70 shows the percentage change in the $\tan\delta$ as an effect of baking prior to making measurement.

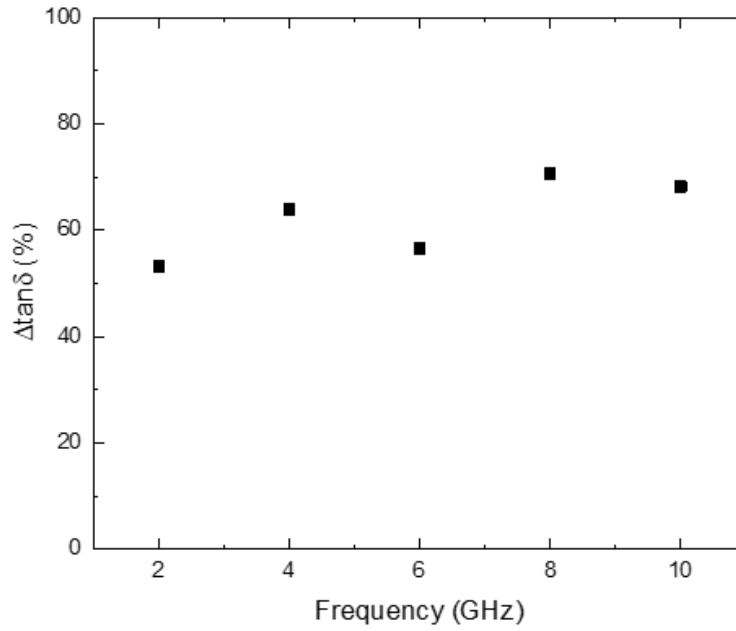


Figure 5.70. Percentage change of $\Delta \tan \delta$ vs. frequency for non-embedded sample.

Similar to the case of non-embedded sample, $1/Q_c$ was calculated using Eq. 5.21. Fig. 5.71 shows the plot of $1/Q_c$ vs. frequency for the embedded sample. A small variance was observed in the conductor loss as an effect of baking the sample.

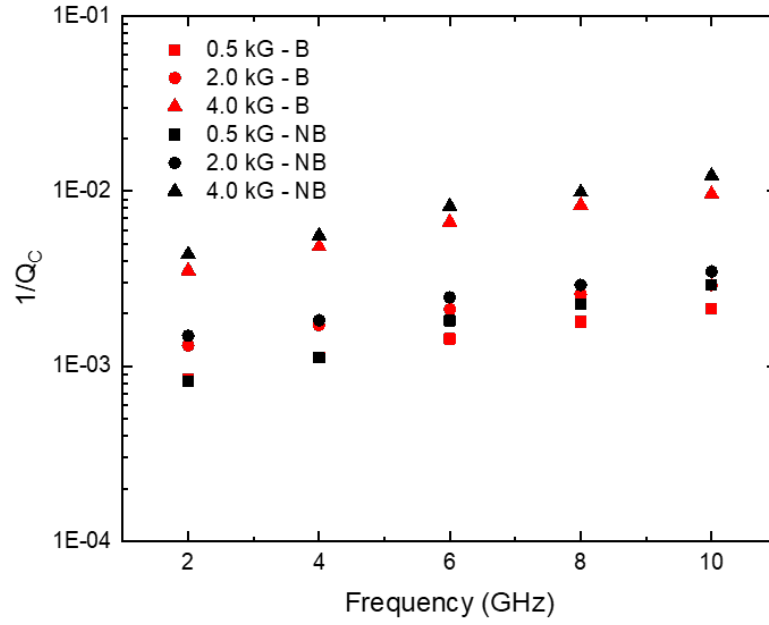


Figure 5.71. $1/Q_c$ vs. frequency for embedded sample. NB represents not baked and B represents baked.

Fig. 5.72 shows the difference in $1/Q_c$ values between the baked and not-baked cases for the embedded resonator.

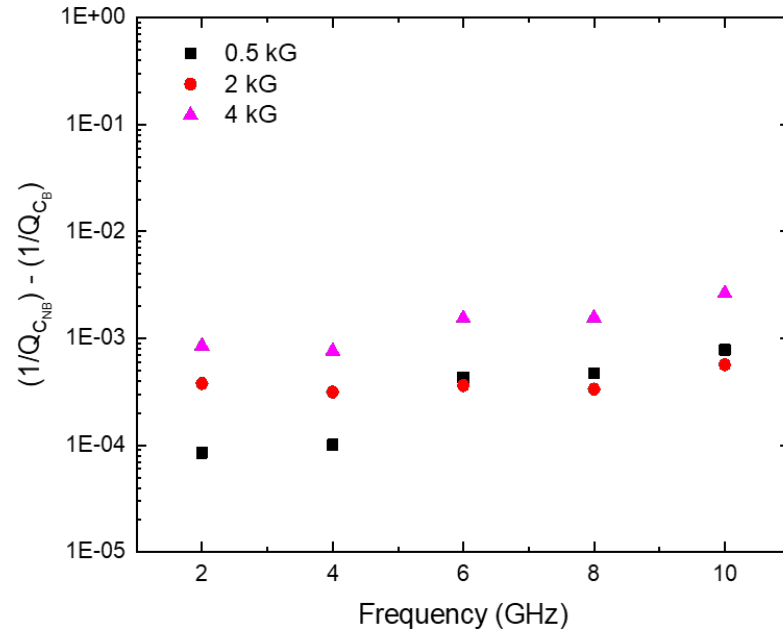


Figure 5.72. $1/Q_c$ vs. frequency for embedded sample. NB represents not baked and B represents baked.

Fig. 5.73 shows the percentage change in the conductor loss as an effect of baking prior to making measurement for the embedded resonators.

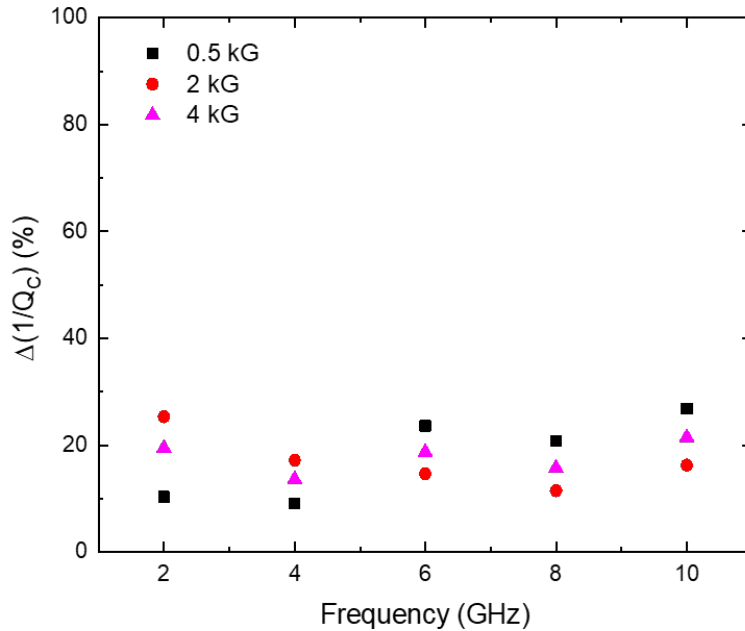


Figure 5.73. Percentage change of $\Delta(1/Q_c)$ vs. frequency for embedded sample.

In this section, the conductor loss and dielectric loss are separated using microstrip resonators in presence of an external magnetic field. We have successfully extracted $1/Q_D$ and used that to calculate $1/Q_c$ by subtracting $1/Q_D$ from $1/Q_l$. The effect of baking to lower the humidity is demonstrated by using both embedded and non-embedded resonator structures. Essentially, baking the sample leads to evaporation of moisture in the dielectric which yields a higher Q_l whereas not baking the sample increases humidity in the sample and lowers Q_l . We have demonstrated that the extra loss in the case of not baked samples comes mainly from the dielectric loss and has minimal effect on the conductor loss.

5.5 Surface Resistance Analysis for Resonator Structures Cured at Multiple Temperatures

For direct current (DC) applications, the conventional superconductors show no energy dissipation, whereas in the case of alternating currents (AC) a finite resistance is observed at

temperatures below T_c . This response of a superconductor in the presence of AC fields is well understood by complex surface impedance (Z_s) according to two-fluid model (expressed in Eq. 5.24). One of the most common application of R_s is in SRF, due to its dependence on the cavity quality factor [51–55]. Several groups have been working on ways to reduce R_s in order to get a higher Q -value for their SRF cavity [56–59] .

$$Z_s = R_s + jX_s \quad (5.24)$$

The surface resistance (R_s) represents the dissipation and the surface reactance (X_s) represents the field screening of superconductors. R_s can be expressed as:

$$R_s = \frac{\Gamma}{Q} \quad (5.25)$$

Γ is a geometry factor and Q is the measured quality factor. To obtain Γ , the following set of equations were followed [60].

$$\omega' = \omega + \frac{t}{h} [\ln(\frac{2h}{t} + 1)] \quad (5.26)$$

$$B = 1 - \frac{\omega'^2}{16h^2} \quad (5.27)$$

$$C = \frac{1}{h} (1 - \frac{t}{\omega'h}) \quad (5.28)$$

$$D = \frac{2}{\omega'} [1 + \frac{1}{\pi} \ln(\frac{2h}{t})] \quad (5.29)$$

$$\Gamma = \frac{4\pi^2 Z_0}{\lambda_g B(2C + D)} \quad (5.30)$$

In the above equations, ω represents the width of the microstrip resonator line, h represents the thickness of the substrate, t represents the thickness of the conductor, Z_0 is the characteristic impedance of the microstrip resonator and λ_g represents the guided wavelength.

In order to characterize the surface resistance, three different configuration of microstrip resonators were used - non-embedded, embedded, embedded with Al_2O_3 barrier layer. The fabrication process and stack ups of these three resonators structures were discussed in detail in the previous sections. Each resonator stack up was exposed to elevated temperatures of 225 °C, 250 °C and 275 °C. R_s was calculated for each resonator structures at each frequency, based on the Q_l values shown in section 5.2.

Fig. 5.74, 5.75 and 5.76 shows the R_s vs. temperature plots for embedded resonator at multiple frequencies. From all the R_s plots shown below, it can be seen that R_s has an exponential dependence on temperature. This indicates an exponential fall in the density of normal electrons by a factor of $e^{\frac{-\Delta}{k_b T}}$ (shown in Eq. 5.17).

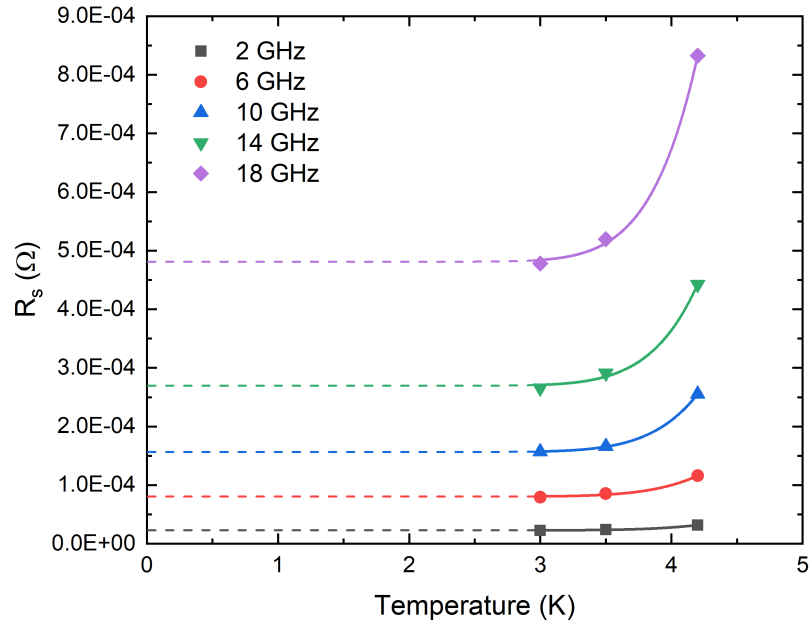


Figure 5.74. Surface resistance vs. temperature for embedded sample cured at 225 °C.

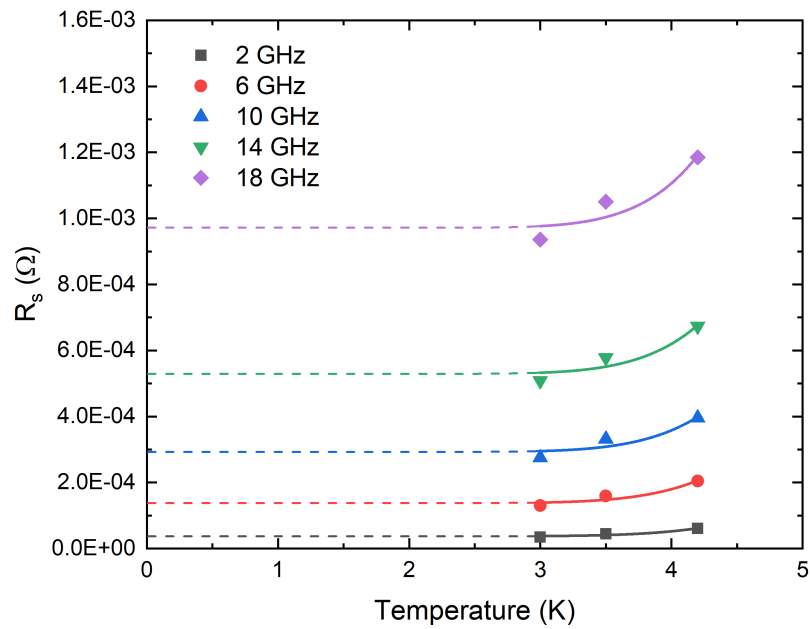


Figure 5.75. Surface resistance vs. temperature for embedded sample cured at 250 °C.

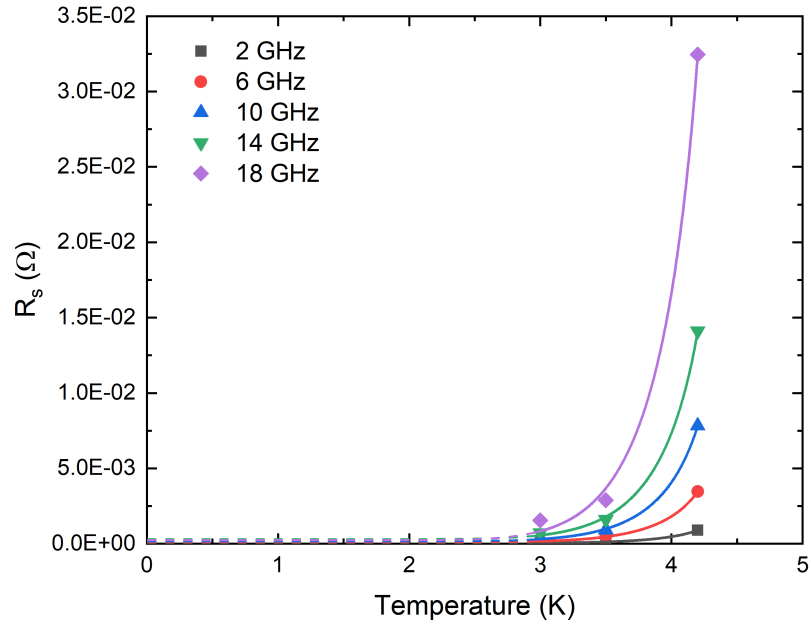


Figure 5.76. Surface resistance vs. temperature for embedded sample cured at 275 °C.

Figs. 5.77, 5.78 and 5.79 shows the R_s vs. temperature plots for non-embedded resonator measured at multiple frequencies.

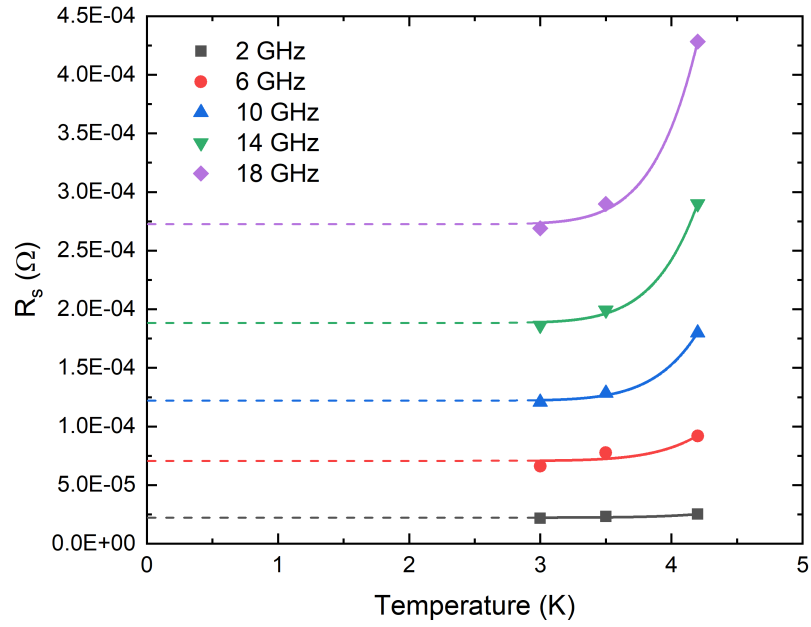


Figure 5.77. Surface resistance vs. temperature for non-embedded sample cured at 225 °C.

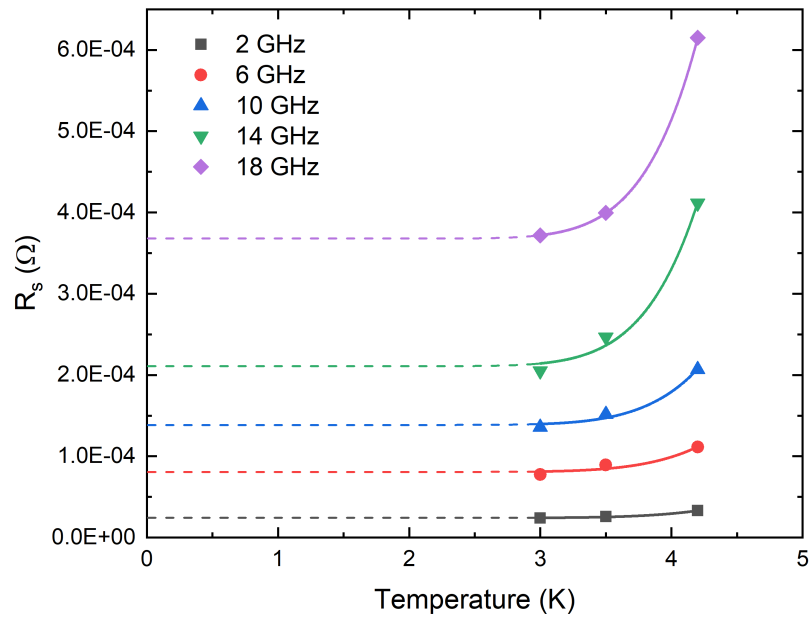


Figure 5.78. Surface resistance vs. temperature for non-embedded sample cured at 250 °C.

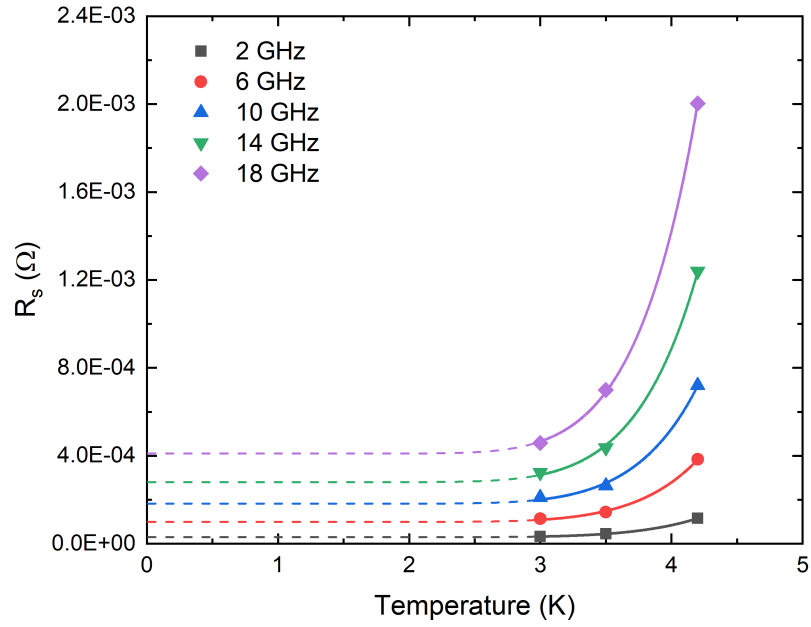


Figure 5.79. Surface resistance vs. temperature for non-embedded sample cured at 275 °C.

Figs. 5.80, 5.81 and 5.82 shows the R_s vs. temperature plots for the embedded resonator with a barrier layer of Al_2O_3 measured at multiple frequencies.

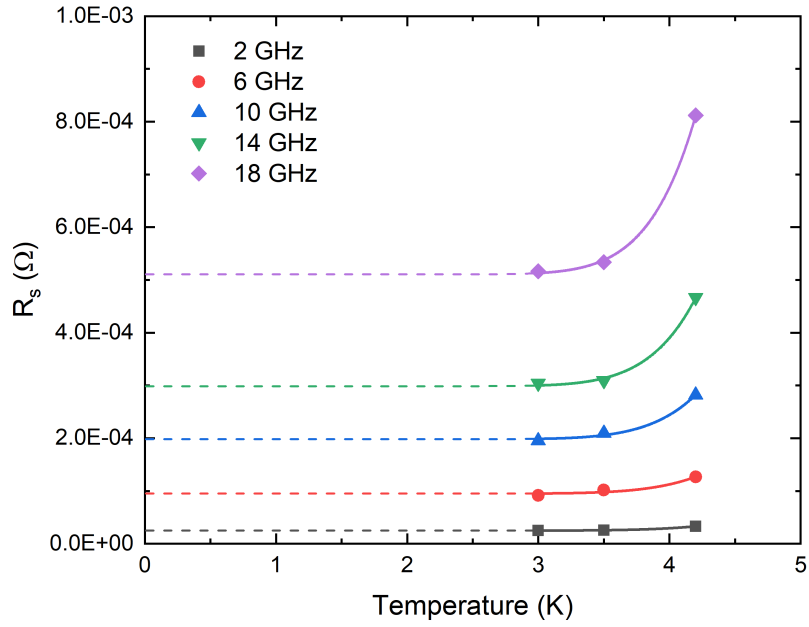


Figure 5.80. Surface resistance vs. temperature for $\text{Al}_2\text{O}_3/\text{Nb}/\text{Al}_2\text{O}_3$ sample cured at 225 °C.

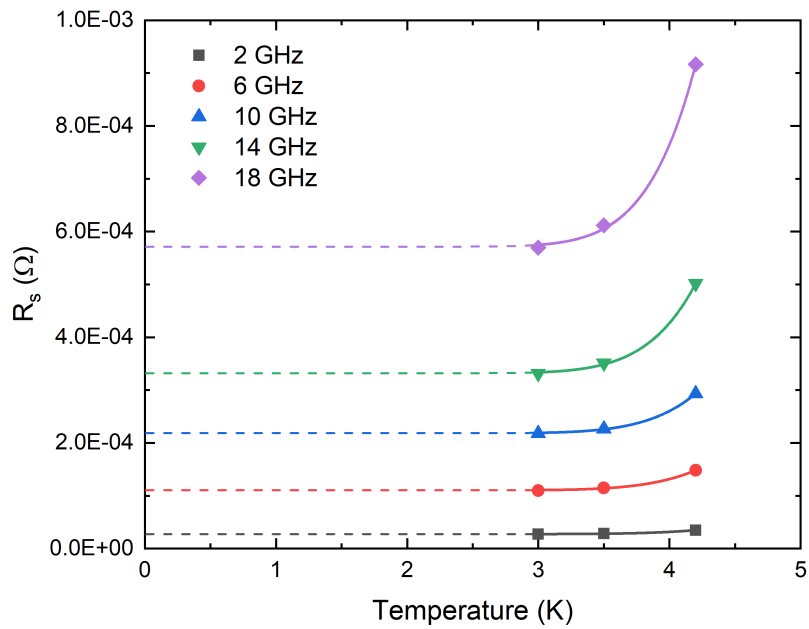


Figure 5.81. Surface resistance vs. temperature for $\text{Al}_2\text{O}_3/\text{Nb}/\text{Al}_2\text{O}_3$ sample cured at 250 °C.

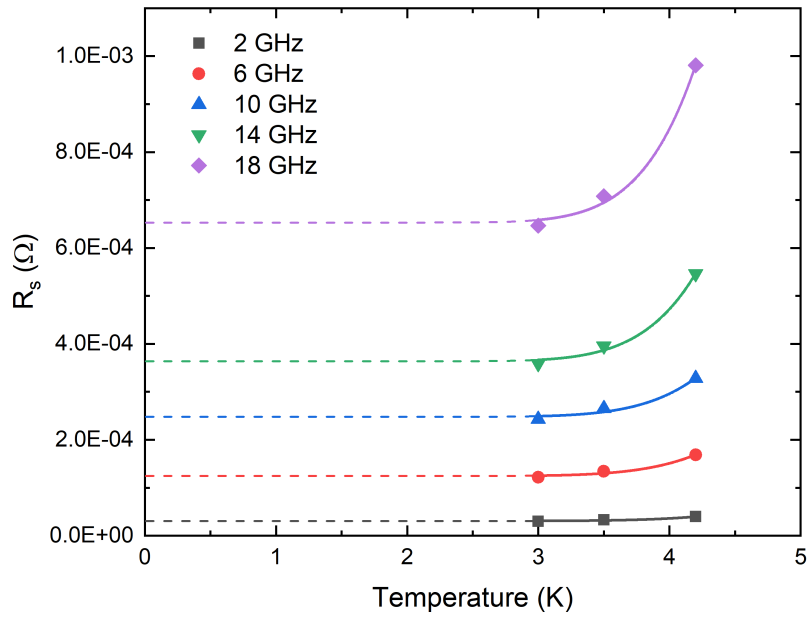


Figure 5.82. Surface resistance vs. temperature for $\text{Al}_2\text{O}_3/\text{Nb}/\text{Al}_2\text{O}_3$ sample cured at 275 °C.

5.5.1 Residual Resistance

One of the main factor that contributes to R_{res} is the surface contamination, possibly due to formation of surface oxides in case of Nb. Some other causes for R_{res} include surface roughness, grain boundaries and trapped flux. Residual resistance (R_{res}) was extracted by extrapolating the exponential fits of the data shown in R_s plots to 0 K temperature for each resonator structure. An increase in the intercept point was observed with increasing frequency, suggesting that the R_{res} increases with increasing frequency. It is evident that for all three resonator cases the R_{res} increases with the increase in curing temperature. Fig. 5.83 shows the plot of R_{res} vs. frequency for embedded resonator structure cured at multiple temperatures.

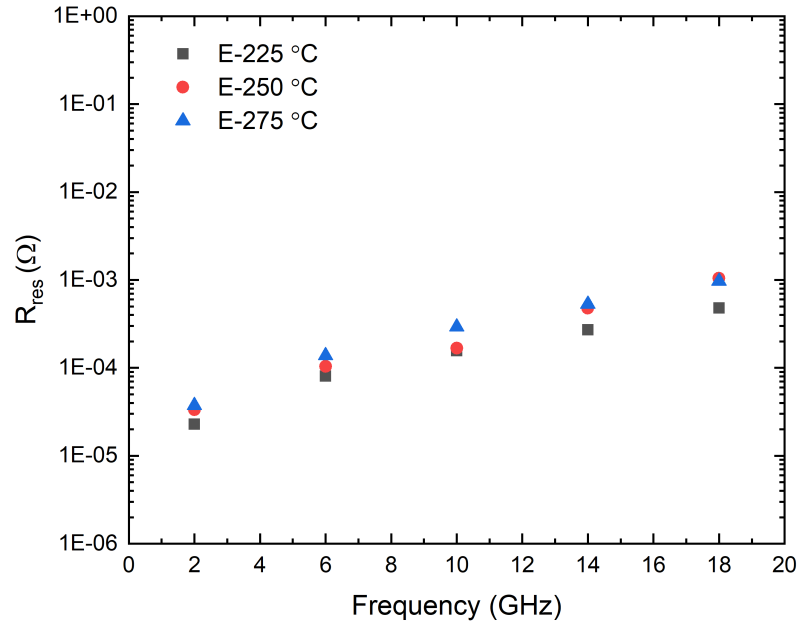


Figure 5.83. Residual resistance vs. frequency for embedded resonator structure cured at multiple temperatures.

Fig. 5.84 shows the plot of R_{res} vs. frequency for non-embedded resonator structure cured at multiple temperatures.

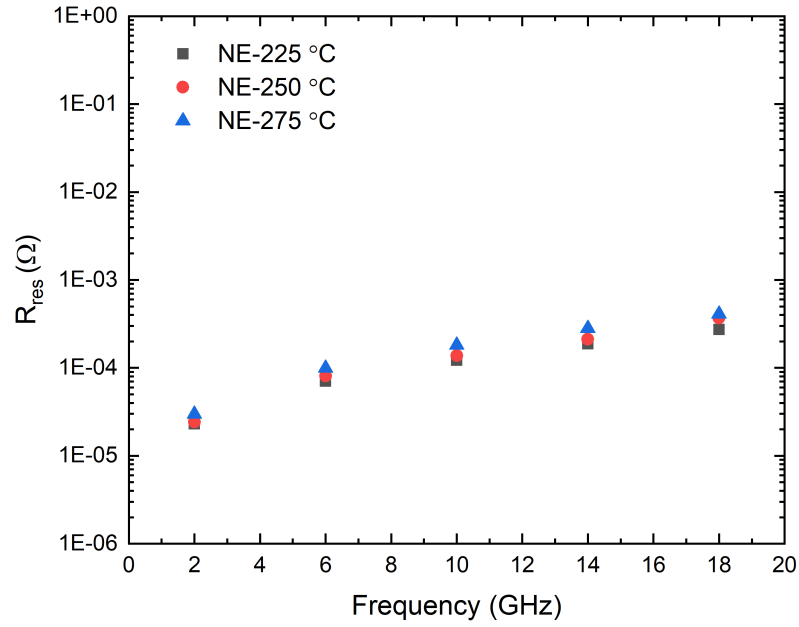


Figure 5.84. Residual resistance vs. frequency for non-embedded resonator structure cured at multiple temperatures.

Figs. 5.85 shows the plot of R_{res} vs. frequency for embedded resonator structure with a barrier layer of Al_2O_3 cured at multiple temperatures.

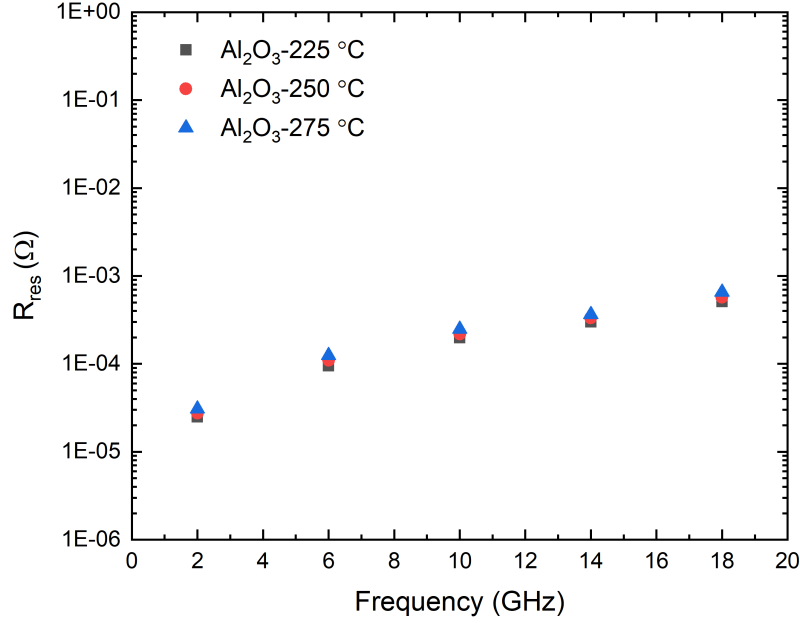


Figure 5.85. Residual resistance vs. frequency for embedded resonator structure with a barrier layer of Al_2O_3 cured at multiple temperatures.

5.5.2 BCS Resistance

R_s is a combination of superconducting resistance (R_{BCS}) and R_{res} , written in an equation form below. R_{BCS} is calculated at 4.2 K for each resonator type by subtracting the extracted R_{res} from R_s .

$$R_s = R_{res} + R_{BCS} \quad (5.31)$$

A clear trend of increased BCS resistance can be seen when all the resonator samples were exposed to elevated temperatures. This increase in R_{BCS} is due to the degradation of Nb as a conductor at higher temperatures [8, 9]. Fig. 5.86 shows the plot of R_{BCS} vs. frequency for embedded resonator structure cured at multiple temperatures.

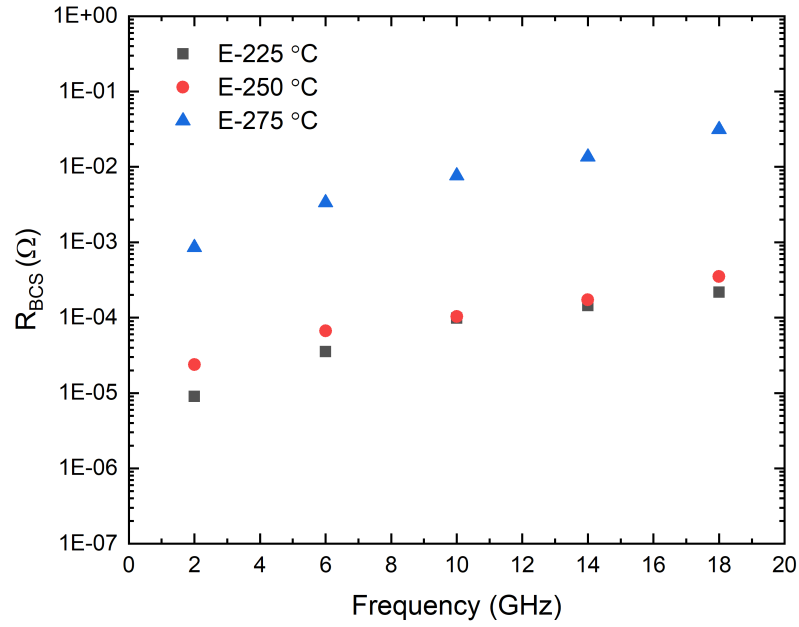


Figure 5.86. BCS resistance vs. frequency for embedded resonator structure cured at multiple temperatures. The plot shows measurement at 4.2 K.

Fig. 5.87 shows the plot of R_{BCS} vs. frequency for non-embedded resonator structure cured at multiple temperatures.

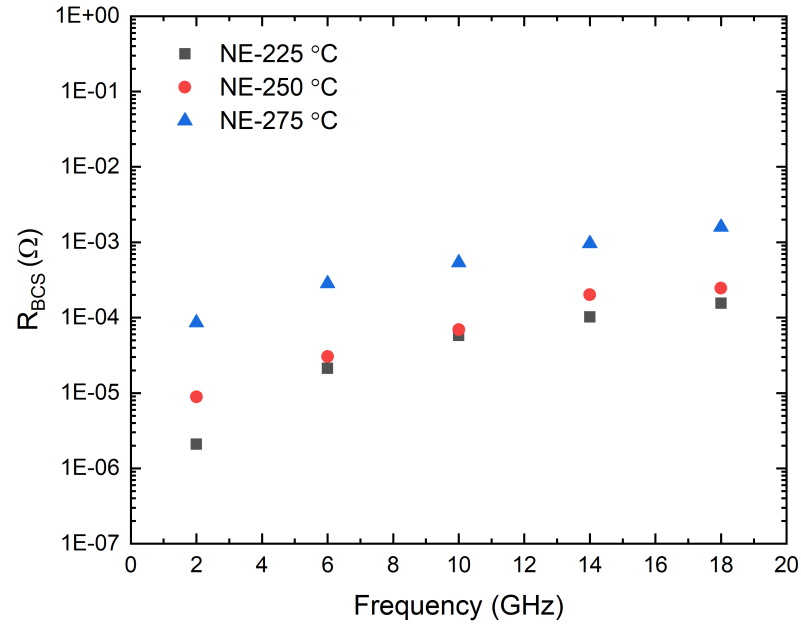


Figure 5.87. BCS resistance vs. frequency for non-embedded resonator structure cured at multiple temperatures. The plot shows measurement at 4.2 K.

Fig. 5.88 shows the plot of R_{BCS} vs. frequency for embedded resonator structure with a barrier layer of Al_2O_3 cured at multiple temperatures.

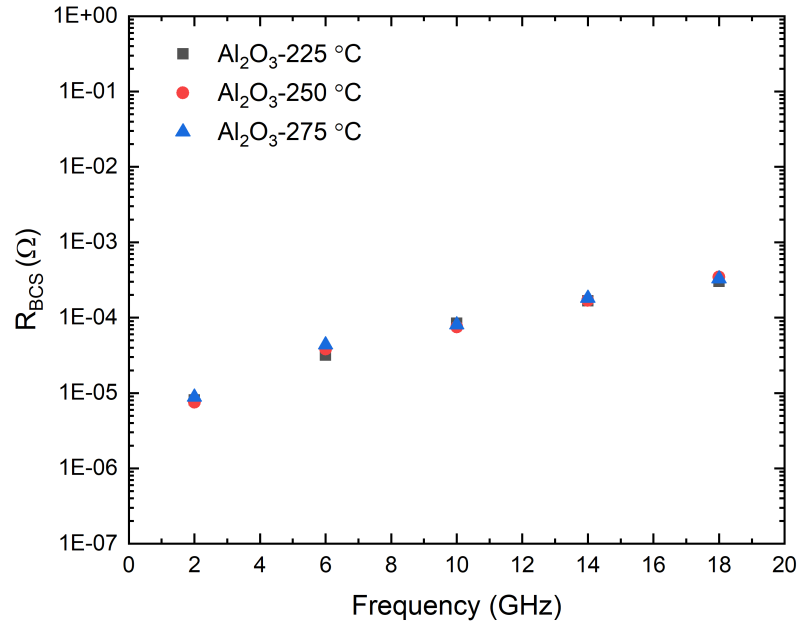


Figure 5.88. BCS resistance vs. frequency for embedded resonator structure with a barrier layer of Al_2O_3 cured at multiple temperatures. The plot shows measurement at 4.2 K.

The following plots were generated to better compare the BCS resistance of all resonator structures at different curing temperatures. Fig. 5.89 shows the measurement results of the R_{BCS} vs. frequency for all resonator structures cured at 225 °C.

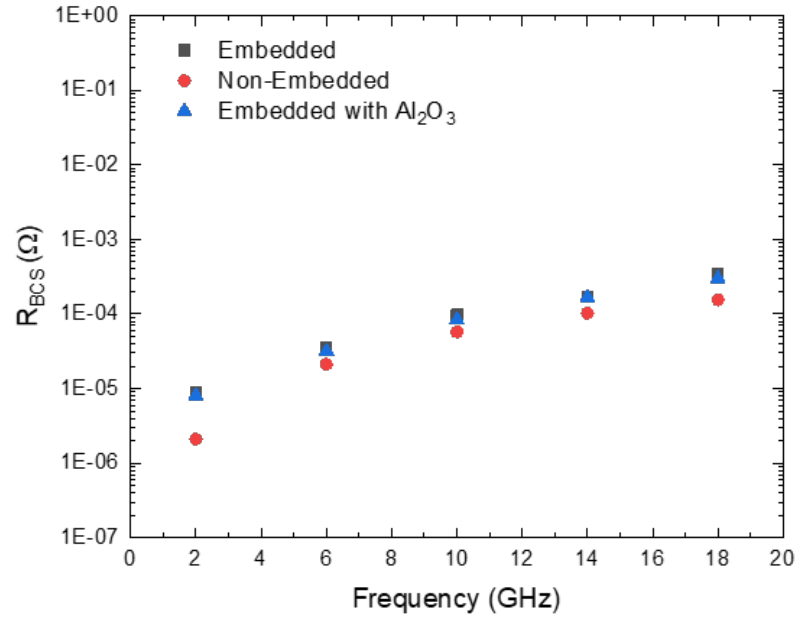


Figure 5.89. BCS resistance vs. frequency for all resonator structures cured at 225 °C.

Fig. 5.90 shows the measurement results of the R_{BCS} vs. frequency for all resonator structures cured at 250 °C.

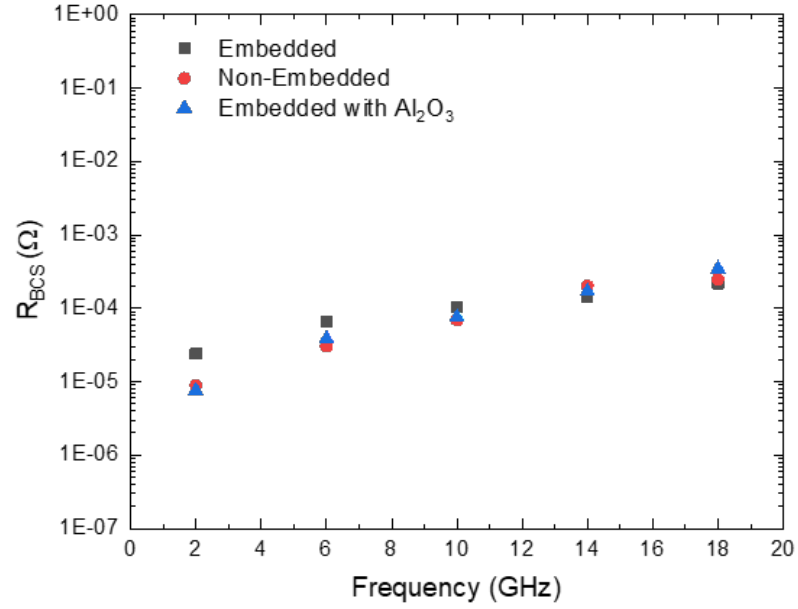


Figure 5.90. BCS resistance vs. frequency for all resonator structures cured at 250 °C.

Fig. 5.91 shows the measurement results of the R_{BCS} vs. frequency for all resonator structures cured at 275 °C.

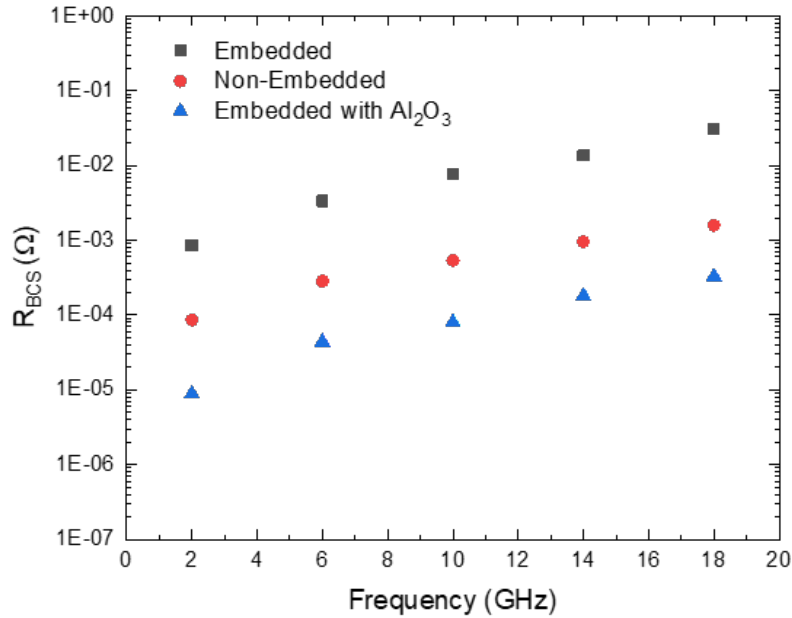


Figure 5.91. BCS resistance vs. frequency for all resonator structures cured at 275 °C.

In this work, we have demonstrated that all the the resonator structures show comparable values of R_{BCS} after being exposed to temperatures of 225 °C and 250 °C, but a significant increase in the R_{BCS} was observed for embedded and non-embedded resonator structures, after curing the same structures at 275 °C. Whereas in the case of resonator with Al_2O_3 barrier layer, very little increase in the R_{BCS} was observed after subjecting the resonator to temperature of 275 °C. This demonstrates that Al_2O_3 is a potentially promising material to protect Nb superconductivity at temperatures higher than 250 °C.

Chapter 6

Summary and Conclusion

In this work, thin-film Nb-based superconducting flexible cables were presented. The main purpose of building these cables was to minimize thermal load and space inside a cryogenic system. A spin-on polyimide, which acts as an insulating and passivation layer, was used as a flexible substrate. Several polymers such as PI-2611, HD-4110 and HD-4100 by HD-Microsystems were explored.

As a part of the work presented, I have investigated multiple material stack ups to minimize degradation of Nb superconducting properties when subjected to high temperatures during subsequent fabrication processes, such as the curing of passivating polyimide layer at 350 °C. Multiple tests were performed to come up with an effective barrier layer to protect Nb from subsequent high temperature steps for multi-layer structures. A thin-layer of Al was demonstrated as a good barrier layer since it did not degrade the high frequency signal propagation due to microwave skin effects or proximity effects. We also investigated Al₂O₃ as a thin interface material between Nb and polyimide. It was deposited using a relatively low temperature thermal atomic layer deposition (ALD) process to preserve the superconducting properties of the Nb layer. As an alternate solution to preserve Nb superconductivity, we cured polyimide at the lower temperature of 225 °C and observed promising results. Results of these experiments provide insight into material stack-ups and fabrication process options for robust, multi-layer superconducting flexible structures such as embedded microstrips, striplines etc.

Design, fabrication, and characterization of thin film superconducting stripline transmission line and resonator were presented. Al/Nb/Al stack-ups were used as conductor layers and HD-4110 was used as polyimide dielectric layers. We measured T_c as high as 8.8 K

and 8.6 K for signal and ground traces respectively. The stripline transmission lines showed reasonable match for S_{11} (reflections) of ~ -15 dB and S_{21} (insertion loss) of less than 0.5 dB (~ 0.04 dB/cm). We also measured near-end and far-end cross talk, which was typically near or below -60 dB up to 10 GHz. For DC measurements, a pulse-tube cryostat was used, and the RF measurements were carried out in LHe dewar with frequencies up to 10 GHz. Superconducting stripline resonators, fabricated in the same manner as the transmission line, were characterized at multiple temperatures up to 14 GHz. The resonators were baked at 90 °C prior to loading in the PT cryostat for measurements. We obtained high quality factors of the order of 7000 at 10 GHz and 1.2 K. The results of this work showed that superconducting, flexible cables with multiple layers can be fabricated in stripline configuration (ground-signal-ground) that is robust enough to withstand multiple elevated temperature processing steps.

Embedded microstrip transmission line structures were used to optimize the connector transition regions by minimizing capacitive discontinuities. We have essentially used anti-pads at each end of the transmission line where the signal pin of the SMA connector touches the pads on the samples to cancel out the extra capacitance. Several anti-pad designs were fabricated such as - $132 \mu\text{m} \times 1200\mu\text{m}$, $176 \mu\text{m} \times 1200\mu\text{m}$ and $220 \mu\text{m} \times 1200\mu\text{m}$. S_{21} was measured for all the respective anti-pad dimensions and it was observed that the microstrip with the anti-pad size of $176 \mu\text{m} \times 1200\mu\text{m}$ showed the least amount of oscillations (hence lower capacitive discontinuities) in the insertion loss.

In order to have a better understanding of internal loss mechanism contributing to microwave losses, weakly coupled microstrip SC resonator structures were fabricated. Different configurations for the microstrip resonator structure were tested, including embedded, non-embedded and embedded with Al_2O_3 barrier layer. All the resonator structures were exposed to elevated temperatures of 225 °C, 250 °C and 275 °C. Q_l was measured after each temperature cycle for all resonators. All the samples were measured in PT cryostat at multiple temperatures. We demonstrate the degradation in T_c after each temperature cycle

for each resonator type and also present the effectiveness of using Al_2O_3 as a barrier layer for minimizing Nb degradation. We further used these resonator structures to plot $1/Q_l$ vs. temperature and used an exponential fit to signify the exponential drop in number of normal electrons as the temperature is lowered. We were able to extract the dielectric loss ($1/Q_D$) using the exponential extrapolation at $T=0$ K. Conductor loss ($1/Q_c$) was calculated using the Eq. 5.11. In addition to this, we also studied the effect of external magnetic field on all these different resonator structures. In particular, we built three fixtures to apply different magnetic field strength on the sample - 0.5 kG, 2 kG and 4 kG. From the applied magnetic field strength, the suppression in T_c was calculated using Eq. 5.23. The measurements were performed in LHe dewar for each magnetic field strength case. We were able to extract $1/Q_D$ by extrapolation to $T=0$ K from the $1/Q_l$ vs. T/T_c plot. Similar to the previous case, $1/Q_c$ was calculated using the Eq. 5.11.

Finally, surface resistance analysis was performed for all three resonator structures. Based on the geometry and the measured quality factor, R_s was calculated for each resonator structure. We determined R_{res} by using Eq. 5.17, which was essentially the extrapolated intercept for R_s as a function of temperature. R_{BCS} was calculated using the Eq. 5.31 for all the resonator structures.

Chapter 7

Future Work

In this work we have mainly focused on designing and fabricating superconducting cables for use in cryogenic applications, but there is still a vast scope for further extension to these cables for use in the quantum industry.

In order to optimize the functionality in quantum computer, highly densely integrated superconducting cables with low loss and better EM shielding are preferred. Based on our stripline fabrication technique shown in section 4 that resulted in a low cross-talk, multiple parallel signal lines with proper isolation could be placed on a single substrate. In order to further lower the microwave losses, other dielectrics such as benzocyclobutene (BCB), spin on glass (SOG) and HD-8000 etc. could be used to fabricate similar structures and dielectric losses could be extracted and compared using the analysis presented in this work.

There has been a rapid development in the advancement of quantum integrated circuits [?,61–63]. To transmit microwave signal from room temperature to various stages of dilution refrigerator, a reliable and stable implementation of cryo-packaging with dense interconnects is needed. Flip-chip bonding of chip-to-chip or chip-to-flex can improve the scalability aspect of quantum integrated circuits.

Thermalization has been a topic of discussion for decades. Several groups have made significant progress to understand the effect of thermalization in quantum symptoms [64–68]. Thermalization essentially refers to thermal equilibrium in isolated symptoms. Using materials that can reduce thermalization are desired. Molybdenum (Mo) is viable choice for substrate to improve thermal leakage. Microwave structures such as transmission lines and resonators can be fabricated and measured in a similar fashion on Mo substrate as presented in this work, to understand the thermalization behavior of different materials.

Another area that needs some improvement is optimization of RF/microwave cables using other superconducting materials such as NbTi and NbTiN. Significant effort has been made by several groups to fabricate NbTi ribbon cables to work at millikelvin (mK) temperatures for frequencies up to (20 GHz) [69–72]. The key properties that make NbTi a good contender for use in various superconducting cables are: non-magnetic, high heat capacity, relatively low thermal conductivity and low ductility. It can also support high critical current and critical fields at 4.2 K. Fabricating and testing these cables comprised of NbTi will provide useful insight into future generations of superconducting RF cables.

Bibliography

- [1] U. of York, “Temperature variation of electrical resistance of a superconductor.” [Online]. Available: <https://www.york.ac.uk/media/physics/publicandschools/Temperature%20variation%20of%20electrical%20resistance%20of%20a%20superconductor%20-%20NEW.pdf>
- [2] G. S. University, “Hyperphysics.” [Online]. Available: <http://hyperphysics.phy-astr.gsu.edu/hbase/Solids/scbc.html>
- [3] M. Academy, “Superconductivity 101.” [Online]. Available: <https://nationalmaglab.org/education/magnet-academy/learn-the-basics/stories/superconductivity-101>
- [4] A. A. Circuits, “Symmetric stripline impedance calculator.” [Online]. Available: <https://www.allaboutcircuits.com/tools/symmetric-stripline-impedance-calculator/>
- [5] A. Point, “About bcs theory.” [Online]. Available: <https://www.assignmentpoint.com/science/physics/about-bcs-theory.html>
- [6] S. M. Anlage, “Fundamentals of microwave superconductivity.” [Online]. Available: <http://anlage.umd.edu/Anlage%20ASC2002%20SCandCryoMicroSub%20Tutorial%20Talk.pdf>
- [7] C. P. Poole, R. Prozorov, H. A. Farach, and R. J. Creswick, “Phenomenon of superconductivity,” in *Superconductivity*, third edition ed., C. P. Poole, R. Prozorov, H. A. Farach, and R. J. Creswick, Eds. London: Elsevier, 2014, pp. 33–85. [Online]. Available: <https://www.sciencedirect.com/science/article/pii/B9780124095090000020>
- [8] M. P. Bruijn, A. J. Linden, M. L. Ridder, and H. J. Weers, “Fdm readout assembly with flexible, superconducting connection to cryogenic kilopixel tes detectors,” *Journal of Low Temperature Physics*, vol. 184, no. 1-2, pp. 369–373, 2016.
- [9] H. van Weers, G. Kunkel, M. Lindeman, , and M. Leeman, “Niobium flex cable for low temperature high density interconnects,” *Cryogenics*.
- [10] R. U. S. Labratory. Time-of-flight secondary ion mass spectrometry laboratory. [Online]. Available: <http://simslab.rice.edu/surface-analysis-lab/teaching-activities-resources/time-of-flight-secondary-ion-mass-spectrometry/>
- [11] D. K. Misra, *Radio-frequency and microwave communication circuits: analysis and design*. Wiley Online Library, 2004.

- [12] D. M. Pozar, "Microwave engineering," *Fourth Editions, University of Massachusetts at Amherst, John Wiley & Sons, Inc*, pp. 26–30, 2012.
- [13] H. health and technology matters, "Intelligibility vs. bandwidth." [Online]. Available: <https://hearinghealthmatters.org/waynesworld/2014/intelligibility-vs-bandwidth/>
- [14] Questions and A. in MRI, "Superconductivity." [Online]. Available: <http://mriquestions.com/superconductivity.html>
- [15] M. Groner, F. Fabreguette, J. Elam, and S. George, "Low-temperature al₂o₃ atomic layer deposition," *Chemistry of materials*, vol. 16, no. 4, pp. 639–645, 2004.
- [16] V. Naumann, M. Otto, R. Wehrspohn, M. Werner, and C. Hagendorf, "Interface and material characterization of thin ald-al₂o₃ layers on crystalline silicon," *Energy Procedia*, vol. 27, pp. 312–318, 2012.
- [17] S. Shi, S. Qian, X. Hou, J. Mu, J. He, and X. Chou, "Structural and optical properties of amorphous al₂o₃ thin film deposited by atomic layer deposition," *Advances in Condensed Matter Physics*, vol. 2018, 2018.
- [18] L. Gosset, J.-F. Damlencourt, O. Renault, D. Rouchon, P. Holliger, A. Ermolieff, I. Trimaille, J.-J. Ganem, F. Martin, and M.-N. Semeria, "Interface and material characterization of thin al₂o₃ layers deposited by ald using tma/h₂o," *Journal of non-crystalline solids*, vol. 303, no. 1, pp. 17–23, 2002.
- [19] J. Haeberle, K. Henkel, H. Gargouri, F. Naumann, B. Gruska, M. Arens, M. Tallarida, and D. Schmeißer, "Ellipsometry and xps comparative studies of thermal and plasma enhanced atomic layer deposited al₂o₃-films," *Beilstein journal of nanotechnology*, vol. 4, no. 1, pp. 732–742, 2013.
- [20] A. Abdulagatov, Y. Yan, J. Cooper, Y. Zhang, Z. Gibbs, A. Cavanagh, R. Yang, Y. Lee, and S. George, "Al₂o₃ and tio₂ atomic layer deposition on copper for water corrosion resistance," *ACS applied materials & interfaces*, vol. 3, no. 12, pp. 4593–4601, 2011.
- [21] T. Proslie, J. Zasadzinski, J. Moore, M. Pellin, J. Elam, L. Cooley, C. Antoine, J. Norem, and K. Gray, "Improvement and protection of niobium surface superconductivity by atomic layer deposition and heat treatment," *Applied Physics Letters*, vol. 93, no. 19, p. 192504, 2008.
- [22] T. Proslie, Y. Ha, J. Zasadzinski, G. Ciovati, P. Kneissel, C. Reece, R. Rimmer, A. Gurevich, L. Cooley, G. Wu *et al.*, "Atomic layer deposition for SRF cavities," Fermi National Accelerator Lab.(FNAL), Batavia, IL (United States), Tech. Rep. FERMILAB-PUB-09-714-TD, 2009.
- [23] J. Norem, M. Pellin, J. Elam, C. Antoine, L. Cooley, T. Proslie, J. Zasadzinski, R. Rimmer, and J. Moore, "Initial tests of atomic layer deposition (ALD) coatings for superconducting RF systems," Argonne National Laboratory (United States). Funding organisation: USDOE., Tech. Rep. ANL-HEP-CP-07-93, 2007.

- [24] C. Barbos, D. Blanc-Pelissier, A. Fave, C. Botella, P. Regreny, G. Grenet, E. Blanquet, A. Crisci, and M. Lemiti, "Al₂O₃ thin films deposited by thermal atomic layer deposition: Characterization for photovoltaic applications," *Thin Solid Films*, vol. 617, pp. 108–113, 2016.
- [25] V. Gupta, J. A. Sellers, C. D. Ellis, S. Zou, G. Hernandez, R. Bai, Y. Cao, D. B. Tuckerman, and M. C. Hamilton, "Preserving niobium superconductivity in thin-film superconducting flexible cables," *Additional Papers and Presentations*, vol. 2016, no. DPC, pp. 002 075–002 094, 2016.
- [26] V. Gupta, J. A. Sellers, C. D. Ellis, B. Yelamanchili, S. Zou, Y. Cao, D. B. Tuckerman, and M. C. Hamilton, "Minimizing film stress and degradation in thin-film niobium superconducting cables," vol. 2017, no. DPC, pp. 1–25, 2017.
- [27] S. Sheraz nee Rabbani, A. Barber, J. S. Fletcher, N. P. Lockyer, and J. C. Vickerman, "Enhancing secondary ion yields in time of flight-secondary ion mass spectrometry using water cluster primary beams," *Analytical chemistry*, vol. 85, no. 12, pp. 5654–5658, 2013.
- [28] T. B. Angerer, P. Blenkinsopp, and J. S. Fletcher, "High energy gas cluster ions for organic and biological analysis by time-of-flight secondary ion mass spectrometry," *International Journal of Mass Spectrometry*, vol. 377, pp. 591–598, 2015.
- [29] R. Peterson, A. Nair, S. Dambach, H. Arlinghaus, and B. Tyler, "Characterization of individual atmospheric aerosol particles with sims and laser-snms," *Applied surface science*, vol. 252, no. 19, pp. 7006–7009, 2006.
- [30] D. Touboul, F. Kollmer, E. Niehuis, A. Brunelle, and O. Lapr evote, "Improvement of biological time-of-flight-secondary ion mass spectrometry imaging with a bismuth cluster ion source," *Journal of the American Society for Mass Spectrometry*, vol. 16, no. 10, pp. 1608–1618, 2005.
- [31] R. B. Bass, L. T. Lichtenberger, and A. W. Lichtenbergers, "Effects of substrate preparation on the stress of Nb thin films," *IEEE Transactions on Applied Superconductivity*, vol. 13.
- [32] J. Liu, J. Li, T. Li, T. Li, W. Wu, and W. Chen, "Study of stress and morphology of superconducting niobium thin films," *IEEE Transactions on Applied Superconductivity*, vol. 19, no. 3, pp. 245–248, 2009.
- [33] D. W. Hoffman, "Perspective on stresses in magnetron-sputtered thin films," *Journal of Vacuum Science & Technology A: Vacuum, Surfaces, and Films*, vol. 12, no. 4, pp. 953–961, 1994.
- [34] D. B. Tuckerman, M. C. Hamilton, D. J. Reilly, R. Bai, G. A. Hernandez, J. M. Hornibrook, J. Sellers, and C. D. Ellis, "Flexible superconducting Nb transmission lines on thin film polyimide for quantum computing applications," *Superconductor Science and Technology*, no. 8, p. 084007, 2016.

- [35] G. A. Hernandez, R. Bai, Y. Cao, J. A. Sellers, C. D. Ellis, D. B. Tuckerman, and M. C. Hamilton, "Microwave performance of niobium/kapton superconducting flexible cables," *IEEE Transactions on Applied Superconductivity*, vol. 27, no. 4, pp. 1–4, 2017.
- [36] S. Zou, Y. Cao, G. Hernandez, R. Bai, V. Gupta, J. A. Sellers, C. D. Ellis, D. B. Tuckerman, and M. C. Hamilton, "Embedded niobium using pi-2611 for superconducting flexible cables," *MRS Advances*, vol. 2, no. 41, pp. 2199–2204, 2017.
- [37] R. Bai, G. A. Hernandez, Y. Cao, J. Sellers, C. D. Ellis, D. B. Tuckerman, and M. C. Hamilton, "Microwave loss measurements of copper-clad superconducting niobium microstrip resonators on flexible polyimide substrates." *IEEE Transactions on Applied Superconductivity*, vol. 27, no. 4, pp. 1–7, 2017.
- [38] V. Gupta, J. A. Sellers, C. D. Ellis, S. Zou, G. A. Hernandez, R. Bai, Y. Cao, D. B. Tuckerman, and M. C. Hamilton, "Barrier layers to protect Nb superconductivity in thin film superconducting flexible cables," in *Applied Superconductivity Conference*, Denver, CO, Sep. 4-9, 2016.
- [39] M. Bozack, S. Snipes, and G. Flowers, "Methods for fast, reliable growth of sn whiskers," *Surface Science*, vol. 652, pp. 355–366, 2016.
- [40] S. Metz, A. Bertsch, and P. Renaud, "Partial release and detachment of microfabricated metal and polymer structures by anodic metal dissolution," *J. Microelectromech. Syst.*, vol. 14, no. 2, pp. 383-391, 2005.
- [41] V. Gupta, B. Yelamanchili, S. Zou, T.-I. Smith, and J. A. Sellers, "Distinguishing dielectric loss from superconductor loss using flexible thin film superconducting resonator structures," pp. 1–1, 2019.
- [42] P. J. Petersan and S. M. Anlage, "Measurement of resonant frequency and quality factor of microwave resonators: Comparison of methods," *Journal of applied physics*, vol. 84, no. 6, pp. 3392–3402, 1998.
- [43] H. Padamsee, J. Knobloch, and T. Hays, "Rf superconductivity for accelerators john wiley & sons," *Inc., New York*, p. 199, 1998.
- [44] H. S. Padamsee, "Superconducting radio-frequency cavities," *Annual review of nuclear and particle science*, vol. 64, pp. 175–196, 2014.
- [45] A. Gurevich, "Multiscale mechanisms of srf breakdown," *Physica C: Superconductivity*, vol. 441, no. 1-2, pp. 38–43, 2006.
- [46] M. Checchin, M. Martinello, A. Romanenko, A. Grassellino, D. Sergatskov, S. Posen, O. Melnychuk, and J. Zasadzinski, "Quench-induced degradation of the quality factor in superconducting resonators," *Physical Review Applied*, vol. 5, no. 4, p. 044019, 2016.
- [47] K. Saito *et al.*, "Theoretical critical field in rf application," *KEK, Accelerator Lab*, pp. 1–1, 2003.

- [48] J. Knobloch and H. Padamsee, “Flux trapping in niobium cavities during breakdown events,” in *Proc. 8th Workshop on RF Superconductivity, Abano Terme, Italy*. Citeseer, 1997, p. 337.
- [49] I. Terechkine, T. Khabiboulline, and D. Sergatskov, “Performance degradation of a superconducting cavity quenching in magnetic field,” Fermi National Accelerator Lab.(FNAL), Batavia, IL (United States), Tech. Rep., 2013.
- [50] A. M. Kadin, *Introduction to superconducting circuits*. Wiley-Interscience, 1999.
- [51] J.-M. Vogt, O. Kugeler, and J. Knobloch, “Impact of cool-down conditions at t c on the superconducting rf cavity quality factor,” *Physical Review Special Topics-Accelerators and Beams*, vol. 16, no. 10, p. 102002, 2013.
- [52] P. Dhakal, G. Ciovati, P. Kneisel, and G. R. Myneni, “Superconducting dc and rf properties of ingot niobium,” *arXiv preprint arXiv:1202.0811*, 2012.
- [53] D. Hafner, M. Dressel, and M. Scheffler, “Surface-resistance measurements using superconducting stripline resonators,” *Review of Scientific Instruments*, vol. 85, no. 1, p. 014702, 2014.
- [54] G. Ciovati, R. Geng, J. Mammosser, and J. W. Saunders, “Residual resistance data from cavity production projects at jefferson lab,” *IEEE Transactions on applied superconductivity*, vol. 21, no. 3, pp. 1914–1917, 2010.
- [55] M. Ge, F. Furuta, M. Liepe, and G. Hoffstaetter, “Field-dependent surface resistance of a superconducting rf cavity caused by surface impurity,” *arXiv preprint arXiv:1507.08704*, 2015.
- [56] S. Keckert, J. Knobloch, O. Kugeler *et al.*, “Error analysis of surface resistance fits to experimental data,” in *Proc. of International Conference on RF Superconductivity (SRF’17), Lanzhou, China*, vol. 2018, 2017, pp. 859–862.
- [57] C.-J. Wu and T.-Y. Tseng, “Effective microwave surface impedance of superconducting films in the mixed state,” *IEEE transactions on magnetics*, vol. 33, no. 3, pp. 2348–2355, 1997.
- [58] R. D. Sherman, “Surface impedance theory for superconductors in large static magnetic fields,” Ph.D. dissertation, California Institute of Technology, 1971.
- [59] F. Palmer, “Surface resistance of superconductors-examples from nb-o systems,” Tech. Rep., 1988.
- [60] J. H. Takemoto, C. M. Jackson, R. Hu, J. F. Burch, K. P. Daly, and R. W. Simon, “Microstrip resonators and filters using high-t/sub c/superconducting thin films on laalo/sub 3,” *IEEE transactions on magnetics*, vol. 27, no. 2, pp. 2549–2552, 1991.

- [61] B. Lienhard, J. Braumüller, W. Woods, D. Rosenberg, G. Calusine, S. Weber, A. Vepsäläinen, K. O’Brien, T. P. Orlando, S. Gustavsson *et al.*, “Microwave packaging for superconducting qubits,” in *2019 IEEE MTT-S International Microwave Symposium (IMS)*. IEEE, 2019, pp. 275–278.
- [62] C. J. Burroughs, S. P. Benz, P. D. Dresselhaus, Y. Chong, and H. Yamamori, “Flexible cryo-packages for josephson devices,” *IEEE transactions on applied superconductivity*, vol. 15, no. 2, pp. 465–468, 2005.
- [63] S. Deshpande, J.-P. Paquette, M. Vahidpour, M. Selvanayagam, R. Lion, M. Pelstring, S. Caldwell, M. Reagor, and D. Russell, “Integrating high-density microwave signalling and packaging with superconducting qubits,” in *2019 IEEE MTT-S International Microwave Symposium (IMS)*. IEEE, 2019, pp. 271–274.
- [64] S. Krinner, S. Storz, P. Kurpiers, P. Magnard, J. Heinsoo, R. Keller, J. Luetolf, C. Eichler, and A. Wallraff, “Engineering cryogenic setups for 100-qubit scale superconducting circuit systems,” *EPJ Quantum Technology*, vol. 6, no. 1, p. 2, 2019.
- [65] M. Rigol, V. Dunjko, and M. Olshanii, “Thermalization and its mechanism for generic isolated quantum systems,” *Nature*, vol. 452, no. 7189, pp. 854–858, 2008.
- [66] R. Nandkishore and D. A. Huse, “Many-body localization and thermalization in quantum statistical mechanics,” *Annu. Rev. Condens. Matter Phys.*, vol. 6, no. 1, pp. 15–38, 2015.
- [67] J. Kysela, “Thermalization in quantum networks.”
- [68] E. Canovi, D. Rossini, R. Fazio, G. E. Santoro, and A. Silva, “Quantum quenches, thermalization, and many-body localization,” *Physical Review B*, vol. 83, no. 9, p. 094431, 2011.
- [69] A. L. Woodcraft, G. Ventura, V. Martelli, and W. S. Holland, “Thermal conductance at millikelvin temperatures of woven ribbon cable with phosphor-bronze clad superconducting wires,” *Cryogenics*, vol. 50, no. 8, pp. 465–468, 2010.
- [70] A. Harris, M. Sieth, J. Lau, S. Church, L. Samoska, and K. Cleary, “Note: Cryogenic microstripline-on-kapton microwave interconnects,” *Review of Scientific Instruments*, vol. 83, no. 8, p. 086105, 2012.
- [71] J. P. Smith, B. A. Mazin, A. B. Walter, M. Daal, J. Bailey III, C. Bockstiegel, N. Zobrist, N. Swimmer, S. Steiger, and N. Fruitwala, “Flexible coaxial ribbon cable for high-density superconducting microwave device arrays,” *IEEE Transactions on Applied Superconductivity*, vol. 31, no. 1, pp. 1–5, 2020.
- [72] A. B. Walter, C. Bockstiegel, B. A. Mazin, and M. Daal, “Laminated nbti-on-kapton microstrip cables for flexible sub-kelvin rf electronics,” *IEEE Transactions on Applied Superconductivity*, vol. 28, no. 1, pp. 1–5, 2017.

Appendices

Appendix A

Microwave Measurement of Thin Film Superconducting Resonator Structures with Different Linewidth

We fabricated weakly-coupled, superconducting microstrip resonators with different resonator trace linewidths - 50 μm , 100 μm and 150 μm . Fig. A.1 shows a plot of $1/Q$ (i.e., loaded Q) vs. resonant frequency for resonators with different trace linewidth, measured at multiple temperatures and frequencies. At 1.2 K, the Q_l values are similar for all three linewidths (the black markers in Fig. A.1). At higher temperatures, there is an increased difference in the Q_l value for resonators with different trace widths. Each data point on the graph represents an average of ten measurements with error bars to consider temperature drift in the pulse tube cryostat. The included ADS simulation results shown in Fig. A.1 are for simulated resonators with only coupling loss (i.e., with zero conductor loss and zero dielectric loss). From Fig. A.1 it can be seen that $1/Q_l$ values have a linear dependence on frequency, which is consistent with BCS superconductor resonator theory. According to BCS theory, the number of quasiparticles, which are responsible for energy loss in the system, decreases exponentially as the sample is cooled, which is evident from Fig. A.1, as the slope is reduced as the temperature is changed from 4.2 K to 1.2 K. The slope at a temperature of ~ 1.2 K is approaching zero since Nb at that temperature has a greatly-reduced quasi-particle loss and the Q_l is expected to be governed primarily, but not completely, by the dielectric loss. For resonators with different trace width, the loaded Q exhibited a measureable dependence on linewidth. We measured quality factors as high as $Q \sim 22\,500$ at 1.2 K. The results of this work are important for understanding loss and transmission properties of similarly designed and fabricated transmission line interconnects. .

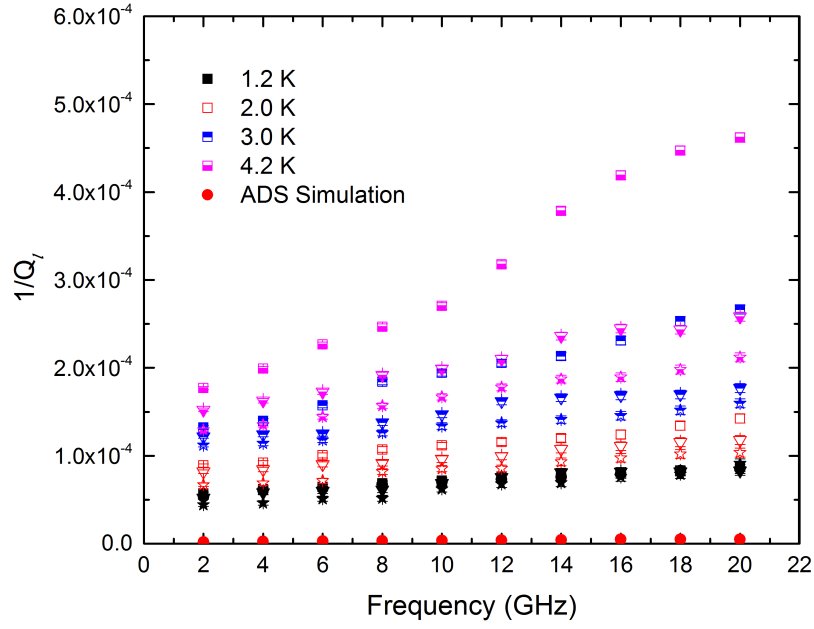


Figure A.1. $1/Q_l$ vs. resonant frequency for resonators with different linewidths at different temperatures. Square = $50 \mu\text{m}$, triangle = $100 \mu\text{m}$, star = $150 \mu\text{m}$, circle = ADS simulation with $\tan \delta = 0$ and zero conductor loss.

Appendix B

Moisture Effect on Microwave Performance of Microstrip Resonators on Polyimide

In order to study the effect of moisture, bake tests were performed on different resonator structures shown in chapter 5. In this test all three resonator configurations - embedded, non-embedded and embedded with barrier layer of Al_2O_3 were measured before and after baking in a vacuum oven at $90\text{ }^\circ\text{C}$ for 2 hr. In the following section the Q_l values for all resonators were recorded after they were exposed to a temperature of $250\text{ }^\circ\text{C}$. This is an extension of the work presented in section 5.2.

B.1 Embedded Resonator Structure

Fig. B.1 shows the plot of $1/Q$ vs. temperature before and after baking for the embedded resonator. A slight degradation in T_c from $\sim 6.7\text{ K}$ to $\sim 6.5\text{ K}$ can be observed as an effect of not baking the sample.

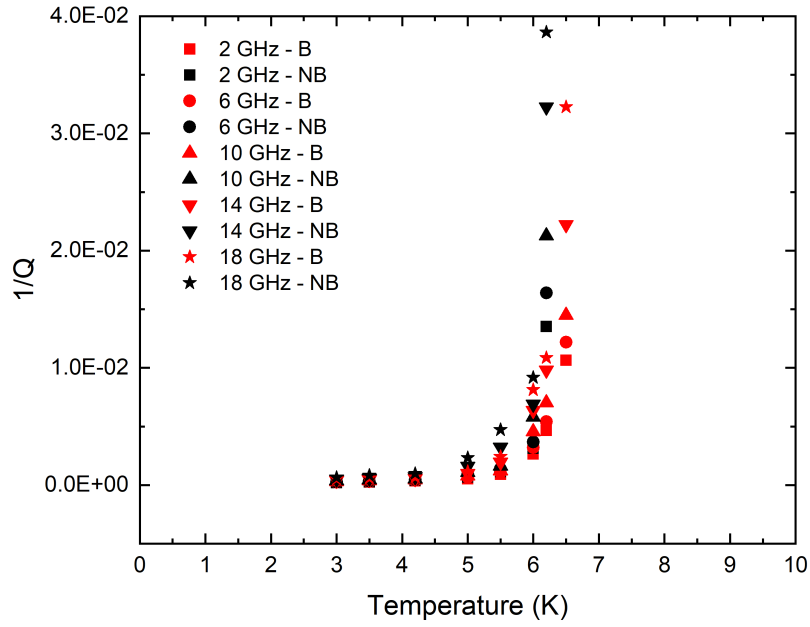


Figure B.1. $1/Q_l$ vs. Temperature plot before and after baking of an embedded sample at 250 °C.

Fig. B.2 shows the same data from the previous plot in log scale to better interpret the data points for each case.

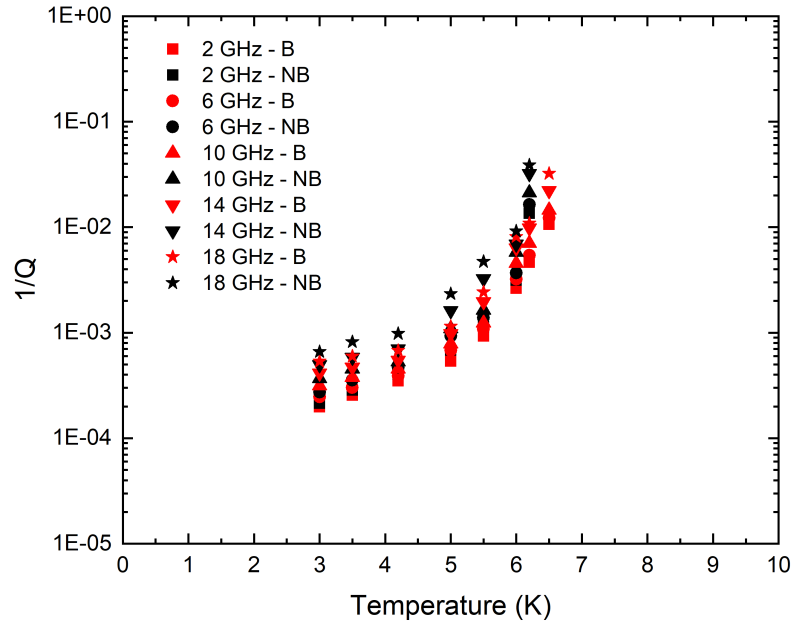


Figure B.2. $1/Q_l$ vs. Temperature plot before and after baking of an embedded sample at 250 °C on a log scale.

B.2 Non-embedded Resonator Structure

Fig. B.3 shows the plot of $1/Q_l$ vs. temperature before and after baking for the non-embedded resonator. Similar to the case embedded resonator, minimal amount of degradation in T_c from ~ 7.2 K to ~ 7 K can be observed as an effect of not baking the sample.

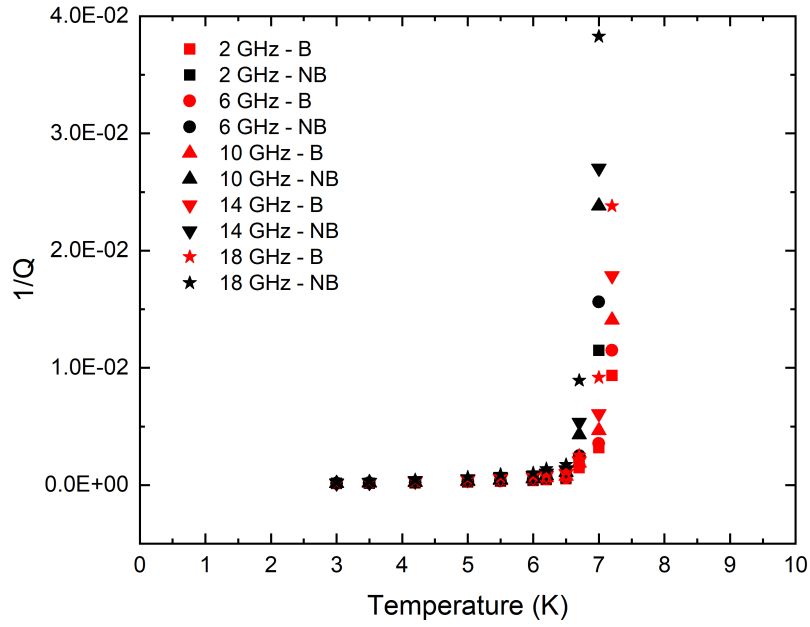


Figure B.3. $1/Q_t$ vs. Temperature plot before and after baking of non-embedded sample at 250 °C.

Fig. B.4 shows the same data from the previous plot in log scale to better interpret the data points for each case.

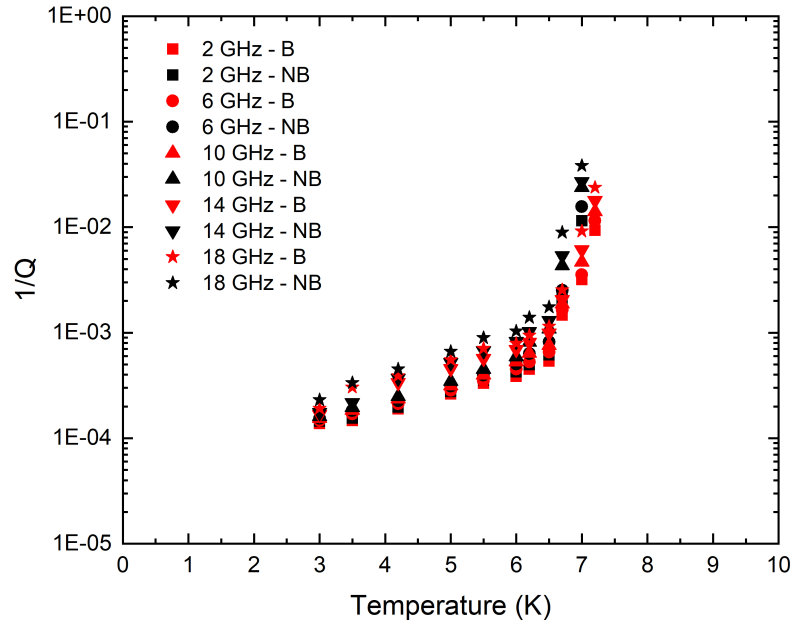


Figure B.4. $1/Q_l$ vs. Temperature plot before and after baking of non-embedded sample at 250 °C on a log scale.

B.3 Embedded Resonator Structure With a Barrier Layer of Al_2O_3

Fig. B.5 shows the plot of $1/Q_l$ vs. temperature before and after baking for the embedded resonator with barrier layer of Al_2O_3 . A similar trend was seen in the degradation of T_c from ~ 8.2 K to ~ 8 K.

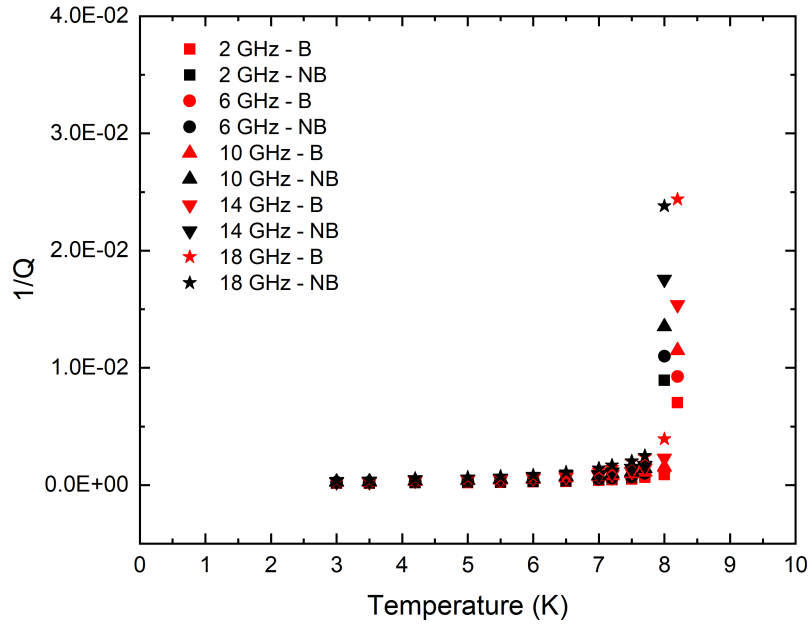


Figure B.5. $1/Q_l$ vs. Temperature plot before and after baking of $\text{Al}_2\text{O}_3/\text{Nb}/\text{Al}_2\text{O}_3$ sample at 250 °C.

Fig. B.6 shows the same data from the previous plot in log scale to better interpret the data points for each case.

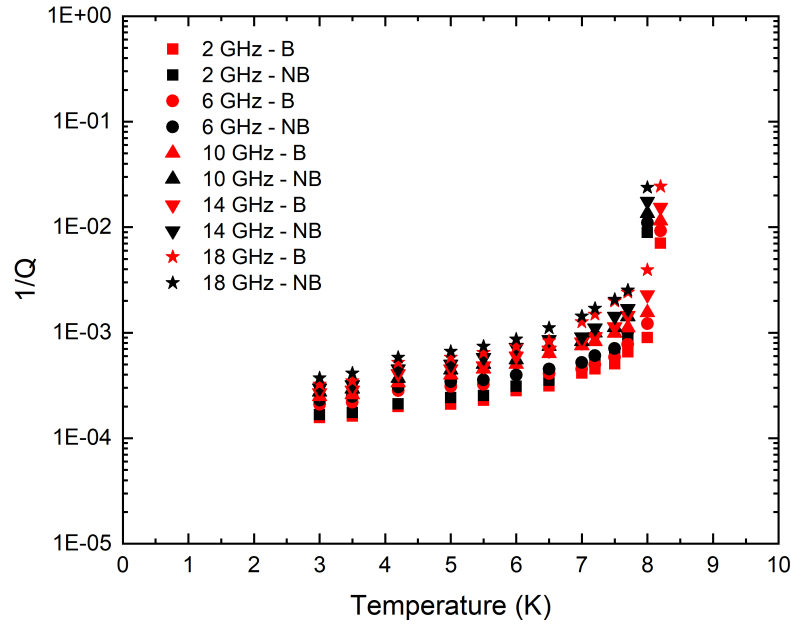


Figure B.6. $1/Q_l$ vs. Temperature plot before and after baking of $\text{Al}_2\text{O}_3/\text{Nb}/\text{Al}_2\text{O}_3$ sample at 250 °C on a log scale.

This test demonstrates that all three resonator configurations were sensitive to moisture. Therefore baking of samples in vacuum oven is necessary for precise microwave performance. As a standard practice, all the resonators used in this work were baked at 90 °C for 2 hr prior to making measurements in the PT.

Appendix C

Fabrication Travelers

This section illustrates detailed and step by step information of multiple fabricated structures used in this work.

Step #	Process	Process parameters
1	Dehydration bake	120 °C for 30 mins
2	HMDS	While wafers are warm, transfer to HMDS bell jar for 10 mins
3	Spin coat	PR: AZ 9245 1. Spread: 1700 RPM for 5 seconds. 500 RPM/s 2. Spin speed: 2200 RPM Acceleration: 1000 RPM/s Time=25 seconds
4	Soft bake	Soft bake & 110 C on hot plate for 90 seconds (1 minute and 30 seconds)
5	Mask Alignment	Mask alignment & Exposure time: 30 seconds on channel 2 (2mW/cm ²)
6	Development	Development & 3:1 DI water: AZ 400K Developer, 1 min and 10 second, watch carefully the development, shake 1-5 sec before transferring into DI water, rinsing 5 min., N ₂ blow dry
7	Metal deposition	Metal deposition & Base Pressure: < 3.0 x 10 ⁻⁶ Torr (a) 2 minutes of ion milling (b) 5 mins pre-sputter followed by 30 mins sputter
8	Lift-off	Lift-off & Rinse in Methanol/IPA/Water. Use Profilometry to determine Nb thickness

Figure C.1. Traveler for T_c and I_c measurements of Nb.

Step #	Process	Process parameters
1	Dehydration bake	120 °C for 30 mins
2	Spin coat	HD-4110: 1. Spin speed 500 RPM. ACC. 500 rpm/s time=5 secs. 2. 1700 RPM Acc. 1000 RPM/s Time=30 secs.
3	Soft bake 1	90 C for 180 s
4	Soft bake 2	110 C for 180 s
5	Development	(Wait 1 hour before developing) PA-401D and PA-400R. Followed by N2 Dry.
6	Cure In N2 Oven	Profile 7: 1. 90°C, 30 min ramp @ 10°C/min 2. 120°C, 30 min, ramp @ 10°C/min 3. 375°C, 60 min ramp @ 20°C/min 4. Cool back to RT in N2
Signal layer		
7	Dehydration bake	110 °C for 30 mins in oven
8	Spin coat	PR: AZ 9245 1. Spread: 1700 RPM for 5 seconds. 500 RPM/s 2. Spin speed: 2200 RPM Acceleration: 1000 RPM/s Time=25 seconds
9	Soft bake	110 C for 90 s
10	Alignment	Exposure : 45s
11	Development	Developer. 1: 3 developer, 100 mL AZ400K: 300 mL DI H2O. 1 min 30 sec in developer. Followed by 2 min. DI Water Rinse. N2 Dry.
12	Metal deposition	Base Pressure: < 3.0 x 10 ⁻⁶ Torr (a) 2 minutes of ion milling (b) 5 mins pre-sputter followed by 30 mins sputter
Under bump metallization (UBM)		
13	Dehydration bake	110 °C for 30 mins in oven
14	Spin coat	PR: AZ 9245 1. Spread: 1700 RPM for 5 seconds. 500 RPM/s 2. Spin speed: 2200 RPM Acceleration: 1000 RPM/s Time=25 seconds
15	Soft bake	110 C for 90 s
16	Alignment	Exposure : 60s
17	Development	Developer. 1: 3 developer, 100 mL AZ400K: 300 mL DI H2O. 1 min 30 sec in developer. Followed by 2 min. DI Water Rinse. N2 Dry.
18	Metal Deposition	Deposition of Ti (50 nm)/Cu (250 nm)/Au/(10 nm)
19	Lift-Off	Rinse in Acetone/IPA. Followed by 2 min. DI Water Rinse/N2 Dry.
Top protective polyimide (PI)		
20	Dehydration bake	110 °C for 30 mins in oven
21	Polyimide Spin	HD-4100: 1. Spin speed 500 RPM. ACC. 500 rpm/s time=5 secs. 2. 6000 RPM Acc. 1000 RPM/s, Time=30 secs
22	Soft Bake 1	90 °C for 100 seconds
23	Soft Bake 2	100°C for 100 seconds
24	Alignment	Exposure : 18s
25	Development	(Wait 1 hour before developing) PA-401D and PA-400R. Followed by N2 Dry.

Figure C.2. Resonator Traveler-1/2.

26	Cure	Profile 6: 1. 90°C, 30 min ramp @ 10°C/min 2. 120°C, 30 min, ramp @ 10°C/min 3. 225°C, 60 min ramp @ 20°C/min 4. Cool back to RT in N2
27	Release Sample	Using Excimer laser
28	Invert sample	Mount the sample to a wafer
29	Backplane deposition	Base Pressure: $< 3.0 \times 10^{-6}$ Torr (a) 2 minutes of ion milling (b) 5 mins pre-sputter followed by 30 mins sputter

Figure C.3. Resonator Traveler-2/2.

Step #	Process	Process parameters
Release layer		
1	Metal deposition	Deposition of Cr/Al for release layer
HD-4100 Protective layer		
2	Dehydration bake	110 °C for 30 mins in oven
3	Polyimide Spin	HD-4100: 1. Spin speed 500 RPM. ACC. 500 rpm/s time=5 secs. 2. 6000 RPM Acc. 1000 RPM/s, Time=30 secs
4	Soft Bake 1	90 °C for 100 seconds
5	Soft Bake 2	100°C for 100 seconds
6	Alignment	Exposure : 18s
7	Development	(Wait 1 hour before developing) PA-401D and PA-400R. Followed by N2 Dry.
8	Cure	Profile 7: 1. 90°C, 30 min ramp @ 10°C/min 2. 120°C, 30 min, ramp @ 10°C/min 3. 375°C, 60 min ramp @ 20°C/min 4. Cool back to RT in N2
Ground layer		
9	Dehydration bake	110 °C for 30 mins in oven
10	Spin coat	PR: AZ 9245 1. Spread: 1700 RPM for 5 seconds. 500 RPM/s 2. Spin speed: 2200 RPM Acceleration: 1000 RPM/s Time=25 seconds
11	Soft bake	110 C for 90 s
12	Alignment	Exposure : 45s
13	Development	Developer. 1: 3 developer, 100 mL AZ400K: 300 mL DI H2O. 1 min 30 sec in developer. Followed by 2 min. DI Water Rinse. N2 Dry.
14	Metal deposition	Deposition of Al/Nb/Al for bottom ground plane
Catch pads for electroplating		
15	Dehydration bake	110 °C for 30 mins in oven
16	Spin coat	PR: AZ 9245 1. Spread: 1700 RPM for 5 seconds. 500 RPM/s 2. Spin speed: 2200 RPM Acceleration: 1000 RPM/s Time=25 seconds
17	Soft bake	110 C for 90 s
18	Alignment	Exposure : 45s
19	Development	Developer. 1: 3 developer, 100 mL AZ400K: 300 mL DI H2O. 1 min 30 sec in developer. Followed by 2 min. DI Water Rinse. N2 Dry.
20	Metal Deposition	Deposition of Ti (50 nm)/Cu (250 nm)/
21	Lift-Off	Rinse in Acetone/IPA. Followed by 2 min. DI Water Rinse/N2 Dry.
Via openings – HD-4110 (1)		
22	Dehydration bake	110 °C for 30 mins in oven
23	Polyimide Spin	HD-4110: 1. Spin speed 500 RPM. ACC. 500 rpm/s time=5 secs. 2. 1900 RPM Acc. 1000 RPM/s, Time=30 secs

Figure C.4. stripline Traveler-1/4.

24	Soft Bake 1	90 °C for 180 seconds
25	Soft Bake 2	110°C for 180 seconds
26	Alignment	Exposure : 18s
27	Development	(Wait 1 hour before developing) PA-401D and PA-400R. Followed by N2 Dry.
28	Cure	Profile 6: 1. 90°C, 30 min ramp @ 10°C/min 2. 120°C, 30 min, ramp @ 10°C/min 3. 225°C, 60 min ramp @20°C/min 4. Cool back to RT in N2
29	Plasma descum	1 min O2 plasma
30	Clean oxide of Cu before plating	50:1 (DI water: HCl)
31	Electroplate	Electroplate Cu for 20 µm using direct current plating
Signal layer		
32	Dehydration bake	110 °C for 30 mins in oven
33	Spin coat	PR: AZ 9245 1. Spread: 1700 RPM for 5 seconds. 500 RPM/s 2. Spin speed: 2200 RPM Acceleration: 1000 RPM/s Time=25 seconds
34	Soft bake	110 C for 90 s
35	Alignment	Exposure : 45s
36	Development	Developer. 1: 3 developer, 100 mL AZ400K: 300 mL DI H2O. 1 min 30 sec in developer. Followed by 2 min. DI Water Rinse. N2 Dry.
37	Metal deposition	Deposition of Al/Nb/Al for bottom ground plane
Catch pad on top of signal layer		
38	Dehydration bake	110 °C for 30 mins in oven
39	Spin coat	PR: AZ 9245 1. Spread: 1700 RPM for 5 seconds. 500 RPM/s 2. Spin speed: 2200 RPM Acceleration: 1000 RPM/s Time=25 seconds
40	Soft bake	110 C for 90 s
41	Alignment	Exposure : 45s
42	Development	Developer. 1: 3 developer, 100 mL AZ400K: 300 mL DI H2O. 1 min 30 sec in developer. Followed by 2 min. DI Water Rinse. N2 Dry.
43	Metal Deposition	Deposition of Ti (50 nm)/Cu (250 nm)/
44	Lift-Off	Rinse in Acetone/IPA. Followed by 2 min. DI Water Rinse/N2 Dry.
Via openings – HD-4110 (2)		
45	Dehydration bake	110 °C for 30 mins in oven
46	Polyimide Spin	HD-4110: 1. Spin speed 500 RPM. ACC. 500 rpm/s time=5 secs. 2. 1900 RPM Acc. 1000 RPM/s, Time=30 secs
47	Soft Bake 1	90 °C for 180 seconds
48	Soft Bake 2	110°C for 180 seconds
49	Alignment	Exposure : 18s

Figure C.5. stripline Traveler-2/4.

50	Development	(Wait 1 hour before developing) PA-401D and PA-400R. Followed by N2 Dry.
51	Cure	Profile 6: 1. 90°C, 30 min ramp @ 10°C/min 2. 120°C, 30 min, ramp @ 10°C/min 3. 225°C, 60 min ramp @ 20°C/min 4. Cool back to RT in N2
52	Plasma descum	1 min O2 plasma
53	Clean oxide of Cu before plating	50:1 (DI water: HCl)
54	Electroplate	Electroplate Cu for 20 µm using direct current plating
Top Ground		
55	Dehydration bake	110 °C for 30 mins in oven
56	Spin coat	PR: AZ 9245 1. Spread: 1700 RPM for 5 seconds. 500 RPM/s 2. Spin speed: 2200 RPM Acceleration: 1000 RPM/s Time=25 seconds
57	Soft bake	110 C for 90 s
58	Alignment	Exposure : 45s
59	Development	Developer. 1: 3 developer, 100 mL AZ400K: 300 mL DI H2O. 1 min 30 sec in developer. Followed by 2 min. DI Water Rinse. N2 Dry.
60	Metal deposition	Deposition of Al/Nb/Al for bottom ground plane
Top Protective PI – HD-4100		
61	Dehydration bake	110 °C for 30 mins in oven
62	Polyimide Spin	HD-4100: 1. Spin speed 500 RPM. ACC. 500 rpm/s time=5 secs. 2. 6000 RPM Acc. 1000 RPM/s, Time=30 secs
63	Soft Bake 1	90 °C for 100 seconds
64	Soft Bake 2	100°C for 100 seconds
65	Alignment	Exposure : 18s
66	Development	(Wait 1 hour before developing) PA-401D and PA-400R. Followed by N2 Dry.
67	Cure	Profile 6: 1. 90°C, 30 min ramp @ 10°C/min 2. 120°C, 30 min, ramp @ 10°C/min 3. 225°C, 60 min ramp @ 20°C/min 4. Cool back to RT in N2
UBM contacts for signal and ground connections		
68	Dehydration bake	110 °C for 30 mins in oven
69	Spin coat	PR: AZ 9245 1. Spread: 1700 RPM for 5 seconds. 500 RPM/s 2. Spin speed: 2200 RPM Acceleration: 1000 RPM/s Time=25 seconds
70	Soft bake	110 C for 90 s
71	Alignment	Exposure : 60s
72	Development	Developer. 1: 3 developer, 100 mL AZ400K: 300 mL DI H2O. 1 min 30 sec in developer. Followed by 2 min. DI Water Rinse. N2 Dry.
73	Metal Deposition	Deposition of Ti (50 nm)/Cu (250 nm)/Au/(10 nm)
74	Lift-Off	Rinse in Acetone/IPA. Followed by 2 min. DI Water Rinse/N2 Dry.
Release samples of the wafer		
75	Dehydration bake	110 °C for 30 mins in oven

Figure C.6. stripline Traveler-3/4.

76	Spin coat	PR: AZ 9245 1. Spread: 1700 RPM for 5 seconds. 500 RPM/s 2. Spin speed: 2200 RPM Acceleration: 1000 RPM/s Time=25 seconds
77	Soft bake	110 C for 90 s
78	Wafer dice	Dice silicon using diamond blade
79	Release solution	Make solution consisting of 700 mL of H ₂ O, 81.9 g of NaCl and mix with stir bar.
80	Release sample	Bias wafer at 0.6 V in a salt solution

Figure C.7. stripline Traveler-4/4.

Step #	Process	Process parameters
Signal layer		
1	Dehydration bake	110 °C for 30 mins in oven
2	Spin coat	PR: AZ 9245 1. Spread: 1700 RPM for 5 seconds. 500 RPM/s 2. Spin speed: 2200 RPM Acceleration: 1000 RPM/s Time=25 seconds
3	Soft bake	110 C for 90 s
4	Alignment	Exposure : 45s
5	Development	Developer. 1: 3 developer, 100 mL AZ400K: 300 mL DI H2O. 1 min 30 sec in developer. Followed by 2 min. DI Water Rinse. N2 Dry.
6	Metal deposition	Deposit Nb (250 nm)/Cr (20 nm) or Deposit Nb (250 nm)/Cr (10 nm) or Deposit Nb (250 nm)/Ta (20 nm) or Deposit Nb (250 nm)/Ta (50 nm) or Deposit Nb (250 nm)/Al (20 nm) or Deposit Nb (250 nm)/Al (10 nm)
7	Lift-off	Lift-off & Rinse in Methanol/IPA/Water. Use Profilometry to determine Nb thickness
Polyimide layer (PI-2611)		
8	Dehydration bake	120 °C for 30 mins
9	Adhesion Promoter	Adhesion Promoter: VM652 Spin speed: 1. 500 RPM Acc. 500 rpm/s time=5 secs. 2. 4000 RPM Acc. 1000 rpm/s time=30 secs
10	Soft Bake	120 °C for 60 seconds on hot plate
11	Polyimide spin	PI-2611: 1. Spin speed 500 RPM. ACC. 500 rpm/s time=5 secs. 2. 1600 RPM Acc. 1000 RPM/s time=30 secs
12	Soft bake	120 °C for 5 minutes on hot plate
13	Cure in N2 oven	Profile 2: 1. 90°C, 30 min ramp @ 10°C/min (1hr) 2. 120°C, 30 min, ramp @ 10°C/min (1hr) 3. 350°C, 60 min ramp @20°C/min (3hr). 4. Cool back to RT in N2

Figure C.8. Different barrier layer to protect Nb.

Step #	Process	Process parameters
Signal layer		
1	Dehydration bake	110 °C for 30 mins in oven
2	Spin coat	PR: AZ 9245 1. Spread: 1700 RPM for 5 seconds. 500 RPM/s 2. Spin speed: 2200 RPM Acceleration: 1000 RPM/s Time=25 seconds
3	Soft bake	110 C for 90 s
4	Alignment	Exposure : 45s
5	Development	Developer. 1: 3 developer, 100 mL AZ400K: 300 mL DI H2O. 1 min 30 sec in developer. Followed by 2 min. DI Water Rinse. N2 Dry.
6	Metal deposition	Deposit Nb (250 nm)
7	Lift-off	Lift-off & Rinse in Methanol/IPA/Water. Use Profilometry to determine Nb thickness
Polyimide layer (PI-2611)		
8	Dehydration bake	120 °C for 30 mins
9	Adhesion Promoter	Adhesion Promoter: VM652 Spin speed: 1. 500 RPM Acc. 500 rpm/s time=5 secs. 2. 4000 RPM Acc. 1000 rpm/s time=30 secs
10	Soft Bake	120 °C for 60 seconds on hot plate
11	Polyimide spin	PI-2611: 1. Spin speed 500 RPM. ACC. 500 rpm/s time=5 secs. 2. 1600 RPM Acc. 1000 RPM/s time=30 secs
12	Soft bake	120 °C for 5 minutes on hot plate
13	Cure in N2 oven	Profile 2: 1. 90°C, 30 min ramp @ 10°C/min (1hr) 2. 120°C, 30 min, ramp @ 10°C/min (1hr) 3. 225 °C, 60 min ramp @20°C/min (2hr). 4. Cool back to RT in N2
14	Cure in N2 oven	Profile 2: 1. 90°C, 30 min ramp @ 10°C/min (1hr) 2. 120°C, 30 min, ramp @ 10°C/min (1hr) 3. 235 °C, 60 min ramp @20°C/min (2hr). 4. Cool back to RT in N2
15	Cure in N2 oven	Profile 2: 1. 90°C, 30 min ramp @ 10°C/min (1hr) 2. 120°C, 30 min, ramp @ 10°C/min (1hr) 3. 245 °C, 60 min ramp @20°C/min (2hr). 4. Cool back to RT in N2
16	Cure in N2 oven	Profile 2: 1. 90°C, 30 min ramp @ 10°C/min (1hr) 2. 120°C, 30 min, ramp @ 10°C/min (1hr) 3. 255 °C, 60 min ramp @20°C/min (2hr). 4. Cool back to RT in N2

Figure C.9. Different curing temperatures of PI-2611.

Step #	Process	Process parameters
Signal layer		
1	Dehydration bake	110 °C for 30 mins in oven
2	Spin coat	PR: AZ 9245 1. Spread: 1700 RPM for 5 seconds. 500 RPM/s 2. Spin speed: 2200 RPM Acceleration: 1000 RPM/s Time=25 seconds
3	Soft bake	110 C for 90 s
4	Alignment	Exposure : 45s
5	Development	Developer. 1: 3 developer, 100 mL AZ400K: 300 mL DI H2O. 1 min 30 sec in developer. Followed by 2 min. DI Water Rinse. N2 Dry.
6	Metal deposition	Deposit Nb (250 nm)/Cr (20 nm) or Deposit Nb (250 nm)/Cr (10 nm) or Deposit Nb (250 nm)/Ta (20 nm) or Deposit Nb (250 nm)/Ta (50 nm) or Deposit Nb (250 nm)/Al (20 nm) or Deposit Nb (250 nm)/Al (10 nm)
7	Lift-off	Lift-off & Rinse in Methanol/IPA/Water. Use Profilometry to determine Nb thickness
Polyimide layer (AL-X)		
8	Dehydration bake	120 °C for 30 mins
9	Adhesion Promoter	AGC AP903: 1. 500 RPM Acc. 500 RPM/s t= 5 seconds time=5 secs 2. 2500 RPM Acc. 1000 RPM/S t=30 seconds
10	Soft Bake	100 °C for 90 seconds on hot plate
11	AL-X spin	AL-X: 1. 500 RPM Acc. 500 RPM/s t= 5 secs. 2. 1000 RPM Acc. 1000 RPM/s t = 30 secs
12	Soft bake	120 °C for 5 minutes on hot plate
13	Cure in N2 oven	Profile 2: 1. 90°C, 30 min ramp @ 10°C/min (1hr) 2. 120°C, 30 min, ramp @ 10°C/min (1hr) 3. 190°C, 60 min ramp @20°C/min (2hr). 4. Cool back to RT in N2

Figure C.10. Different barrier layer after curing AL-X.